Quantitative Evaluation of Ultrasonic Wave Propagation in Inhomogeneous Anisotropic Austenitic Welds using 3D Ray Tracing Method: Numerical and Experimental Validation

vorgelegt von
Master of Technology
Sanjeevareddy Kolkoori
aus Hyderabad, Indien

von der Fakultät V - Verkehrs- und Maschinensysteme
der Technischen Universität Berlin
zur Erlangung des akademischen Grades
Doktor der Ingenieurwissenschaften
Dr.-Ing.
genehmigte Dissertation

Promotionsausschuss:

Vorsitzender: Prof. Dr.-Ing. Jörg Krüger, TU Berlin
Gutachter: Prof. Dr.-Ing. Michael Rethmeier, TU Berlin
Gutachter: Dir. u. Prof. Dr. habil. Marc Kreutzbruck, BAM Berlin

Tag der wissenschaftlichen Aussprache: 10. April 2013

Berlin 2013

D 83

Declaration

I hereby declare that this thesis has not been previously submitted as an exercise for a degree at this or any other university. Except where otherwise acknowledged, the research is entirely the work of the author.

To succeed in your mission, you must have single-minded devotion to your goal.

Abdul Kalam

Dedicated to my beloved parents

Acknowledgements

I would like to express first and foremost gratitude towards my doctoral thesis supervisor Dir. u. Prof. Dr. rer. nat. habil. Marc Kreutzbruck**,** Head, Acoustical and Electromagnetic Methods, Department of Non-Destructive Testing, Bundesanstalt für Materialforschung und - prüfung (BAM) for giving me an opportunity to carry out my Ph.D work at BAM and his excellent guidance, moral support and continuous encouragement throughout my Ph.D work.

It is with deep attitude that I express my sincere thanks to Univ. -Prof. Dr. -Ing. Michael Rethmeier, Head, Safety of Joined Components, Technical University Berlin for his valuable suggestions and continuous encouragement throughout this research project. I also wish to thank him for accepting to be reviewer of this dissertation.

I would like to thank Univ.-Prof. Dr.-Ing. Jörg Krüger, Head, Industrial Automation Technology, Institut für Werkzeugmaschinen und Fabrikbetrieb (IWF), Technical University Berlin for accepting to be the chairman of my doctoral thesis examination committee.

I take this opportunity to express my sincere thanks to my advisor Dr.-Ing. Jens Prager, Acoustical and Electromagnetic methods, BAM, for his valuable guidance and enlightening discussions during the course of this research work.

This work was financially supported by BMWi (Bundesministerium fur Wirtschaft und Technologie) under the grant 1501365 which is gratefully acknowledged.

I express my heartfelt thanks to Dipl.-Phys. Rainer Boehm and Dr.-Ing. Gerhard Brekow for sharing their scientific knowledge and experience in the area of ultrasonic inspection of austenitic weld materials. Dr.-Ing. Mehbub and Dipl.-Phys. C. Hoehne deserve special acknowledgement for their perseverance invaluable assistance in validating the simulation results with experiments. I would also like to thank Dr.-Ing.

P.K. Chinta and Dr. P. Shokouhi for their helpful discussions in validating ray tracing results with EFIT and CIVA simulation results.

I sincerely thank Dr.-Ing. V.K. Munikoti from ALSTOM Power Industries Berlin and Dipl.-Ing. U. Völz for helping me in understanding the theoretical concepts in anisotropic materials. I also thank Ing. W. Gieschler for his readiness to help in solving system administration problems. My special thanks to Ms R. Gierke and Ms R. Kotlow for helping me out many secretarial jobs and in preparing excellent quality diagrams. My sincere thanks to Dr. Norma Wrobel for her kind help and support at numerous times. I thank my friends Kishore, Purv, Maalolan, Santhosh and Kirthi for their scientific help and refreshing discussion with topics 'The source of superior energies' and 'Nectar of devotion'.

My parent's K. Lakshmi and K. Yadava reddy and their love, affection and immutable support for every endeavor of mine have made me all that I am today. I wish to thank my brothers K.Narasimha reddy, K. Shyamsunder reddy and my sister Sukanya for their support and encouragement on my way to explore myself and for enabling my education and my academic career. Finally, I would like to express my profound gratitude to the almighty. He has blessed me with a wonderful family and a great place to carry out my Ph.D work.

Zusammenfassung

Austenitische Schweißnähte und Mischnähte werden aufgrund ihrer hohen Bruchfestigkeit und ihres Widerstands gegen Korrosion und Risswachstum bei hohen Temperaturen bevorzugt in Rohrleitungen und Druckbehältern von Kernkraftwerken, Anlagen der chemischen Industrie und Kohlekraftwerken eingesetzt. Während des Herstellungsprozesses oder durch im Betrieb auftretende mechanische Spannungen können sich jedoch Risse bilden, weshalb die Überwachung des Zustandes dieser Materialien unter Einsatz zuverlässiger zerstörungsfreier Prüfmethoden von großer Wichtigkeit ist.

Die zerstörungsfreie Ultraschallprüfung austenitischer Schweißnähte und Mischnähte wird durch anisotrope Stängelkristallstrukturen erschwert, welche zur Teilung und Ablenkung des Schallbündels führen können. Simulationsprogramme spielen in der Entwicklung fortschrittlicher Prüfverfahren und der Optimierung der Parameter für die Prüfung derartiger Schweißnähte eine bedeutende Rolle.

Das Hauptziel dieser Dissertation besteht in der Entwicklung eines 3D Ray-Tracing Modells zur quantitativen Auswertung der Ultraschallwellenausbreitung in inhomogenen anisotropen Füllmaterialien von Schweißnähten. Die Inhomogenität der Schweißnähte wird durch eine Diskretisierung in mehrere homogene Schichten abgebildet. Gemäß des Ray-Tracing Modells, werden die Strahlverläufe des Ultraschalls im Sinne der Energieausbreitung durch die verschiedenen Schichten verfolgt und an jeder Grenzfläche Reflexion und Transmission berechnet. Der Einfluss der Anisotropie auf das Reflexions- und Transmissionsverhalten von Ultraschall in austenitischen Schweißnähten wird quantitativ in allen drei Raumrichtungen untersucht. Die Richtcharakteristik von Ultraschallquellen in der Stängelkristallstruktur austenitischer Stähle, wird dabei im dreidimensionalen Fall durch das Lamb'sche Reziprozitätsgesetz bestimmt. Das entwickelte Ray-Tracing Modells erlaubt eine Auswertung des vom Sender erzeugten Ultraschallfeldes unter Berücksichtigung der Richtcharakteristik des Senders, der Divergenz des Strahlbündels, der Strahldichte und der Phasenbeziehungen sowie der

Transmissionskoeffizienten mit hoher Genauigkeit. Das Ray-Tracing Modell ist im Stande sowohl die von einer Punktquelle, als auch die von einem ausgedehntem Phased-Array Prüfkopf erzeugten Schallfelder zu bestimmen.

Der Einfluss der Inhomogenität auf die Ultraschallausbreitung und die Wechselwirkung des Schallfeldes mit Materialfehlern in austenitischen Schweißnähten sowie die Anwendung des 3D-Ray-Tracing Modells zur Optimierung experimenteller Parameter während der zerstörungsfreien Ultraschallprüfung auf Querfehler in austenitischen Schweißnähten werden dargestellt.

Ultraschall-C-Bilder in homogenen und aus verschiedenen Schichten aufgebauten Blöcken aus anisotropen austenitischen Stählen werden unter Verwendung eines neuartigen 3D Ray-Tracing Verfahrens quantitativ ausgewertet. Der Einfluss der Stängelkristallstruktur und des Layback-Winkels auf Ultraschall-C-Bilder in der praktischen Prüfung anisotroper Materialen wird dargestellt.

Die Ergebnisse des Ray-Tracing Modells werden quantitativ gegen Ergebnisse validiert, die mit der 2D Elastodynamic Finite Integration Technique (EFIT) an verschiedenen wichtigen Testfällen, wie anisotropem und homogenem austenitischen Stahl, Schichtstrukturen aus austenitischen Stählen und Schweißnahtstrukturen gewonnen wurden, welche in der Praxis der zerstörungsfreien Ultraschallprüfung anisotroper Materialien auftreten. Dabei wird festgestellt, dass die Abweichungen von der Ultraschallquelle abhängen. Quantitative betragen diese 8,6% für die punktquelle und 10,2% für die Phased-Array Prüfköpfe.

Die unter Verwendung des Ray-Tracing Verfahrens gewonnenen Vorhersagen über Schallfelder für Phased-Array Prüfköpfe in einem inhomogenem, anisotropen Schweißnahtmaterial mit räumlich veränderlicher Stängelkristallstruktur, werden gegen die Ergebnisse einer kommerziellen Simulationssoftware (CIVA) validiert. Mit dem Ray-Tracing Model wird eine Übereinstimmung von 89,5% erzielt.

Experimente wurden an 32 mm hohen austenitischen Schweißnähten und 62 mm dicken plattierten Testkörpern durchgeführt, wobei die Verzerrung und das Profil der Ultraschallfelder mit Hilfe einer elektrodynamischen Sonde quantitativ bestimmt wurden. Die Inhomogenität der Schweißnahtstruktur wurde basierend auf den von Ogilvy gefundenen empirischen Formeln modelliert. Die Modellparameter wurden dabei dahingehend optimiert, dass die Modellstruktur eine möglichst gute Übereinstimmung mit dem Schliffbild der realen Schweißnaht im verwendeten Testkörper liefert. Ultraschallausbreitung und die Profile der Ultraschallfelder werden unter Verwendung des Ray-Tracing Modells mit hoher Genauigkeit berechnet. Die mittels Ray-Tracing Verfahren entlang der Unterseite eines Testkörpers mit austenitischer Schweißnaht und austenitischer Pufferung simulierten Profile der Ultraschallfelder, werden quantitativ mit den experimentellen Daten verglichen. Für die Simulation ergib sich eine Abweichung von 5,2% für das isotropische austenitische Material, 16,5% für die austenitische Schweißnaht und 5,46% für das austenitische plattierte Material gegenüber den experimentellen Ergebnissen. Abschließend werden die Unterschiede zwischen der Simulation und den experimentellen Ergebnissen erläutert.

Abstract

Austenitic welds and dissimilar welds are extensively used in primary circuit pipes and pressure vessels in nuclear power plants, chemical industries and fossil fuelled power plants because of their high fracture toughness, resistance to corrosion and creep at elevated temperatures. However, cracks may initiate in these weld materials during fabrication process or stress operations in service. Thus, it is very important to evaluate the structural integrity of these materials using highly reliable non-destructive testing (NDT) methods.

Ultrasonic non-destructive inspection of austenitic welds and dissimilar weld components is complicated because of anisotropic columnar grain structure leading to beam splitting and beam deflection. Simulation tools play an important role in developing advanced reliable ultrasonic testing (UT) techniques and optimizing experimental parameters for inspection of austenitic welds and dissimilar weld components.

The main aim of the thesis is to develop a 3D ray tracing model for quantitative evaluation of ultrasonic wave propagation in an inhomogeneous anisotropic austenitic weld material. Inhomogenity in the anisotropic weld material is represented by discretizing into several homogeneous layers. According to ray tracing model, ultrasonic ray paths are traced during its energy propagation through various discretized layers of the material and at each interface the problem of reflection and transmission is solved. The influence of anisotropy on ultrasonic reflection and transmission behaviour in an anisotropic austenitic weld material are quantitatively analyzed in three dimensions. The ultrasonic beam directivity in columnar grained austenitic steel material is determined three dimensionally using Lamb's reciprocity theorem. The developed ray tracing model evaluates the transducer excited ultrasonic fields accurately by taking into account the directivity of the transducer, divergence of the ray bundle, density of rays and phase relations as well as transmission coefficients. The ray tracing model is able to determine the ultrasonic wave fields generated by a point source as well as finite dimension array transducers.

The influence of inhomogenity on ultrasonic ray propagation and its interaction with defects in inhomogeneous austenitic welds is presented. The applications of 3D ray tracing model for optimizing experimental parameters during the ultrasonic non-destructive testing of transversal cracks in austenitic welds are presented. An ultrasonic C-scan image in homogeneous and multi-layered anisotropic austenitic steel materials is quantitatively evaluated using a novel 3D ray tracing method. The influence of the columnar grain orientation and the layback orientation on an ultrasonic C-scan image is presented. The ray tracing model results are validated first time quantitatively with the results obtained from 2D Elastodynamic Finite Integration Technique (EFIT) on several important configurations such as anisotropic and homogeneous austenitic steel material, layered austenitic steel material and austenitic weld material which are generally occurring in the ultrasonic non-destructive testing of anisotropic materials. Quantitatively a deviation of 8.6% was observed in the point source generated ultrasonic fields whereas in the case of array source ultrasound fields a deviation of 10.2% was observed. The predicted ultrasonic fields for array transducers in an inhomogeneous austenitic weld material with spatially varying columnar grain orientation using ray tracing method are validated against the results of a commercially available NDT simulation tool (CIVA). The result shows that an accuracy of 89.5% was achieved in the presented ray tracing model in this thesis.

Experiments have been conducted on 32 mm thick inhomogeneous austenitic weld material, 62 mm thick austenitic clad material and quantitatively measured the ultrasound beam distortion and field profiles using electrodynamical probes. The inhomogenity in the weld material is modeled based on the Ogilvy's empirical relation. The weld parameters are optimized in the empirical relation such a way that to match with the macrograph of the real life austenitic weld specimen. The ultrasound beam propagation and field profiles are accurately computed using ray tracing model. The simulated ultrasound field profiles using ray tracing model along the back wall of an austenitic weld component and clad material are compared quantitatively with the experimental results. It turned out that the deviation between simulation and experiments was about 5.2% in the isotropic austenitic material, 16.5% in the austenitic weld material and 5.46% in the austenitic clad material. Finally, the reasons for differences between simulation and experimental results are explored.

Table of Contents

CHAPTER 1

Introduction: Statement of the Problem and Status of Research

1.1 Importance of Austenitic Weld Materials

Austenitic welds and dissimilar welds are extensively used in primary circuit pipes and pressure vessels in nuclear power plants, chemical industries and fossil fuelled power plants because of their high fracture toughness, resistance to corrosion and creep at elevated temperatures [1-4]. However, cracks may initiate in these weld materials during fabrication process or stress operations in service. Failures of safety relevant austenitic weld components may result in large economic damage due to lack of plant availability during repairs and it might even lead to loss of human lives. Thus, it is very important to evaluate the structural integrity of these materials using highly reliable non-destructive testing (NDT) methods. Generally ultrasonic inspection technique as a volume based inspection technique is widely used in power plant industries for the detection of defects in austenitic weld materials [5-13].

1.1.1 Microstructure of the Austenitic Weld Material

The most common welding process used for the austenitic components is arc welding which includes the following [5]:

(a) Manual Metal Arc (MMA),
(b) Submerged Arc (SAW),
(c) Metal Inert Gas (MIG),
(d) Tungsten Inert Gas (TIG).

In welding, as the heat source interacts with the material, resulting in three distinct regions in the weldment. These are the fusion zone (FZ), also known as the weld metal, the heat-affected zone (HAZ), and the unaffected base metal (BM) [14, 15]. The FZ experiences melting and solidification during welding process. The weld microstructure development in the FZ is more complicated because of physical processes that occur due to the interaction of the heat source with the metal during welding, including re-melting, heat and fluid flow, vaporization, dissolution of gasses, solidification, subsequent solid-

state transformation, stresses, and distortion. These processes and their interactions profoundly affect weld pool solidification and microstructure [16, 17]. Temperature gradient, dendritic growth rate, undercooling and alloy constitution are important factors in determining the FZ microstructure. Depending on the cooling rates during welding, the solidification process is classified into two types: equilibrium and non-equilibrium. The rapid cooling conditions during welding increases the growth rate, resulting non-equilibrium solidification effects. In case of non-equilibrium solidification process, the solidification occurs spontaneously by epitaxial growth on the partially melted grains.

A typical Cr-Ni based austenitic weld material consists of 17 to 20% of Cr content and 8 to 12% of Ni content. The atoms of austenitic stainless steel materials exhibit FCC crystal structure whereas ferritic steel materials exhibit BCC crystal structure. Thus, the microstructure of the austenitic stainless steel materials is significantly different from that found in ferritic steel materials. During the solidification process the austenitic phase forms long columnar grains, which grow along the directions of maximum heat loss during cooling [12]. The columnar grain growth behaviour in an austenitic weld material is not uniform throughout the weld region. The diameter of the columnar grains varies in the range from 20 μm to 3 mm [18, 19]. Depending on the type of welding technique and the solidification process, the columnar grain growth in the weld material varies. The influence of welding passes on the grain orientation in V-butt austenitic welds was discussed by Jing Ye et al. [20].

Fig. 1.1 shows a macrograph of the Cr-Ni based V- butt austenitic weld. The filler layers in the austenitic weld metal were made using multipass Manual Metal Arc (MMA) welding and the root pass was carried out using TIG welding. The base material of the austenitic weld generally consists of fine grained austenitic steel material which exhibits isotropic behaviour. It can be recognized from Fig.1.1 that the austenitic weld materials exhibit epitaxial grain growth starting from the weld root and the weld fusion face up to the weld crown. Consequently, the columnar grain orientation in the austenitic weld material varies spatially. It can be seen from Fig.1.1 that the long grain axis is nearly vertical along the centre of the austenitic weld. The slope of the long grain axis direction decreases with increasing distance from the centre of the weld.

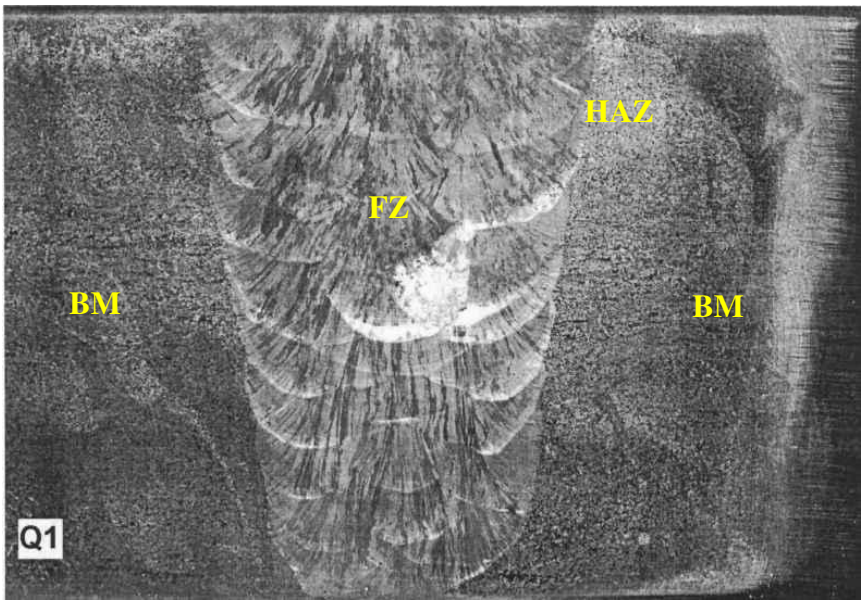

Figure 1.1: *Macrograph of the Cr-Ni based austenitic weld material. Weld data: root tungsten inert gas welded, filler layers manual metal arc welded, V- butt austenitic weld thickness 32 mm. BM: Base Metal, FZ: Fusion Zone, HAZ: Heat Affected Zone.*

Due to the local thermal gradients in the austenitic weld material, the grains could be tilted both in the direction of welding and in the plane perpendicular to it. The columnar grain orientation along the weld run direction is defined as layback orientation. Welds typically have a layback angle in between 5° and 10° [21, 22].

1.1.2 Symmetry of the Austenitic Weld Material

Extensive metallographic investigations using crystallographic techniques such as X-ray diffraction (XRD) and electron diffraction (ED) techniques on microstructure of the austenitic weld materials were carried out and concluded that the austenitic weld material is polycrystalline and can be assumed as transverse isotropic [19].

Transversely Isotropic Material:

An austenitic weld material is generally considered to be transversely isotropic such that the elastic properties of the material are directional independent in the plane containing along the weld run direction (i.e. the XY plane in Fig. 1.2).

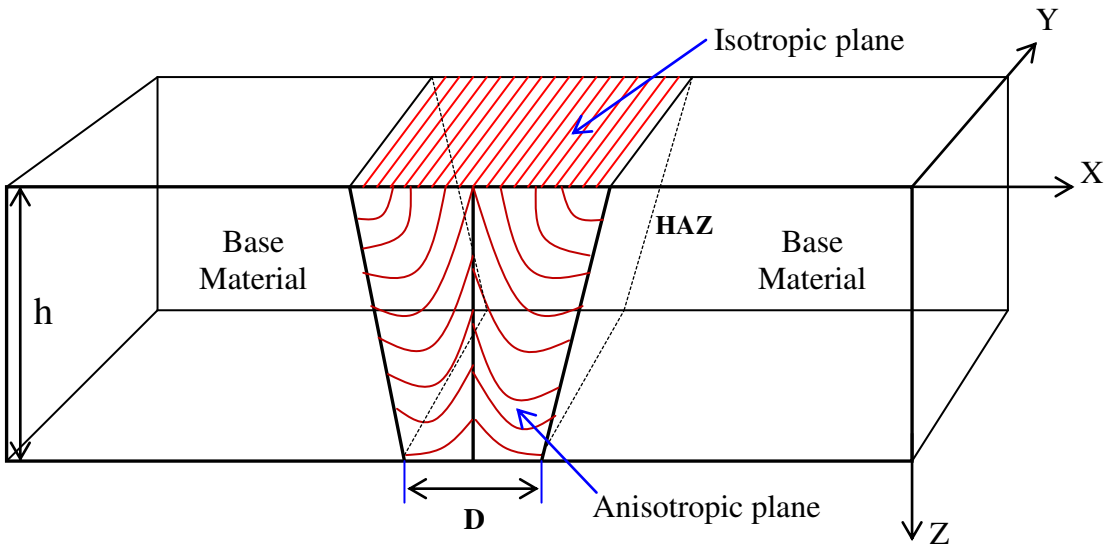

Figure 1.2: *Illustration of transverse isotropic symmetry in an austenitic weld material.*

Whereas the plane perpendicular to the weld run direction (i.e. the XZ plane in Fig. 1.2), the columnar grain structure exists and resulting elastic properties of the material are directional dependent. Macroscopically the austenitic weld material has to be treated as transverse isotropic due to the anisotropic columnar grain structure [23].

Using the surface acoustic wave (SAW) technique, Curtis and Ibrahim [24] conducted texture studies in austenitic weld materials and suggested that the austenitic welds exhibit transverse isotropic symmetry. They measured the ultrasonic pole figures on the surface of the austenitic weld material and compared with the X-ray pole figures and achieved good correlation. They also found that the surface wave velocity is extremely sensitive to the direction of the propagated wave and suggested that the surface acoustic wave technique is preferable for quantitative determination of texture (i.e. columnar grain structure) information in an inhomogeneous austenitic weld material. Dewey et al. [25] conducted the ultrasonic velocity measurements to determine the elastic constants in Type 308 austenitic steel electroslag weld and concluded that austenitic welds exhibit transverse isotropic symmetry. In a transverse isotropic austenitic weld material, the plane containing along the weld run direction exhibits isotropic behavior and perpendicular to this plane exhibits anisotropic behavior [23].

1.2 Non-Destructive Testing and Evaluation of Austenitic Welds

Generally, isotropic weld materials such as ferritic steel welds are inspected using different non-destructive testing (NDT) methods such as radiographic testing (RT), ultrasonic testing (UT) as volume methods, and magnetic particle inspection (MT), liquid penetrant testing (PT) as surface methods respectively. If the flaws are open to the surface of the specimen, generally liquid penetrant testing and magnetic particle testing methods are used for the detection. These techniques are not applicable when the welds contain subsurface defects and it is even more complicated when the welds exhibit inhomogeneous and anisotropic behaviour. Ultrasonic testing replaced by conventional techniques such as radiography, liquid penetrant and magnetic particle testing techniques to detect the flaws in weld materials [26-28]. Over the last three decades, ultrasonic testing techniques have been developed and established in the nuclear power plants for the inspection of austenitic weld materials [29-32]. However, ultrasonic testing of critical defects such as transversal cracks in austenitic weld materials is complicated because of their inhomogeneous anisotropic columnar grain structure.

1.2.1 Difficulties in Ultrasonic Inspection of Austenitic Welds

Difficulties in ultrasonic inspection of anisotropic and inhomogeneous austenitic welds are as follows [33-44]

- Elastic properties of the austenitic weld material are directional dependent. The wave vector and group velocity (energy flow) directions are no longer equal resulting beam skewing phenomenon.
- The dimensions of the columnar grains in the austenitic weld materials are large as compared to the ultrasonic wavelengths resulting ultrasound is influenced by the anisotropy of the grains.
- Directional dependency of wave vector and energy velocities.
- Due to the inhomogeneous columnar grain structure, curved ultrasound paths are resulted (for example see Fig. 1.3).

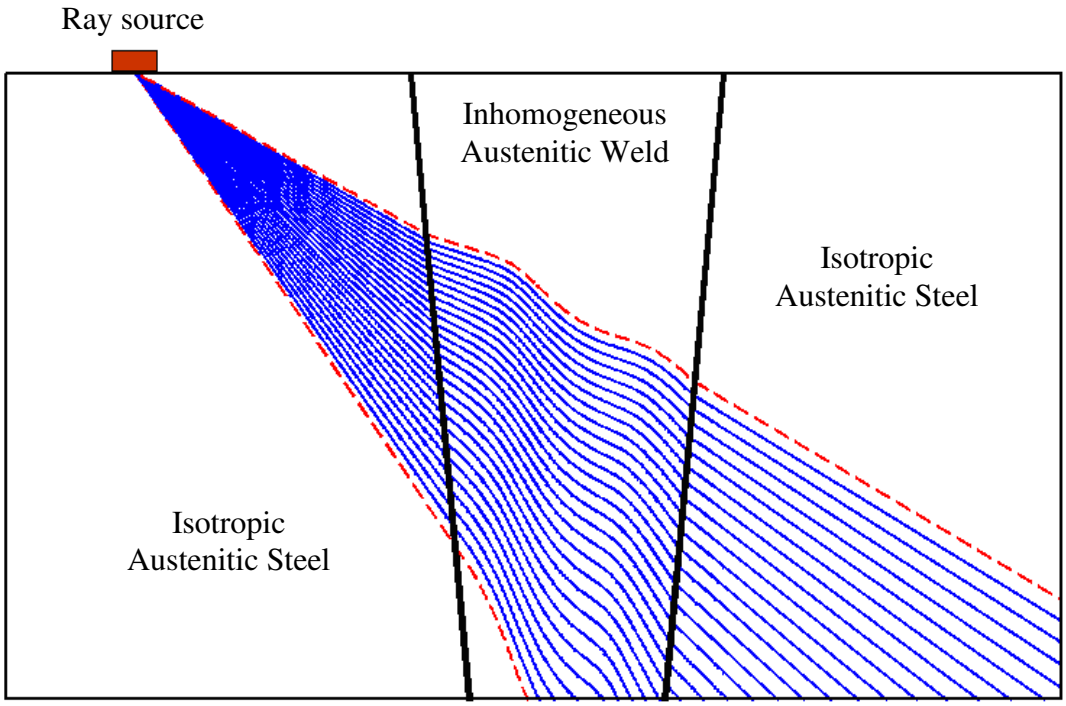

Figure 1.3: *Illustration of curved ultrasound paths in an inhomogeneous anisotropic austenitic weld material.*

- Large beam divergence, beam splitting and beam spreading effects are resulted.
- Scattering of ultrasound at the grain boundaries (one of most significant problems) leads to the high attenuation of the ultrasound beam. Due to this reason, spatially separate low frequency sending and receiving transducer arrangement is used for ultrasonic inspection of austenitic welds.
- Increasing noise level in the experimental ultrasonic signal results difficulty in interpretation of the experimental outcome.
- In case of austenitic weld materials, when an ultrasound is incident at an interface between two adjacent anisotropic columnar grains resulting three reflected and three transmitted waves. In contrast to the isotropic ferritic steel materials where two transverse waves are degenerate and coupling exists only between longitudinal and shear vertical waves. Complicated reflection and transmission behaviour of ultrasound in austenitic weld materials as compared to the isotropic steel materials (for example see Fig. 1.4).

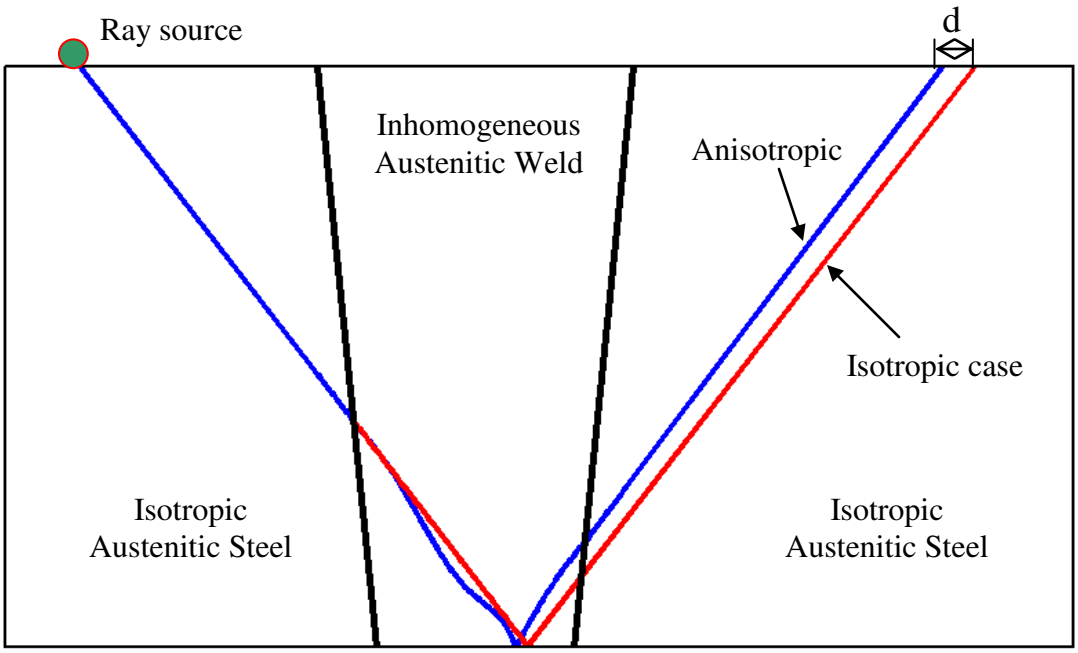

Figure 1.4: *Illustration of the reflection and transmission behaviour of the ray in isotropic and anisotropic weld materials. 'd' represents the deviation between locations of the reflected signals in isotropic and anisotropic weld materials.*

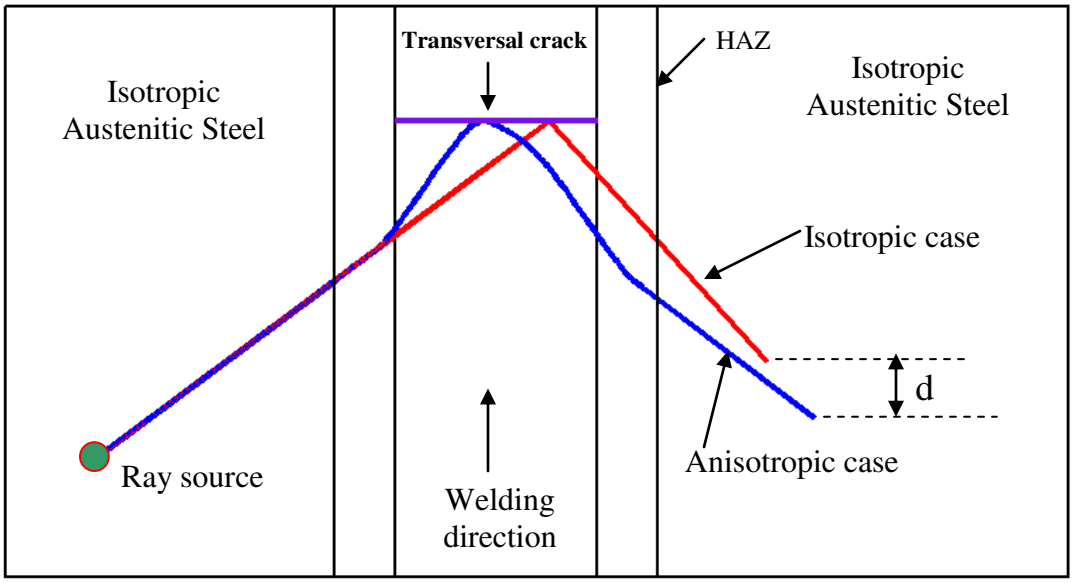

Figure 1.5: *Illustration of the interaction of an ultrasonic ray with transversal crack in isotropic and anisotropic weld materials (top view of the weld). 'd' represents the deviation between the locations of the specularly reflected signal from the transversal crack.*

- Defect response in homogeneous isotropic material is easily calculated based on the basic geometric principles whereas in anisotropic austenitic welds geometric laws are not valid due to inhomogeneous anisotropic columnar grain structure leading to complicated defect response (for example see Fig.1.5).

In order to develop reliable ultrasonic testing techniques for the inspection of critical defects such as transversal cracks in inhomogeneous austenitic weld materials, understanding of ultrasonic wave propagation and its interaction with defects in anisotropic materials is very important. Therefore it is possible to overcome the above difficulties arising in ultrasonic inspection of anisotropic welds by quantitative analysis of ultrasound wave propagation characteristics in these inhomogeneous anisotropic columnar grained materials, which is the main aim of this thesis work.

1.3 Modeling of Ultrasonic Wave Propagation in Anisotropic Welds: State of the Art

Modeling and simulation tools play an important role in developing new experimental procedures and optimizing the experimental parameters such as transducer positions, transducer frequency, incident angle and type of incident wave mode. The ultrasonic wave propagation models are classified based on calculation procedures and these are explained below:

1.3.1 Numerical Approaches

Elastodynamic Finite Integration Technique

Elastodynamic Finite Integration Technique (EFIT) is a numerical time domain modelling tool to model the ultrasound wave propagation in homogeneous isotropic and anisotropic materials [45-50]. EFIT discretizes the governing equations of linear elastodynamics on a staggered voxel in grid space. Recently, a three-dimensional EFIT model for anisotropic materials has been presented [51]. Visualization of ultrasonic wave fields in homogeneous anisotropic austenitic material (X6CrNi1811) using 2D EFIT is shown in Fig. 1.6. In order to solve the wave propagation problems using EFIT, large computational power (i.e. multiprocessor / parallel computers) is required. Numerical dispersion may occur during the calculations.

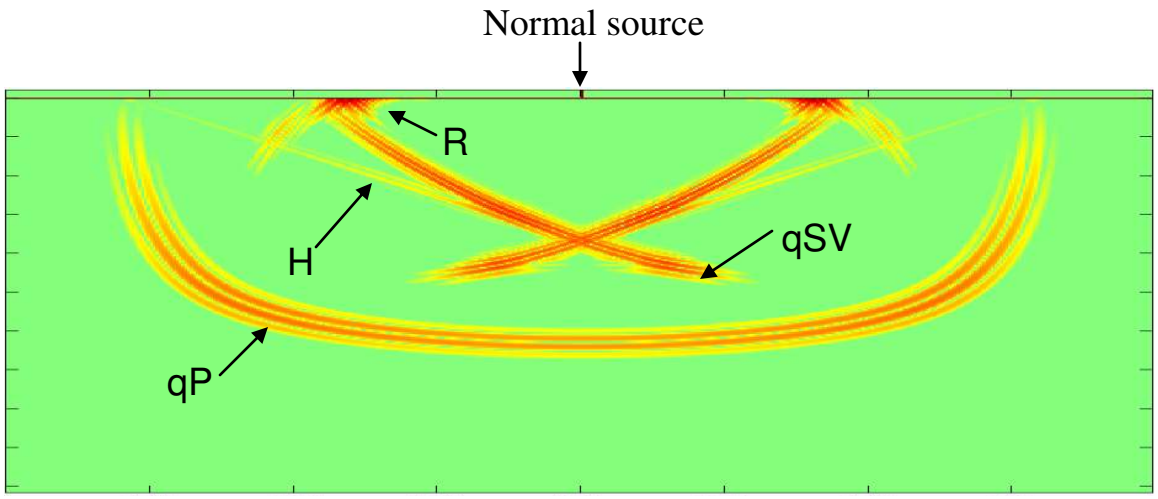

Figure 1.6: *Visualization of ultrasonic wave fields in the homogeneous anisotropic austenitic steel material (X6 Cr Ni 18 11) for the normal point force excitation (centre frequency 2.25 MHz) using 2D EFIT [45]. The columnar grain orientation in the austenitic steel material is 90º. R: Raleigh wave, H: Head wave, qSV: quasi shear vertical wave, qP: quasi longitudinal wave.*

Finite Element Model

Finite element modeling (FEM) is a numerical method where the complex geometry is discretized into mesh of finite elements. Ultrasonic wave propagation in homogeneous isotropic materials and anisotropic materials based on the finite element method was discussed by Harumi and Uchida [52]. They combined the finite element method and particle models for numerically evaluating radiation characteristics of ultrasound in homogeneous anisotropic materials and wave interaction with defects in layered materials. The accuracy of the numerical results depends on the fineness of the mesh. Generally finite element methods require large CPU time and high amount of memory.

Finite Difference Model

Finite difference model (FDM) is a numerical simulation method where the elastodynamic wave propagation is analyzed by solving the differential equations. A numerical finite difference model for studying elastic wave propagation and scattering of ultrasound in inhomogeneous anisotropic materials was presented by JAG Temple [53]. Eunsol et al. [54] presented a 2D rectangular mass spring lattice model (RMSLM) for modelling and simulation of ultrasonic propagation in a homogeneous austenitic weld. In FDM, stress free boundaries require layer of artificial nodes and also special care should

be taken at regions of corners and cracks. Implementing absorbing boundary conditions in a 3D anisotropic geometry using FDM is a complicated task. Generally, the model calculations were executed on the supercomputer. The model is also able to calculate the scattering of ultrasound in the near field.

Boundary Element Method

The boundary element method (BEM) is a numerical method to simulate the ultrasonic wave propagation in materials by solving boundary integral equations [55]. The method consists of discretizing the boundary of the specimen using boundary elements, which are line elements for 2D problems and surface elements for 3D problems. A time domain BEM for transient elastodynamic crack analysis was presented by Zhang [56]. A boundary element approach for wave propagation problems in transversely isotropic solids were presented by A. Saez and J. Dominguez [57]. The discretization of crack surface with complex profile using BEM can be difficult to implement. Numerical dispersion may occur during the calculations.

1.3.2 Approximated Approaches

Gaussian Beam Superposition Method

Gaussian Beam Superposition (GBS) method uses a paraxial approximation where Gaussian base functions are evaluated based on the concept of Gaussian wave packets [58-63]. A Gaussian wave packet is composed of a superposition of waves of different wave vectors, which will spread by diffraction. A computationally efficient three dimensional Gaussian beam model for calculating transducer field patterns in anisotropic and layered materials was presented by Spies [64]. Due to the paraxial approximation, the deviations in the calculated field patterns only exist in the regions off the vicinity of the central ray [64]. Gaussian beam superposition approach has been implemented for calculating beam fields in immersed components [65, 66]. Jing Ye et al. [67] proposed a linear phasing multi- Gaussian beam model for simulating focussed beam fields produced by a phased array ultrasonic transducer in dissimilar metal welds. A 2D modular multi Gaussian beam (MMGB) for calculating beam profiles in homogeneous anisotropic

materials was presented by Hyunjo et al. [68]. They assumed a paraxial approximation in evaluating ultrasonic beam propagation in anisotropic materials.

1.3.3 Analytical Approaches

Ray tracing methods

In case of ray tracing model, the complete wave propagation phenomena such as wave reflection, refraction and mode conversion are evaluated based on the analytical expressions resulting from elastic plane wave theory [69-74] and calculations such as reflection and transmission involved only at the interfaces between different layers. This drastically reduces computational time as compared to the Finite Element [52] and Finite Difference [53] techniques.

State of the art: Existing ray tracing methods and their limitations

In the early 90's, Johnson et al. [75] presented the first ray tracing approach to calculate ultrasonic transducer fields in homogeneous isotropic solids. A 2D ray tracing model for simulating ultrasound wave propagation in an isotropic weld material was presented by Furukawa et al. [76]. RAYTRAIM a commercially available ray tracing software package was developed by Ogilvy [77-83].This algorithm is primarily proposed for evaluating ray energy paths and propagation times in inhomogeneous austenitic welds. Based on the several investigations on macrographs of the V-butt austenitic welds, Ogilvy [77] developed a mathematical empirical relation to describe the local columnar grain structure of the inhomogeneous austenitic weld material and described the virtual grain boundary between two adjacent columnar grains by a vector representing half of the difference between two adjacent crystal orientations. Later, Ogilvy [83] modified the definition of grain boundary within the weld material and selected the interface between the layers to be parallel to the local directions of ray group velocity magnitude. Based on the first order Bessel functions, the approximated spherical point source beam profiles in homogeneous austenitic materials were also presented by Ogilvy [23]. Combining the ray tracing principles and Kirchhoff theory, the ultrasound fields in austenitic weld materials were presented by Hawker et al. [84].

A computer model for evaluating ultrasound ray paths in complex orthotropic textured materials was discussed by Silk [85]. Schmitz et al. [86, 87] presented the 3D-Ray-SAFT algorithm to calculate the direction of the ultrasound beam and the deformation of the transmitted sound field in inhomogeneous weld material and discussed the qualitative comparison with experiments on unidirectional weld structure. The 3D-Ray-SAFT algorithm does not evaluate the ray amplitude information. Recently synthetic aperture focusing technique (SAFT) for defect imaging in anisotropic and inhomogeneous weld materials was discussed in [88, 89, 90, 91]. Gengembre et al. [92] computed the ultrasonic fields in homogeneous and inhomogeneous materials based on the pencil method. They used approximated Rayleigh integrals to describe the transducer effects. The commercially available ultrasonic modeling software tool CIVA model [93, 94, 95] is able to compute the ultrasonic beam fields in homogeneous and inhomogeneous material where ultrasonic beam is evaluated based on the semi analytical solutions.

Apfel et al. [96, 97] and J. Moysan et al. [98, 99] presented the MINA (Modeling anisotropy from Notebook of Arc welding) model to calculate the local grain direction of the weld material and they coupled the MINA model with ATHENA (a finite element code developed by EDF France) to predict the ultrasound propagation in austenitic welds. A ray theory based homogenization method for simulating transmitted fields in multi layered composites was presented by Deydier et al. [100, 101]. According to this homogenization method, the parallel regions are simplified with one homogeneous medium whereas non-parallel regions are replaced by progressively rotated homogeneous media. Connolly et al. [102, 103] were presented the application of Fermat's principle in imaging inhomogeneous austenitic weld materials. The 2D ray path behavior and defect images in the presence of longitudinal crack in austenitic welds were compared using finite element simulations [104, 105, 106]. A 2D ray tracing model in anisotropic austenitic welds which includes a probe model based on Fourier integral method in an isotropic half space was presented by Liu et al. [107]. Halkjaer et al. [108] used the Ogilvy's [77] empirical relation for grain structure model and compared the experimental normal beam amplitude profiles with the numerical EFIT simulation results.

1.4 Motivation for the Present Research Work

Quantitative evaluation of ultrasound fields in inhomogeneous anisotropic austenitic welds and dissimilar welds using ray tracing method is very important for optimizing the experimental parameters and analyzing the ultrasound field propagation. There are several important aspects to be considered when a ray propagating in an inhomogeneous anisotropic material such as ray directivity factor in the isotropic base material, anisotropic weld material and ray divergence variation at boundary separating two dissimilar materials, ray transmission coefficients, phase relations and finally ray amplitudes are represented in terms of density of rays. Apart from that a reliable weld model is considered which accounts the spatial variation of grain orientation in the macrograph of real life austenitic weld materials. These important aspects improve the reliability of the ray tracing predictions and helps in optimization and defect assessment during the ultrasonic inspection of inhomogeneous anisotropic austenitic weld materials.

The main aim of the presented research work is to develop a complete analytical, efficient and accurate 3D ray tracing method including all the above mentioned important aspects for modeling and simulation of both point source as well as array source ultrasound fields in inhomogeneous anisotropic austenitic weld materials. Applications of ray tracing model in optimizing experimental parameters during the ultrasonic inspection of transversal cracks in inhomogeneous austenitic weld materials are demonstrated. An ultrasonic C-scan image in anisotropic layered materials is quantitatively evaluated using 3D ray tracing method. Another aim is to validate first time quantitatively the ray tracing results with numerical Elastodynamic Finite Integration Technique (EFIT) simulation results on columnar grained anisotropic austenitic materials.

Experiments are performed on austenitic weld materials using ultrasonic phased array transducers and ultrasonic fields in inhomogeneous welds are scanned using electro-dynamical probes. The accuracy of the ray tracing model results is verified by comparing the predicted ultrasonic fields with the experimental results on real life inhomogeneous anisotropic austenitic welds.

1.5 Outline of the Thesis

In the present research work a 3D ray tracing method (RTM) is developed to evaluate the ultrasound propagation for point sources as well as phased array transducers quantitatively and optimizing the experimental parameters for the ultrasonic non-destructive inspection of inhomogeneous anisotropic austenitic weld materials.

- In chapter 2, ultrasonic wave propagation problem is solved three dimensionally in general anisotropic materials with arbitrary stiffness matrices of 21 elastic constants. Explicit analytical expressions for Poynting vector and energy velocities in columnar grained anisotropic materials are presented. The anisotropy influenced parameters such as phase velocity, slowness vector, energy velocity, polarization, beam divergence, beam spreading factor and beam skewing for the three wave modes namely quasi longitudinal, quasi shear vertical and pure shear horizontal waves are analyzed for the transversely isotropic austenitic steel materials with 3D columnar grain orientation.

- In chapter 3, the presented fundamental concepts such as slowness and energy velocity vectors in chapter 2 are applied and the problem of ultrasonic plane wave energy reflection and transmission coefficients at an interface between two general anisotropic materials are evaluated for a 3D geometry. Quantitative analysis on energy transported by direct as well as mode converted waves in columnar grained austenitic weld materials is presented. Additionally, valid domains of incident wave vector angles, angular dependency of energy reflection and transmission coefficients and critical angles for reflected and transmitted waves are discussed.

  Energy reflection behavior of plane elastic waves at a free surface boundary of a columnar grained austenitic weld material is analyzed. This is very important during the ultrasonic non-destructive testing of austenitic welds in order to characterize the reflected waves from the material boundaries and inhomogenities such as a crack face. The existence of reflected (or) transmitted

second branch of quasi shear vertical waves and its consequence to the ultrasonic non-destructive inspection of austenitic weld materials are discussed. The reflection, transmission angles and coefficients obtained in chapter 3 play an important role in evaluating ultrasonic ray propagation behavior and ultrasound fields quantitatively using ray tracing method and it will be discussed in chapter 5.

- In chapter 4, the ultrasonic beam directivity in a general anisotropic austenitic weld material, including layback orientation, is evaluated three dimensionally based on Lamb's reciprocity theorem [61, 109, 110, 111]. The influence of columnar grain orientation and layback orientation on point source directivity for the three wave modes quasi longitudinal (qP), quasi shear vertical (qSV) and pure shear horizontal (SH) waves, under the excitation of normal as well as tangential forces on semi infinite columnar grained austenitic steel material is investigated. The results of this chapter are used in chapters 5 and 6 to evaluate the accurate ultrasound fields generated by point source as well as array transducer in inhomogeneous anisotropic materials.

- In chapter 5, a 3D ray tracing method for evaluating ray energy paths and amplitudes for the point sources and distributed sources is presented. The inhomogenity of the austenitic weld material is modeled based on previously developed mathematical empirical relation [77]. The influence of inhomogeneous weld structure on ultrasonic energy ray paths for quasi longitudinal, quasi shear vertical and shear horizontal waves in austenitic welds are analyzed. The direct as well as mode converted reflected ray paths from the back wall of the austenitic weld materials are investigated.

  The specularly reflected ultrasonic rays from the transversal cracks in inhomogeneous austenitic weld materials are calculated three dimensionally and its importance to the ultrasonic examination of transversal cracks in austenitic weld materials is presented.

- In chapter 6, the applications of ray tracing model for the ultrasonic non-destructive inspection of anisotropic materials such as austenitic clad materials and austenitic weld materials are discussed. The point source as well as array source ultrasound fields obtained from the ray tracing model in columnar grained austenitic steel materials, layered austenitic clad materials and austenitic weld materials are compared first time quantitatively with the 2D Elastodynamic Finite Integration Technique (EFIT) [45-49] results. The ray tracing model is successfully validated using EFIT model. The reasons for minor differences between ray tracing model and EFIT model are discussed.

- In chapter 7, ultrasonic C-scan images in homogeneous and multi layered anisotropic austenitic steel materials are quantitatively evaluated using 3D ray tracing method. The influence of columnar grain orientation and layback orientation on ultrasonic C-scan image in an anisotropic columnar grained austenitic steel material is investigated and its practical consequences to the ultrasonic non-destructive testing of an anisotropic austenitic material are presented. The calculated ultrasonic field profiles for the angle beam array transducer in an inhomogeneous anisotropic austenitic weld material using ray tracing model are quantitatively compared with CIVA simulation results.

- In chapter 8, experimental technique used for evaluating ultrasonic beam distortion and field profiles in inhomogeneous austenitic welds and clad materials are presented. The calculated ultrasonic fields for the normal beam as well as angle beam finite dimension array transducer using ray tracing model are compared quantitatively with the experiments in real-life inhomogeneous austenitic weld (X6 Cr Ni 18 11) and austenitic clad material. The reasons for differences between ray tracing model and experiments are discussed.

- In chapter 9, conclusions which include major findings of the thesis and important contributions to the field of Non-Destructive Testing and Evaluation (NDT&E) of

inhomogeneous anisotropic austenitic weld materials are presented. The suggested areas for continued research and future prospectives are summarized.

CHAPTER 2

Ultrasonic Wave Propagation in General Anisotropic Media

2.1 Introduction

The theory of elastic wave propagation in general anisotropic solids is well described in the literature [69, 70, 71, 112, 113]. A review is carried out and obtained the analytical solutions for ultrasonic wave propagation in general anisotropic solids. The resulting fundamental concepts in this chapter will be employed in the rest of the thesis. The ultrasonic wave propagation problem in anisotropic solids is presented in three dimensions with arbitrary stiffness matrices of 21 elastic constants. The anisotropy influenced parameters such as phase velocity, energy velocity, beam divergence, beam spreading factor and beam skewing for the three wave modes namely quasi longitudinal (qP), quasi shear vertical (qSV) and pure shear horizontal (SH) waves are analyzed quantitatively for the columnar grained transversely isotropic austenitic steel materials.

2.2 Basic Physics in General Anisotropic Medium

2.2.1 Christoffel Equation for General Anisotropic Solids

A general form to represent the plane wave displacements in anisotropic solids is given as

$$\mathbf{u} = A\mathbf{p}\exp(i(\mathbf{k}.\mathbf{r} - \omega t)), \tag{2.1}$$

where A is the particle displacement amplitude, $\mathbf{p}$ is the polarization vector, $\mathbf{k}$ is the wave vector and $\mathbf{r}$ is the position vector represented in Cartesian coordinates x, y, z, ω is the angular frequency.

The strain-displacement relation in solids is expressed as [69]

$$\mathbf{S} = \nabla\mathbf{u}. \tag{2.2}$$

The equation of motion in general solids is defined as

$$\nabla \cdot \mathbf{T} = \rho\frac{\partial^2\mathbf{u}}{\partial t^2}, \tag{2.3}$$

where **S** is the strain field, **u** is the particle displacement field and **T** is the stress field.

According to Hooke's Law the stress is linearly proportional to the strain and it is mathematically represented as

$$\mathbf{T} = \mathbf{c} : \mathbf{S} = \mathbf{c} : \nabla \mathbf{u}. \tag{2.4}$$

The stress field in Eq. (2.3) is eliminated by differentiating with respect to t,

$$\nabla \cdot \frac{\partial \mathbf{T}}{\partial t} = \rho \frac{\partial^2 \mathbf{v}}{\partial t^2}. \tag{2.5}$$

The acoustic wave equation in a lossless medium is obtained by substituting Eq. (2.4) into Eq. (2.5),

$$\nabla \cdot \mathbf{c} : \nabla \mathbf{v} = \rho \frac{\partial^2 \mathbf{v}}{\partial t^2}. \tag{2.6}$$

The acoustic wave equation in a lossless medium in matrix form with abbreviated subscripts can be represented as

$$\nabla_{iK} c_{KL} \nabla_{Lj} v_j = \rho \frac{\partial^2 v_j}{\partial t^2} \ , \tag{2.7}$$

where

$$\nabla_{iK} = \begin{bmatrix} \frac{\partial}{\partial x} & 0 & 0 & 0 & \frac{\partial}{\partial z} & \frac{\partial}{\partial y} \\ 0 & \frac{\partial}{\partial y} & 0 & \frac{\partial}{\partial z} & 0 & \frac{\partial}{\partial x} \\ 0 & 0 & \frac{\partial}{\partial z} & \frac{\partial}{\partial y} & \frac{\partial}{\partial x} & 0 \end{bmatrix} \tag{2.8}$$

is the divergence matrix operator,

$$\nabla_{Lj} = \begin{bmatrix} \frac{\partial}{\partial x} & 0 & 0 \\ 0 & \frac{\partial}{\partial y} & 0 \\ 0 & 0 & \frac{\partial}{\partial z} \\ 0 & \frac{\partial}{\partial z} & \frac{\partial}{\partial y} \\ \frac{\partial}{\partial z} & 0 & \frac{\partial}{\partial x} \\ \frac{\partial}{\partial y} & \frac{\partial}{\partial x} & 0 \end{bmatrix} \tag{2.9}$$

is the symmetric gradient matrix operator

and

$$[\mathbf{c}] = \begin{bmatrix} c_{11} & c_{12} & c_{13} & c_{14} & c_{15} & c_{16} \\ c_{12} & c_{22} & c_{23} & c_{24} & c_{25} & c_{26} \\ c_{13} & c_{23} & c_{33} & c_{34} & c_{35} & c_{36} \\ c_{14} & c_{24} & c_{34} & c_{44} & c_{45} & c_{46} \\ c_{15} & c_{25} & c_{35} & c_{45} & c_{55} & c_{56} \\ c_{16} & c_{26} & c_{36} & c_{46} & c_{56} & c_{66} \end{bmatrix} \tag{2.10}$$

is the elastic stiffness matrix; i, j = 1….3; K, L = 1….6;

ρ is density of the material and v_j is the particle velocity component.

Transformation of elastic stiffness matrix $[\mathbf{c}]$ of global coordinate system to the local coordinate system is obtained using Bond transformation matrix [69] as follows

$$\left[\mathbf{c}^T\right] = [\mathbf{M}][\mathbf{c}][\mathbf{N}] \tag{2.11}$$

The coefficients of transformation matrices $[\mathbf{M}], [\mathbf{N}]$ are presented in Appendix A.

Let us consider a uniform plane wave propagating along the direction

$$\mathrm{I} = \mathbf{x} l_x + \mathbf{y} l_y + \mathbf{z} l_z . \tag{2.12}$$

The matrix differential operators ∇_{iK} and ∇_{Lj} in Eq. (2.7) can be replaced by the matrices $-ik_{iK}$ and $-ik_{Lj}$ respectively, where

$$-ik_{iK} = -ikl_{iK} \rightarrow -ik\begin{bmatrix} l_x & 0 & 0 & 0 & l_z & l_y \\ 0 & l_y & 0 & l_z & 0 & l_x \\ 0 & 0 & l_z & l_y & l_x & 0 \end{bmatrix} \tag{2.13}$$

and

$$-ik_{Lj} = -ikl_{Lj} \rightarrow -ik\begin{bmatrix} l_x & 0 & 0 \\ 0 & l_y & 0 \\ 0 & 0 & l_z \\ 0 & l_z & l_y \\ l_z & 0 & l_x \\ l_y & l_x & 0 \end{bmatrix}. \tag{2.14}$$

The substitution of Eq. (2.13) and Eq. (2.14) into Eq. (2.7) yields the Christoffel equation

$$k^2\left(l_{iK}c_{KL}l_{Lj}\right)v_j = \rho\omega^2 v_j \tag{2.15}$$

where $\Gamma_{ij} = l_{iK}\mathbf{c}_{KL}l_{Lj}$ is called the Christoffels matrix.

The wave propagation characteristics in general anisotropic solids can be found from the following representation of Eq. (2.15)

$$\left[k^2\Gamma_{ij} - \rho\omega^2\delta_{ij}\right]\left[v_j\right] = 0 \tag{2.16}$$

where δ_{ij} is the identity matrix.

The dispersion relation is obtained by taking the determinant of Eq. (2.16) equals to zero,

$$\begin{vmatrix} \left(\frac{k}{\omega}\right)^2\Gamma_{11} - \rho & \left(\frac{k}{\omega}\right)^2\Gamma_{12} & \left(\frac{k}{\omega}\right)^2\Gamma_{13} \\ \left(\frac{k}{\omega}\right)^2\Gamma_{12} & \left(\frac{k}{\omega}\right)^2\Gamma_{22} - \rho & \left(\frac{k}{\omega}\right)^2\Gamma_{23} \\ \left(\frac{k}{\omega}\right)^2\Gamma_{13} & \left(\frac{k}{\omega}\right)^2\Gamma_{23} & \left(\frac{k}{\omega}\right)^2\Gamma_{33} - \rho \end{vmatrix} = 0, \tag{2.17}$$

where

$$\left.\begin{aligned}
\Gamma_{11} &= c_{11}l_x^2 + c_{66}l_y^2 + c_{55}l_z^2 + 2c_{56}l_yl_z + 2c_{15}l_zl_x + 2c_{16}l_xl_y \\
\Gamma_{12} &= \Gamma_{21} = c_{16}l_x^2 + c_{26}l_y^2 + c_{45}l_z^2 + (c_{46}+c_{25})l_yl_z + (c_{14}+c_{56})l_zl_x + (c_{12}+c_{66})l_xl_y \\
\Gamma_{13} &= \Gamma_{31} = c_{15}l_x^2 + c_{46}l_y^2 + c_{35}l_z^2 + (c_{45}+c_{36})l_yl_z + (c_{13}+c_{55})l_zl_x + (c_{14}+c_{56})l_xl_y \\
\Gamma_{22} &= c_{66}l_x^2 + c_{22}l_y^2 + c_{44}l_z^2 + 2c_{24}l_yl_z + 2c_{46}l_zl_x + 2c_{26}l_xl_y \\
\Gamma_{23} &= \Gamma_{32} = c_{56}l_x^2 + c_{24}l_y^2 + c_{34}l_z^2 + (c_{44}+c_{23})l_yl_z + (c_{36}+c_{45})l_zl_x + (c_{25}+c_{46})l_xl_y \\
\Gamma_{33} &= c_{55}l_x^2 + c_{44}l_y^2 + c_{33}l_z^2 + 2c_{34}l_yl_z + 2c_{35}l_zl_x + 2c_{45}l_xl_y
\end{aligned}\right\} \qquad (2.18)$$

Eq. (2.17) reduces into the cubic equation in $X = \left(\frac{k}{\omega}\right)^2$ and it is given as follows

$$AX^3 + BX^2 + CX + D = 0\ , \qquad (2.19)$$

where

$$\left.\begin{aligned}
A &= \Gamma_{11}\Gamma_{33}\Gamma_{22} + 2\Gamma_{12}\Gamma_{23}\Gamma_{13} - \left(\Gamma_{33}\Gamma_{12}^2 + \Gamma_{13}^2\Gamma_{22} + \Gamma_{23}^2\Gamma_{11}\right) \\
B &= -\rho\left(\Gamma_{33}\Gamma_{22} + \Gamma_{11}\Gamma_{22} + \Gamma_{33}\Gamma_{11}\right) + \rho\left(\Gamma_{13}^2 + \Gamma_{12}^2 + \Gamma_{23}^2\right) \\
C &= \rho^2\left(\Gamma_{11} + \Gamma_{22} + \Gamma_{33}\right) \\
D &= -\rho^3
\end{aligned}\right\} \qquad (2.20)$$

Eq. (2.19) is solved based on the Cardano's cubic resolvent method [114]. The three roots of the Eq. (2.19) correspond to the propagation characteristics of the three wave modes existing in general anisotropic solids.

Pure wave modes:

In case of general isotropic solids, the polarization direction of an acoustic wave is determined by the particle displacement field. If the direction of particle displacement field is parallel to the wave propagation vector, then the wave is called pure longitudinal wave and perpendicular to the wave propagation vector is called pure shear vertical wave. The wave propagation properties such as velocity and polarization direction of pure wave modes are directional independent.

Quasi wave modes:

In case of general anisotropic solids, the wave propagation properties are directional dependent. The polarization directions of three wave modes exist in the anisotropic solids neither perpendicular nor parallel to the wave propagation vector. The particle motion of longitudinal wave in anisotropic solids contains not only parallel to the wave propagation direction but also perpendicular to it. This unusual behaviour of the longitudinal wave is called quasi nature of the longitudinal wave [115]. The same behaviour is also applicable for other shear wave modes namely quasi shear vertical and quasi shear horizontal waves. Beam skewing is one of significant anisotropic parameters for measuring quasi nature of the wave mode. A detailed description on beam skewing is presented in Section 2.3.

The roots of the Eq. (2.19) are processed to yield the phase velocity magnitudes for the three wave modes namely quasi longitudinal (qP), quasi shear vertical (qSV) and quasi shear horizontal (qSH) waves respectively. The velocity magnitude for the qP wave is higher as compared to qSV and qSH waves. The two shear waves can be distinguished based on slow and fast shear waves. Particle polarization components for the three wave modes can be obtained by substituting the phase velocity magnitudes in Eq. (2.16) yields

$$\begin{bmatrix} \Gamma_{11}-\rho V_i^2 & \Gamma_{12} & \Gamma_{13} \\ \Gamma_{12} & \Gamma_{22}-\rho V_i^2 & \Gamma_{23} \\ \Gamma_{13} & \Gamma_{23} & \Gamma_{33}-\rho V_i^2 \end{bmatrix} \begin{bmatrix} v_x \\ v_y \\ v_z \end{bmatrix} = 0, \tag{2.21}$$

where v_x, v_y, v_z are the particle polarization components along x, y and z directions respectively.

Simplifying the Eq. (2.21) reduces into

$$\left(\Gamma_{11}-\rho V_i\right)v_x + \Gamma_{12}v_y + \Gamma_{13}v_z = 0 \tag{2.22}$$

$$\Gamma_{12}v_x + \left(\Gamma_{22}-\rho V_I\right)v_y + \Gamma_{23}v_z = 0 \tag{2.23}$$

$$\Gamma_{13}v_x + \Gamma_{23}v_y + \left(\Gamma_{33}-\rho V_i\right)v_z = 0 \tag{2.24}$$

where V_i with $i = qP, qSV, qSH$ represent the particle velocity magnitude for a particular wave type.

Eliminating v_x from the Eq. (2.22) and Eq. (2.23), a relation among v_y and v_z will be obtained as follows

$$v_y = \frac{\Gamma_{32}\left(\Gamma_{11} - \rho V_i\right) - \Gamma_{13}\Gamma_{12}}{\Gamma_{13}\left(\Gamma_{22} - \rho V_i\right) - \Gamma_{12}\Gamma_{32}} \tag{2.25}$$

and

$$v_z = \frac{\left(\Gamma_{11} - \rho V_i\right)\left(\Gamma_{22} - \rho V_i\right) - \Gamma_{12}^2}{\Gamma_{12}\Gamma_{32} - \Gamma_{31}\Gamma_{22}} \ . \tag{2.26}$$

The normalized particle polarization components for a particular wave mode are given as

$$\mathbf{v} = \begin{bmatrix} 1 \\ \dfrac{v_y}{\sqrt{1 + v_y^2 + v_z^2}} \\ \dfrac{v_z}{\sqrt{1 + v_y^2 + v_z^2}} \end{bmatrix} \tag{2.27}$$

2.2.2 Phase Velocity and Slowness Surface

The material studied in this research work is austenitic weld material. Austenitic weld materials are assumed as transverse isotropic, as explained in section 1.1.2. Generally three wave modes will exist in which one with quasi longitudinal wave character (qP), one with quasi shear wave character (qSV) and one pure shear wave (SH). The selection of proper phase velocity magnitudes for the two shear wave modes is obtained by imposing the boundary condition for shear horizontal waves. Pure shear horizontal wave (SH) polarizes exactly perpendicular to the plane of wave propagation, i.e. in the plane of isotropy so that polarization direction of this mode is always perpendicular to the wave

vector direction. In this study we considered the incident ultrasonic wave propagates in three dimensional space. With this consideration, the coupling between all the three wave modes (i.e. qP, qSV and SH) exists.

Generally the austenitic weld materials exhibit columnar grain orientation in 3D. The 3D columnar grain orientation of the austenitic weld material is represented by rotating the coordinate system over the crystallographic axes as shown in Figure 2.1. The illustration of three dimensional representation of columnar grain orientation in transverse isotropic austenitic weld material is depicted in Fig. 2.1. If the incident wave propagates in the xz-plane and the columnar grain orientation in the plane perpendicular to the incident plane (i.e. layback angle) is zero, then the problem of evaluating wave propagation properties in transversely isotropic material reduces to two dimensions. Consequently, the coupling exists only between quasi longitudinal and quasi shear vertical waves. Whereas the shear horizontal wave decouples with quasi longitudinal and quasi shear vertical waves.

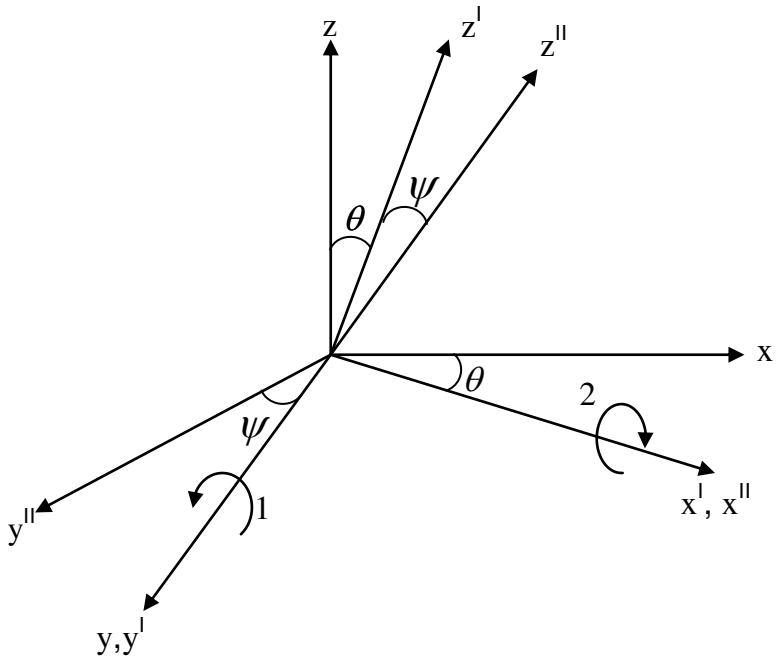

Figure 2.1: *Coordinate system used to represent the three dimensional crystal orientation of the transversal isotropic austenitic weld material.* θ *represents the columnar grain orientation and* ψ *represents the layback orientation.*

Table 1: *Material properties for the isotropic steel, Plexy glass and austenitic steel (X6 - Cr Ni 18 11) material.* ρ*[kg/m*^{3}*],* C_{ij}*[GPa].*

Material parameter	Isotropic steel	Plexy glass	Austenitic steel (X6 Cr Ni 18 11)
ρ	7820	1180	7820
C_{11}	272.21	8.79	241.1
C_{12}	112.06	3.96	96.91
C_{13}	112.06	3.96	138.03
C_{33}	272.21	8.79	240.12
C_{44}	80.07	2.413	112.29
C_{66}	80.07	2.413	72.092

The elastic properties for the transversely isotropic austenitic material to visualize the wave propagation are taken from Munikoti et al. [116] and values are presented in Table1.

The derived analytical expressions for phase velocity magnitudes in Section 2.2.1 are utilized to compute the phase velocity surfaces for the three wave modes in transverse isotropic austenitic material (X6CrNi1811) exhibiting different columnar grain orientations. Fig. 2.2 illustrates the phase velocity magnitudes for the three wave modes namely qP, qSV and SH waves in an austenitic steel material exhibiting 0º columnar grain orientation and 0º lay back orientation. In case of isotropic material the phase velocity surfaces for the three wave modes are spherical because the velocity magnitudes of longitudinal and shear waves are directional independent as shown in Fig. 2.3. The shear horizontal and shear vertical waves existing in the isotropic material are degenerated (i.e. both the shear waves have equal velocity magnitudes but polarize differently). It is apparent from Fig. 2.2(left), that the phase velocity surfaces for three wave modes are non-spherical because the phase velocity direction does not represent the actual energy direction except along the acoustical axes. In Fig. 2.2(right) the results of phase velocity surfaces for the three wave modes in an austenitic steel material exhibiting 45º columnar grain orientation and 20º layback orientation are presented.

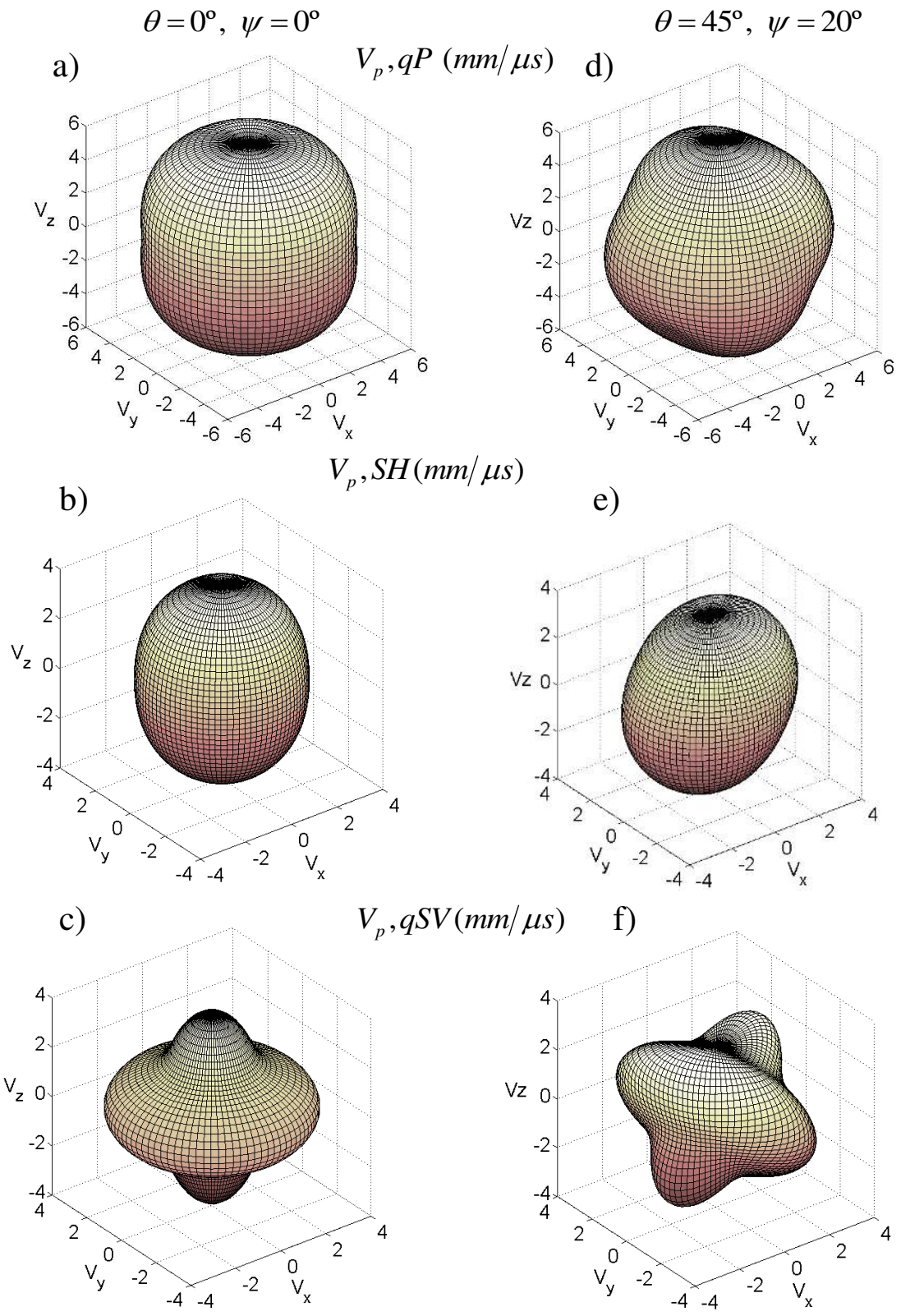

Figure 2.2: *Phase velocity surfaces in the transversely isotropic austenitic stainless steel material(X6 CrNi 1811): a), d) quasi longitudinal waves, b), e) Shear horizontal waves and c), f) quasi shear vertical waves.* θ *represents the columnar grain orientation and* ψ *represents the layback orientation.*

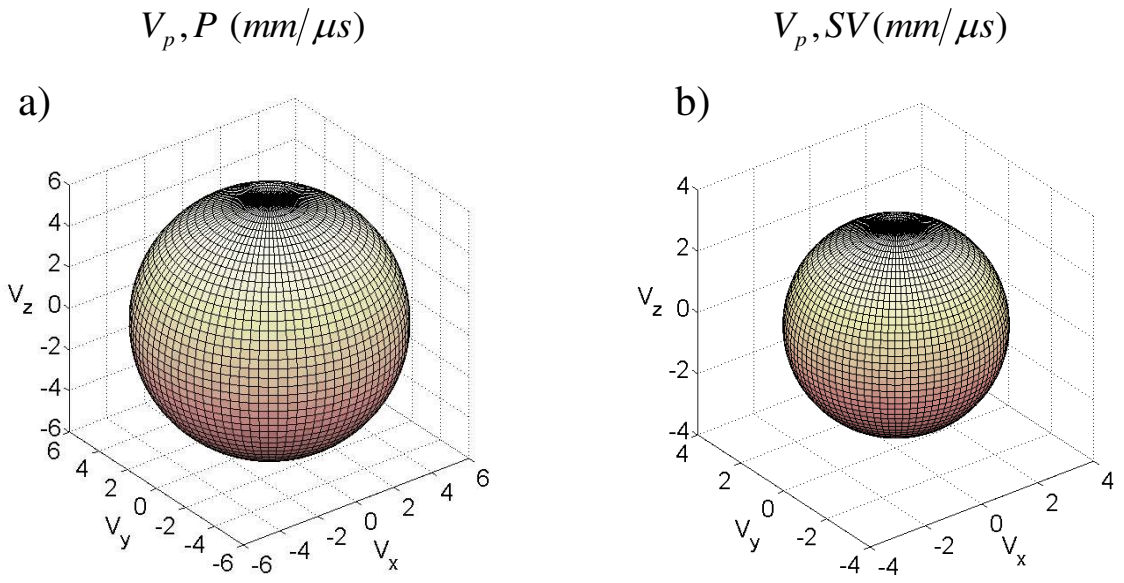

Figure 2.3: *Acoustic wave phase velocity surfaces in the isotropic steel material: a) longitudinal wave and b) shear vertical wave.*

It is obvious from Fig 2.2 (right), that the existence of the layback orientation results even complicated asymmetrical surfaces. As expected, the quasi shear vertical waves are strongly influenced by the anisotropy of the austenitic weld material as compared to the other two wave modes.

Inverse of the phase velocity vector is defined as the slowness vector [69]. The significance of slowness surface is that the energy velocity direction and beam skewing angle can be calculated graphically. In Fig. 2.4(left) the results of slowness surfaces for the three wave modes in an austenitic material exhibiting columnar grain orientation 0º and lay back orientation 0º are presented. As expected, the slowness surfaces for qP, qSV and SH waves are non-spherical. As can be seen from Figs. 2.4(b) and (e), the SH wave slowness surface is close to the spherical behaviour because these waves polarize in the plane of isotropy. The main importance of slowness surfaces are one can evaluate graphically the problem of reflection and transmission at an interface between two anisotropic media with different elastic properties and it will be presented in chapter 3.

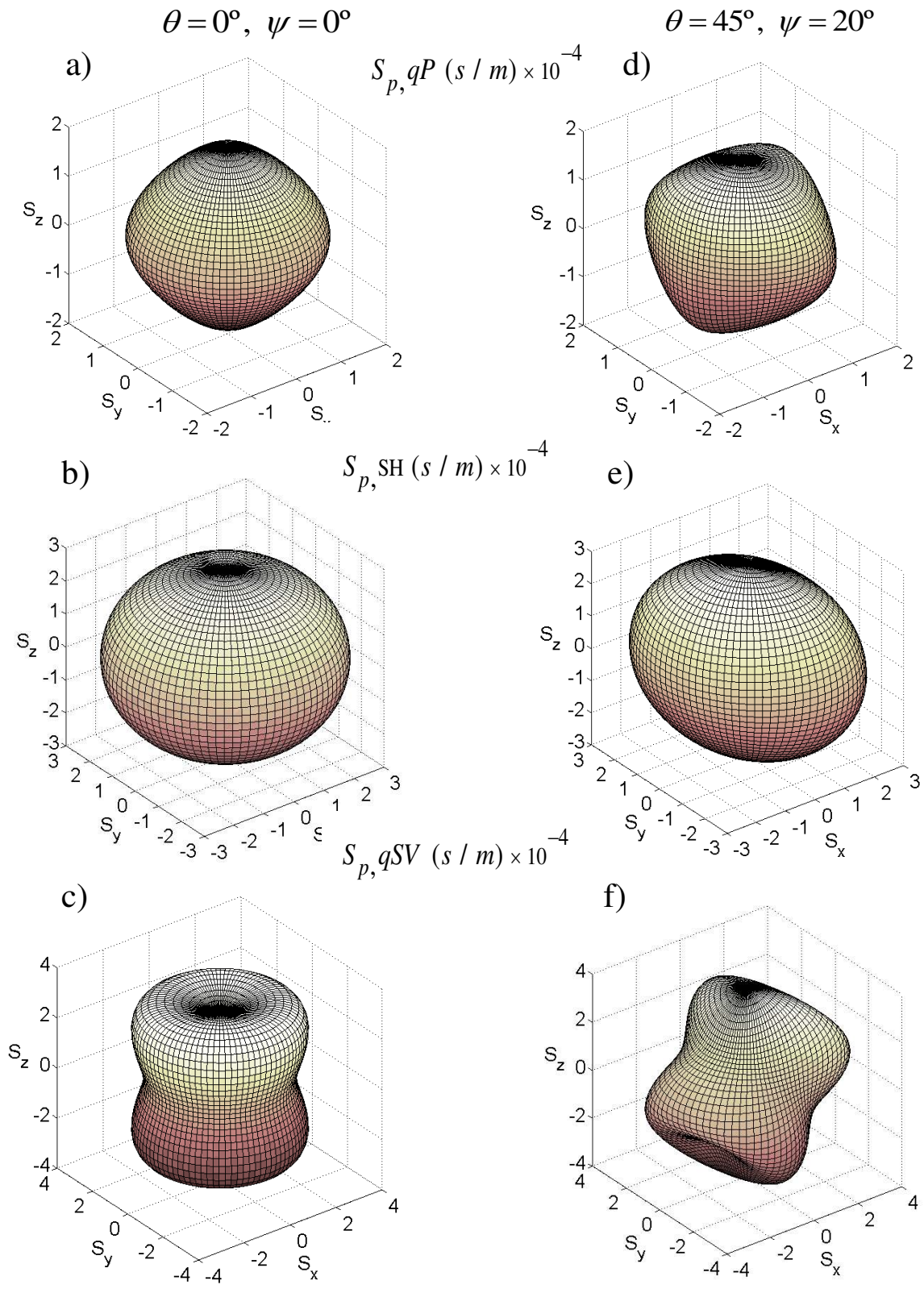

Figure 2.4: *Phase slowness surfaces in the transversely isotropic austenitic stainless steel material (X6 CrNi 1811): a), d) quasi longitudinal waves; b), e) Shear horizontal waves and c), f) quasi shear vertical waves.* θ *represents the columnar grain orientation and* ψ *represents the layback orientation.*

2.2.3 Polarization Vector

The polarization vectors for the qP, qSV and SH waves, as described in Eq. (2.27), are numerically evaluated for the austenitic steel material. Fig. 2.5 shows the polarization vector representation for the longitudinal (P) and shear vertical (SV) waves in isotropic steel material. The material properties for the isotropic steel material are presented in Table1.

It is apparent from Fig. 2.5 that the polarization directions of P and SV waves in isotropic steel material are equal to the wave vector directions because their phase velocity components are directional independent, as explained in Section 2.2.2. The polarization vectors for the qP and qSV waves in transverse isotropic austenitic steel material exhibiting columnar grain orientations 0º and 50º are shown in Fig. 2.6(a) and (b). It is apparent from the Fig. 2.6 (a) and (b) that the polarization directions for the qP and qSV waves are deviated from the wave vector direction because their phase velocity components vary with propagation direction. Whereas, pure SH wave polarizes in the plane of isotropy. Therefore, the polarization direction of SH wave is always perpendicular to the wave vector direction.

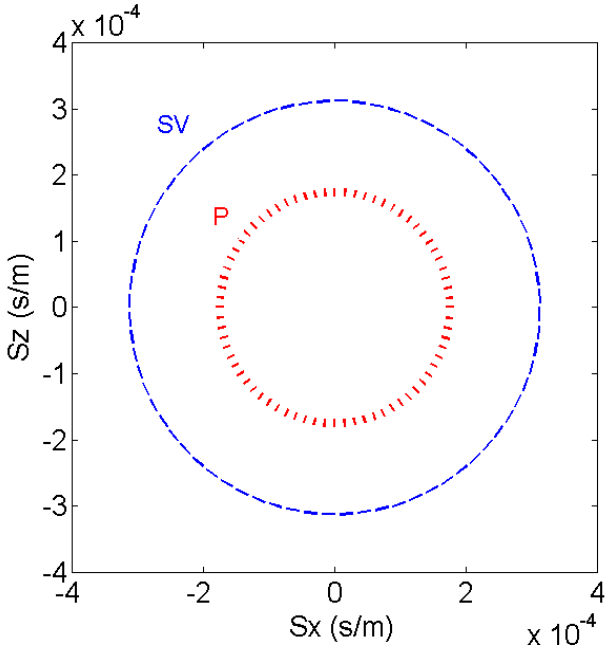

Figure 2.5: *Polarization vectors for the longitudinal (P) and shear vertical (SV) waves in the isotropic steel material.*

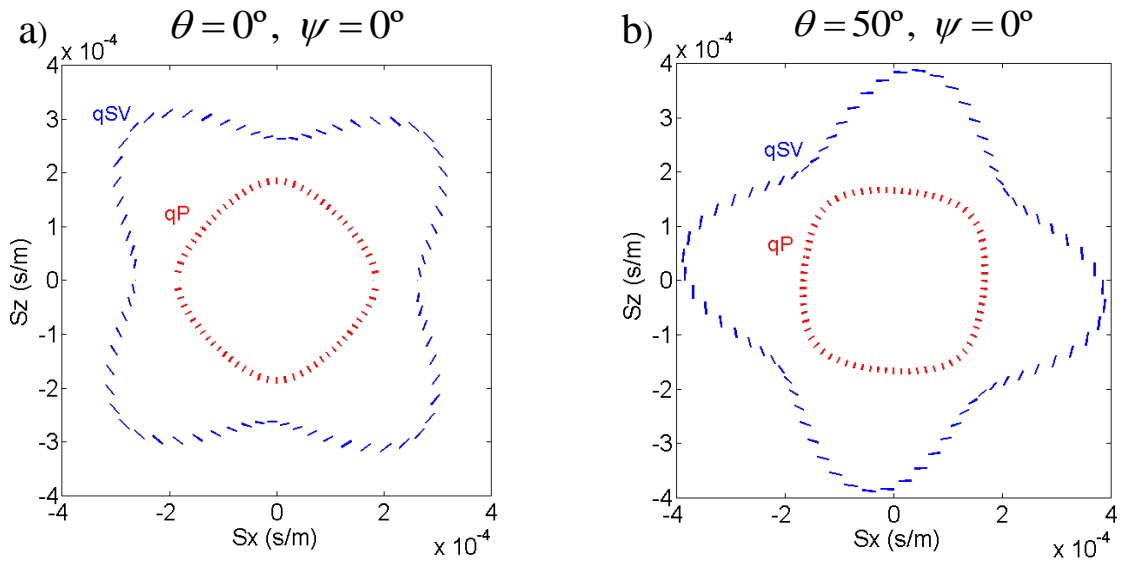

Figure 2.6: *Polarization vectors for the quasi longitudinal (qP) and quasi shear vertical (qSV) waves in the austenitic stainless steel material(X6 CrNi 1811) with a) 0° and b) 50° columnar grain orientation.*

2.2.4 Poynting Vector and Energy Density

The average power flow density of an acoustic wave is called the acoustic Poynting vector. The direction of the Poynting vector defines the direction of energy flow. Visualization of acoustic wave propagation in general anisotropic medium requires a better understanding between the phase velocity and the energy velocity because the energy flow direction is different from the wave vector direction. The Poynting vector is one of most significant acoustic wave properties to determine the energy velocity magnitude as well as direction [69, 117].

The analytical expressions for the Poynting vector and energy density for the three wave modes exist in general anisotropic solids are evaluated three dimensionally. Let us consider an incident wave polarizes in xyz space and associated particle velocity components along x, y, z directions as follows

$$v_x = A_x \exp\left(i\left(\omega t - k_x x - k_y y - k_z z\right)\right) \tag{2.28}$$

$$v_y = A_y \exp\left(i\left(\omega t - k_x x - k_y y - k_z z\right)\right) \tag{2.29}$$

$$v_z = A_z \exp\left(i\left(\omega t - k_x x - k_y y - k_z z\right)\right). \tag{2.30}$$

The associated strain components are given as

$$[\mathbf{S}] = \begin{bmatrix} S_1 \\ S_2 \\ S_3 \\ S_4 \\ S_5 \\ S_6 \end{bmatrix} = \begin{bmatrix} \dfrac{\partial u_x}{\partial x} \\ \dfrac{\partial u_y}{\partial y} \\ \dfrac{\partial u_z}{\partial z} \\ \dfrac{\partial u_z}{\partial y} + \dfrac{\partial u_y}{\partial z} \\ \dfrac{\partial u_x}{\partial z} + \dfrac{\partial u_z}{\partial x} \\ \dfrac{\partial u_x}{\partial y} + \dfrac{\partial u_y}{\partial x} \end{bmatrix} \tag{2.31}$$

where u_i with $i = x, y, z$ represent the particle displacement components.

The stress matrix can be expressed as follows

$$[\mathbf{T}] = \begin{bmatrix} T_1 \\ T_2 \\ T_3 \\ T_4 \\ T_5 \\ T_6 \end{bmatrix} = \begin{bmatrix} c_{11} & c_{12} & c_{13} & c_{14} & c_{15} & c_{16} \\ c_{12} & c_{22} & c_{23} & c_{24} & c_{25} & c_{26} \\ c_{13} & c_{23} & c_{33} & c_{34} & c_{35} & c_{36} \\ c_{14} & c_{24} & c_{34} & c_{44} & c_{45} & c_{46} \\ c_{15} & c_{25} & c_{35} & c_{45} & c_{55} & c_{56} \\ c_{16} & c_{26} & c_{36} & c_{46} & c_{56} & c_{66} \end{bmatrix} \begin{bmatrix} S_1 \\ S_2 \\ S_3 \\ S_4 \\ S_5 \\ S_6 \end{bmatrix} \tag{2.32}$$

In acoustics the power delivered to a solid medium is equal to the applied stress times the velocity of the wave. The complex Poynting vector in a general anisotropic solid is determined as [69]

$$\mathbf{P}_{av} = -\frac{\mathbf{v}^* \cdot \mathbf{T}}{2} \tag{2.33}$$

$$= -\frac{\hat{x}}{2}\left(v_x^* T_{xx} + v_y^* T_{yx} + v_z^* T_{zx}\right) - \frac{\hat{y}}{2}\left(v_x^* T_{xy} + v_y^* T_{yy} + v_z^* T_{zy}\right) - \frac{\hat{z}}{2}\left(v_x^* T_{xz} + v_y^* T_{yz} + v_z^* T_{zz}\right) \quad (2.34)$$

Substituting Eq. (2.32) into the Eq. (2.34) and expanding the terms gives the following general expressions for the components of Poynting vector (energy vector)

$$P_x = \frac{1}{2}\left(\frac{A_x^2}{(V_i)}\right)\left[\frac{A_y}{A_x}(a_1) + \frac{A_z}{A_x}(a_2) + \left(\frac{A_z}{A_x}\cdot\frac{A_y}{A_x}\right)(a_3) + \left(\frac{A_y}{A_x}\right)^2(a_4) + \left(\frac{A_z}{A_x}\right)^2(a_5) + a_6\right] \quad (2.35)$$

$$P_y = \frac{1}{2}\left(\frac{A_x^2}{V_i}\right)\left[\frac{A_y}{A_x}(b_1) + \frac{A_z}{A_x}(b_2) + \left(\frac{A_z}{A_x}\cdot\frac{A_y}{A_x}\right)(b_3) + \left(\frac{A_y}{A_x}\right)^2(b_4) + \left(\frac{A_z}{A_x}\right)^2(b_5) + b_6\right] \quad (2.36)$$

$$P_z = \frac{1}{2}\left(\frac{A_x^2}{V_i}\right)\left[\frac{A_y}{A_x}(c_1) + \frac{A_z}{A_x}(c_2) + \left(\frac{A_z}{A_x}\cdot\frac{A_y}{A_x}\right)(c_3) + \left(\frac{A_y}{A_x}\right)^2(c_4) + \left(\frac{A_z}{A_x}\right)^2(c_5) + c_6\right], \quad (2.37)$$

where the coefficients a_k, b_k and c_k with $k = 1,2,3,4,5,6$ are expressed in terms of elastic stiffness components of the material and directional cosines of the propagating wave. The explicit expressions for the a_k, b_k and c_k are presented in Appendix B.

The particle displacement amplitude ratios $\frac{A_y}{A_x}, \frac{A_z}{A_x}$ are obtained from the Eq. (2.21) and resulting expressions are given as

$$\frac{A_y}{A_x} = \frac{\rho V_i^2 \Gamma_{23} - \left(\left(\Gamma_{11}\Gamma_{23} - \Gamma_{12}\Gamma_{13}\right)\right)}{\left(\left(\Gamma_{12}\Gamma_{23} - \Gamma_{22}\Gamma_{13}\right)\right) + \rho V_i^2 \Gamma_{13}} \quad (2.38)$$

$$\frac{A_z}{A_x} = \frac{\left(\Gamma_{11} - \rho V_i^2\right)\left(\Gamma_{22} - \rho V_i^2\right) - \left(\Gamma_{12}^2\right)}{\left(\left(\Gamma_{12}\Gamma_{23} - \Gamma_{22}\Gamma_{13}\right) + \rho V_i^2 \Gamma_{13}\right)} \; . \quad (2.39)$$

In case of isotropic materials the Poynting vector direction is equal to the wave vector direction whereas in an anisotropic material the Poynting vector direction is deviated from the wave vector direction. This deviation leads to beam skewing phenomenon and it will be discussed in Section 2.3.

Averaged stored energy density in a general anisotropic medium is expressed as

$$U_{av} = \frac{\rho}{2}\left(v_x^* v_x + v_y^* v_y + v_z^* v_z\right) \tag{2.40}$$

Substituting Eq. (2.28), Eq. (2.29) and Eq. (2.30) in Eq. (2.40) yields

$$U_{av} = \frac{\rho}{2} A_x^2 \left(1 + \left(\frac{A_y}{A_x}\right)^2 + \left(\frac{A_z}{A_x}\right)^2\right). \tag{2.41}$$

2.2.5 Energy Velocity Surface

Energy velocity in a general homogenous anisotropic medium is defined as the ratio of averaged complex Poynting vector and the averaged stored energy density [69]. The energy velocity in a lossless general anisotropic medium is represented as

$$V_g = \frac{P_{av}}{U_{av}}. \tag{2.42}$$

By introducing Eq. (2.35), Eq. (2.36), Eq. (2.37) and Eq. (2.41) into Eq. (2.42) yields the energy velocity components along x, y and z directions.

The magnitude of the energy velocity for a particular incident mode is expressed as

$$V_g = \sqrt{V_{gx}^2 + V_{gy}^2 + V_{gz}^2} \tag{2.43}$$

The numerical algorithm for evaluation of energy velocity surfaces in general anisotropic solids is written in MATLAB software. The energy velocity surfaces for the three wave modes namely qP, qSV and SH waves in transverse isotropic austenitic steel material exhibiting 0º columnar and lay back orientation is shown in Fig. 2.7(left). The cusps on the qSV wave energy surface are apparent from Fig. 2.7 (c). These cusps result from the complicated slowness surface of the quasi shear vertical waves as shown in Fig. 2.4. The influence of layback orientation on energy velocity surfaces of the three wave modes in an austenitic steel material is shown in Fig. 2.7(right). Energy slowness vector is defined as inverse of energy velocity vector. Three dimensional calculation of energy velocity surfaces are used in the next chapters to solve the 3D reflection and transmission problem. Further these results will be employed in 3D ray tracing algorithm.

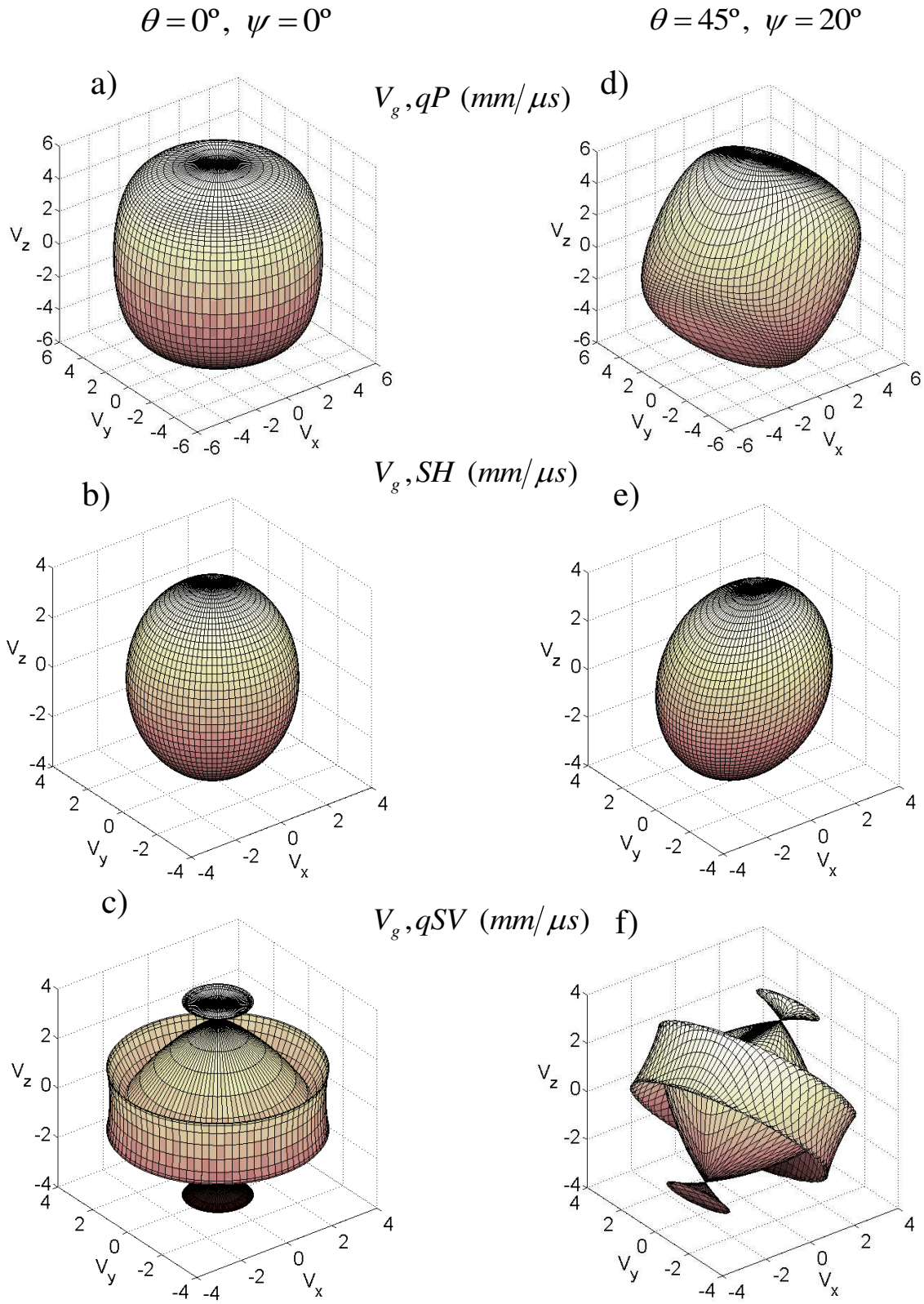

Figure 2.7: *Energy velocity surfaces in the transversely isotropic austenitic stainless steel material(X6 CrNi 1811): a), d) quasi longitudinal waves; b), e) Shear horizontal waves and c), f) quasi shear vertical waves.* θ *represents the columnar grain orientation and* ψ *represents the layback orientation.*

2.3 Beam Distortion in Anisotropic Solids

2.3.1 Beam Divergence

When an ultrasonic wave propagates in an anisotropic medium it associates with certain beam divergence. Beam divergence is defined as fractional change in the phase velocity direction and finding the associated change in energy velocity direction [23]. Beam divergence is expressed as follows

$$BD = \left| \frac{\Delta\theta_g}{\Delta\theta_p} \right|, \tag{2.44}$$

where θ_g, θ_p are directions of group velocity and phase velocity respectively.

In case of isotropic medium the beam divergence is always unity, which means that the energy is fully concentrated along the wave vector direction. Beam divergence of a conventional ultrasonic transducer, when an ultrasonic wave propagates into the transversely isotropic austenitic weld, is more diffuse or narrower and depends on the columnar grain orientation of the material as well as angle of incidence. Fig. 2.8 shows the angular dependence of beam divergence of the three wave modes namely qP, qSV and SH waves in the transversely isotropic austenitic weld material exhibiting 3D columnar grain orientation. As expected, the influence of anisotropy on beam divergence is more predominant for the qSV waves as compared to the qP and SH waves (see Fig. 2.8). It can be seen from Fig. 2.8 that the SH wave beam divergence properties are close to the isotropic ferritic steel material.

2.3.2 Beam Skewing

In case of anisotropic medium the phase velocity and group velocity directions do not coincide. Because the phase velocity vector is perpendicular to the wavefront and the group velocity vector is parallel to the energy flux. Consequently, the group velocity vector is not perpendicular to the wavefront. The deviation between phase and energy velocity direction is defined as beam skewing.

Beam skewing is expressed as follows

$$\beta = \cos^{-1}\left(\frac{\mathbf{V}_p \cdot \mathbf{V}_g}{|\mathbf{V}_p||\mathbf{V}_g|}\right). \tag{2.45}$$

During the ultrasonic non-destructive inspection of transverse isotropic austenitic weld material, the beam skewing effects are considered in order to position the receipting transducer at optimum energy directions.

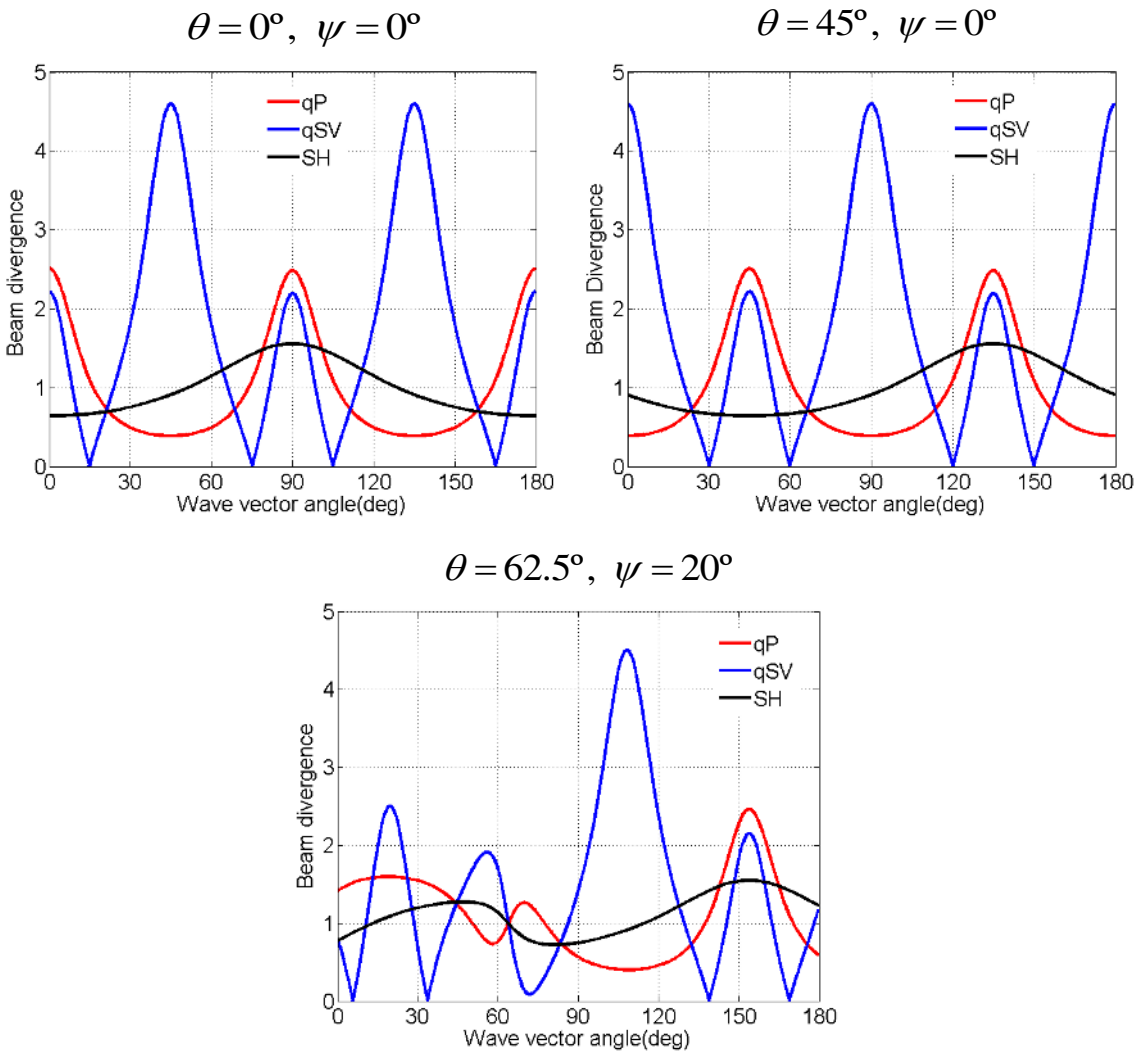

Figure 2.8: *Variation of beam divergence factor with incident wave vector angle for the three wave modes in the columnar grained austenitic steel material.* θ *represents the columnar grain orientation and* ψ *represents the layback orientation.*

Fig. 2.9 displays the variation of beam skewing angles for the qP, qSV and SH waves in an austenitic weld material exhibiting different columnar grain orientations with the angle of incidence. As can be seen in Fig. 2.9, the horizontally polarized shear waves (SH) have low beam skewing angles over a wide range of phase velocity angles. Whereas the qSV waves have large beam skewing angles over a wide range of incidence angles. It is observed that the quasi longitudinal waves (qP) have the beam skewing angles in between qSV and SH waves.

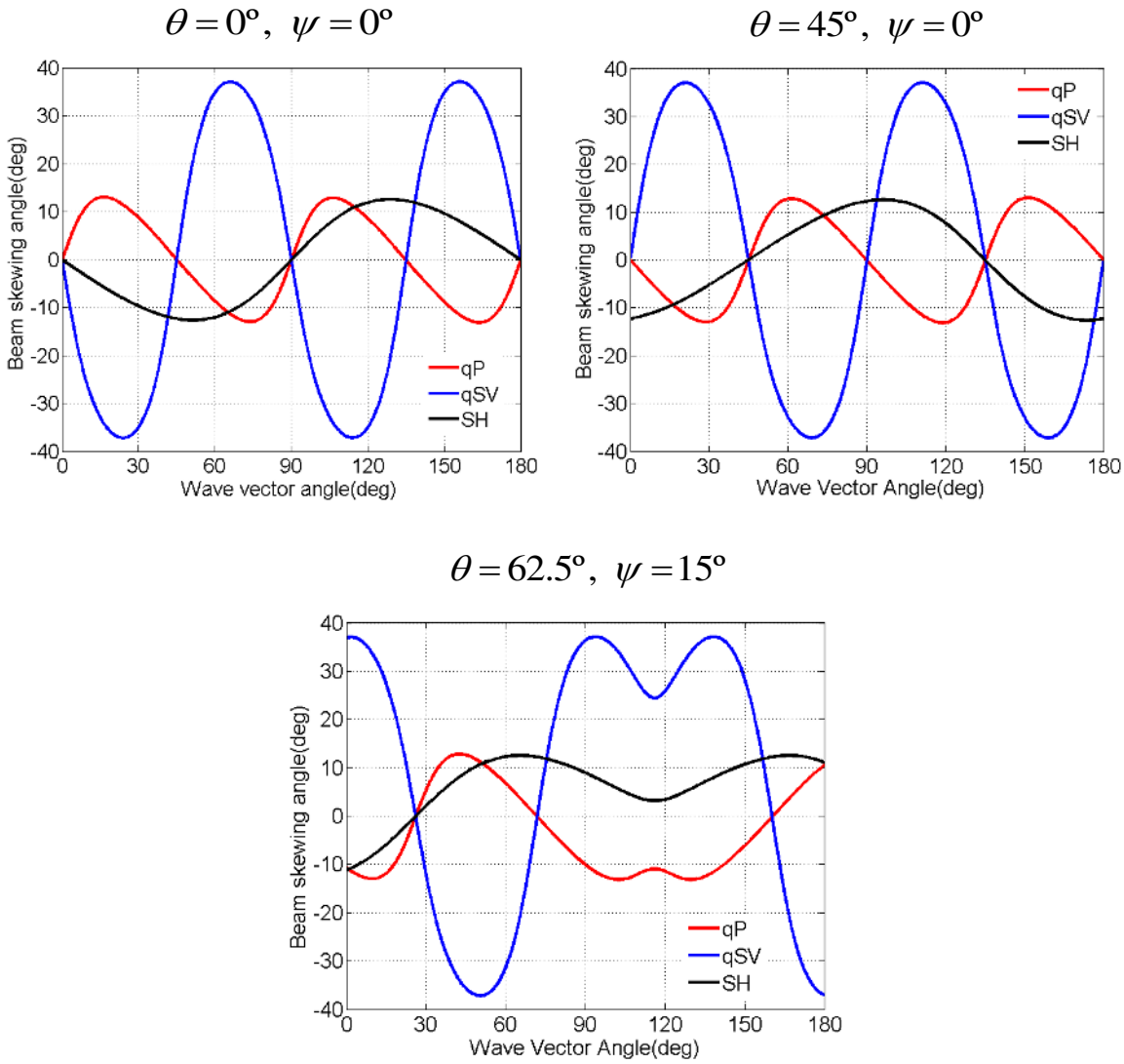

Figure 2.9: *Variation of beam skewing angle with incident wave vector angle for the three wave modes in the columnar grained austenitic steel material.* θ *represents the columnar grain orientation and* ψ *represents the layback orientation.*

2.3.3 Beam Spreading Factor

Beam spreading factor is defined as fractional change in the phase velocity magnitude and finding the associated change in the energy velocity magnitude. Beam spreading factor is expressed as

$$BS = \left| \frac{\Delta V_g}{\Delta V_p} \right|. \tag{2.46}$$

Beam spreading factor for the isotropic ferritic steel materials is zero because of the fact that the energy velocity magnitude is equal to the phase velocity magnitude. In case of anisotropic materials the beam spreading factor varies with respect to the phase velocity direction. Higher beam spreading factor results in higher energy scatter as well as reducing the energy density. Fig. 2.10 shows the variation of beam spreading factor for qP, qSV and SH waves in transverse isotropic austenitic steel material with phase velocity direction. It can be observed from Fig. 2.10 that the presence of layback orientation in austenitic weld materials reduces the beam spreading factor. For the ultrasonic non-destructive inspection of austenitic weld materials, it is more important to prefer the range of incidence angles at which beam spreading factor is close to zero.

The theory of ultrasonic wave propagation in general anisotropic media has been reviewed in this chapter and ultrasonic wave propagation properties were evaluated three dimensionally. The anisotropy influenced parameters such as slowness vector, polarization vector, Poynting vector, energy velocity vector, beam divergence, beam skewing and beam spreading factor in the transversely isotropic austenitic weld material exhibiting 3D columnar grain orientation were quantitatively analyzed. The theory presented in this chapter will be used in the subsequent chapters to solve the reflection and transmission problem at an interface between two dissimilar materials and employing the consequent results in the 3D ray tracing calculations.

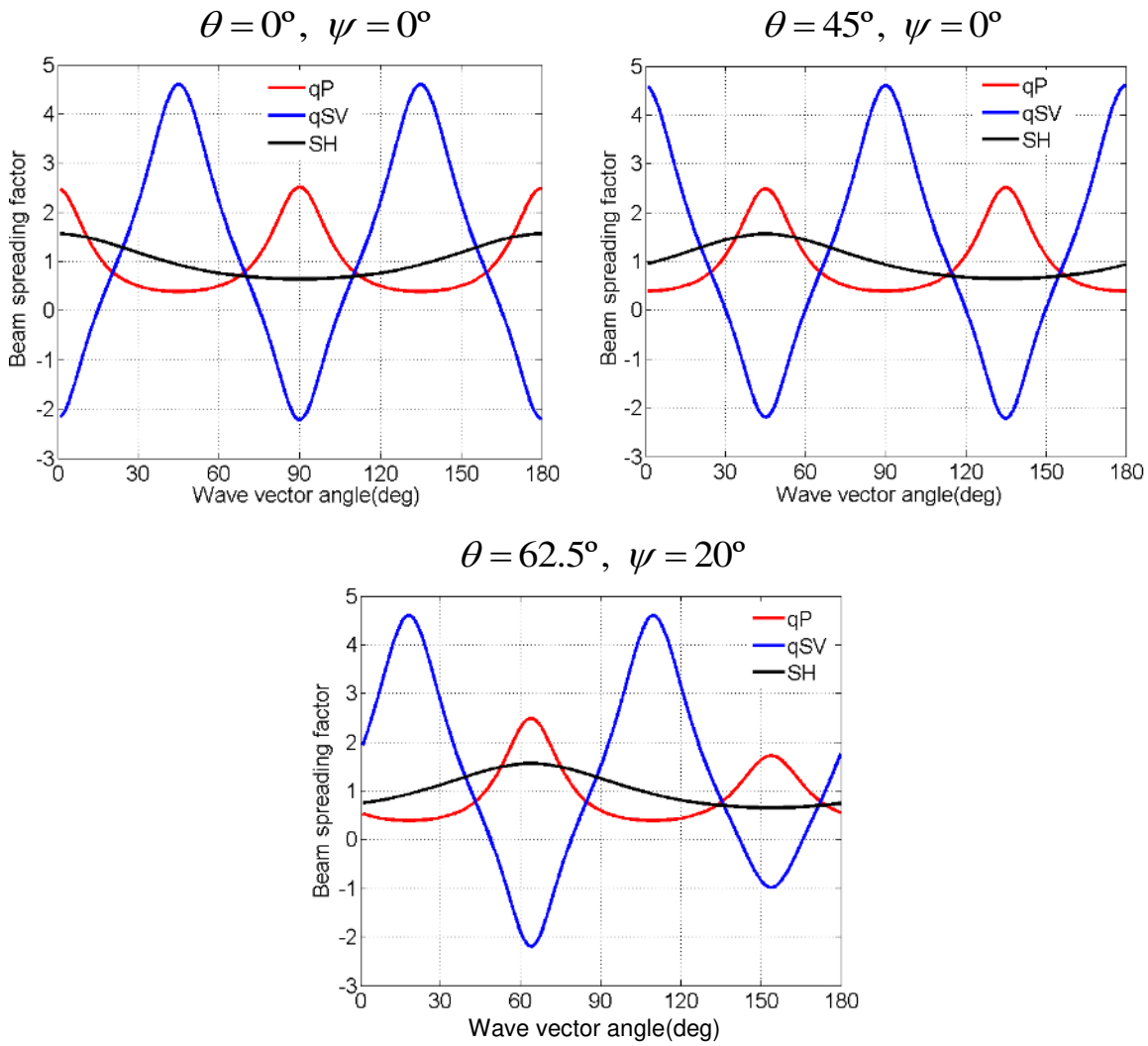

Figure 2.10: *Variation of beam spreading factor with incidence wave vector angle for the three wave modes in the columnar grained austenitic steel material.* θ *represents the columnar grain orientation and* ψ *represents the layback orientation.*

CHAPTER 3

Ultrasound Energy Reflection and Transmission Coefficients at an Interface between two Anisotropic Materials: Application to Austenitic Welds

3.1 Introduction

In this chapter, ultrasonic plane wave energy reflection and transmission coefficients at an interface between two general anisotropic materials are evaluated for a 3D geometry. During the ultrasonic non-destructive testing of austenitic welds several possible interfaces generally occur such as in case of immersion techniques water as coupling medium and arbitrarily oriented austenitic weld specimen as transmitted medium as well as in case of contact techniques where rigid contact between Perspex wedge material and weld specimen and vice versa. The reflection and transmission at an interface between isotropic ferritic base material and austenitic weld material and vice versa are of general importance for the selection of the proper incident ultrasonic wave mode and optimal incident angles. Because of spatially varying grain orientation in the weld material, it is important to evaluate the energy behavior at a boundary between two adjacent columnar grained regions of the weld material. Energy reflection phenomena of plane elastic waves at a free boundary of columnar grained austenitic weld material arises during the ultrasonic testing in order to characterize the reflected waves from the material boundaries and inhomgenities such as a crack face.

Quantitative evaluation of energy transported by direct as well as mode converted waves in general columnar grained austenitic weld materials provide a greater insight in developing theoretical procedures and experimental methodologies. Three dimensional representation of columnar grain orientation in austenitic weld material is appropriate for both longitudinal as well as transversal cracks detection. The results of this chapter play an important role in developing three dimensional ray tracing algorithm and evaluating ray amplitudes in inhomogeneous anisotropic austenitic weld materials.

3.2 Reflection and Transmission of Ultrasound at an Interface between two General Anisotropic Materials

3.2.1 Theoretical Procedure

When an ultrasonic wave impinges at an interface between two anisotropic solids generally three reflected and three transmitted waves propagate in the medium 1 and medium 2, respectively [69, 70, 71].

Let us consider a plane monochromatic wave with its particle displacement vector

$$\mathbf{u}^{I} = A^{I}\mathbf{a}^{I}\exp\left(i\omega\mathbf{S}^{I}\cdot\mathbf{r}\right), \tag{3.1}$$

incident from the medium 1 onto a boundary between two general anisotropic solids, where A^{I} is the amplitude of the incident wave, $\mathbf{a}^{I}$ is the incident wave polarization vector, $\mathbf{S}^{I}$ is the slowness vector of the incident wave and $\mathbf{r}$ is the position vector. I represents the incident quasi longitudinal (qP) or quasi shear vertical (qSV) or quasi shear horizontal (qSH) wave respectively. For illustration, Fig. 3.1 shows reflection and transmission phenomena at an interface between two columnar grained austenitic steel materials. In chapter 2, it is already discussed that one of the shear waves i.e. shear horizontal wave exhibits pure wave characteristics in austenitic weld materials.

The reflected and transmitted particle displacements are expressed as

$$\mathbf{u}^{R\alpha} = A^{R\alpha}\mathbf{a}^{R\alpha}\exp\left(i\omega\mathbf{S}^{R\alpha}\cdot\mathbf{r}\right) \tag{3.2}$$

and

$$\mathbf{u}^{T\alpha} = A^{T\alpha}\mathbf{a}^{T\alpha}\exp\left(i\omega\mathbf{S}^{T\alpha}\cdot\mathbf{r}\right) \tag{3.3}$$

where $A^{R\alpha}$, $A^{T\alpha}$ and $\mathbf{a}^{R\alpha}, \mathbf{a}^{T\alpha}$ are the amplitudes and particle polarization vectors for the reflected and transmitted waves. $\mathbf{S}^{R\alpha}$ and $\mathbf{S}^{T\alpha}$ are the slowness vectors for the reflected and transmitted waves, respectively.

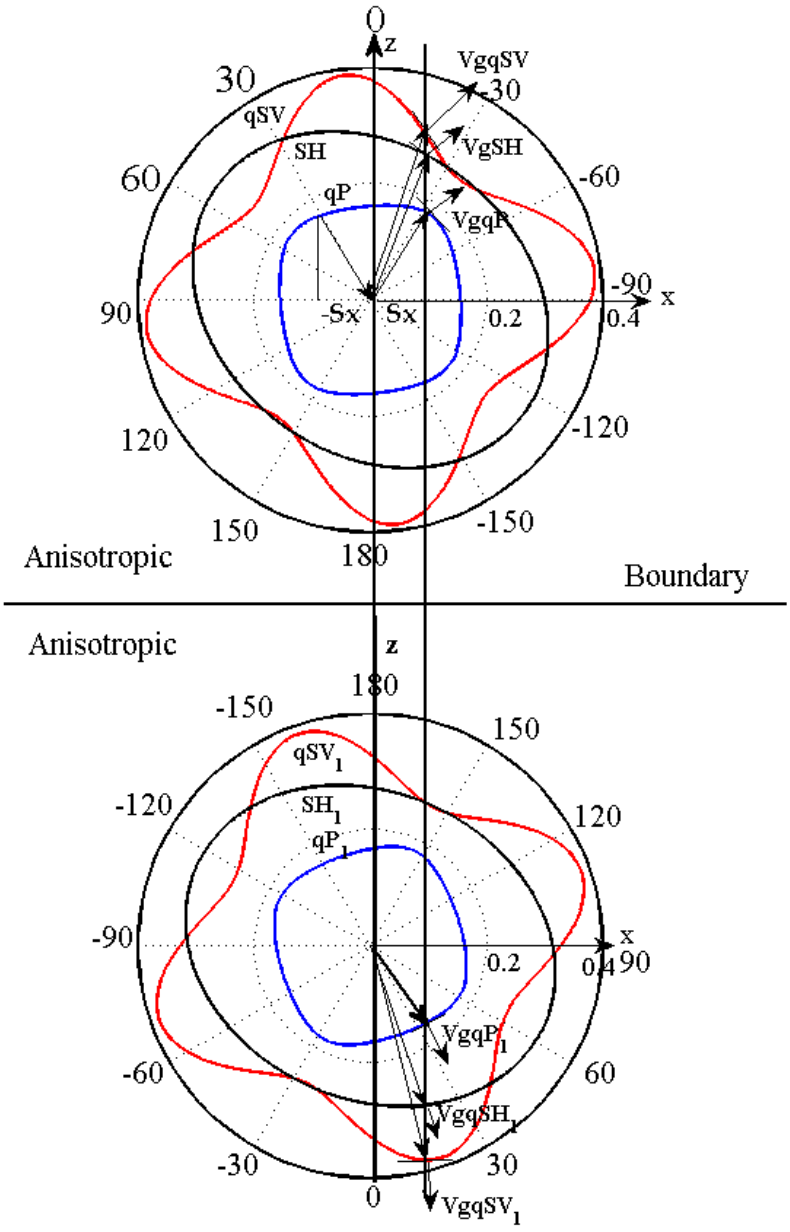

Figure 3.1: *Graphical representation of ultrasonic plane wave reflection and transmission phenomena at an interface between two columnar grained austenitic steel materials.*

According to the Snell's law [70, 71] all the projections of the slowness vector on the interface are equal to another (see Fig. 3.1), which leads to the following relations:

$$S_x^I = S_x^{R\alpha} = S_x^{T\alpha} = S_x, \tag{3.4}$$

$$S_y^I = S_y^{R\alpha} = S_y^{T\alpha} = S_y. \tag{3.5}$$

The unknown vertical components (S_z) of reflected and transmitted slowness vectors are determined using modified Christoffel equation

$$\begin{vmatrix} M_{11}-\rho & M_{12} & M_{13} \\ M_{12} & M_{22}-\rho & M_{23} \\ M_{13} & M_{23} & M_{33}-\rho \end{vmatrix} = 0 \ , \tag{3.6}$$

where

$$\left.\begin{aligned} M_{11} &= c_{11}S_x^2 + c_{66}S_y^2 + c_{55}S_z^2 + 2c_{56}S_yS_z + 2c_{15}S_zS_x + 2c_{16}S_xS_y \\ M_{12} &= c_{16}S_x^2 + c_{26}S_y^2 + c_{45}S_z^2 + (c_{46}+c_{25})S_yS_z + (c_{14}+c_{56})S_zS_x + (c_{12}+c_{66})S_xS_y \\ M_{13} &= c_{15}S_x^2 + c_{46}S_y^2 + c_{35}S_z^2 + (c_{45}+c_{36})S_yS_z + (c_{13}+c_{55})S_zS_x + (c_{14}+c_{56})S_xS_y \\ M_{22} &= c_{66}S_x^2 + c_{22}S_y^2 + c_{44}S_z^2 + 2c_{24}S_yS_z + 2c_{46}S_zS_x + 2c_{26}S_xS_y \\ M_{23} &= c_{56}S_x^2 + c_{24}S_y^2 + c_{34}S_z^2 + (c_{44}+c_{23})S_yS_z + (c_{36}+c_{45})S_zS_x + (c_{25}+c_{46})S_xS_y \\ M_{33} &= c_{55}S_x^2 + c_{44}S_y^2 + c_{33}S_z^2 + 2c_{34}S_yS_z + 2c_{35}S_zS_x + 2c_{45}S_xS_y \end{aligned}\right\} \tag{3.7}$$

3.2.2 Six - degree Polynomial Equation

The Eq. (3.6) is solved separately for the reflected and transmitted waves in medium 1 and medium 2. The resulting six degree polynomial equations for the reflected and transmitted media are expressed as follows

$$A^R\left(S_z^R\right)^6 + B^R\left(S_z^R\right)^5 + C^R\left(S_z^R\right)^4 + D^R\left(S_z^R\right)^3 + E^R\left(S_z^R\right)^2 + F^RS_z^R + G^R = 0 \tag{3.8}$$

$$A^T\left(S_z^T\right)^6 + B^T\left(S_z^T\right)^5 + C^T\left(S_z^T\right)^4 + D^T\left(S_z^T\right)^3 + E^T\left(S_z^T\right)^2 + F^TS_z^T + G^T = 0 \tag{3.9}$$

The coefficients in the Eqs. (3.8) and (3.9) are expressed in terms of horizontal slowness components and material elastic constants of the medium 1 and medium 2. These coefficients are presented in Appendix C. Six solutions are found in each medium, three of which only correspond to physically real solutions. The energy flow directions for the reflected and transmitted waves are the criterion for selecting the valid roots [18, 118, 119, 120]. According to the energy flow direction criterion, for reflected and transmitted waves the energy flow direction point away from the interface. The roots of six degree polynomial are generally complex. Purely real roots correspond to propagating waves,

purely imaginary roots correspond to evanescent waves, whose amplitude decay in the direction perpendicular to the wave energy direction and complex roots represent inhomogeneous waves.

Special Case:

In the particular case of sound propagation in the transverse isotropic columnar grained austenitic materials, the horizontally polarized shear wave (SH) does not couple with qP and qSV waves because pure SH wave polarizes perpendicular to the plane of wave propagation as stated previously. The Eq. (3.6) is reduced to one coupled fourth order polynomial equation and one uncoupled second order polynomial equation [61, 121]. The solutions of the resulting quadratic equations correspond to the reflected and transmitted SH waves. The solution of fourth order polynomial equations corresponds to the reflected and transmitted qP and qSV waves. The solutions for the reflected and transmitted vertical slowness components for the qP and qSV waves are obtained from the roots of the fourth order polynomial equation in S_z as

$$A^R\left(S_z^R\right)^4 + B^R\left(S_z^R\right)^3 + C^R\left(S_z^R\right)^2 + D^R S_z^R + E^R = 0\ , \tag{3.10}$$

$$A^T\left(S_z^T\right)^4 + B^T\left(S_z^T\right)^3 + C^T\left(S_z^T\right)^2 + D^T S_z^T + E^T = 0\,. \tag{3.11}$$

The coefficients in the Eq. (3.10) and Eq. (3.11) are obtained by substituting the respective medium material properties in the Eq. (3.12).

$$\left.\begin{aligned}
A^{R,T} &= c_{55}c_{33} - c_{35}^2 \\
B^{R,T} &= \left(2\left(\left(c_{15}c_{33}\right) - c_{35}c_{13}\right)\right)S_x \\
C^{R,T} &= S_x^2\left(c_{11}c_{33} + \left(2\left(\left(c_{35}c_{15}\right) - c_{13}c_{55}\right)\right) - c_{13}^2\right) - \rho\left(c_{33} + c_{55}\right) \\
D^{R,T} &= S_x^3\left(2\left(\left(c_{11}c_{35}\right) - c_{15}c_{13}\right)\right) - S_x\left(2\rho\left(c_{15} + c_{35}\right)\right) \\
E^{R,T} &= S_x^4\left(\left(c_{11}c_{55}\right) - c_{15}^2\right) - S_x^2\left(\rho\left(c_{11} + c_{55}\right)\right) + \rho^2
\end{aligned}\right\} \tag{3.12}$$

Euler's quartic method [114, 122] is used for analytically evaluating the four roots of the quartic Equations (3.10) and (3.11). A detailed description is presented in Appendix D.

3.2.3 Amplitude Coefficients for Reflected and Transmitted Waves

Once the valid roots for the reflected and transmitted waves are obtained, the corresponding phase velocity magnitudes, polarization vectors, polarization angles and group velocity magnitudes are computed. The energy skewing angles for the reflected and transmitted waves are obtained by calculating the energy angle deviation from the corresponding wave vector angle. The boundary conditions are the continuity of traction forces and particle displacement components at an interface between two general anisotropic solids. They are given by

$$\left(\mathrm{T}_J^I + \sum \mathrm{T}_J^{R\alpha} = \sum \mathrm{T}_J^{T\alpha}\right)_{z\,=\,0}, \tag{3.13}$$

$$\left(v_k^I + \sum v_k^{R\alpha} = \sum v_k^{T\alpha}\right)_{z\,=\,0}, \tag{3.14}$$

where T_J is the traction force component with $J = xz,\ zz,\ yz$. Furthermore, I, R and T indicate the incident, reflected and transmitted waves, respectively. v_k is the particle displacement component with $k = x,\ \mathrm{y},\ \mathrm{z}$. Insertion of Equations (3.1), (3.2) and (3.3) in Equations (3.13) and (3.14) results in six linear algebraic equations which can be solved for evaluating three reflected and three transmitted amplitude coefficients.

3.2.4 Energy Coefficients for the Reflected and Transmitted Waves

In case of anisotropic materials, the energy vector direction does not coincide with the wave vector direction. It is more useful to represent the energy flux ratios rather than amplitude ratios [120]. The ratio of the normal components of the reflected and transmitted energy flux vectors with incident normal component of the energy flux vector result the energy reflection and transmission coefficients and are expressed as

$$E^{R\alpha} = \left(\frac{A^{R\alpha}}{A^{I\alpha}}\right)^2 * \left(\frac{v_{gz}^{R\alpha}}{v_{gz}^{I\alpha}}\right)^2, \tag{3.15}$$

$$E^{T\alpha} = \left(\frac{A^{T\alpha}}{A^{I\alpha}}\right)^2 * \left(\frac{v_{gz}^{T\alpha}}{v_{gz}^{I\alpha}}\right)^2 * \left(\frac{\rho_2}{\rho_1}\right), \tag{3.16}$$

where $v_{gz}^{I\alpha}$, $v_{gz}^{R\alpha}$, $v_{gz}^{T\alpha}$ and $A^{I\alpha}$, $A^{R\alpha}$, $A^{T\alpha}$ are the normal component of the group velocity vectors and amplitudes of the incident, reflected and transmitted waves, respectively.

Additionally, ρ_1 and ρ_2 are the densities of the medium 1 and medium 2. Explicit analytical expressions for energy reflection and transmission coefficients at an interface between two arbitrarily oriented transversal isotropic austenitic steel materials are presented in Appendix E.

3.2.5 Critical Angle Phenomenon

In case of general anisotropic solids, energy flow direction does not coincide with the wave vector direction, as stated above. Depending on the type of wave mode of excitation and anisotropy of the medium an incident wave is directed towards the interface but the corresponding energy flow direction directed away from the interface. Critical angle for the incident wave is defined as angle at which the energy flow direction is parallel to the interface (so called grazing angle) [69]. In this chapter, the energy reflection and transmission coefficients are calculated for the valid range of incident angles whose energy flow direction is directed towards the interface.

3.3 General Interfaces Occur During Ultrasonic Inspection of Anisotropic Austenitic Welds

In this section numerical results for analytically evaluated energy reflection and transmission coefficients for several configurations generally occurring in relation to the ultrasonic non-destructive evaluation of transverse isotropic austenitic weld material are presented. Influence of columnar grain orientation as well as layback orientation on the energy reflected and transmitted waves in austenitic weld materials are analyzed. For the presentation of quantitative results, it is considered that the columnar grain orientations and lay back orientations vary between 0° and 90°. An algorithm is developed to calculate the reflected and transmitted energy coefficients in anisotropic materials three dimensionally.

For calculating energy reflection and transmission behavior at the interfaces, the adjacent media are assumed as homogeneous. This assumption is in contrast to the real properties of an austenitic weld. For the present quantitative evaluation of analytical results, inhomogeneous region of the austenitic weld material is discretized into several

homogeneous layers and each layer exhibits 3-D columnar grain orientation and domain of the austenitic weld material is considered for the calculations. The elastic constants $C_{\alpha\beta}$ (GPa) and density ρ (kg/m^3) [116] of the austenitic weld material (X6 Cr Ni 18 11) used for the calculation are given in Table 1.

3.3.1 Austenitic Weld Material – Isotropic Steel Interface

The incident medium is austenitic weld material exhibiting 3D columnar grain orientation and the transmitted medium is the isotropic ferritic steel material (with parameters defined in Table 1). The incident wave is the quasi longitudinal wave (qP). Fig. 3.2 shows the schematic of possible reflected and transmitted waves at an interface between anisotropic austenitic steel and isotropic steel material. The assumed layback orientation in the austenitic weld material is 20° and columnar grain orientation is varied in between 0° and 90° with a step size of 25°. In the presented case, coupling between all the three wave modes qP, qSV and SH waves exist. In case of anisotropic medium, the reflected and transmitted waves may not be in the same plane as the incident wave, as explained in chapter 2.

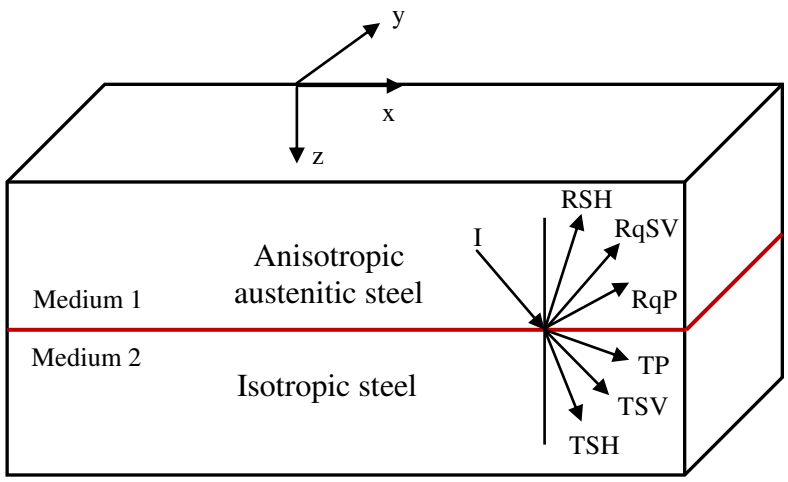

Figure 3.2: *Schematic of the energy reflection and transmission behavior at an interface between columnar grained austenitic steel material and isotropic ferritic steel material. I: incident wave, RqP: reflected quasi longitudinal wave, RqSV: reflected quasi shear vertical wave, RSH: reflected shear horizontal wave, TP: transmitted longitudinal wave, TSV: transmitted shear vertical wave and TSH: transmitted shear horizontal wave.*

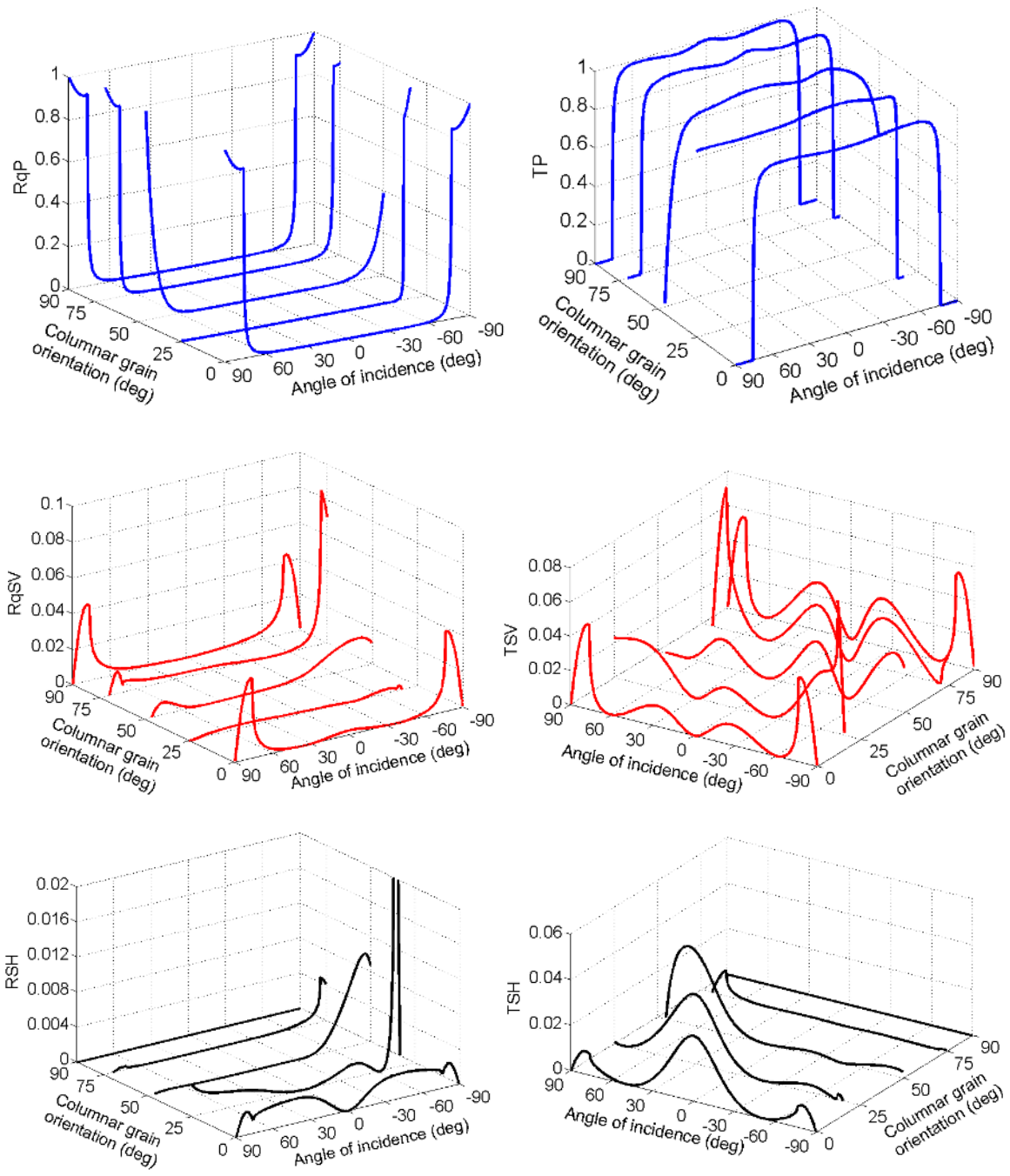

Figure 3.3: *Energy reflection and transmission coefficients for the reflected and transmitted waves when a quasi longitudinal wave (qP) is incident at an interface between anisotropic columnar grained austenitic weld material and isotropic ferritic steel material. The columnar grain angle of the austenitic weld material is varied between 0° and 90º with a step size of 25° and layback angle is 20° (kept constant).*

Figure 3.3 shows the influence of columnar grain orientation on energy reflection and transmission coefficients for the possible wave modes generated in the space of reflected and transmitted waves. There are three reflected and three transmitted waves generated at the interface. The comprehensive quantitative analysis reveals that energy transmission coefficients for the transmitted longitudinal waves (TP) depend on the columnar grain orientation. Beyond the critical angle, the incident wave energy is redistributed among other propagating wave types in reflection and transmission in order to satisfy the energy conservation criterion. The energy coefficients for the reflected quasi longitudinal waves (RqP) at transversal isotropic austenitic steel and isotropic steel interface are negligible for a wide range of incidence angles (see Fig. 3.3). The energy coefficients for the reflected quasi shear vertical waves (RqSV) vary up to 9% of the incident qP wave energy and that of transmitted shear vertical waves (TSV) vary up to 8%. The energy coefficients for the mode converted reflected pure shear horizontal waves (RSH) vary up to 6% of the incident qP wave energy and that of transmitted shear horizontal waves (TSH) vary up to 4%. It can be seen from Figure 3.3 that the energy coefficient for the reflected pure shear horizontal wave in case of 25° columnar grain orientation of the austenitic material rises sharply at an incident angle of 73.1° and reaches 6% of the incident energy.

Figure 3.4 shows the influence of layback orientation on energy reflection and transmission coefficients when a qP wave is incident at an interface between austenitic weld and isotropic ferritic steel material. The assumed columnar grain orientation in the austenitic material is 0° and layback orientation is varied in between 0° and 90° with a step size of 25°. The comprehensive quantitative analysis reveals that the transmissibility of incident qP wave at an interface between austenitic weld and isotropic ferritic steel is fairly high. The energy coefficients for the RqSV waves vary up to 5% of the incident qP wave energy and that of transmitted shear vertical waves (TSV) vary up to 6%. Whereas, the energy coefficients for the reflected pure shear horizontal waves (RSH) vary up to 0.8% of the incident qP wave energy and that of transmitted horizontal waves (TSH) vary up to 5%. It can be seen from Figure 3.4 that the coupling between shear modes does not exist for the 0º layback orientation of the austenitic weld material.

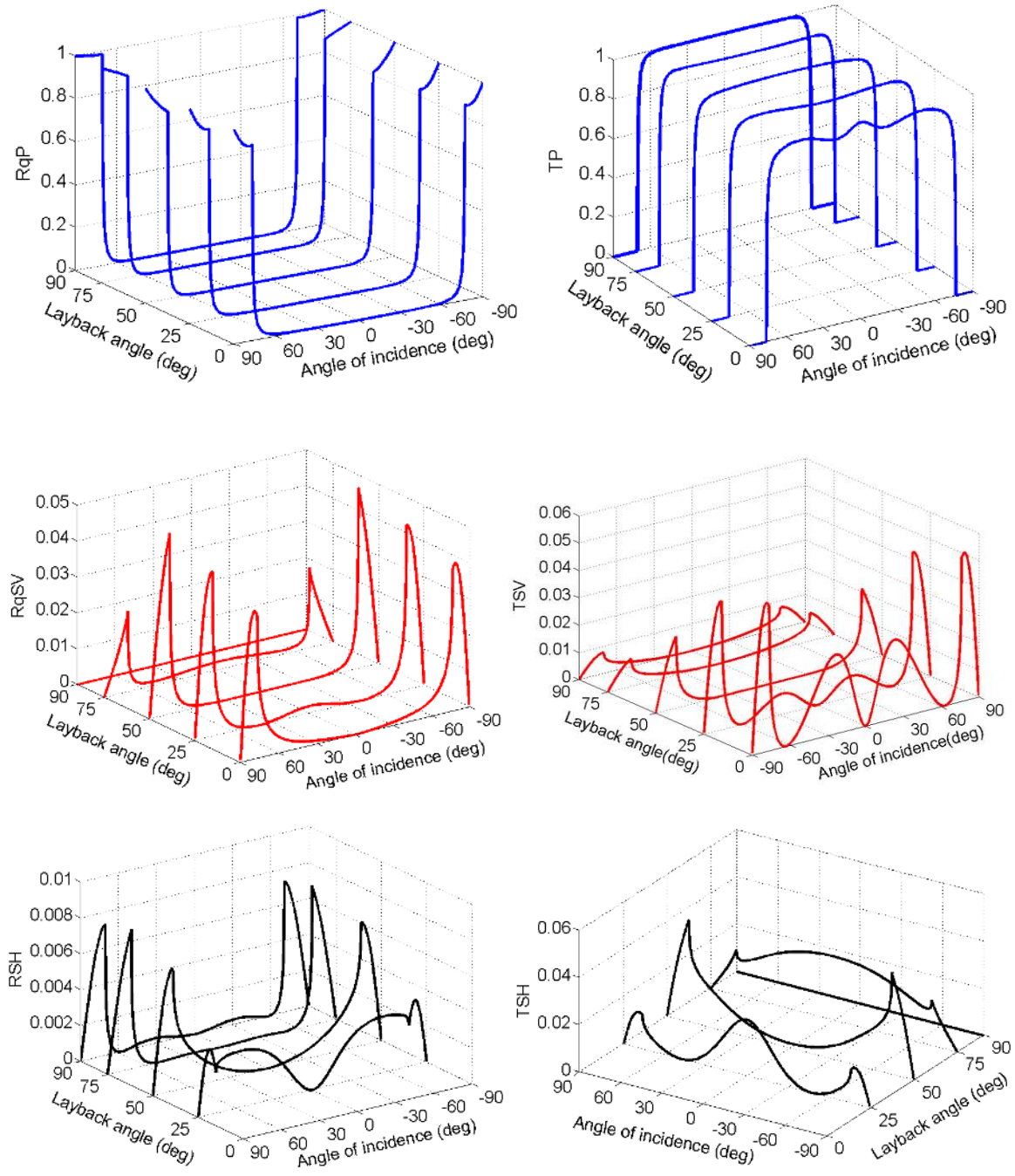

Figure 3.4: *Energy reflection and transmission coefficients for the reflected and transmitted waves when a quasi longitudinal wave (qP) is incident at an interface between anisotropic columnar grained austenitic weld material and isotropic ferritic steel material. The layback angle of the austenitic weld material is varied between 0° and 90º with a step size of 25° and columnar grain angle is 0° (kept constant).*

3.3.2 Austenitic Weld Material – Isotropic Perspex Wedge Interface

The incident medium is austenitic weld material exhibiting 3D columnar grain orientation and transmitted medium is the isotropic Perspex wedge (PMMA) which is the typical case occurring during the ultrasonic non-destructive investigation of austenitic welds where an ultrasonic signal is received from austenitic steel material into the Perspex wedge material. Fig. 3.5 shows the schematic of the energy reflection and transmission behavior at an interface between columnar grained austenitic steel and Perspex wedge material. The assumed layback orientation in the austenitic weld material is 20° and columnar grain orientation is varied in between 0° and 75° with a step size of 25°.

Figure 3.6 shows the influence of columnar grain orientation on energy reflection and transmission coefficients for the reflected and transmitted waves when a qP wave incident at an interface between austenitic weld material and Perspex wedge material. The energy coefficients for the transmitted longitudinal (TP) wave stays below 25% of the incident energy. The mode conversion of the incident qP wave energy into transmitted shear vertical (TSV) reaches 22% and that of transmitted shear horizontal (TSH) waves are negligible for all angles of incidence. The reflected energy coefficients for the quasi shear vertical (TqSV) wave attain up to 55% of the incident energy. Around 70% of the incident wave energy is carried by the reflected waves (see Fig. 3.6).

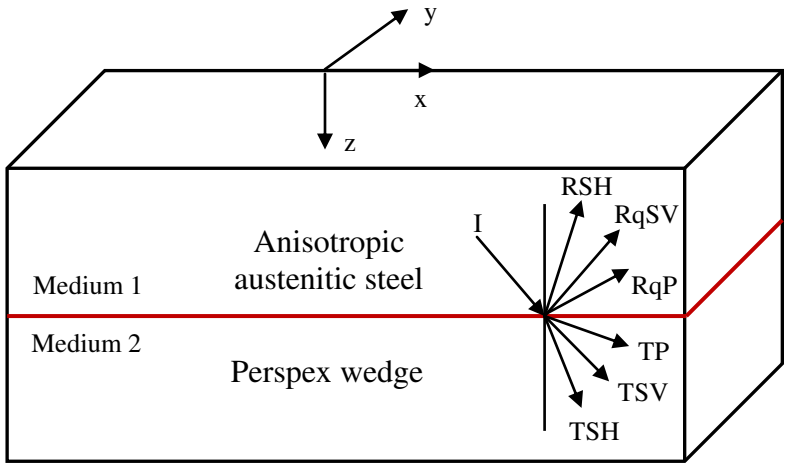

Figure 3.5: *Schematic of the energy reflection and transmission behavior at an interface between columnar grained austenitic steel material and Perspex wedge material.*

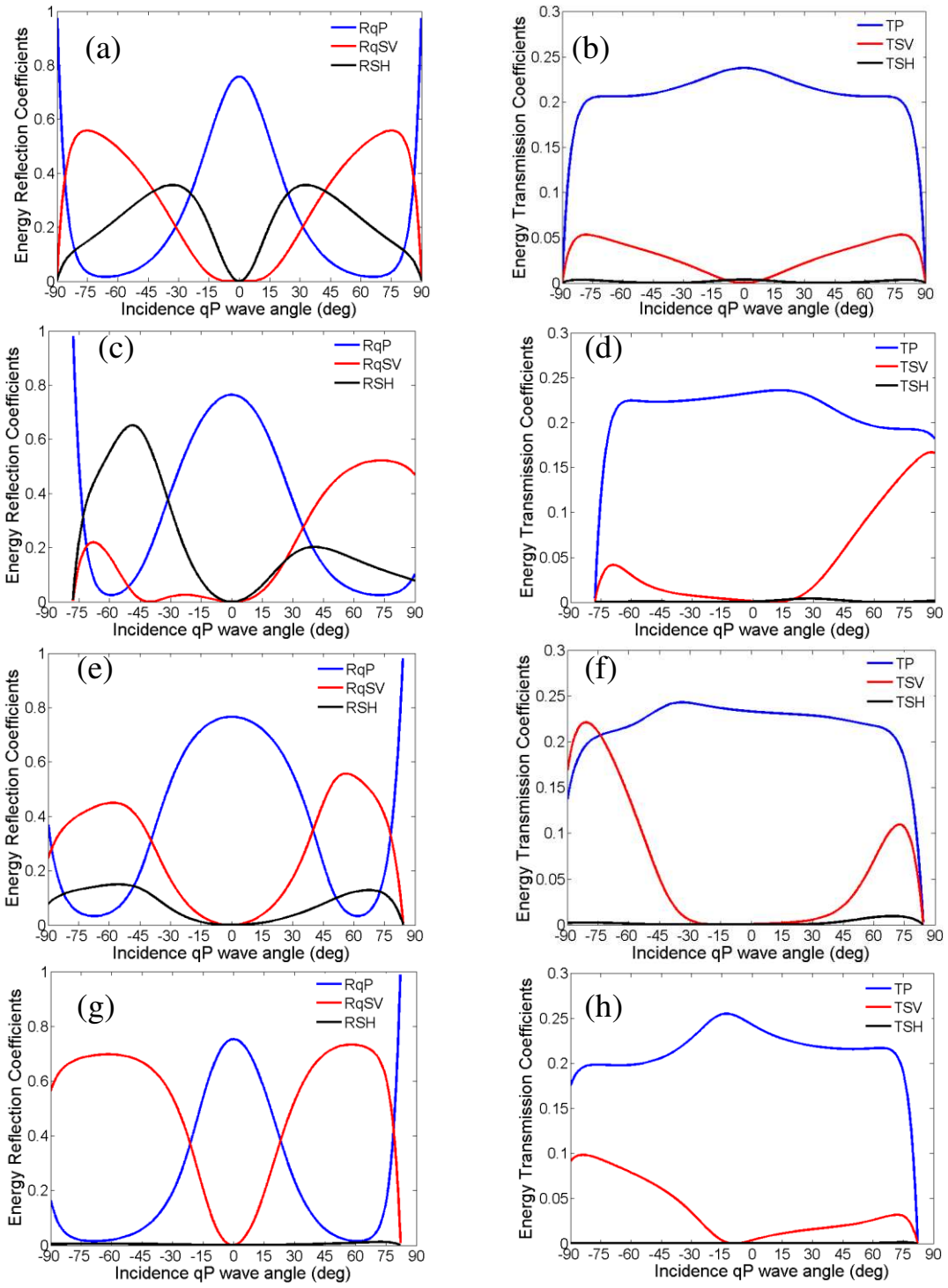

Figure 3.6: *Energy reflection and transmission coefficients for the reflected and transmitted waves when a quasi longitudinal wave is incident at an interface between anisotropic columnar grained austenitic weld and Perspex wedge material. (a), (b)* $\theta = 20^{\circ}$, $\psi = 20^{\circ}$. *(c), (d)* $\theta = 25^{\circ}$, $\psi = 20^{\circ}$. *(e), (f)* $\theta = 50^{\circ}$, $\psi = 20^{\circ}$. *(g), (h)* $\theta = 75^{\circ}$, $\psi = 20^{\circ}$. θ *represents the columnar grain orientation and* ψ *represents the layback orientation.*

For the incident angles between 45º and 85º, the reflection coefficients for quasi longitudinal wave are close to zero. The same behavior occurs in the range of negative incident angles -85º to -45º. An interesting effect is, by increasing columnar grain orientation of the austenitic weld material, the energy of the RSH wave decreases. The presented calculations are limited to the valid domain of incident wave vectors because of some particular angle of incidence, the energy orientation of the incident wave does not direct towards interface which means no incident wave reaches the boundary (so called grazing angle for the incident wave).

Figure 3.7 shows the influence of layback orientation on energy reflection and transmission coefficients for the reflected and transmitted waves when a qP wave incident at an interface between austenitic weld material and Perspex wedge material. The assumed columnar grain orientation in the austenitic weld material is 0° and layback orientation is varied in between 0° and 75° with a step size of 25°. It can be seen from Fig. 3.7 that the transmitted longitudinal wave (TP) energy stays below 25% of the incident energy. Whereas, the transmitted shear vertical (TSV) waves carry up to 10% of the incident energy. It is obvious from Figure 3.7, thus increasing layback orientation the energy coefficients for the reflected shear horizontal (RSH) wave increases and on the other hand the energy coefficients for the reflected quasi shear vertical wave (RqSV) decreases. For a wide range of incident angles, the energy coefficients for the transmitted shear horizontal (TSH) wave are negligible. No critical angles are observed for the reflected or transmitted waves and all reflected and transmitted angles are real.

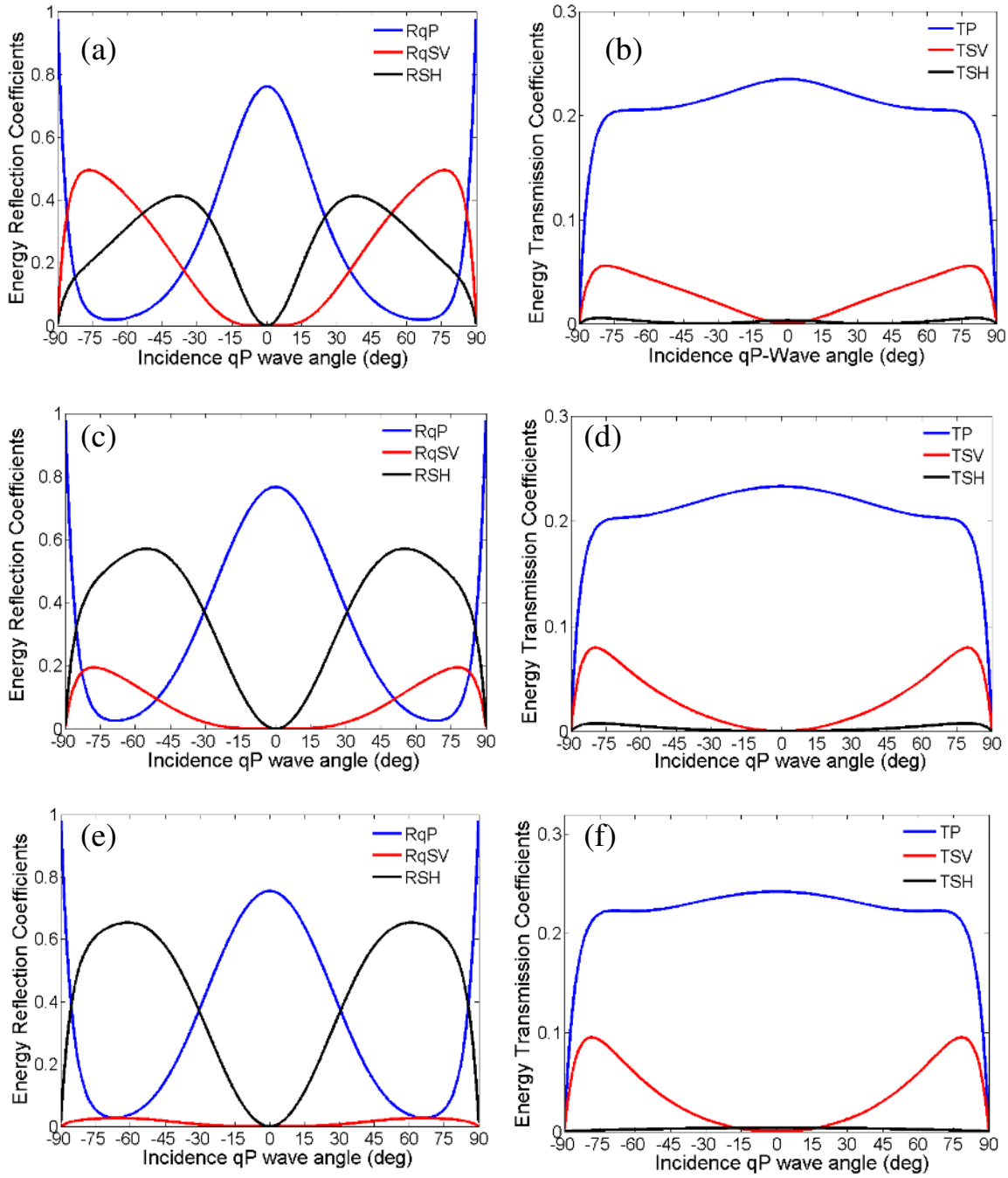

Figure 3.7: *Energy reflection and transmission coefficients for the reflected and transmitted waves when a quasi longitudinal wave (qP) is incident at an interface between anisotropic columnar grained austenitic weld material and isotropic Perspex wedge material. (a), (b)* $\theta = 0^{\circ}$, ψ=25°. *(c), (d)* $\theta = 0^{\circ}$, ψ=50°. *(e), (f)* $\theta = 0^{\circ}$, ψ=75°. θ *represents the columnar grain orientation and* ψ *represents the layback orientation.*

3.3.3 Isotropic Ferritic Steel – Austenitic Weld Material Interface

The transmitted medium is austenitic weld material exhibiting 3D columnar grain orientation and the incident medium is the isotropic ferritic steel material (see Fig. 3.8). The incident wave is the pure longitudinal wave. Figure 3.9 shows the influence of columnar grain orientation on energy reflection and transmission coefficients for the reflected and transmitted waves. The assumed layback orientation in the austenitic weld material is 20º and columnar grain orientation of the weld material is varied in between 0º and 90º with a step size of 25º.

The transmissibility of the incident longitudinal wave energy into the refracted quasi longitudinal wave (TqP) energy is fairly high. Energy conversion coefficients for the reflected shear vertical waves (RSV) are below 10% of the incident energy and that of transmitted quasi shear vertical waves (TqSV) reach up to 8% of the incident energy. The conversion coefficients for the transmitted shear horizontal (TSH) wave and reflected shear horizontal (RSH) wave are negligible.

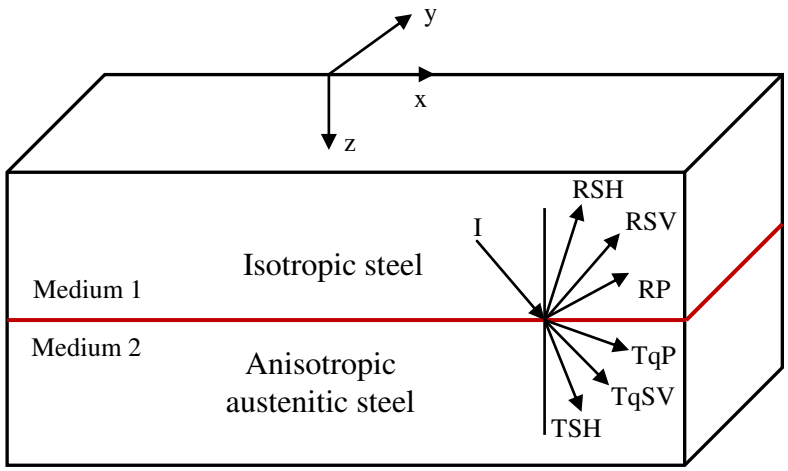

Figure 3.8: *Schematic of the energy reflection and transmission behavior at an interface between isotropic steel material and columnar grained austenitic steel material.*

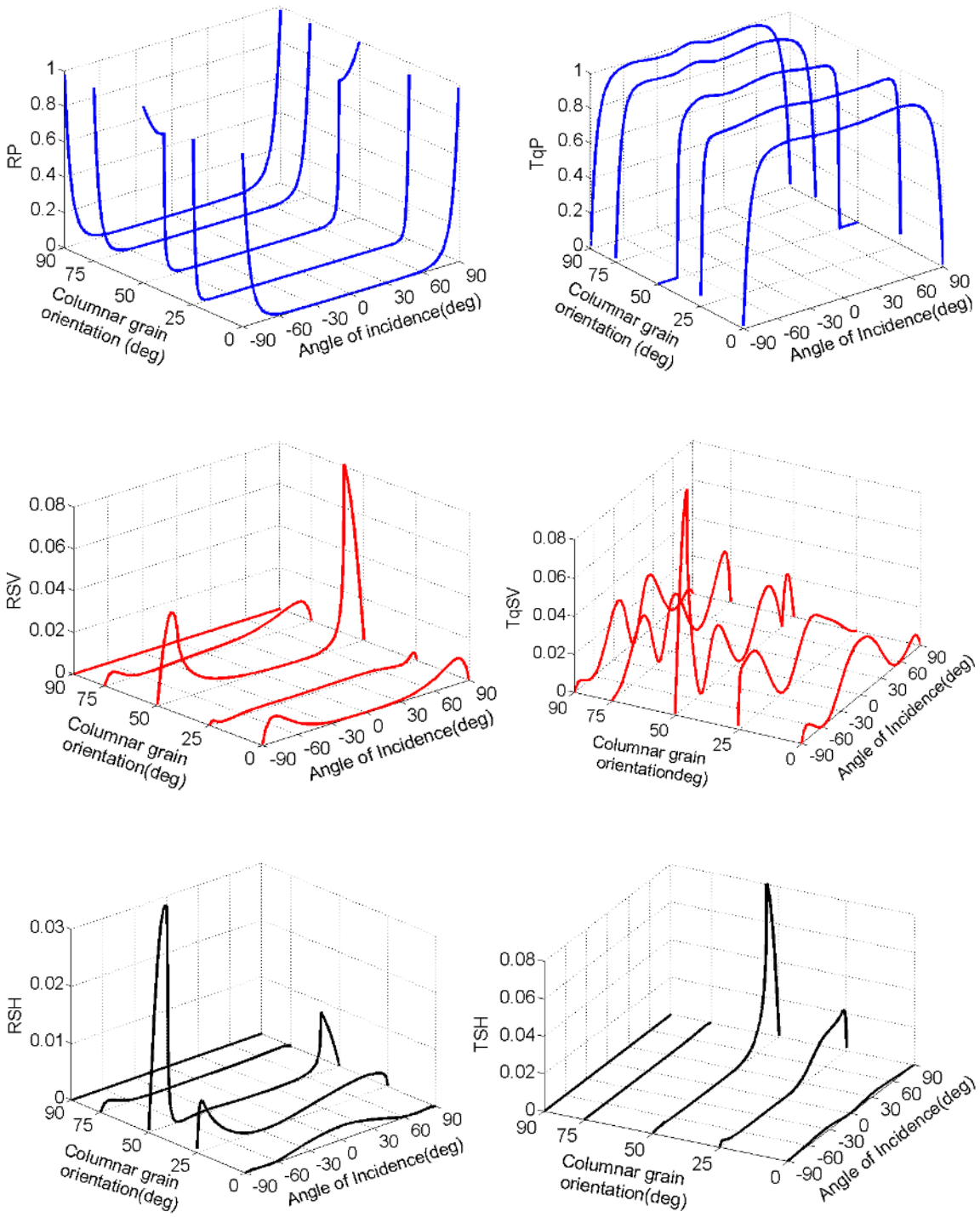

Figure 3.9: *Energy reflection and transmission coefficients for the reflected and transmitted waves when a pure longitudinal wave is incident at an interface between isotropic ferritic steel material and columnar grained austenitic weld material. The columnar grain angle of the austenitic weld material is varied between 0° and 90º with a step size of 25° and lay back angle is 20° (kept constant).*

A sharp increase in the energy coefficient for the reflected and transmitted shear horizontal and shear vertical waves are observed in case of austenitic weld material exhibiting 50° columnar grain orientation (see Fig. 3.9). For all columnar grain orientations transmitted quasi longitudinal wave (TqP) is capable of propagating for broad range of incidence angles.

Figure 3.10 shows the influence of layback orientation on energy reflection and transmission coefficients when a pure longitudinal wave is incident at an interface between isotropic ferritic steel and columnar grained austenitic weld material. For all incidence angles, the transmissibility of the incident energy into the refracted quasi longitudinal (TP) waves is fairly high. The conversion coefficients for the reflected shear vertical waves (RSV) stay below 1.5% of the incident energy and that of transmitted quasi shear vertical waves (TqSV) vary up to 4%. Whereas, the conversion coefficients for the reflected and transmitted shear horizontal waves are negligible. No critical angles are observed for the reflected or transmitted waves and all the reflected and transmitted wave angles are real.

In the presented reflection and transmission coefficients at a boundary between two dissimilar materials are evaluated under an assumption that the incident wave is a plane monochromatic wave. Hence, the energy reflection and transmission coefficients are independent of frequency. A detailed description on frequency dependent energy reflection and transmission coefficients in an austenitic weld material is presented in Section 3.5.

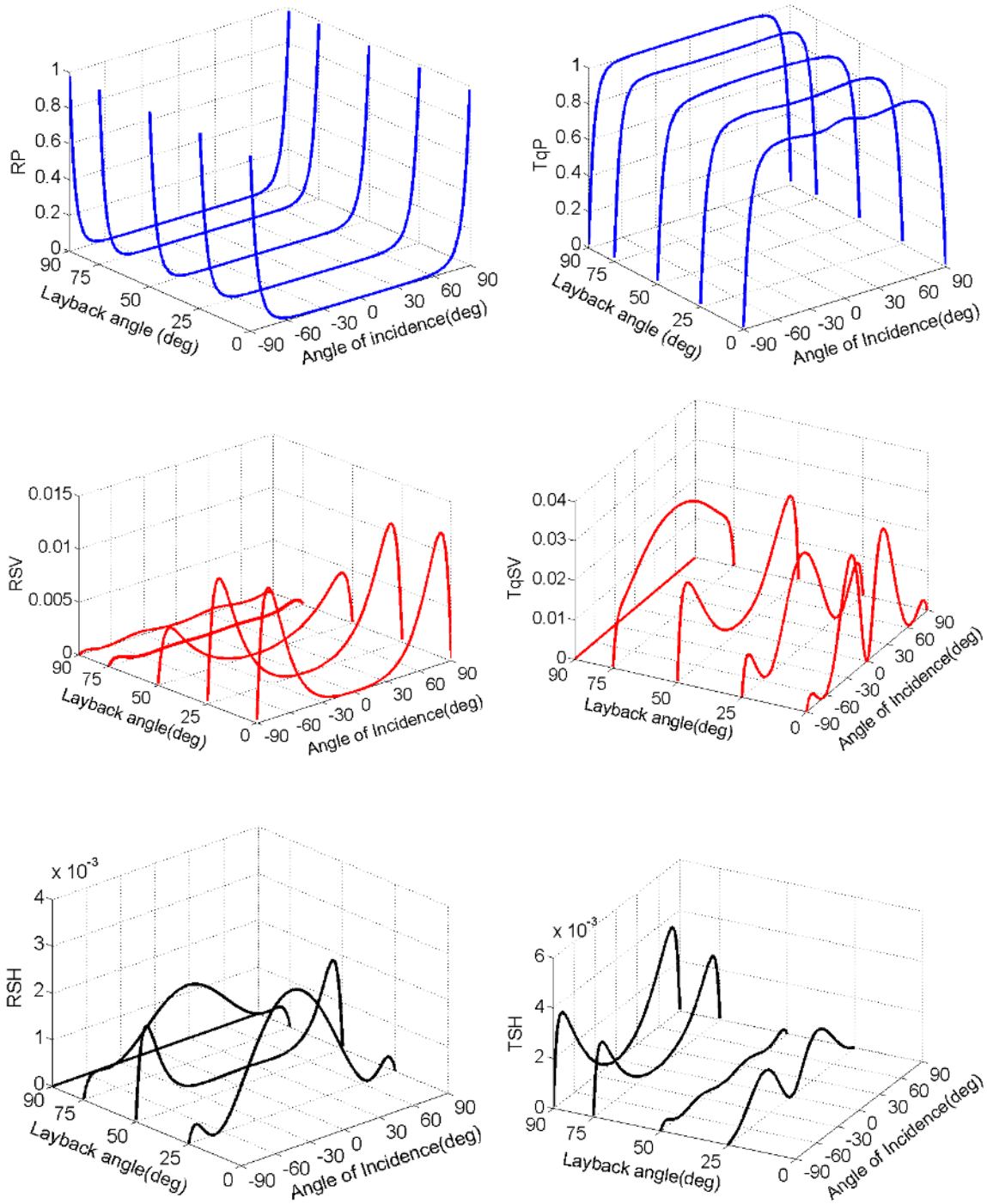

Figure 3.10: *Energy reflection and transmission coefficients for the reflected and transmitted waves when a pure longitudinal wave is incident at an interface between isotropic ferritic steel material and columnar grained austenitic weld material. The layback angle of the austenitic weld material is varied between 0° and 90º with a step size of 25° and the columnar grain angle is 0° (kept constant).*

3.3.4 Isotropic Perspex Wedge – Austenitic Weld Material Interface

The transmitted medium is austenitic weld material exhibiting 3D columnar grain orientation and the incident medium is the isotropic Perspex wedge material. The present case is generally occurring when an ultrasonic wave excited from Perspex wedge material into the austenitic weld material. The incident wave is the pure longitudinal wave. Fig. 3.11 shows the schematic of the energy reflection and transmission at an interface between Perspex wedge material and anisotropic austenitic steel material.

Figure 3.12 shows the influence of layback orientation on the energy reflection and transmission coefficients for the reflected and transmitted waves. The assumed columnar grain orientation in the austenitic weld material is 0º and layback back angle is varied in between 0º and 75º with step size of 25º. It is apparent from Figure 3.12, that the reflected and transmitted waves are strongly influenced by the layback orientation of the austenitic weld material. Complicated critical angle phenomena for the reflected and transmitted waves are observed. The transmissibility of an incident longitudinal wave into the austenitic weld material is limited to a narrow range of incident angles. Energy transmission coefficients for the refracted quasi longitudinal wave are below 25% of the incident energy.

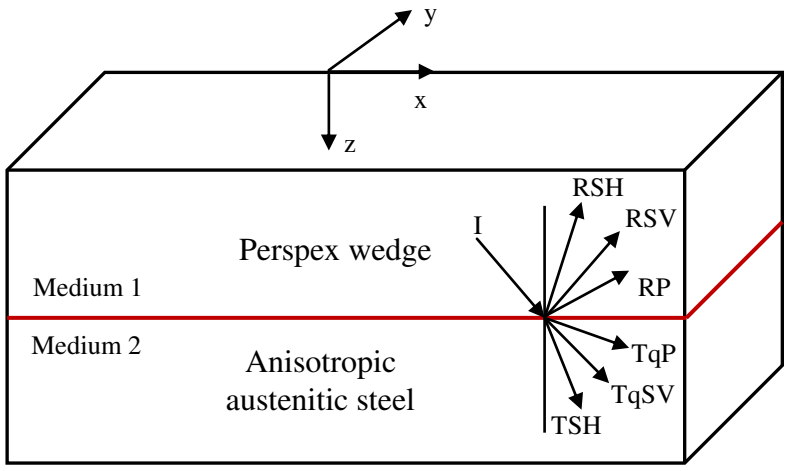

Figure 3.11: *Schematic of the energy reflection and transmission behavior at an interface between isotropic Perspex wedge material and columnar grained austenitic steel material.*

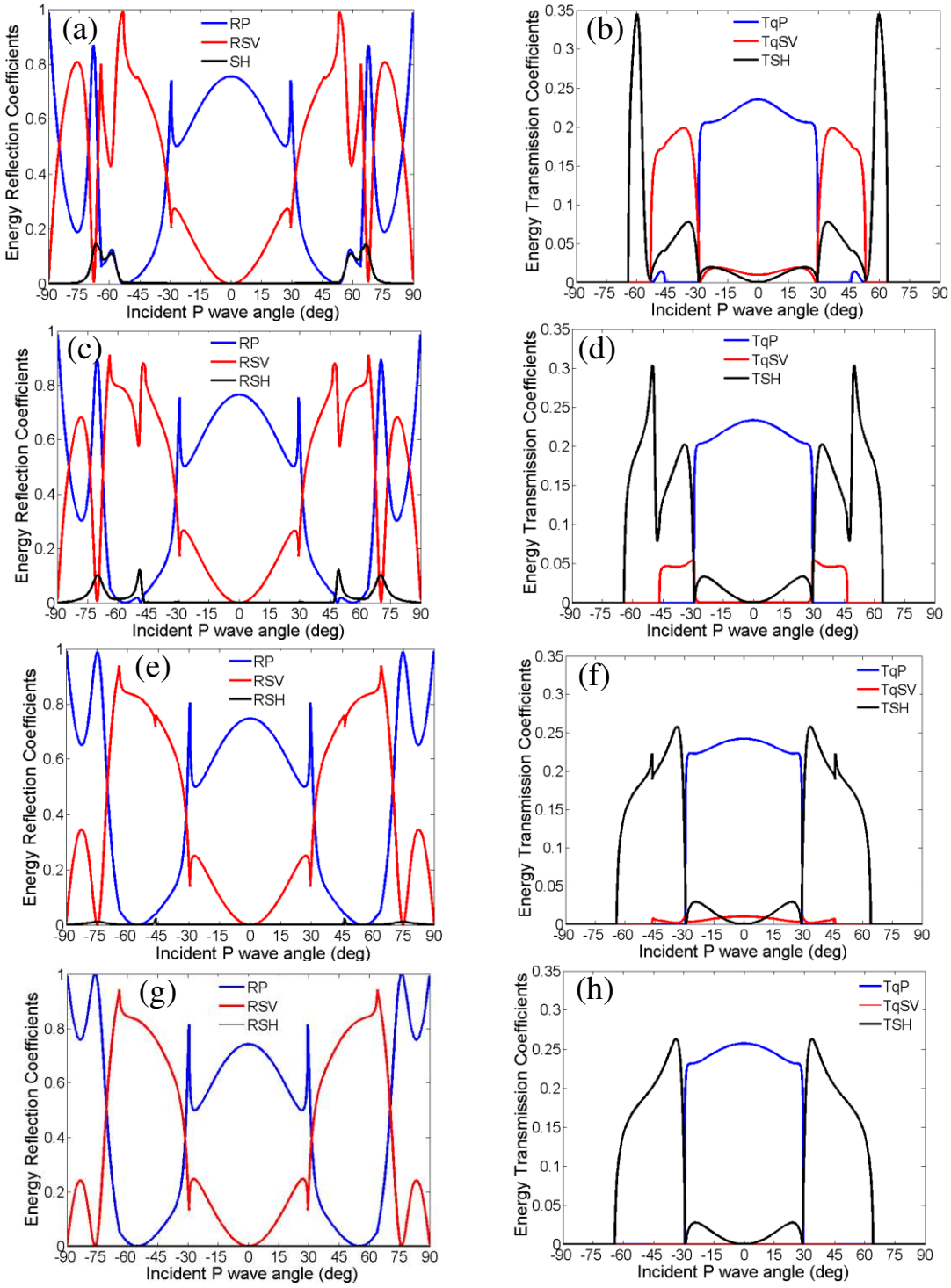

Figure 3.12: *Energy reflection and transmission coefficients for the reflected and transmitted waves when a pure longitudinal wave is incident at an interface between Perspex wedge and austenitic weld material. (a), (b)* $\theta = 0°$, ψ=0°. *(c), (d)* $\theta = 0°$, ψ=25°. *(e), (f)* $\theta = 0°$, ψ=50°. *(g), (h)* $\theta = 0°$, ψ=75°. θ *represents the columnar grain orientation and* ψ *represents the layback orientation.*

The reflected shear horizontal (RSH) wave carries up to 12% and that of refracted shear horizontal (TSH) wave carries 35% of the incident energy. The mode converted refracted quasi shear vertical wave (TqSV) stays below 20% of the incident energy and its energy decreases increasing layback orientation. An interesting effect is existence of second branch of quasi shear vertical waves (TqSV(2)) for certain values of incident angles (see Fig. 3.13). The phenomenon of wave reappearance in general anisotropic solids is originally found by Rokhlin et al [120, 123]. The quantitative analysis has shown that, the TqSV (2) wave carries energy up to 20% of the incident energy and TqSV (2) wave energy is more predominant when the layback orientation of the austenitic weld material is 0º. The energy carried by the TqSV (2) wave decreases with increasing layback orientation (see Figure 3.13).

For certain columnar grain orientations, no transmission zones are observed (see Figure 3.12) where all the transmitted wave modes are inhomogeneous and in these regions the incident energy is redistributed among the reflected wave modes. The existence of TqSV(2) wave results in spurious indications during the ultrasonic investigation of austenitic weld materials. The severity of these false indications varies with incident wave vector angles. During the ultrasonic testing of austenitic welds one has to select the optimum incident angles of the incident wave mode in order to obtain the clear indications which are readily interpretable.

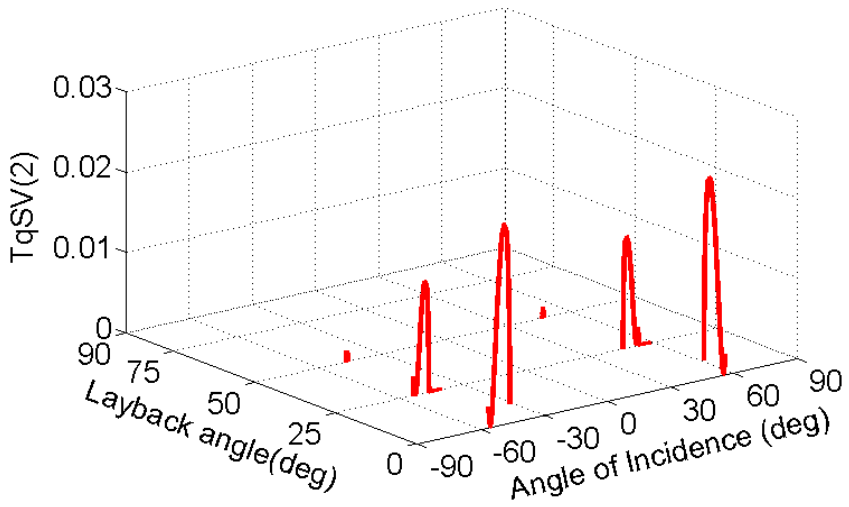

Figure 3.13: *Influence of layback orientation on the energy transmission coefficients for the second branch of quasi shear vertical waves (TqSV(2)).*

3.3.5 Austenitic – Austenitic Stainless Steel Interface

The selected configuration is typically encountered in the ultrasonic investigation of austenitic clad components and dissimilar welds with buffering where ultrasonic wave propagates between two adjacent columnar grain bundles. Elastic anisotropy of the two adjacent columnar grained austenitic weld metal regions plays an important role because density of both the media is the same. Figure 3.14 shows the schematic of the possible reflected and transmitted waves at an interface between two anisotropic austenitic steel materials.

Figure 3.15 shows the influence of layback orientation on energy reflection and transmission coefficients when a quasi longitudinal wave incident at an interface between two arbitrarily oriented austenitic steel materials. The selected columnar grain orientation in the medium 1 is 75º and layback orientation is 20º. The selected columnar grain orientation in the medium 2 is 50º and layback orientation of the medium 2 is varied in between 0º and 90º with a step size of 25º. For the selected configuration the polarizations of all the six waves (three reflected and three transmitted waves) couple together for all layback orientations.

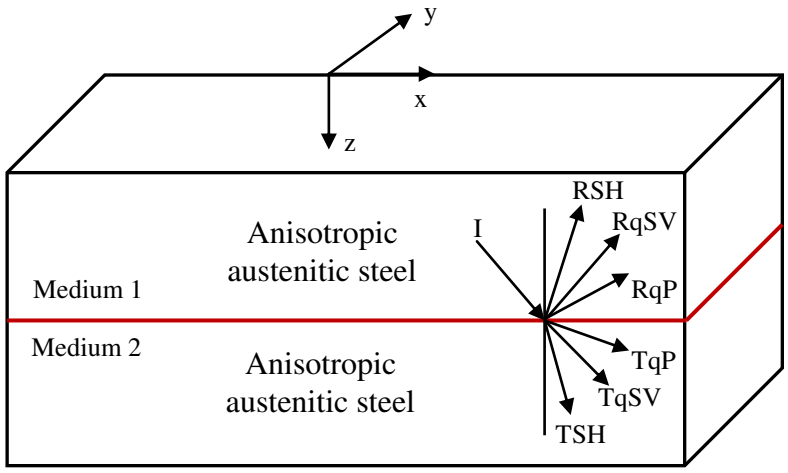

Figure 3.14: *Schematic of the energy reflection and transmission behavior at an interface between two adjacent columnar grained anisotropic austenitic steel materials***.**

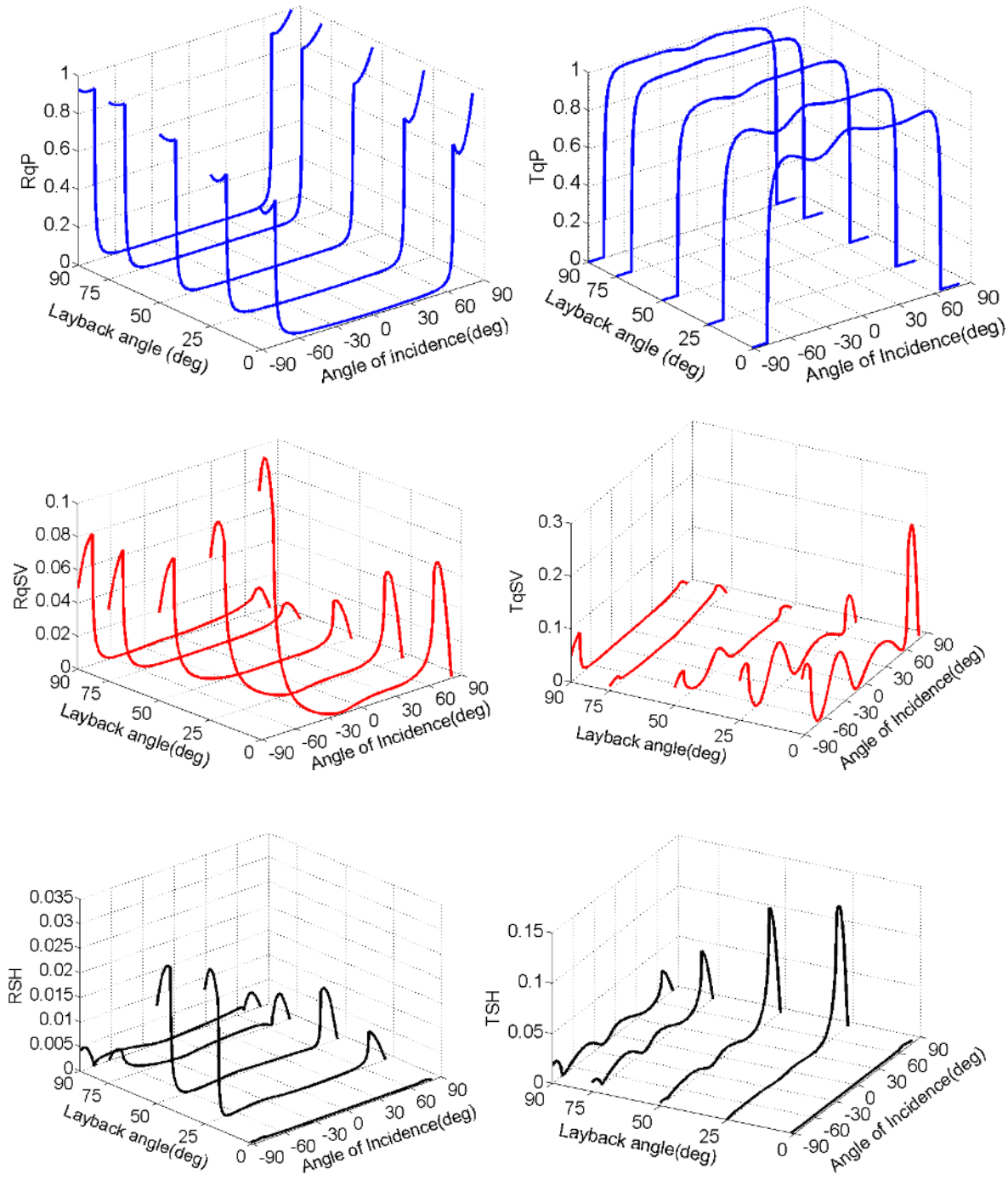

Figure 3.15: *Energy reflection and transmission coefficients for the reflected and transmitted waves when a quasi longitudinal wave is incident at an interface between two anisotropic columnar grained austenitic steel materials. The layback angle of the austenitic weld material (medium 2) is varied between 0° and 90º with a step size of 25°.*

The transmission coefficients for the transmitted quasi longitudinal waves (TqP) are influenced by the anisotropic properties of the austenitic steel material. The mode conversion of incident qP wave energy into reflected quasi shear vertical wave (RqSV) reaches 10% and that of refracted quasi shear vertical wave (TqSV) reaches 20% and even less for layback orientations other than 0º. The energy coefficients for the reflected pure shear horizontal wave (RSH) stay below the 2.5% and that of refracted shear horizontal waves (TSH) reach up to 12% of the incident energy. For the wide range of incidence angles, the energy coefficients for the reflected quasi longitudinal wave (RqP) are negligible. It can be seen from Figure 3.15 that the energy coefficients for the reflected and transmitted shear horizontal waves decrease with increasing layback orientation (see Fig. 3.15). Beyond the critical angle for the transmitted waves, the incident energy is redistributed among the other propagating reflected and transmitted waves.

3.3.6 Water – Austenitic Weld Interface

The selected configuration generally occurs during the practical ultrasonic immersion testing where the water acts as a coupling medium to transmit the ultrasonic waves into the austenitic weld material. Fig 3.16 shows the schematic of the possible reflected and transmitted waves at an interface between water and columnar grained austenitic steel material.

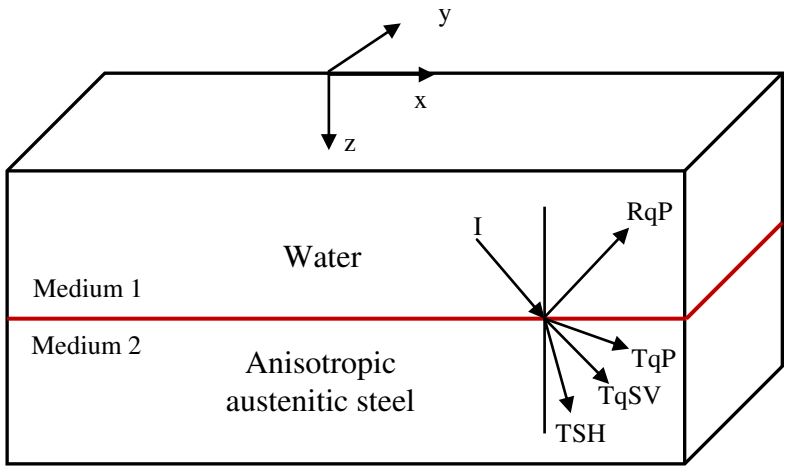

Figure 3.16: *Schematic of the energy reflection and transmission behavior at an interface between water and columnar grained austenitic steel material.*

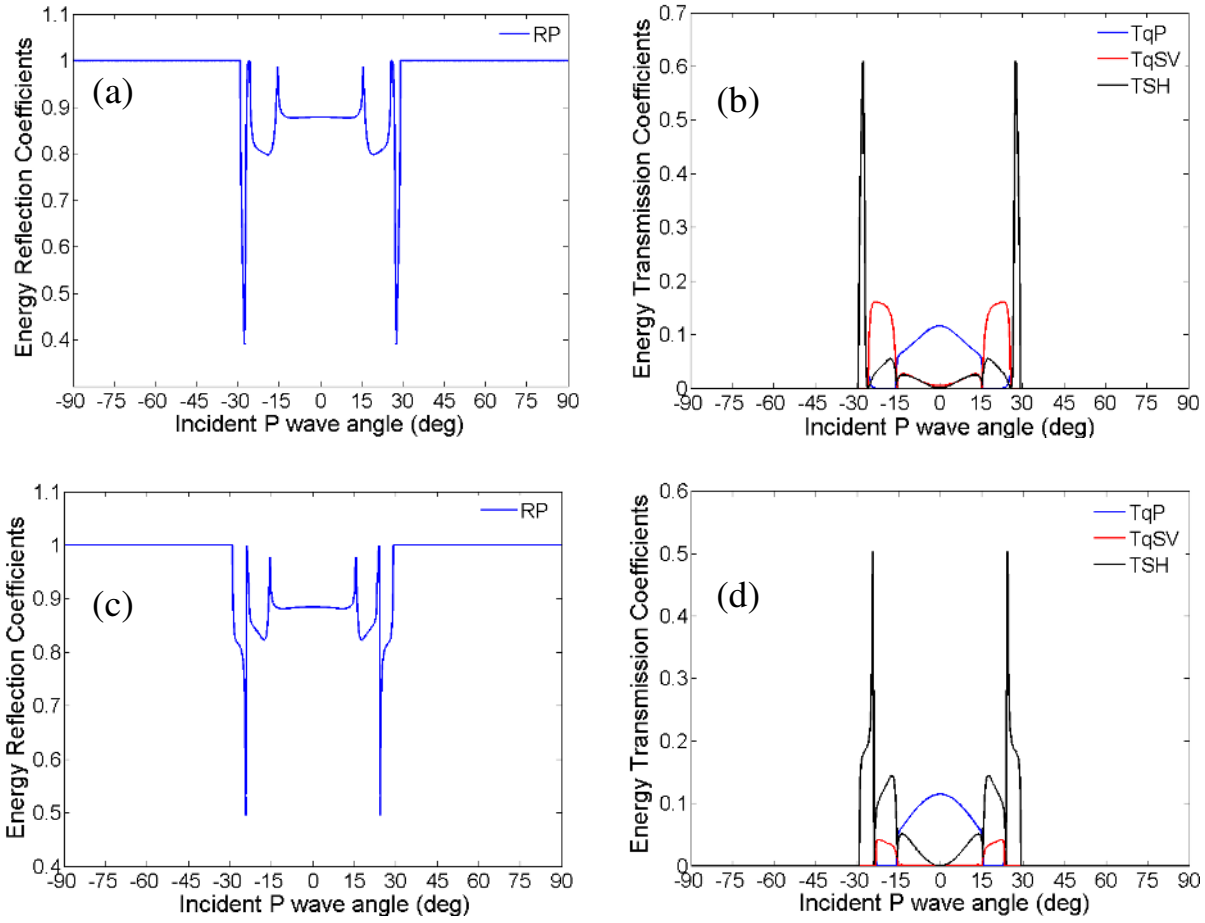

Figure 3.17: *Energy reflection and transmission coefficients for the reflected and transmitted waves when a pure longitudinal wave is incident at an interface between water and austenitic weld material. (a), (b)* $\theta = 0°$, ψ=25°. *(c), (d)* $\theta = 0°$, ψ=50°. θ *represents the columnar grain orientation and* ψ *represents the layback orientation.*

Figure 3.17 and Figure 3.18 show the influence of layback orientation on energy reflection and transmission coefficients for the reflected and transmitted waves when a pure longitudinal wave impinges at an interface between water and columnar grained austenitic weld material. The selected columnar grain orientation in the austenitic material is 0° and layback orientation of the material is varied in between 25° and 90° with a step size of 25°. A complicated critical angle phenomenon is observed. The quantitative analysis has shown that the transmitted quasi longitudinal wave (TqP) carries less than 12% of the incident P wave energy. It can be seen from Figure 3.17 that the most of the incident wave energy is reflected back into the water medium. The mode

conversion of incident energy into transmitted quasi shear vertical (TqSV) waves reach 15% of the incident energy for particular incident angles and generally even less. The energy coefficients for the transmitted shear horizontal (TSH) waves carry up to 60% of the incident P wave energy.

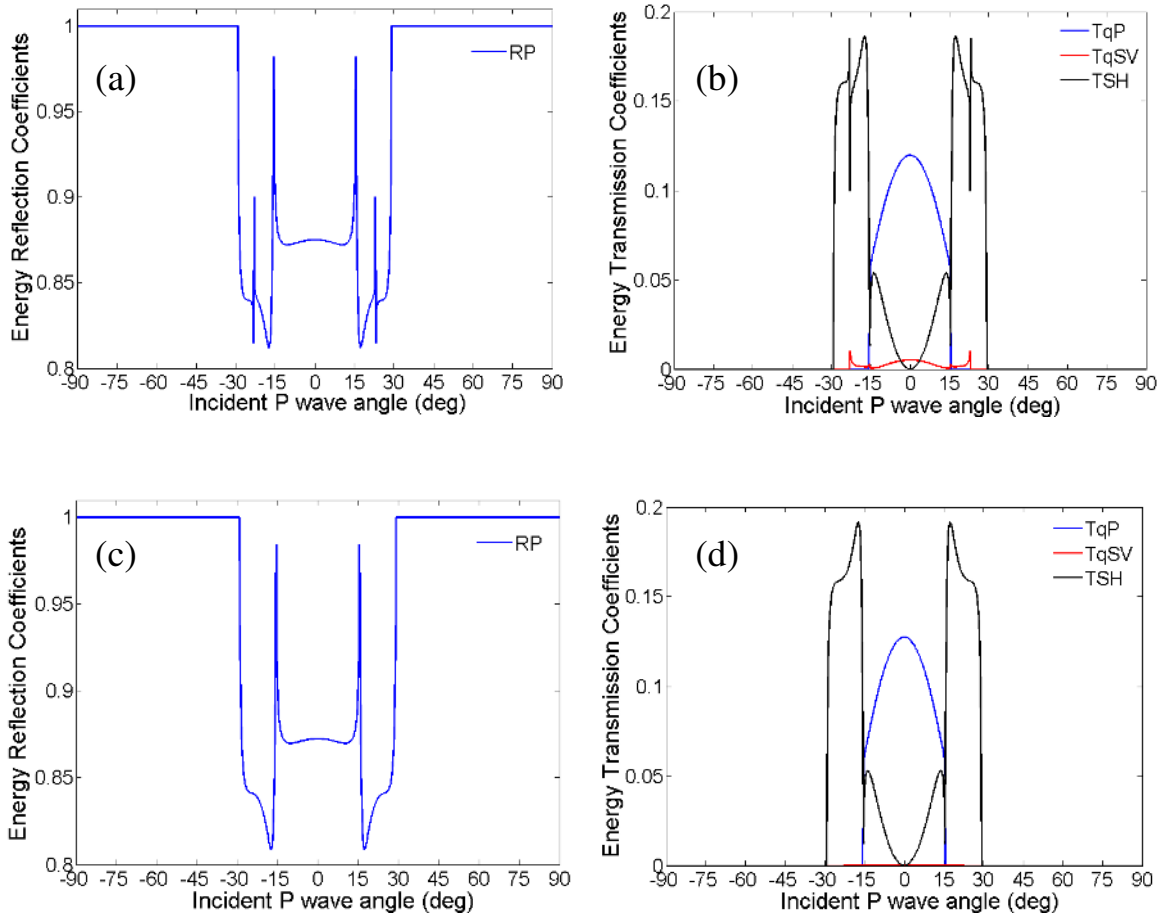

Figure 3.18: *Energy reflection and transmission coefficients for the reflected and transmitted waves when an incident pure longitudinal wave at an interface between water and anisotropic columnar grained austenitic weld material. (a), (b)* $\theta = 0°$, ψ=75°. *(c), (d)* $\theta = 0°$, ψ=90°. θ *represents the columnar grain orientation and* ψ *represents the layback orientation.*

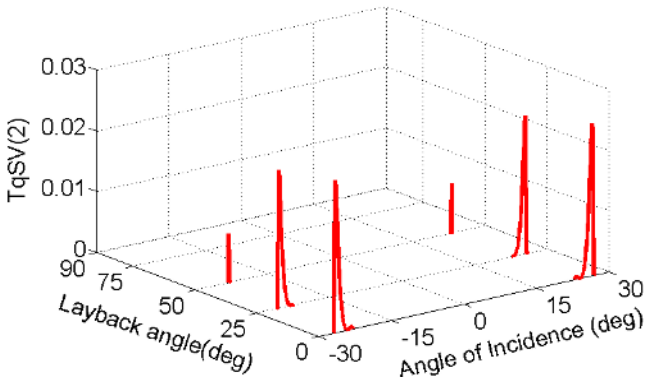

Figure 3.19: *Energy transmission coefficients for the second branch of quasi shear vertical (TqSV(2)) waves.*

The secondary branch of quasi shear vertical waves (TqSV(2)) which appear instead transmitted quasi longitudinal waves for certain incident wave vector angles carry up to 21% of the incident energy (see Figure 3.19). It is apparent from the Figure 3.17 and Figure 3.18, thus increasing layback orientation the energy coefficients for the transmitted quasi shear vertical (TqSV) waves decreases and on the other hand the energy coefficients for the transmitted shear horizontal (TSH) wave increases.

3.3.7 Austenitic Weld – Water Interface

The presented configuration which occur typically during the ultrasonic investigation of columnar grained austenitic weld materials with water as a coupling medium where to receive the wave mode from the test specimen into the coupling medium (see Fig. 3.20).

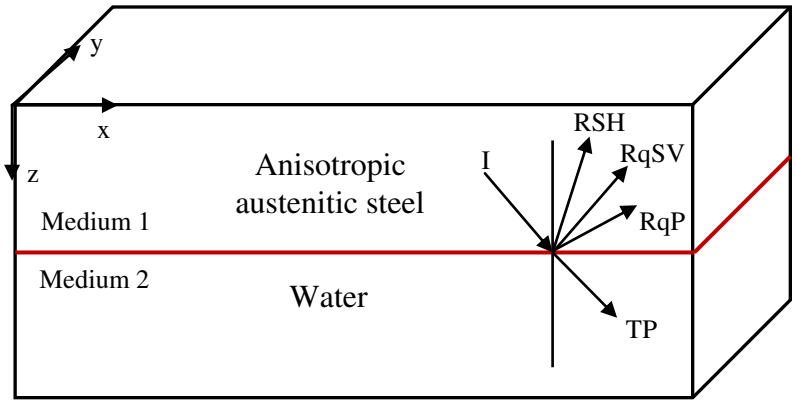

Figure 3.20: *Schematic of the energy reflection and transmission behavior at an interface between columnar grained austenitic steel material and water.*

Figure 3.21 and Figure 3.22 show the influence of columnar grain orientation on energy reflection and transmission coefficients when a quasi longitudinal wave is incident at an interface between anisotropic austenitic weld material and water. The selected layback orientation in the austenitic weld material is 20º and columnar grain orientation of the material is varied in between 0º and 90º with a step size of 25º. The transmissibility of the incident energy into transmitted longitudinal wave (TP) stays below 13% of the incident energy. For all the columnar grain orientations, reflected waves carry around 85% of the incident wave energy. It can be seen from the Figure 3.21 and Figure 3.22, thus increasing columnar grain orientation the energy coefficients for the reflected shear horizontal waves decreases whereas energy coefficients for the reflected quasi shear vertical wave increases.

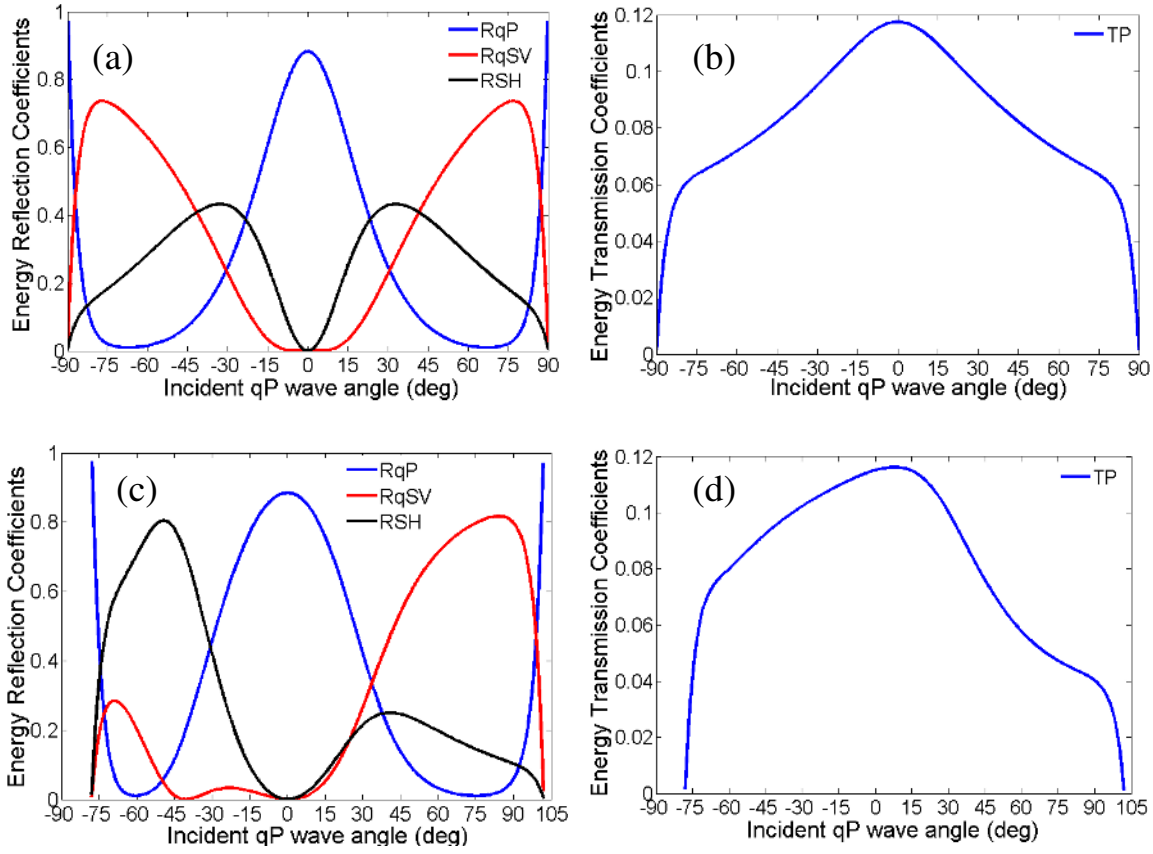

Figure 3.21: *Energy reflection and transmission coefficients for the reflected and transmitted waves when a quasi longitudinal wave is incident at an interface between columnar grained austenitic weld material and water. (a), (b)* $\theta = 0^{\circ}$, $\psi = 20^{\circ}$. *(c), (d)* $\theta = 25^{\circ}$, $\psi = 20^{\circ}$. θ *represents the columnar grain orientation and* ψ *represents the layback orientation.*

The quantitative analysis reveals that the transmitted energy coefficients are strongly influenced by the columnar grain orientation of the material. Figure 3.23 shows the influence of layback orientation on energy reflection and transmission coefficients when a quasi longitudinal wave is incident at an interface between columnar grained austenitic weld material and water. The selected columnar grain orientation in the austenitic material is 0º and layback orientation is varied in between 25º and 75º with a step size of 25º. It can be seen from Figure 3.23, that the energy coefficients for the transmitted longitudinal wave (TP) in water are less influenced by the layback orientation of the austenitic weld material. The transmitted longitudinal wave carries up to 12% of the incident energy.

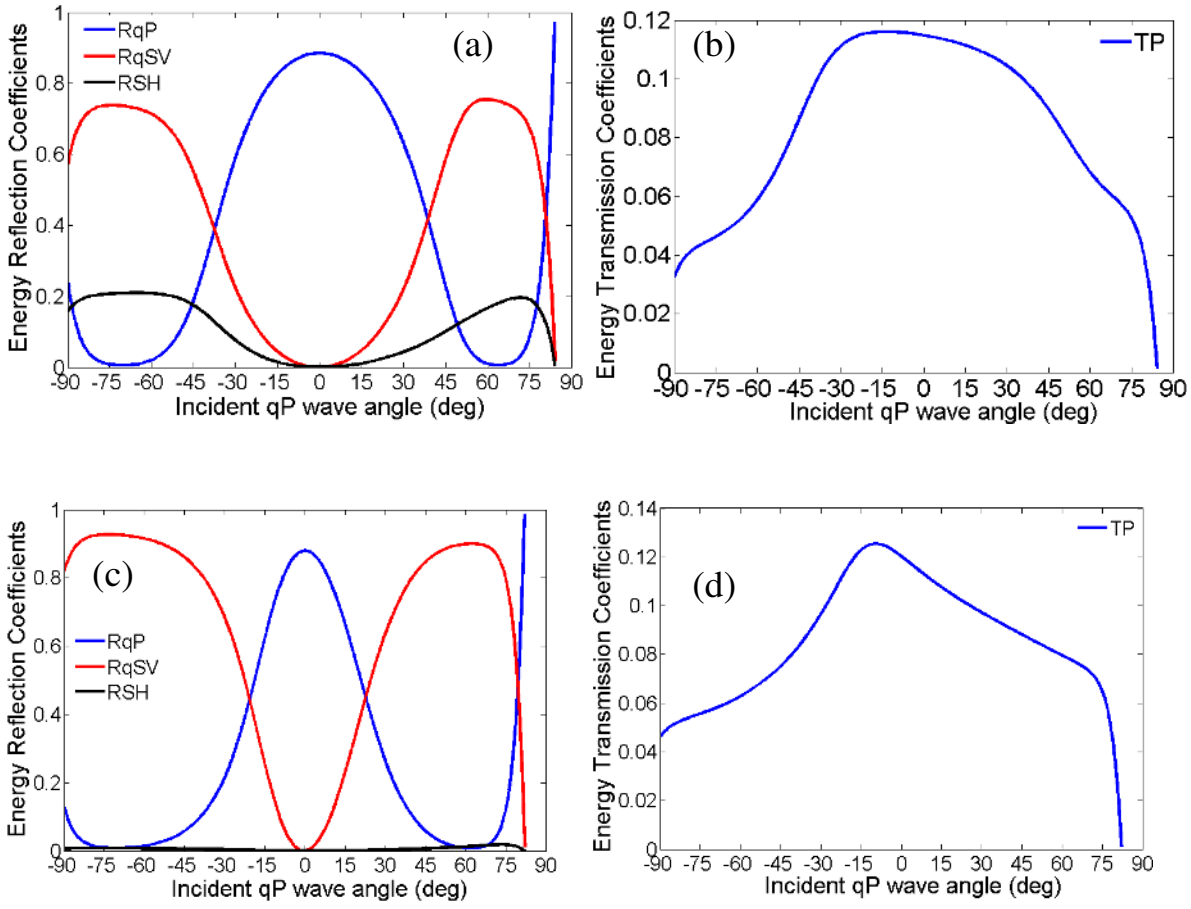

Figure 3.22: *Energy reflection and transmission coefficients for the reflected and transmitted waves when an incident quasi longitudinal wave at an interface between columnar grained austenitic weld material and water. (a), (b)* $\theta = 50º$, ψ=20º. *(c), (d)* $\theta = 75º$, ψ=20º. θ *represents the columnar grain orientation and* ψ *represents the layback orientation.*

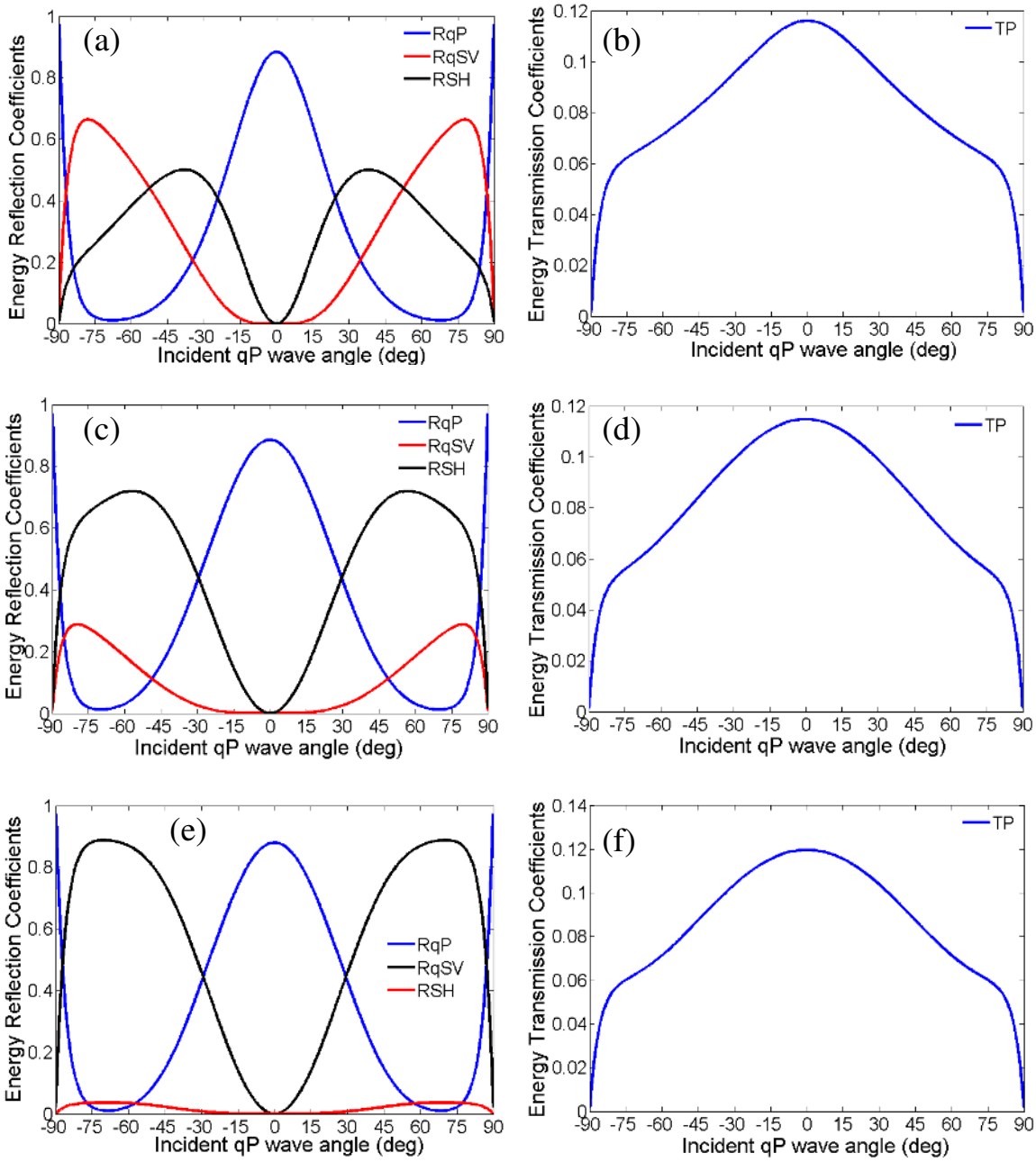

Figure 3.23: *Energy reflection and transmission coefficients for the reflected and transmitted waves when an incident quasi longitudinal wave at an interface between columnar grained austenitic weld material and water. (a), (b)* $\theta = 0°$, ψ=25°. *(c), (d)* $\theta = 0°$, ψ=50°. *(e), (f)* $\theta = 0°$, ψ=75°. θ *represents the columnar grain orientation and* ψ *represents the layback orientation.*

It can be seen from Figure 3.23, thus increasing layback orientation, the energy carried by the reflected quasi shear vertical (RqSV) waves decreases and that of the reflected pure shear horizontal (RSH) waves increases.

3.3.8 Austenitic Weld – Free Surface Interface

The considered case plays an important role while characterizing the reflected waves at a free surface boundary of an austenitic weld material or inhomogenities such as a crack face. Figure 3.24 shows the possible reflected waves at the free surface boundary of a columnar grained austenitic steel material. The influence of columnar grain orientation on energy reflection and transmission coefficients for the reflected and transmitted waves when a qP wave impinges at a free surface boundary of an austenitic weld material is shown in Fig. 3.25. The selected layback orientation in the austenitic weld material is 20º and columnar grain orientation is varied in between 0º and 75º with a step size of 25º.

The quantitative analysis has shown that the energy reflection coefficients are influenced by the columnar grain orientation of the austenitic weld material. Energy coefficients for the reflected quasi longitudinal (RqP) waves are negligible in the angular region 45º and 75º. The same behavior occurs in the negative angular range -75º to -45º. Energy coefficients for the reflected quasi shear vertical (RqSV) wave reach up to 95% of the incident energy. Energy coefficients for the reflected pure shear horizontal (RSH) waves from the free surface of the austenitic weld material reach up to 80% of the incident energy. It can be seen from Figure 3.25 that the energy reflection coefficient for the pure shear horizontal waves decreases as the columnar grain orientation of the material increases.

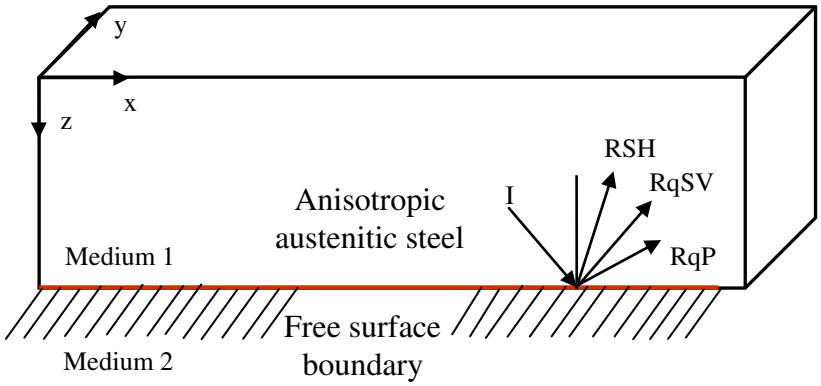

Figure 3.24: *Schematic of the energy reflection behavior at the free surface boundary of a columnar grained austenitic steel material.*

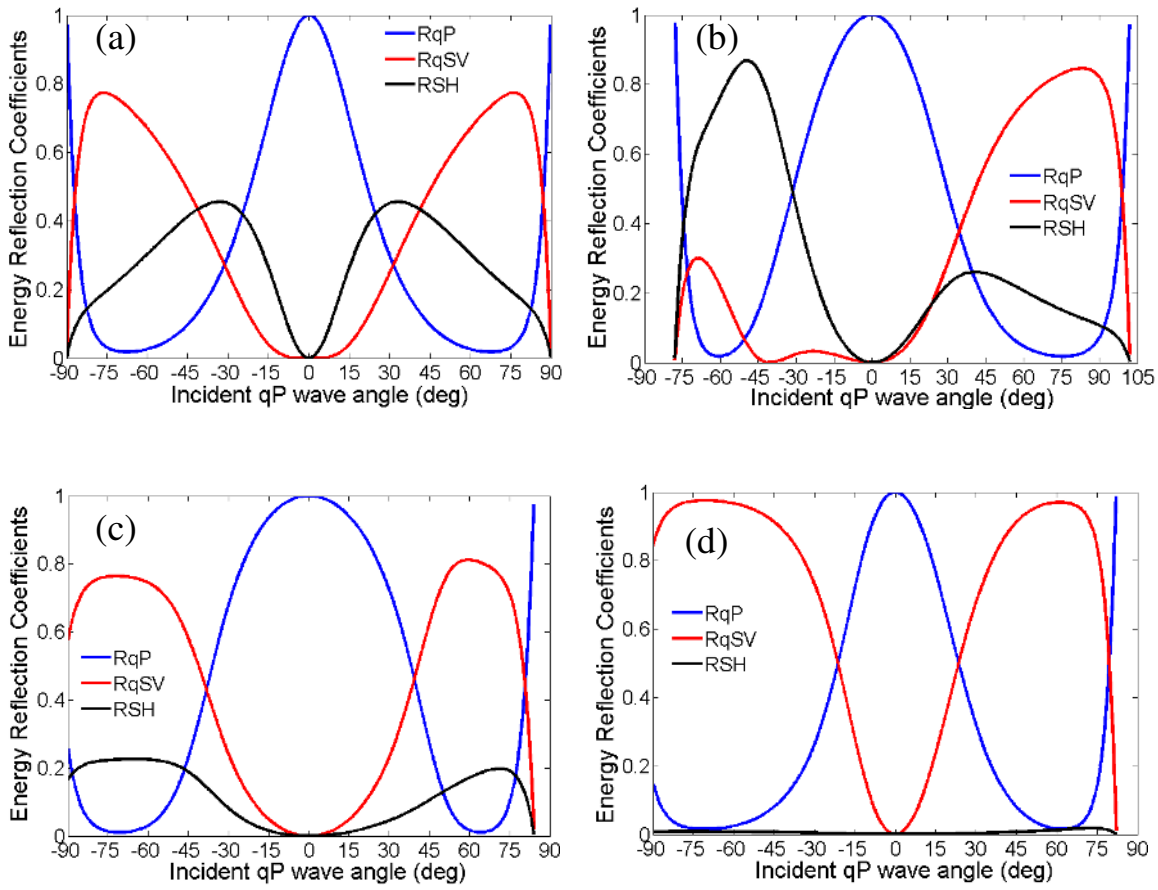

Figure 3.25: *Energy reflection when an incident quasi longitudinal wave impinges at a free surface boundary of the austenitic weld material. (a)* $\theta = 0°$, ψ=20°. *(b)* $\theta = 25°$, ψ=20°. *(c)* $\theta = 50°$, ψ=20°. *(d)* $\theta = 75°$, ψ=20°. θ *represents the columnar grain orientation and* ψ *represents the layback orientation.*

The presented calculations are limited to the valid domain of incident wave vector angles because some particular angle of incidence, the energy orientation of the incident wave does not direct towards the interface which means no incident wave reaches the boundary (so called grazing angle for the incident wave). Figure 3.26 shows the influence of lay back orientation on energy reflection coefficients when a quasi longitudinal (qP) wave is incident at a free surface boundary of an austenitic weld material. The selected columnar grain orientation in the austenitic weld material is 0° and the layback orientation is varied in between 0° and 75° with a step size of 25°.

It can be seen from Figure 3.26, that the energy coefficients for the reflected longitudinal (RqP) waves are negligible for the wide range of incident angles. The energy coefficients for the reflected quasi shear vertical (RqSV) waves reach up to 90% of the incident quasi longitudinal wave energy. As the layback orientation of the austenitic weld material increases, the energy reflection coefficients for the quasi shear vertical waves (RqSV) decreases (see Fig. 3.26). For the practical application, it is important to consider optimum angles for the incident waves for which the energy coefficients are maximum and energy skewing angle is minimum.

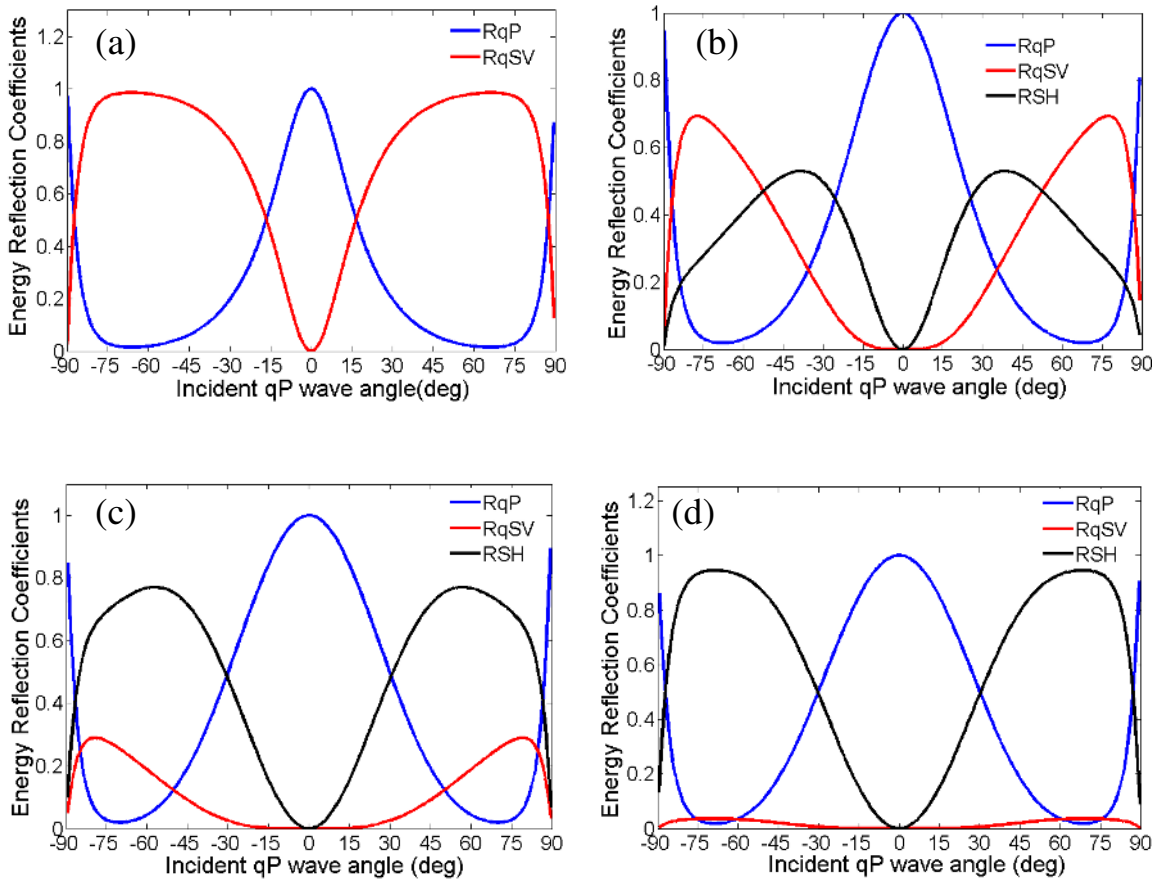

Figure 3.26: *Energy reflection coefficients when an incident quasi longitudinal waves at a free surface boundary of the austenitic weld material. (a)* $\theta = 0°$, ψ=0°. *(b)* $\theta = 0°$, ψ=25°. *(c)* $\theta = 0°$, ψ=50°. *(d)* $\theta = 0°$, ψ=75°. θ *represents the columnar grain orientation and* ψ *represents the layback orientation.*

3.4 Influence of Second Branch of Quasi Shear vertical Waves on Ultrasonic Examination of Austenitic Welds

Figure 3.27 shows the energy reflection and transmission coefficients when a quasi shear vertical wave is incident at a boundary between austenitic weld and Perspex wedge material. For the presented illustration, the columnar grain orientation in the incident medium is considered as 75º with respect to the inspection surface. The assumed layback orientation in the austenitic weld material is 0º. From Figure 3.27(b), it can be seen that, incident angles from -35º to 27.1º, the mode converted reflected quasi longitudinal waves (RqP) are capable of propagating. Between the negative incident angles between -65º and -35º, RqP wave becomes evanescent and the same behaviour occurs for positive angles from 27.1º to 46.6º. In the range of positive incident angles between 46.6º and 52.9º, the second branch of reflected quasi shear vertical wave (RqSV(2)) appears. The same behaviour occurs for the negative angles in the range between -67.2º and -45.2º. Below the incident angle of -45.6º, the reflected quasi shear vertical wave becomes evanescent and the second branch of the reflected quasi shear vertical wave carries most of the incident energy and reaches unity (see Figure 3.27 (a)).

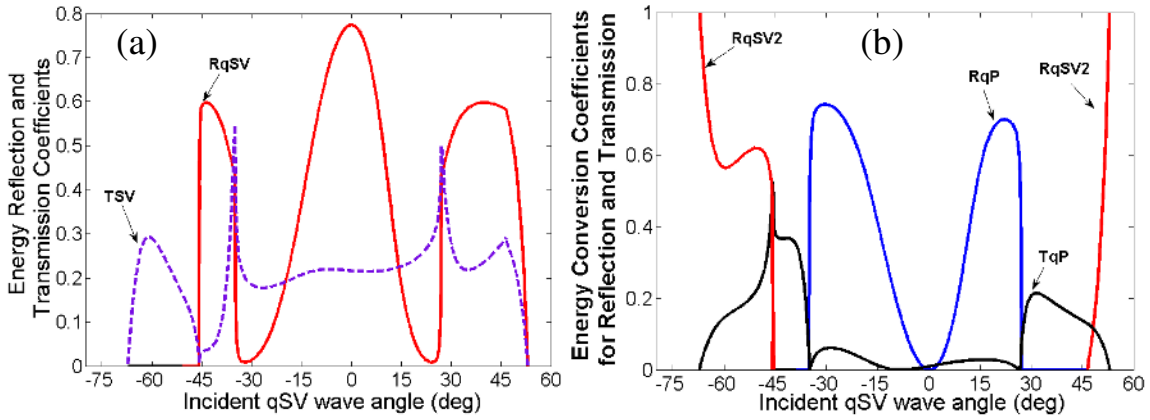

Figure 3.27: *(a) Energy reflection and transmission coefficients, (b) Energy conversion coefficients for reflection and transmission when an incident quasi shear vertical wave at an interface between anisotropic austenitic weld material and Perspex wedge material. The columnar grain orientation in the austenitic weld material is 75º with respect to the inspection surface.*

The critical angles (so called grazing angle) for incident qSV waves are found to be approximately -67.2º and 52.9º. Beyond an incident angle of 46.6º, two reflected quasi shear waves appear with slightly different group velocity magnitudes and energy directions (see Figure 3.27(a) and Figure 3.27 (b)). Thus, difficulties occur for the NDE engineer while identifying and interpreting the experimental results. From Figure 3.27 (a) and 3.27 (b) show that presence of second branch of quasi shear vertical waves, the transmissibility of incident quasi shear vertical waves are minimized and ultrasonic wave amplitudes may appear under the noise level. This leads to errors in defect detection, location and interpretation during the practical ultrasonic testing of columnar grained austenitic welds and austenitic clad materials.

3.5 Frequency Dependence of Energy Reflection and Transmission Coefficients in Anisotropic Austenitic Weld Materials

The slowness (or inverse phase velocity) surface of an ultrasonic wave in a general homogeneous anisotropic medium is independent of angular frequency [69]. This leads to the presented boundary conditions at a perfect interface between two anisotropic austenitic steel materials (i.e. Eqs. (3.13) and (3.14)) are independent of frequency. In practice, the interface between two adjacent weld metals in an inhomogeneous austenitic weld material contains very thin imperfections (i.e. collection of very thin cracks and voids with dimensions in the order of micrometer). In order to account the interface imperfections in an ultrasonic reflection and transmission problem, a quasi static distributed spring model has proven to be an important approach [18, 124, 125, 126]. According to the quasi static distributed spring model, the presence of imperfections at an interface leads to the extra particle vibrations. This is modeled by connecting the two media by a distributed spring with spring stiffness constant K and mass m (see Fig 3.28). The main assumption of this model is the overall thickness of the affected interface region is negligible with respect to the wavelength of the ultrasonic wave used to inspect the boundary. In order to determine the frequency dependence of energy reflection and transmission coefficients in an anisotropic austenitic weld material, we used the finite boundary stiffness model (FBSM) which is the special case of the quasi static distributed

spring model [127]. According to FBSM, the boundary conditions require that the components of stress remain continuous across the interface but there is a discontinuity in the particle displacement components. The discontinuity in the particle displacement components depends linearly on the corresponding stress components. The boundary conditions for the particle displacement and stress components at an imperfect interface between two anisotropic austenitic steel materials are expressed as

$$\left(\mathrm{T}_{xz}^{I} + \sum \mathrm{T}_{xz}^{R\alpha} = \sum \mathrm{T}_{xz}^{T\alpha}\right)_{z=0}, \tag{3.17}$$

$$\left(\mathrm{T}_{yz}^{I} + \sum \mathrm{T}_{yz}^{R\alpha} = \sum \mathrm{T}_{yz}^{T\alpha}\right)_{z=0}, \tag{3.18}$$

$$\left(\mathrm{T}_{zz}^{I} + \sum \mathrm{T}_{zz}^{R\alpha} = \sum \mathrm{T}_{zz}^{T\alpha}\right)_{z=0}, \tag{3.19}$$

$$\left(v_x^I + \sum v_x^{R\alpha} - \sum v_x^{T\alpha} = \frac{j\omega S_x}{2K_1}\left(\mathrm{T}_{xz}^{I} + \sum \mathrm{T}_{xz}^{R\alpha} + \sum \mathrm{T}_{xz}^{T\alpha}\right)\right)_{z=0}, \tag{3.20}$$

$$\left(v_y^I + \sum v_y^{R\alpha} - \sum v_y^{T\alpha} = \frac{j\omega S_x}{2K_2}\left(\mathrm{T}_{yz}^{I} + \sum \mathrm{T}_{yz}^{R\alpha} + \sum \mathrm{T}_{yz}^{T\alpha}\right)\right)_{z=0}, \tag{3.21}$$

$$\left(v_z^I + \sum v_z^{R\alpha} - \sum v_z^{T\alpha} = \frac{j\omega S_x}{2K_3}\left(\mathrm{T}_{zz}^{I} + \sum \mathrm{T}_{zz}^{R\alpha} + \sum \mathrm{T}_{zz}^{T\alpha}\right)\right)_{z=0}, \tag{3.22}$$

where T_{xz}, T_{yz}, T_{zz} are the traction force components, I, R and T indicate the incident, reflected and transmitted waves, respectively. v_x, v_y and v_z are the particle displacement components along x, y and z-directions respectively. K_1, K_2 and K_3 indicate the shear and longitudinal interfacial stiffness constants.

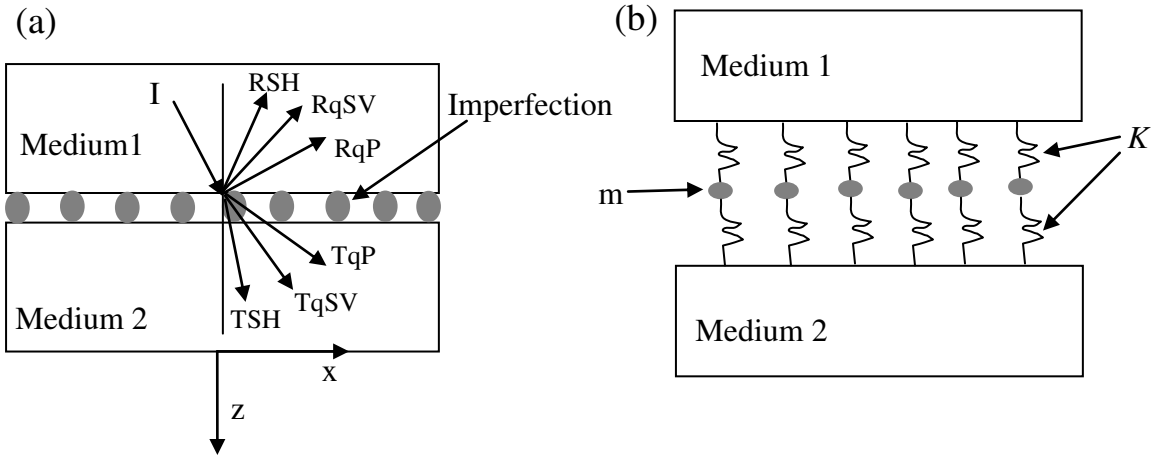

Figure 3.28: *(a) Illustration of energy reflection and transmission at an imperfect interface between two anisotropic austenitic steel materials, (b) quasi static spring model. m is the mass of the imperfection and K is the interfacial spring constant.*

Insertion of Equations (3.1), (3.2) and (3.3) in Equations (3.17), (3.18), (3.19), (3.20), (3.21) and (3.22) results in six linear algebraic equations which can be solved for evaluating three reflected and three transmitted amplitude coefficients. The energy reflection and transmission coefficients are obtained by introducing the amplitude coefficients and energy velocities in Eqs. (3.15) and (3.16), as described in section 3.2.4. The numerical results for the dependence of energy reflection and transmission coefficients on the frequency of an incident quasi longitudinal wave are shown in Fig. 3.29. As an example, we assumed medium1 and medium 2 as anisotropic austenitic steel materials with different columnar and layback orientations. The selected columnar grain orientation in the medium 1 is 75º and layback orientation is 20º. The selected columnar grain orientation in the medium 2 is 25º and layback orientation is 15º. A quasi longitudinal wave with 45° angle of incidence impinges at an imperfect interface between two columnar grained austenitic steel materials. The material parameters for the austenitic steel are presented in Table 1.

It can be seen from Fig. 3.29(a), thus increasing frequency of the incident qP wave, the quasi longitudinal wave energy reflection coefficient (ERqP) increases whereas the energy transmission coefficient (ETqP) decreases. Beyond the frequency of 5 MHz, the quasi longitudinal wave energy reflection coefficient shows negligible increment and attains the saturated value with 9.5% of the incident qP wave energy. As the frequency increases, the energy reflection coefficient for the quasi shear vertical wave (ERqSV) increases monotonically (see Fig. 3.29 (b)). For all frequencies, the energy transmission coefficients for the quasi shear vertical wave (ETqSV) are negligible. From the quantitative analysis on frequency dependence of energy reflection and transmission coefficients, we observed that the low frequencies (between 1 to 3 MHz) are more preferable for ultrasonic inspection of columnar grained austenitic weld materials. At the frequency of 2MHz, the transmitted quasi longitudinal wave carries 74% of the incident qP wave energy whereas the reflected quasi longitudinal wave carries 4.5%. The remaining 21.5% of the incident qP wave energy is distributed among the mode converted quasi shear vertical and pure shear horizontal waves.

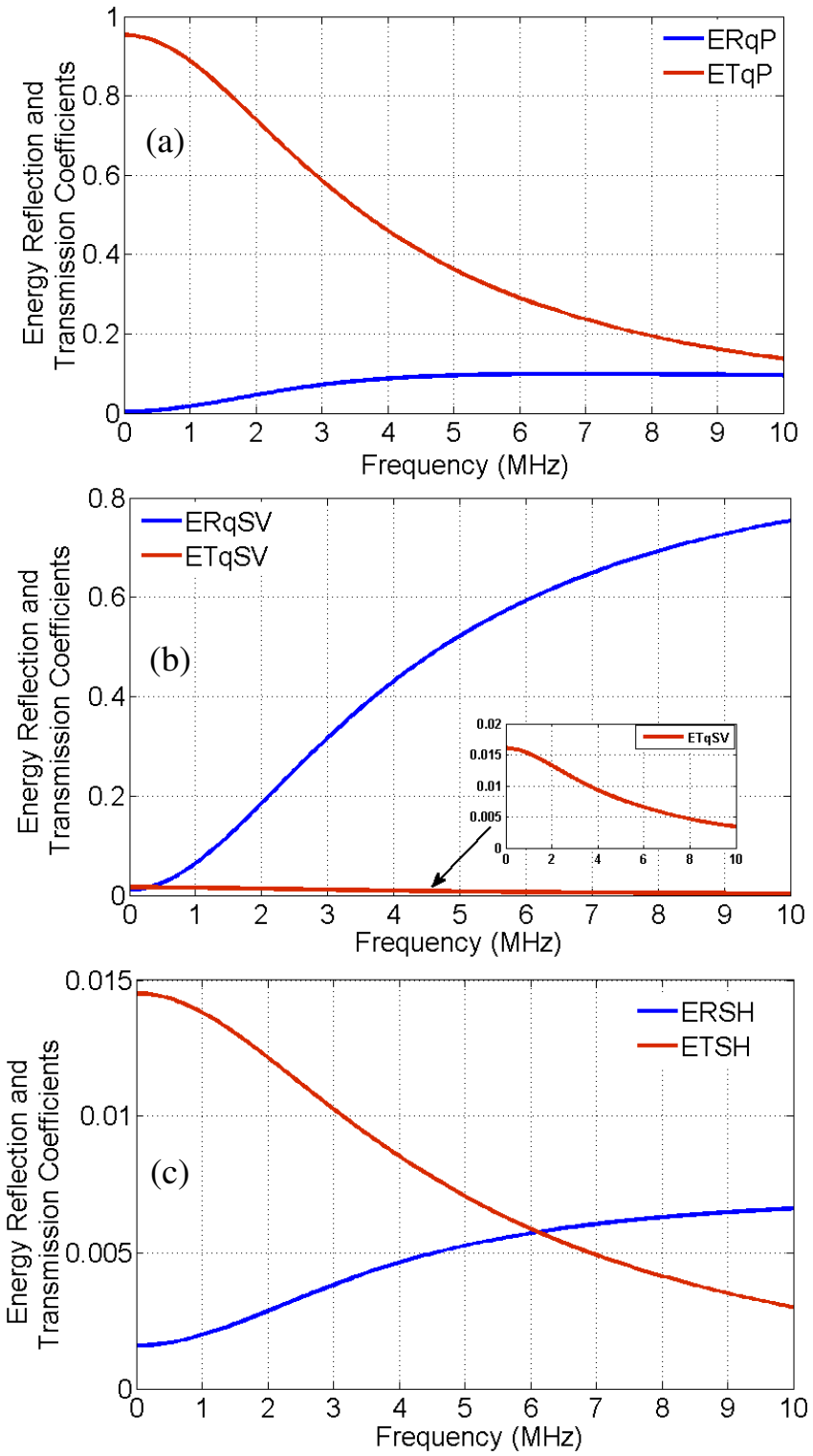

Figure 3.29: *Energy reflection and transmission coefficients versus frequency for (a) quasi longitudinal waves, (b) quasi shear vertical waves and (c) shear horizontal waves. The incident wave is quasi longitudinal with 45° angle of incidence.*

3.6 Validation of Numerical Results Based on Reciprocity Relations for Reflected and Transmitted Plane Elastic Waves

According to the fundamental reciprocity principle [128, 129] when a part of incident quasi longitudinal wave energy at an incident angle of θ_i (from medium 1) converts to the transmitted quasi shear vertical wave with transmission angle of θ_t is same as the part of incident quasi shear vertical wave energy at an incident angle of θ_t (from medium 2) converts to the transmitted quasi longitudinal waves with transmission angle of θ_i.

Let us consider a quasi longitudinal wave impinging at an angle of -55º at the interface between two columnar grained austenitic columnar grained bundles where upper medium exhibits 90º columnar grain orientation and the lower medium columnar grains are oriented at 75º. The obtained transmitted quasi shear vertical wave energy coefficient is 0.01733 at a transmission angle of -20.9º (see Figure 3.30(a)). Now, quasi shear vertical wave (from medium 2) is incident at an angle of -20.9º at an interface resulting transmitted quasi longitudinal wave (in medium 1) has energy coefficient 0.01733 and transmission angle equal to -55º (see Figure 3.30(b)). The reciprocity relations are also successfully verified for quasi longitudinal to quasi longitudinal as well as quasi shear vertical to quasi shear vertical transformations. Thus, the fundamental reciprocity relations are verified for the reflected and refracted waves. This means the presented analytically evaluated energy reflection and transmission coefficients in anisotropic columnar grained austenitic weld materials are validated.

The problem of energy reflection and transmission at an interface between two general anisotropic solids is obtained by solving the resulting six degree polynomial equation in S_Z numerically in both real and complex domain of the reflected and transmitted normal components of slowness vectors. The theory for evaluating energy reflection and transmission is applied for the general anisotropic austenitic weld materials exhibiting both columnar grain and layback orientations.

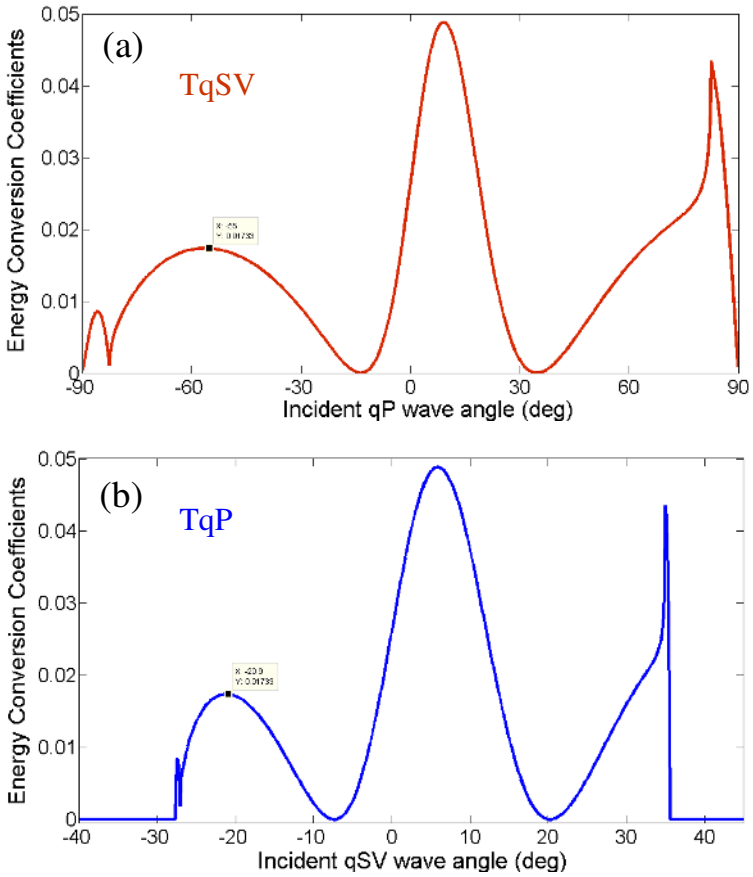

Figure 3.30: *(a) Energy conversion coefficients for the transmitted quasi shear vertical wave (TqSV) when a quasi longitudinal wave is incident at an interface between two columnar grained austenitic weld materials. The upper medium columnar grains are oriented at 90º and lower medium columnar grains are oriented at 75º, (b) energy conversion coefficients for the transmitted quasi longitudinal wave (TqP) for an incident quasi shear vertical wave at an interface between two columnar grained austenitic weld materials. The upper medium grains are oriented at 75º and lower medium grains are oriented at 90º.*

A complete comprehensive quantitative analysis of an effect of columnar grain orientation and layback orientation on energy reflection and transmission coefficients for six interfaces namely a) Isotropic – Anisotropic, b) Water – Anisotropic, c) Anisotropic – Isotropic, d) Anisotropic – Water, e) Anisotropic – Anisotropic and f) Anisotropic – Free surface boundary are discussed in the context of ultrasonic non-destructive investigation of acoustically anisotropic austenitic weld materials. The derived analytical expressions for evaluating reflected and transmitted energy angles and coefficients play an important role in modeling the ultrasonic fields based on three dimensional ray tracing method and it will be discussed in the subsequent chapters.

CHAPTER 4

Analytical Evaluation of 3D Ultrasonic Ray Directivity Factor in Anisotropic Materials: Application to Austenitic Welds

4.1 Introduction

In this chapter the ray directivity in a general anisotropic medium is obtained three dimensionally based on Lamb's reciprocity theorem [61, 109, 111, 130, 131]. The theory is applied first time for evaluating 3D ray directivity in general anisotropic austenitic steel material exhibiting three dimensional columnar grain orientation. The incident ray source is represented in 3D space i.e. considering both elevation and azimuthal angles. The point source directivity for the three wave modes quasi longitudinal (qP), quasi shear vertical (qSV) and pure shear horizontal (SH) waves under the excitation of normal as well as tangential forces on semi infinite columnar grained transversal isotropic austenitic steel material is discussed. The influence of columnar grain angle and layback angle on ray source directivity patterns in an austenitic steel material is investigated. The results of this chapter play an important role in quantitative evaluation of ultrasonic fields in general inhomogeneous austenitic weld materials.

4.2 Theoretical Procedure: Ray Directivity Evaluation

Consider a radial force ***F***, which is applied at a point remote from the origin (see Fig. 4.1). This force is directed parallel to the polarization vector of the quasi longitudinal wave (qP) and it is associated with a wave vector $\mathbf{k}_{qP}$ and phase angle θ_{qP}. The qP wave propagates in the direction of the radius vector pointing towards the origin (i.e. free surface boundary). When a qP wave is incident onto the free surface boundary of a semi infinite anisotropic medium, it converts into three reflected waves (i.e. RqP, RqSV and RSH). The tangential (x, y) or normal (z) displacements at the origin are expressed as follows

$$u_{\alpha,I}(\theta) = A_{\alpha,I} \cdot u_{\alpha,I}(\theta) + A_{\beta_1,I} \cdot u_{\alpha,\beta_1} + A_{\beta_2,I} \cdot u_{\alpha,\beta_2} + A_{\beta 3,I} \cdot u_{\alpha,\beta 3} \ , \tag{4.1}$$

where α represents the normal (z) or tangential components (x, y), I = qP, qSV, SH representing the type of incident wave, $A_{\beta_1}, A_{\beta_2}, A_{\beta_3}$ represent the reflected wave amplitudes from the stress free surface boundary of an anisotropic medium and $u_{\alpha,I}, u_{\alpha,\beta_1}, u_{\alpha,\beta_2}, u_{\alpha,\beta_3}$ are the particle polarization components for incident and reflected waves, respectively.

In Figs. 4.1, 4.2 and 4.3 the red circle at the origin represents the displacement or force acting perpendicular to the xz-plane. Lamb's reciprocity theorem states that if a normal force ***F*** is applied at the origin, then the same displacements (given by Eq. (4.1)) are generated along the radial direction at a point R(x, y, z) in the semi infinite anisotropic medium. Similarly, the theorem can be applied for x-direction tangential force (see Fig. 4.2) and y-direction tangential force excitation (see Figure 4.3) on a free surface boundary of a semi infinite anisotropic medium

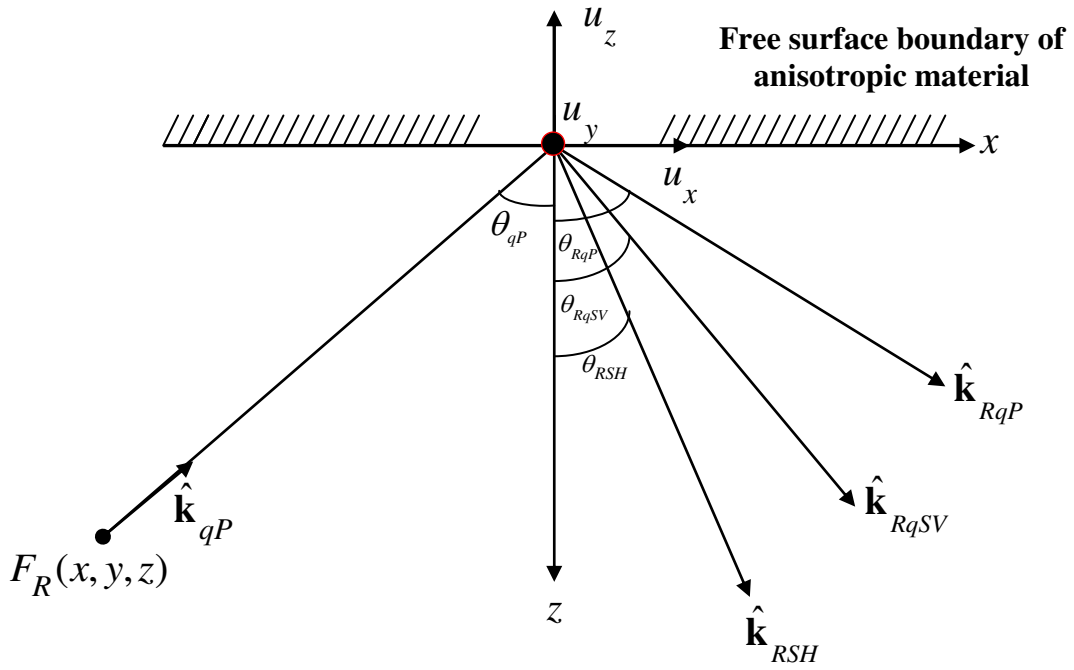

Figure 4.1: *Graphical representation of evaluating particle displacement directivity of the quasi longitudinal (qP) waves using Lamb's reciprocity theorem.*

A generalized form to represent the displacement directivity factor $D_{\alpha,I}$ for the quasi longitudinal, quasi shear vertical and shear horizontal waves under the excitation of normal (z) or tangential (x, y) forces is given as

$$D_{\alpha,I}(\theta) = u_{\alpha,I}(\theta) + R_{\beta_1,I} \cdot u_{\alpha,\beta_1} + R_{\beta_2,I} \cdot u_{\alpha,\beta_2} + R_{\beta 3,I} \cdot u_{\alpha,\beta 3} \ . \tag{4.2}$$

$R_{\beta_1}, R_{\beta_2}, R_{\beta_3}$ represent the reflection coefficients at a free surface boundary of an anisotropic medium. The reflected waves particle polarization components, amplitudes and energy coefficients at a free surface boundary of a general anisotropic medium are obtained based on the elastic plane wave theory [69], as described in chapter 3. In case of anisotropic medium, the wave vector direction does not coincide with the energy direction. While evaluating directivity in general anisotropic medium, it is very important to consider the energy angle instead of wave vector angle [61]. The procedure for evaluating directivity pattern based on Lamb's reciprocity theorem is employed for the general austenitic materials exhibiting columnar grain angle and layback orientation.

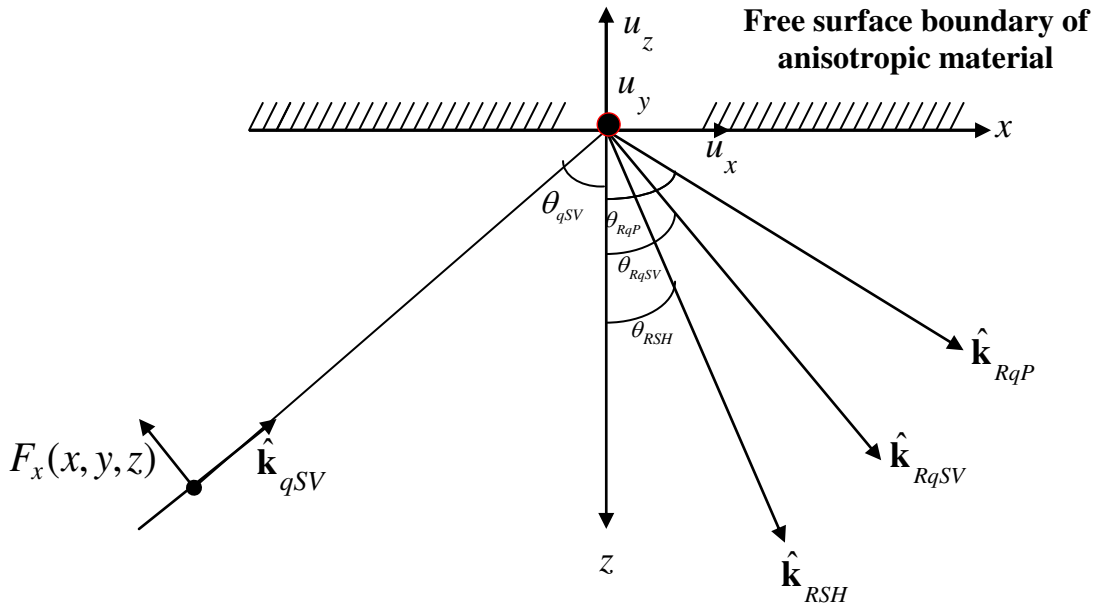

Figure 4.2: *Graphical representation of evaluating particle displacement directivity of the quasi shear vertical (qSV) waves using Lamb's reciprocity theorem.*

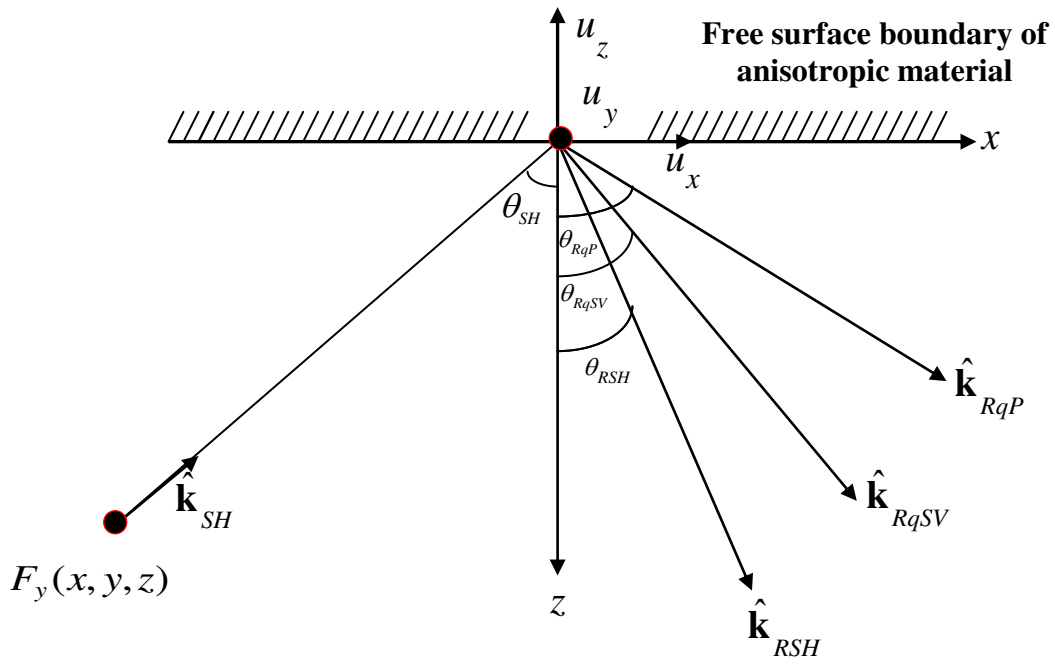

Figure 4.3: *Graphical representation of evaluating particle displacement directivity for the pure shear horizontal (SH) waves using Lamb's reciprocity theorem.*

4.3 Numerical Results and Discussion

In this section, numerical results for analytically evaluated three dimensional directivity patterns for the three wave modes under the excitation of normal (z) and tangential (x, y) forces on a free surface boundary of a columnar grained austenitic steel material (X6 Cr-Ni 18 11) are presented. The material properties for the transversal isotropic austenitic steel material are presented in Table 1. For the presentation of the results, the selected columnar grain orientation in the austenitic steel material is 45º and lay back orientation is 15º. In the presented case all three wave modes namely quasi longitudinal (qP), quasi shear vertical (qSV) and pure shear horizontal (SH) waves couple together.

4.3.1 Amplitude and Energy Reflection Coefficients for the Reflected Waves at a Free Surface Boundary of an Austenitic Steel Material

Figure 4.4 shows the amplitude and energy reflection coefficients for the three wave modes when a quasi longitudinal wave is incident at a free surface boundary of a columnar grained austenitic material.

It can be seen from Figure 4.4, that the amplitude and energy coefficients for the three reflected waves are influenced by the anisotropic properties of the austenitic material. No critical angles for reflected or transmitted waves are observed and all the angles are real.

The numerical results for the dependence of amplitude and energy reflection coefficients on the incident quasi shear vertical wave angle for three different ultrasonic waves are shown in Fig. 4.4. Complicated critical angle phenomena for the reflected waves are observed. From Figure 4.5, the mode converted reflected quasi longitudinal waves (RqP) are capable of propagating for the incident angles from -36º to 32.5º. The critical angles for the reflected quasi longitudinal wave (RqP) are -36.5º and 33º. For the wide range of incident angles, the reflected shear horizontal (RSH) waves are permeable. The critical angles for the RSH wave are -68º and 67.5º. Depending on the magnitudes of the reflection coefficients for the reflected waves, maxima and minima in the directivity patterns occur. This will be explained in the next section.

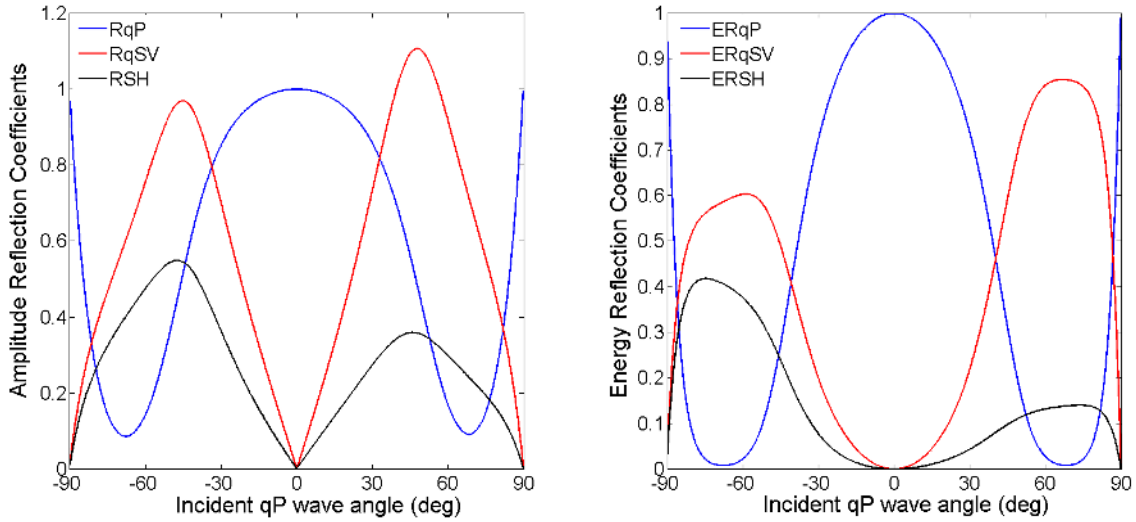

Figure 4.4: *(left) Amplitude coefficients, (right) energy coefficients for the three reflected waves when a quasi longitudinal wave (qP) is incident at a free surface boundary of columnar grained austenitic steel material (X6 CrNi 1811) exhibiting 45º columnar grain orientation and 15º layback orientation.*

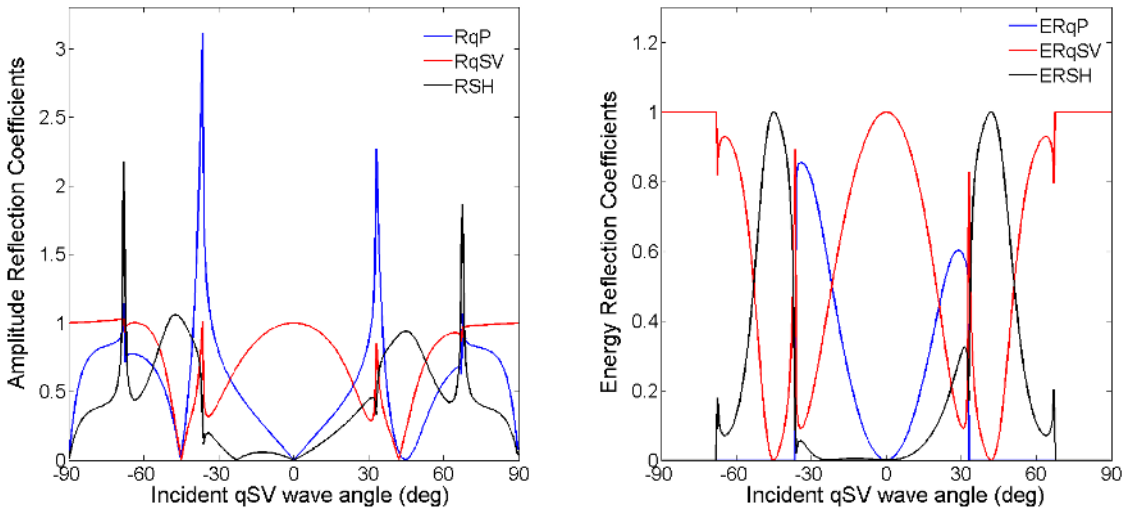

Figure 4.5: *(left) Amplitude coefficients, (right) energy coefficients for the three reflected waves when a quasi shear vertical wave (qSV) is incident at a free surface boundary of columnar grained austenitic steel material (X6 CrNi 1811) exhibiting 45º columnar grain orientation and 15º layback orientation.*

Figure 4.6 shows the angular dependency of amplitude and energy coefficients for the incident pure shear horizontal (SH) waves at a free surface boundary of an austenitic steel material. The reflected quasi longitudinal wave can propagate between the incident angles of -29.7º and 37.1º. Beyond these angles, the RqP wave becomes evanescent. It can be seen from Figure 4.6 that the amplitude coefficient for the reflected quasi longitudinal wave rises sharply at the critical angles. Generally the evanescent waves do not carry any energy but its amplitudes decay exponentially away from the boundary. From Figure 4.6, it can be seen that for a wide range of incident angles, the reflected quasi shear vertical and shear horizontal waves are permeable. The critical angle for the incident shear horizontal wave occurs at an incident angle of -77.9º.

4.3.2 Point Source Directivity Pattern

Figure 4.7 shows the point source directivity patterns for the quasi longitudinal (qP), quasi shear vertical (qSV) and shear horizontal (SH) waves for the normal (z) and tangential (x, y) force excitation on a columnar grained austenitic steel material.

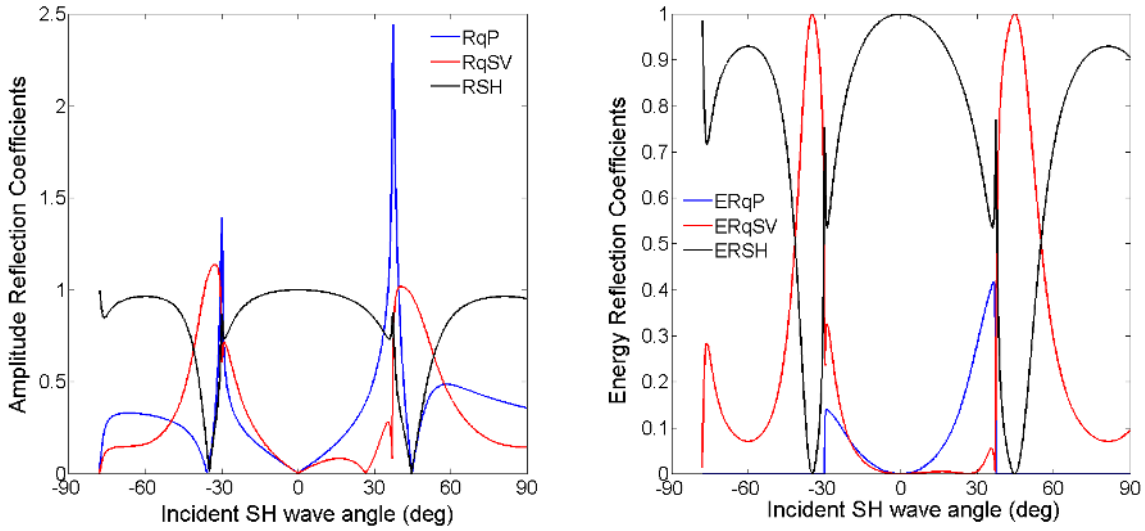

Figure 4.6: *(left) Amplitude coefficients, (right) energy coefficients for the three reflected waves when a pure shear horizontal wave (SH) is incident at a free surface boundary of columnar grained austenitic steel material (X6 CrNi 1811) exhibiting 45º columnar grain orientation and 15º layback orientation.*

The considered columnar grain orientation and layback orientation in the anisotropic austenitic steel material are 45º and 15º respectively. As expected, the directivity patterns for the three waves are nonsymmetrical (see Figure 4.7). In case of normal force excitation (see Figure 4.7(a)), the directivity pattern for the quasi longitudinal wave contains one principal lobe with maximum amplitude close to the normal direction (i.e. near 0º angle) and zero directivity along the tangential direction. For the tangential force excitation in x-direction, qP wave directivity contains two principal lobes and equals zero in direction either parallel or perpendicular to the free surface. Directivity pattern of the quasi longitudinal wave under tangential force excitation in y-direction shows one principal lobe in the positive angular region and side lobes with less displacements in the negative angular region. Interesting is that the displacements for the qP waves produced by the y-direction tangential force are much less than as compared to x-direction tangential force. As expected, the quasi shear vertical wave directivity patterns are strongly influenced by the anisotropy of the columnar grained austenitic steel material.

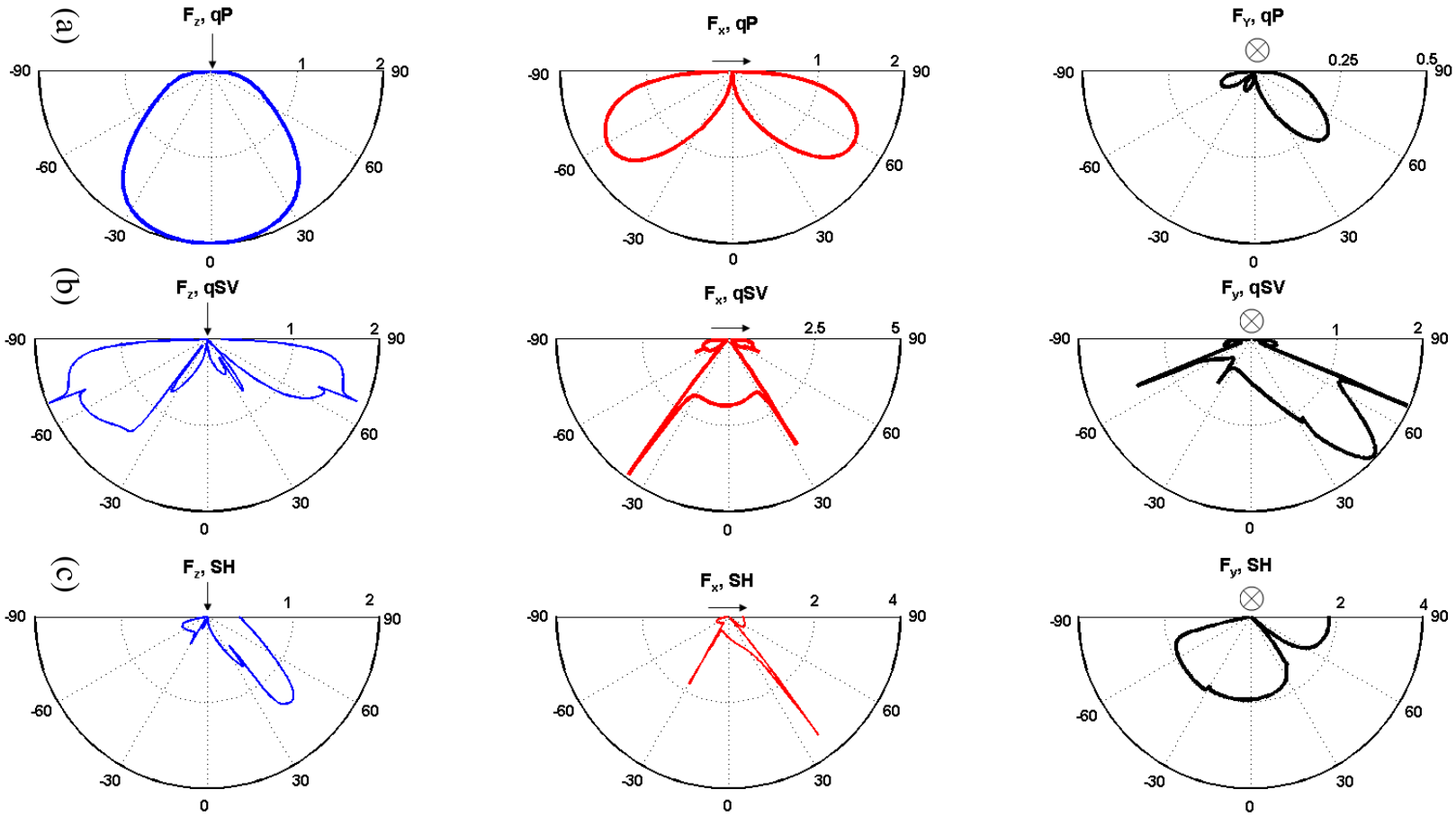

Figure 4.7: Directivity patterns of the (a) quasi longitudinal wave, (b) quasi shear vertical wave and (c) shear horizontal wave for the normal (z) and tangential (x, y) point source excitation on a columnar grained austenitic steel material exhibiting 45º columnar grain orientation and 15º lay back orientation.

In case of x-direction tangential force excitation, the directivity pattern of qSV wave exhibits two maxima and the reason for these maxima can be explained from the reflection coefficients when a qSV wave is incident at a free surface boundary of an austenitic steel material (see Figure 4.5). The two maxima in qSV wave pattern occur at regions of critical angles for the reflected quasi longitudinal waves. The qSV wave directivity pattern under the excitation of normal (z) force is highly deviated from the isotropic case. Interesting is that the focussing effects are observed for the qSV wave directivity patterns when a y-direction tangential force excited on a free surface of an austenitic steel material. At incident angles close to the 45º, a pronounced maximum is observed. Depending on the layback angle of the austenitic steel material, the focussing effects in the directivity pattern vary.

Figure 4.7 (c) shows directivity pattern for the pure shear horizontal waves (SH) under the excitation of normal force (z) on a free surface of an austenitic steel material. It can be seen from Figure 4.7 (c), that the SH wave directivity pattern contains one major lobe and a side lobe in the positive incident angular region and a side lobe formation in the negative incident angular region. These behaviour of showing predominant amplitudes in the positive angular region can be explained based on the energy reflection coefficients for the reflected waves when a SH wave is incident at a free surface boundary of a columnar grained austenitic material (see Fig (4.6)). From Figure 4.6, the energy coefficients for the reflected shear horizontal (RSH) wave carries most of the incident SH wave energy for the incident angles between -75º and -35º and consequently shear horizontal wave amplitudes produced by the normal (z) and x-direction tangential forces decreases. While on the other hand, for positive incident angles between 35º and 60º, the RSH wave carries minimum energy. Consequently, predominant SH wave displacements in positive angles of incidence are resulted for the y-direction tangential force (see Figure 4.7(c)). In case of SH wave directivity pattern for the tangential force in y-direction shows diverging behaviour for a wide range of incident angles. In case of x-direction tangential force excitation, the SH wave directivity pattern contains two principal maxima. Interesting is that non zero directivity of the SH waves occurs in the

tangential direction to the free surface. As expected, for a point source, the directivity patterns are independent of frequency.

Special Case:

In the particular case of sound propagation in the transversal isotropic austenitic steel material, the pure SH wave does not couple with qP and qSV waves because this wave polarizes perpendicular to the plane of wave propagation, as stated in Chapter 2. Figure 4.8 shows directivity patterns for the quasi longitudinal and quasi shear vertical waves for a normal and x-direction tangential force excitation on an austenitic stainless steel material exhibiting columnar grain orientation 0º and layback orientation 0º. It can be seen from Figure 4.8, that the qSV wave directivity pattern for the x-direction tangential force (F_x) contains a principal lobe with two distinct maxima. The directivity pattern for the qSV wave for a normal vibrating force (F_z) has two principal lobes and zero displacements occur along the normal and tangential directions. The directivity pattern for the qP wave for x-direction tangential vibrating force (F_x) has two principal lobes and vanishes directions perpendicular and parallel to the free surface. The directivity pattern of qP wave for the normal force contains one major lobe with maximum in the normal direction to the free surface and exhibits zero directivity in the tangential direction.

Figure 4.9 shows directivity patterns for the quasi longitudinal and quasi shear vertical waves for a normal and x-direction tangential point force excitation on an austenitic stainless steel material exhibiting columnar grain orientation 60º and layback orientation 0º. It can be seen from Figure 4.9, that the directivity patterns are strongly influenced by the anisotropic properties of the austenitic steel material. The directivity pattern for the qSV waves under the excitation of x-direction tangential force (F_x) is more distorted from the directivity patterns for the 0º grain angle (see Figure 4.8). The qSV wave directivity pattern for the x-direction tangential force excitation shows a sharp maximum in negative angles of incidence. These features lead to qSV waves generally not considered for the ultrasonic investigation of austenitic weld material. As expected, the directivity patterns show non-symmetrical behaviour about the direction of the excitation force.

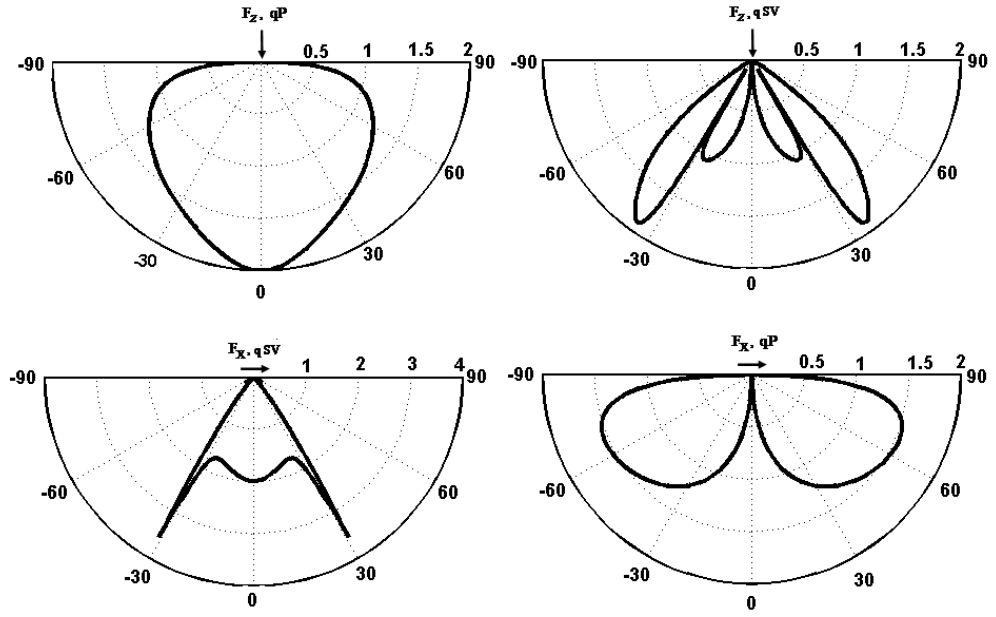

Figure 4.8: *Directivity patterns for the quasi longitudinal wave(qP) and quasi shear vertical waves (qSV) for the normal point force (F_z) and tangential point force (F_x) excitation on a free surface boundary of columnar grained austenitic steel material. The columnar grain orientation of the austenitic stainless steel material is 0º.*

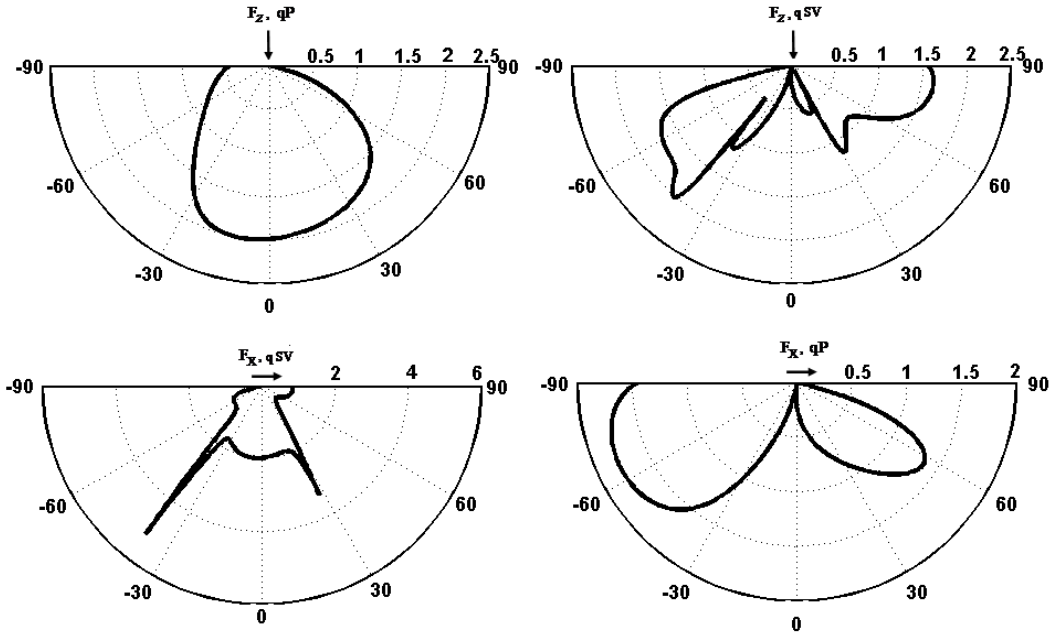

Figure 4.9: *Directivity patterns for the quasi longitudinal wave(qP) and quasi shear vertical waves (qSV) for the normal point force (F_z) and tangential point force (F_x) excitation on a free surface boundary of columnar grained austenitic steel material. The columnar grain orientation of the austenitic stainless steel material is 60º.*

Analytical solution for the ultrasonic point source directivity patterns for three wave modes quasi longitudinal and quasi shear vertical and pure shear horizontal waves for the normal (z) and tangential (x, y) force excitation on a free surface boundary of general columnar grained austenitic steel materials is obtained three dimensionally based on the Lamb's reciprocity theorem. The directivity patterns are calculated in the presence of columnar grain and layback orientations of the anisotropic austenitic steel material. Influence of grain orientation on directivity patterns is quantitatively analyzed. It is shown that, depending on the maximum and minimum in the energy coefficients, the maxima and minima locations occur in the directivity patterns. As expected, the directivity patterns are more distorted from the isotropic behaviour and exhibit non-symmetrical patterns. It is concluded that ray directivity should be included in the ray tracing model in order to improve the reliability of the ray tracing predictions for ultrasonic fields in inhomogeneous anisotropic austenitic weld material. The results of this chapter will be employed in the next chapters in order to model the accurate ultrasonic fields generated by a point source as well as finite dimension transducer in inhomogeneous austenitic welds.

CHAPTER 5

Ray Tracing Model for Ultrasonic Wave Propagation in Inhomogeneous Anisotropic Austenitic Welds

5.1 Introduction

In this chapter a 3D ray tracing model for simulating ultrasonic wave propagation in general anisotropic inhomogeneous austenitic welds is presented. In this thesis work, the point source as well as finite dimension transducer generated ultrasonic fields in inhomogeneous austenitic welds are evaluated quantitatively using a ray tracing method by taking into account all the physical aspects of a ray such as ray directivity factor in an isotropic base material, anisotropic weld material and ray divergence variation, transmission coefficients at a boundary separating two dissimilar materials, phase relations and finally ray amplitudes are represented in terms of density of rays. Apart from that a reliable weld structure model is considered which accounts the spatial variation of grain orientation in the macrograph of real life austenitic and dissimilar weld materials. These important aspects improve the reliability of the ray tracing predictions and helps in optimization and defect assessment during the ultrasonic inspection of inhomogeneous weld material. In this chapter, the ray tracing procedure for point sources as well as distributed sources and influence of inhomogeneous weld structure on ray energy paths for direct, mode converted and back wall reflected waves are presented. The results of this chapter lay the foundation for calculating realistic ultrasonic ray amplitudes in an inhomogeneous austenitic weld material. The quantitative comparison of ray tracing results with Elastodynamic Finite Integration Technique (EFIT) calculations and experiments will be presented in the next chapters.

5.2 Modeling of Austenitic Weld Material Inhomogenity

Based on the several investigations on macrographs of the Cr-Ni based V-butt austenitic welds, Ogilvy [77] developed a mathematical empirical relation to describe the local

columnar grain structure of the inhomogeneous austenitic weld material. Its form is given as

$$G(x,z)=\begin{cases}\tan\theta_1=\dfrac{-T_1\left(D_1+z\tan\alpha_1\right)}{x^{\eta}}, & x\geq 0\\ \tan\theta_2=\dfrac{T_2\left(D_2+z\tan\alpha_2\right)}{(-x)^{\eta}}, & x<0\end{cases} \tag{5.1}$$

where θ_1 and θ_2 are the columnar grain orientations obtained with respect to the positive and negative regions of the reference x-axis, T_1 and T_2 are proportional to the slope of the columnar grain axis at the right and left fusion faces, D_1 and D_2 are the half width of the gap between weld root faces, and α_1 and α_2 denote the angle of the weld preparation at the right and left weld fusion line, respectively.

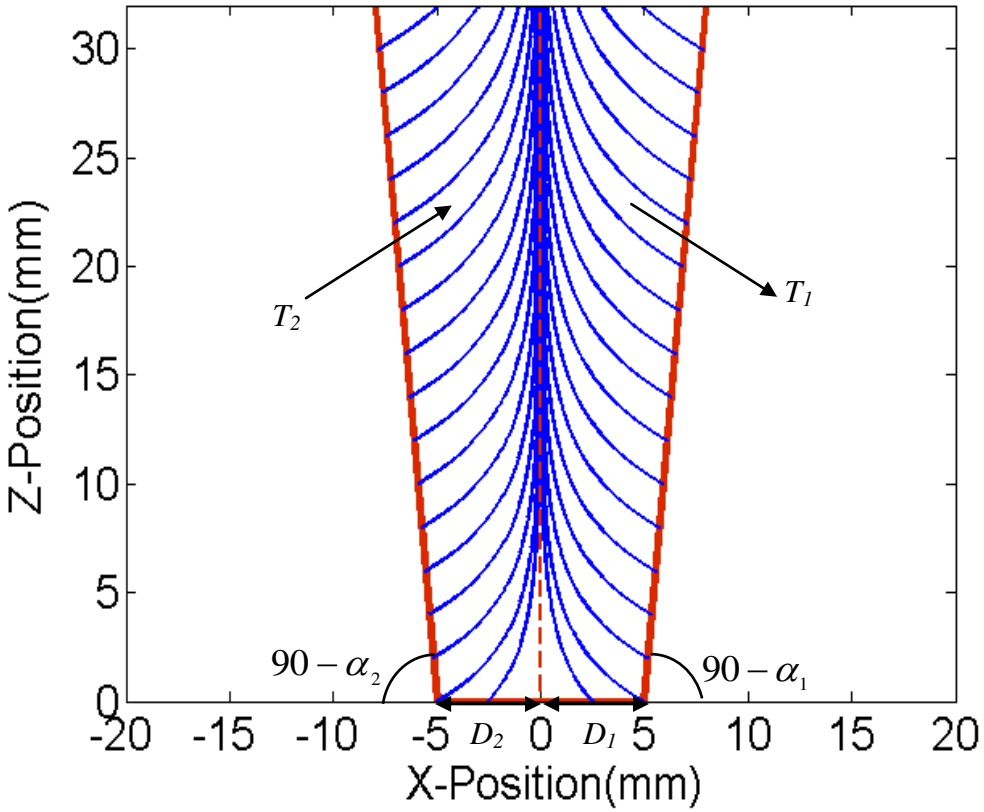

Figure 5.1: *Illustration of weld parameters in the Ogilvy empirical formula for describing the austenitic weld symmetric columnar grain structure. Weld boundary inclination angles* $\alpha_1 = \alpha_2 = 5.36^{o}$. $T_1 = T_2 = 0.54$, *and* $\eta = 1$ *in Eq. (5.1).*

η is a parameter with $0 \le \eta \le 1$ measures the change of grain orientation as a function of the distance x from the weld centre line. The resulted grain structure in a V-butt austenitic weld using the mathematical function $G(x,z)$ is shown in Fig. 5.1. Although the mathematical function $G(x,z)$ was developed under an assumption that the columnar grain structure was symmetric with respect to the weld centreline, it can also be employed for modelling the non-symmetrical grain structure of the weld. This is obtained by taking into account different weld parameters in the positive and negative directions with respect to the weld centreline. As an example Fig. 5.2 shows the non-symmetrical grain structure in an inhomogeneous austenitic weld. The epitaxial growth of columnar grains within the weld material can be observed in Fig. 5.2. Thus, a modified Ogilvy's model with optimal weld parameters can be used for modelling the real life austenitic weld structures.

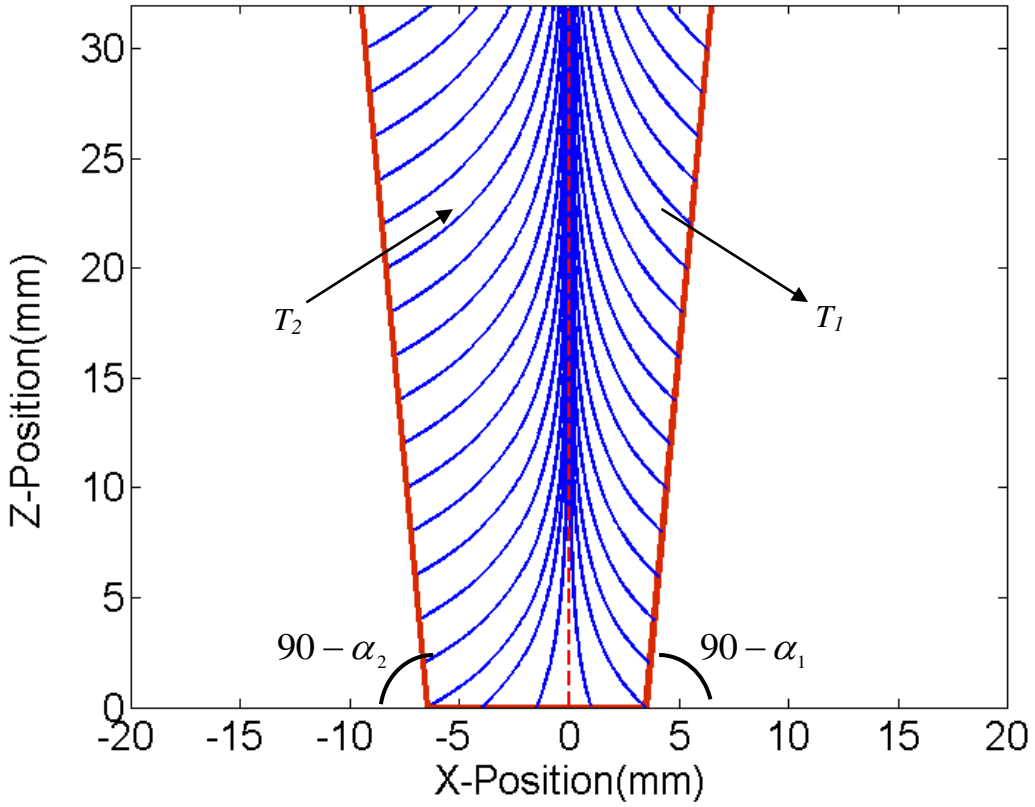

Figure 5.2: *Illustration of nonsymmetrical columnar grain structure in an inhomogeneous austenitic weld material. Weld boundary inclination angles* $\alpha_1 = \alpha_2 =$ *5.36°.* $T_1 = -0.91$, $T_2 = 0.54$, $D_1 = 3.5$ *mm,* $D_2 = 6.5$ *and* $\eta = 1$ *in Eq. (5.1).*

5.2.1 Comparison between Weld Structure Model and Macrograph of the Real-life Austenitic Weld

The main aim of this section is to obtain the optimal weld parameters by comparing modelled weld structure with macrograph of the austenitic weld. The following procedure is applied to obtain the optimal weld parameters:

(a) the weld parameters D_1, D_2, α_1 and α_2 in the mathematical function G(x,z) are obtained directly by careful observation in the real austenitic weld specimen and these parameters are input for the weld structure simulation,

(b) the parameter η is set to be 1 in the simulation. The reason for setting $\eta=1$ is to obtain the lines of constant crystal orientations in the weld material (note that in 3D they are planes of constant crystal orientations). These lines of constant crystal orientations are represented as a boundary between two different columnar grain orientations of the weld metal during the ray tracing calculations. A detailed description on lines of constant crystal orientations and ray tracing in layered austenitic welds will be presented in section 5.3,

(c) the parameters T_1 and T_2 in the weld structure simulation are varied until an optimum match is reached between the modelled grain structure and macrograph of the real life austenitic weld specimen.

In order to verify the validity of the weld structure model, a direct comparison between modelled weld structure and macrograph of the austenitic weld specimen is performed. Fig. 5.3(a) shows macrograph of the Cr-Ni based V- butt austenitic weld (specimen Q1) which is subjected to the experimental investigation. The filler layers in the austenitic weld metal were made using multipass Manual Metal Arc (MMA) welding and the root pass was carried out using Tungsten Inert Gas (TIG) welding. It can be recognized from the Fig. 5.3(a), that the austenitic weld materials exhibit epitaxial grain growth starting from the weld root and weld fusion face up to the weld crown, which results in spatial variation of columnar grain orientation within the weld metal. A comparison between modelled weld structure and macrograph of the weld specimen Q1 is presented in Fig. 5.3(b).

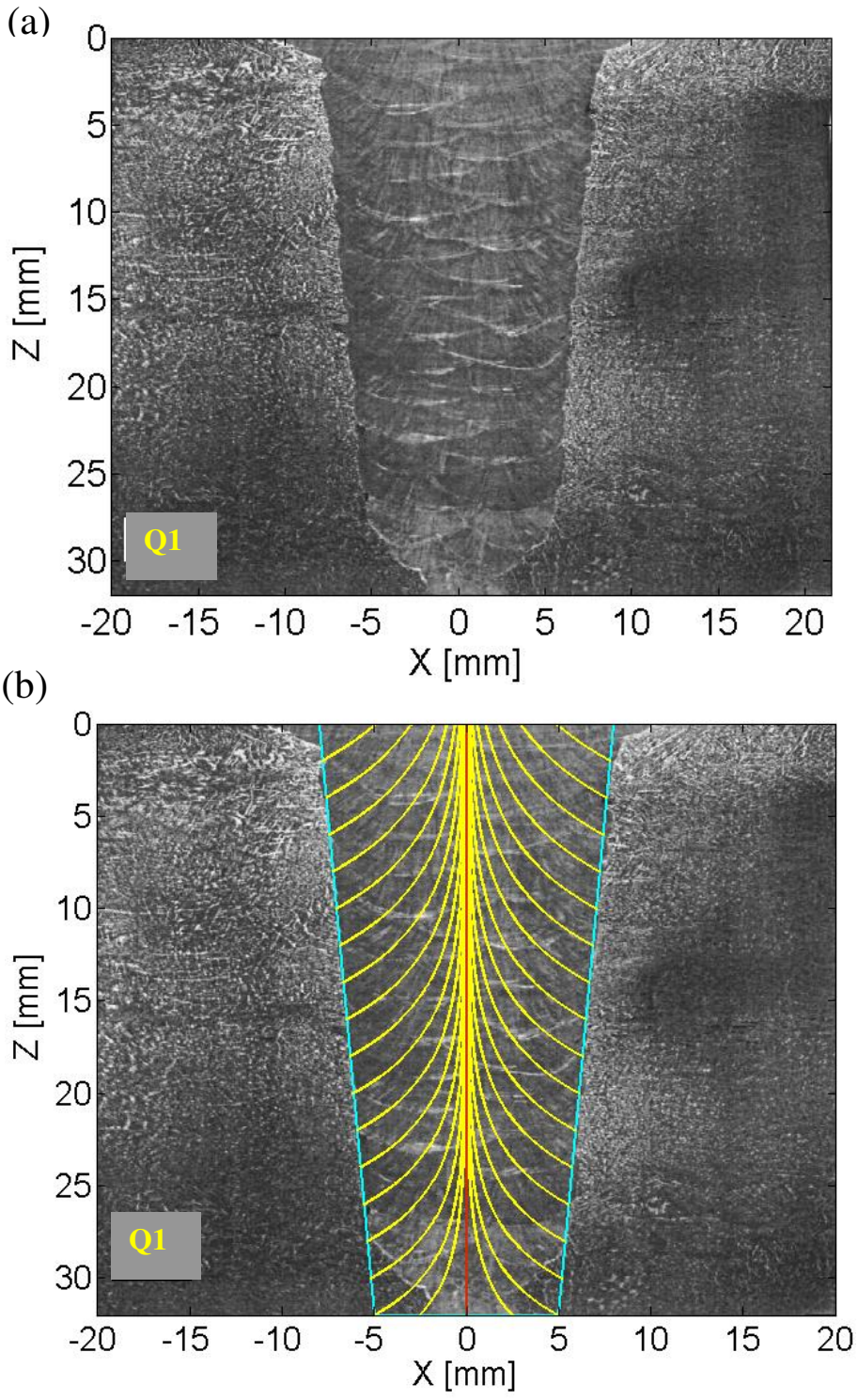

Figure 5.3: *(a) Macrograph of the Cr-Ni based austenitic weld specimen Q1. Weld data: root tungsten inert gas welded, filler layers manual metal arc welded, V-butt austenitic weld thickness 32 mm. (b) Comparison between weld structure model and real macrograph of the specimen Q1.*

Table 2: *Estimated weld parameters for the inhomogeneous austenitic weld samples Q1 and Q2.*

Weld Parameter	Weld Sample Q1	Weld Sample Q2
D_1	5 mm	4.5 mm
D_2	5 mm	7.5 mm
T_1	-0.54	-1.09
T_2	0.54	0.985
α_1	5.3558°	7.125°
α_2	5.3558°	7.125°
η	1	1

The estimated optimal parameters for the austenitic weld specimen Q1 are listed in Table 2. It can be seen from Fig. 5.3(b) a good qualitative agreement is obtained between modelled weld structure and the macrograph of the austenitic weld specimen. A symmetrical columnar grain structure can be observed in Fig. 5.3(b). In general, some of the austenitic weld materials may contain non-symmetrical columnar grain structure due to the different welding conditions such as the welding current, the number of weld passes, the incline of weld passes and the temperature gradient directions in the weld pool during welding process. Fig. 5.4(a) shows macrograph of the austenitic weld specimen Q2. It can be seen from Fig. 5.4(a) that the columnar grains at the left and right weld fusion boundaries start at different crystal orientations resulting non-symmetrical weld structure. Fig. 5.4(b) shows a comparison between modelled weld structure and macrograph of the austenitic weld specimen Q2. The estimated optimal weld parameters for the weld specimen Q2 are listed in Table 2.

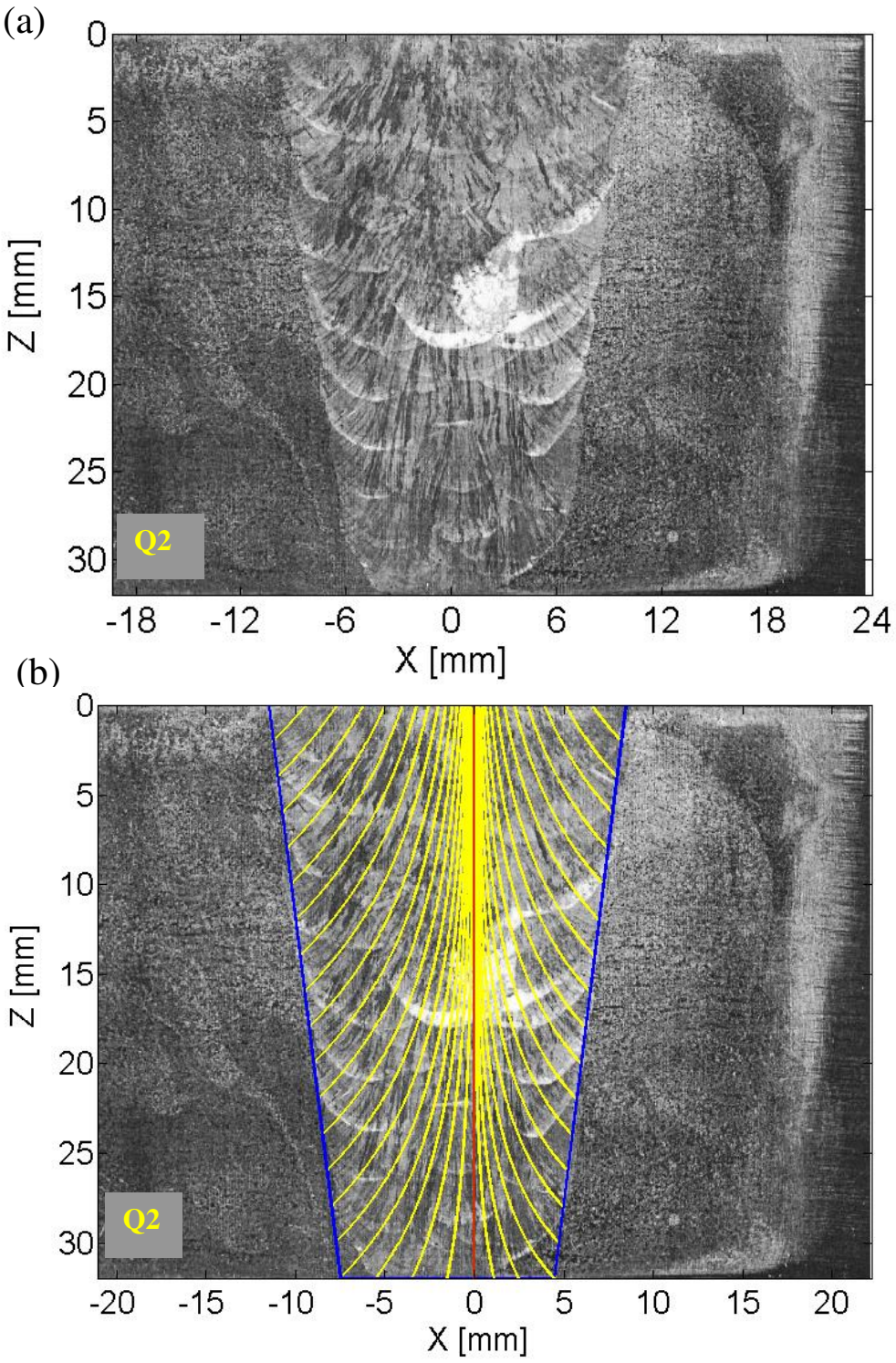

Figure 5.4: *(a) Macrograph of the Cr-Ni based austenitic weld specimen Q2. Weld data: root tungsten inert gas welded, filler layers manual metal arc welded, V-butt austenitic weld thickness 32 mm. (b) Comparison between weld structure model and real macrograph of specimen Q2.*

A good qualitative agreement between modelled weld structure and macrograph of the austenitic weld is achieved (see Fig. 5.4(b)). Although the empirical relation in Eq. (5.1) does not consider the welding input parameters such as the diameter of the electrode, the number and order of passes, the model results agree well with experimental investigations [83]. The estimated optimal parameters for simulating weld structure of the real life austenitic weld specimen Q1 will be used in the ray tracing model to compare the simulated ultrasonic ray amplitudes with experiments.

Throughout the thesis work, the mathematical empirical relation in Eq. (5.1) is used for describing the inhomogeneity of austenitic weld material. The inhomogeneous region of the austenitic weld material is discretized into several homogeneous layers and it is surrounded by a homogeneous isotropic austenitic steel material on either side (see Figure 5.5). Different material regions of the austenitic weld are shown in Fig. 5.5. Inhomogeneous austenitic weld structure and its layered representation are shown in the Fig. 5.6 (a) and Fig. 5.6 (b) respectively.

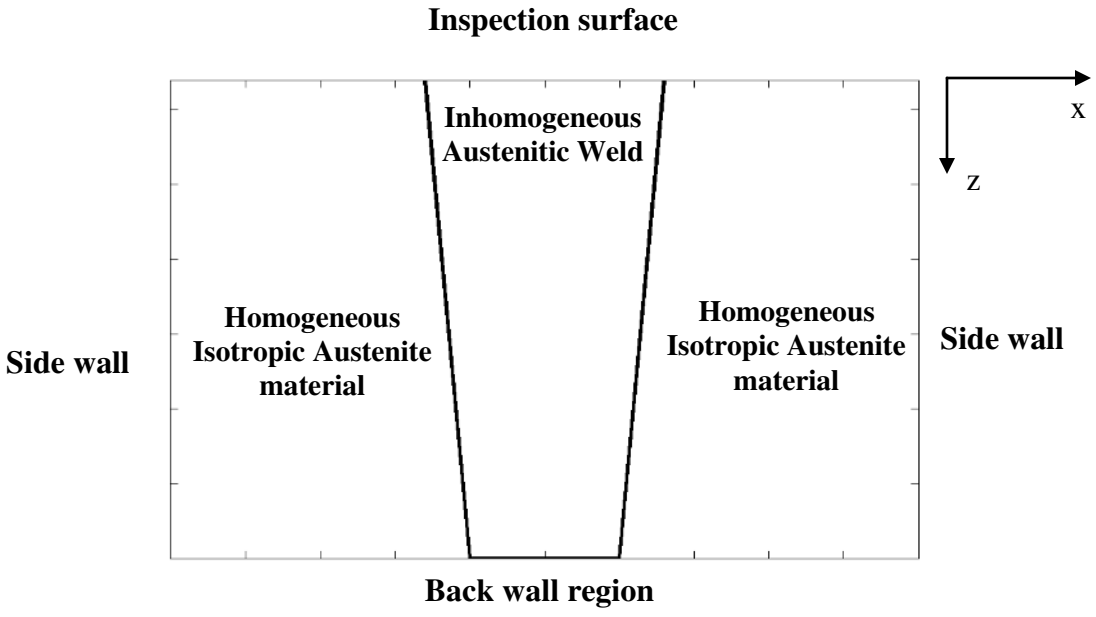

Figure 5.5: *Different material regions in the inhomogeneous austenitic weld material.*

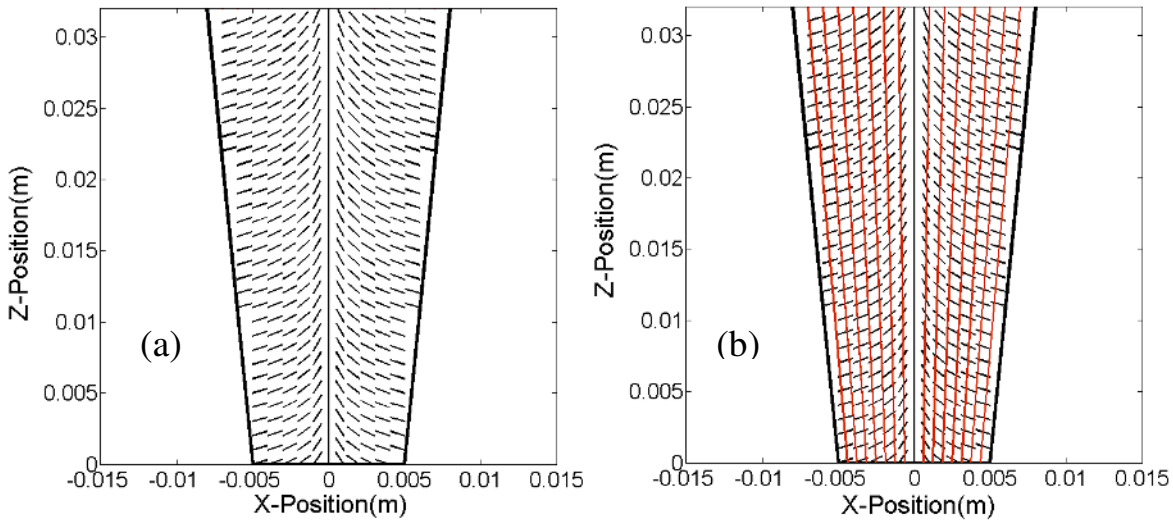

Figure 5.6: *(a) Inhomogeneous weld structure, (b) layered representation of inhomogeneous weld. Weld boundary inclination angles* $\alpha_1 = \alpha_2 = 5.36^o$. $T_1 = -T_2 = -0.54$, $D_1 = D_2 = 5$ *mm and* $\eta = 1$ *in Eq. (5.1).*

5.3 Ray Tracing Model for Point Sources

An illustration of the ray tracing model for point sources is shown in Fig. 5.7. A 30º longitudinal wave (P) with beam divergence of 60º is used in the ray tracing calculation. A step size of 0.05 mm is considered for discretizing the austenitic weld structure. The weld geometry is discretized into 321 steps along the x-direction and 641 steps along the z-direction. A smaller step size in discretization can improve the accuracy of the ray tracing calculations. However, a smaller step size usually leads to increase in computation time. Table 3 summarizes the ray tracing calculation time for different step sizes. The developed ray tracing algorithm in this thesis is able to calculate the ray energy paths and amplitudes in less than 78 seconds for the discretization step size of 0.05 mm on a Dell Optiplex 780 Core 2 Duo 2.8 GHz/2.94 GB PC. The ray tracing calculation times for other ultrasonic wave types namely shear vertical (SV) and shear horizontal (SH) waves are approximately less than a minute. The minimum ray tracing calculation time is observed for the shear horizontal wave because this wave type always decouple from other ultrasonic wave types P and SV waves, which results in less mathematical intricacies involved in solving reflection and transmission problems.

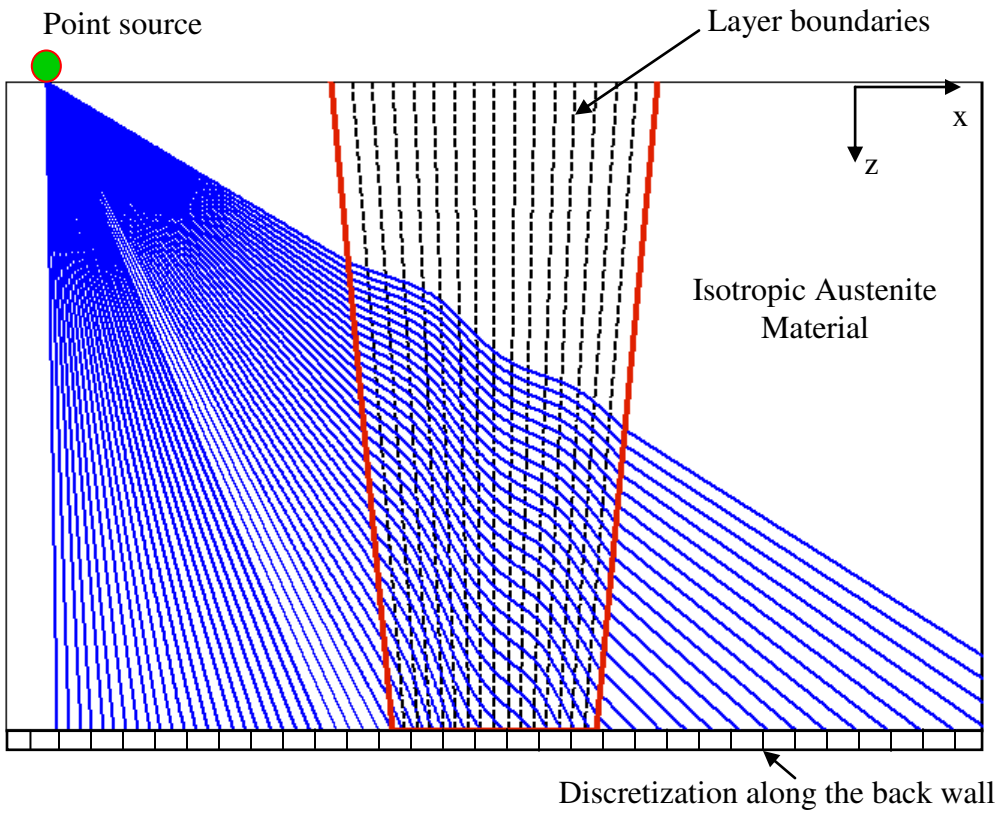

Figure 5.7: *Illustration of the ray tracing model for point source excitation in an austenitic weld material. Weld thickness = 32 mm.*

Table 3: *Ray tracing calculation time for different discretization step sizes.*

Number of rays	Incident ultrasonic wave type	Discretization step size (mm)	Computation time (seconds)
60	Longitudinal wave	0.05	78
		0.1	38
		0.2	21

The principal steps involved in evaluating ultrasonic ray energy paths and amplitude profiles for point source excitation on inhomogeneous layered anisotropic material using ray tracing algorithm are described as follows:

Step 1:

A diverged ray bundle is originated from the point source and it is allowed to propagate from isotropic base material into the inhomogeneous layered anisotropic material (see Fig. 5.7).

Step 2:

The excitation process may be a normal beam or an angle beam excitation. Depending on the nature of the excitation, the directivity factor of the ray in an isotropic solid or general anisotropic solid is calculated based on Lamb's reciprocity theorem [61, 111, 131]. The procedure is explained in the chapter 4.

Step 3:

Stepping forward along the ray in the direction of Poynting vector (i.e. energy velocity direction), the ray's new position is calculated. And check that no region change has occurred.

Step 4:

If the ray reaches the weld flank, then the incident ray slowness vector components are transformed from global coordinate system into the local coordinate system using the Bond matrix method [69]. The tangential components of slowness vectors in both the media are equal and contained in the same plane of incidence. Then the components of slowness vectors normal to the boundary are evaluated by solving the six degree polynomial equation resulted from modified Christoffel equation [120]. The general procedure for evaluating reflection and transmission behaviour of a ray at an interface between two dissimilar materials is discussed in chapter 3. The transmitted ray energy direction, coefficients and directivity factor is evaluated.

Step 5:

Increase the step size from current ray position along its ray energy direction and obtain the new ray position. Then the associated material properties such as columnar grain orientation and elastic properties of the new ray position are read out. A virtual grain boundary is assumed at the interface between two adjacent columnar grains in the weld metal. We assumed the virtual grain boundary is oriented parallel to the lines of constant crystal orientation. Repeat the step 4 and obtain the unknown normal components of slowness vectors in the transmitted medium. Previous ray amplitudes are multiplied by the present ray transmission coefficients and directivity factors.

Step 6:

Return to the step 3 and the iteration is continued till the ray leaves the inhomogeneous weld specimen. The modified ray amplitudes are multiplied by the inverse distance factor. The above procedure is repeated for each ray in the ray bundle and ray amplitudes are stored along the observation region.

Step 7:

The receiving surface is discretized into several cells and dimension of the cell is taken similar to the dimension of the receiving transducer used for the experiments. At the end, the final ray amplitudes at the region of interest in the material are expressed in terms of density of rays and their amplitudes.

Step 8:

Finally the stored ray energy directions are plotted to visualize the ray energy paths and amplitudes and quantitative analysis of ultrasonic field profiles in inhomogeneous anisotropic materials.

5.3.1 Ray Energy Paths for Point Source Excitation

The following possible interfaces can generally occur when a ray propagates in an inhomogeneous austenitic weld material:

a. interface between fine grained isotropic austenite material and columnar grained transversal isotropic austenitic weld material,
b. interface between two adjacent transversal isotropic austenitic columnar grained materials,
c. interface between columnar grained austenitic weld material and fine grained isotropic austenite material.

The plane wave theory for evaluating reflected and transmitted energy directions at an interface of two dissimilar weld materials are presented in Chapter 3. As an illustration, Fig. 5.8(a) shows 3D ray energy pattern for the 45º longitudinal cone of rays propagating into the inhomogeneous austenitic weld material with spatially varying crystal orientations. Fig. 5.8(b) shows the ray energy pattern in the XY-plane (top view). The assumed layback orientation in the austenitic weld material is 10°. A 5° step size is considered along the azimuthal direction. The grain structure used in the numerical calculations is shown in Fig. 5.6. The base material is fine grained austenitic steel material which exhibits isotropic behaviour. For the presented numerical results, the elastic properties for the isotropic austenite material are taken same as that of isotropic ferritic steel material. The material elastic constants for the austenite base and weld materials are presented in Table 1.

As expected, the curved energy ray paths result in the weld region. The beam path distortion can be observed from Fig. 5.8. Depending on the layback orientation, the bending of ray energy paths in the austenitic weld material varies. Generally three dimensional problem of ultrasonic wave propagation in inhomogeneous anisotropic materials requires large computational time and it is convenient to represent the 3D problem into 2D problem without loss of generality. In case of inhomogeneous austenitic

weld materials, the grain orientation along the weld run direction (i.e. layback orientation) is constant and it is possible to consider a slice of the 3D geometry for the better visualization and understanding of ultrasound propagation in an inhomogeneous austenitic weld material.

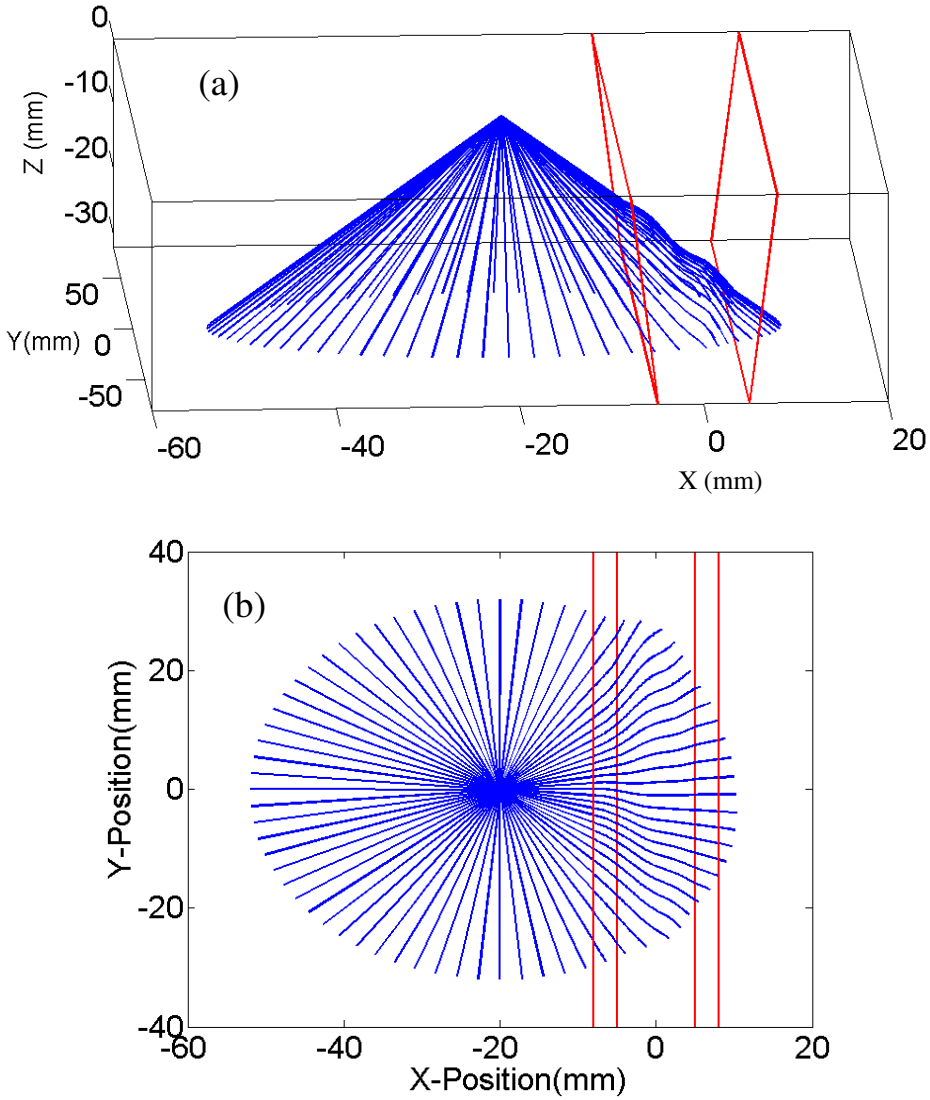

Figure 5.8: *45º longitudinal cone of rays propagate into the inhomogeneous transverse isotropic austenitic weld material (a) 3D view of the ray pattern, (b) ray pattern in the XY plane. Weld thickness = 32 mm.* $\alpha_1 = \alpha_2 = 5.36º$, $T_1 = -T_2 = -0.54$, $D_1 = D_2 = 5$ *mm and* $\eta = 1$ *in Eq. (5.1).The layback orientation along the weld run direction is 10°.*

5.3.2 Ray Incidence from Homogeneous Base Material

Fig. 5.9 shows a 45º diverged longitudinal ray source excitation on homogeneous isotropic austenite material into the region of inhomogeneous austenitic weld material. By assuming no layback orientation and azimuthal angle, the three dimensional ray tracing problem reduces into the two dimensional problem. A beam divergence of 30º is considered for the illustration. In the ray tracing simulation a 45º longitudinal wave probe is positioned 24 mm away from the weld centreline. Fig. 5.9 shows a 45º ray energy paths for three wave modes which exist in a general inhomogeneous austenitic weld material.

It can be seen from Fig. 5.9, that the transmitted ultrasound energy paths for the three wave modes are influenced by the inhomogenity of the austenitic weld material. It is obvious from Fig. 5.9(b), as expected, that the shear vertical wave (SV) ray paths shows rapid changes in the ray direction as they propagate through the weld material. The strong focussing and bending effects are observed for shear vertical waves (see Fig. 5.9(b)). As stated in Chapter 2, these strong focussing effects for the shear vertical waves are appeared due to complex slowness surface of these particular waves. In contrast to SV waves, the longitudinal (P) and shear horizontal wave (SH) energy ray paths are less affected by the anisotropy of the austenitic weld material (see Fig. 5.9).

In case of shear horizontal wave energy paths beyond an incident angle of 55º, we observed that the SH wave is not capable of propagating fully through the weld material (see Fig. 5.9(c)). Because the transmitted SH wave energy direction is parallel to the interface (i.e. so called critical angle). In the ray tracing simulation, we defined a boundary condition, which states that the ray tracing is terminated once the critical angle for the transmitted ray is reached. Otherwise, it leads to the erroneous ray paths which do not have any physical significance. In general, evanescent rays (i.e. critically refracted rays) do not carry any energy but their amplitude decay with increasing distance. A detailed description on evanescent rays will be discussed in later sections.

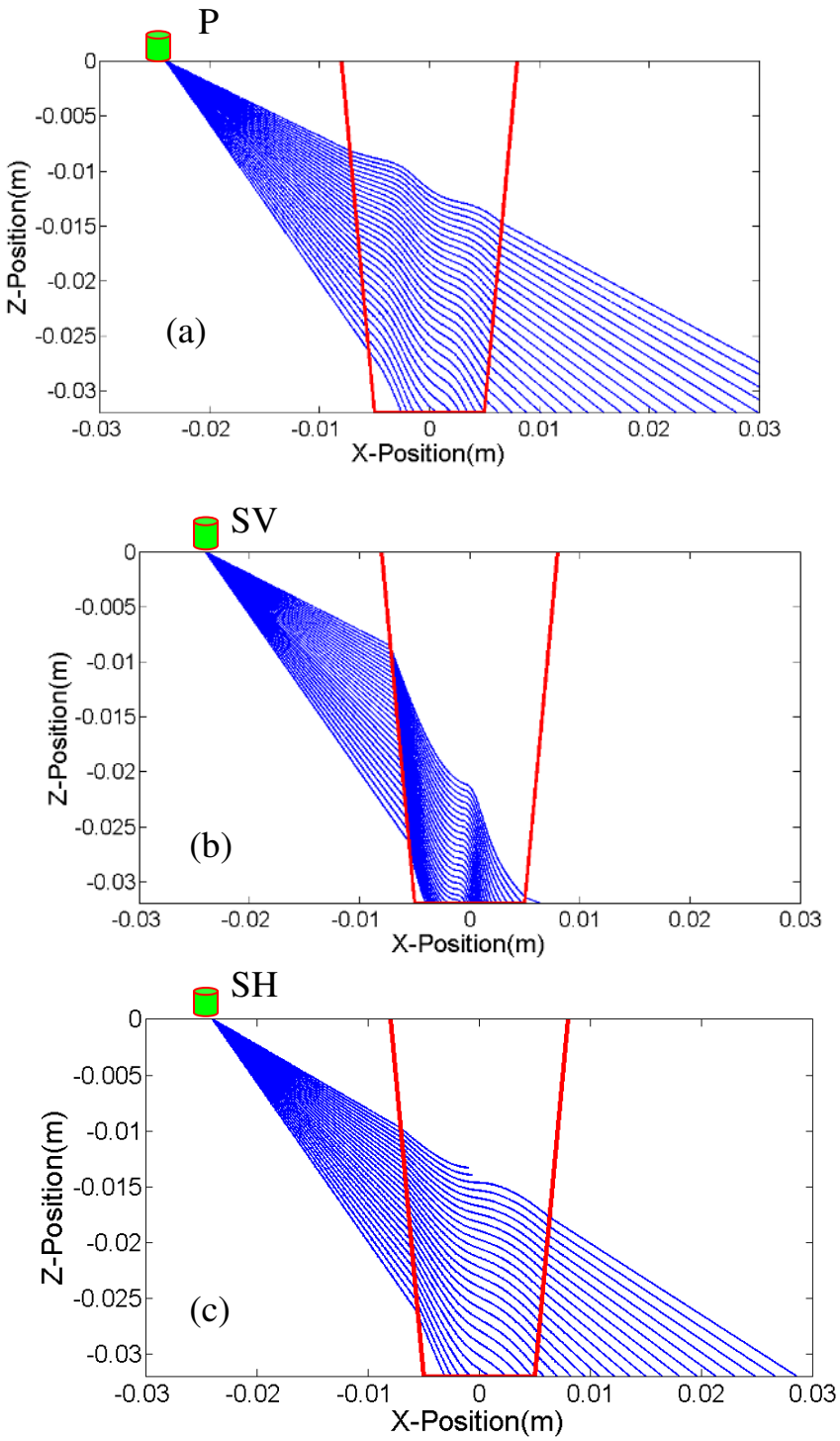

Figure 5.9: *A 45º ultrasonic beam propagation in the inhomogeneous austenitic weld material. (a) Longitudinal waves (P), (b) shear vertical waves (SV) and (c) shear horizontal waves (SH). Weld thickness = 32 mm.* $\alpha_1 = \alpha_2 = 5.36º$, $T_1 = -T_2 = -0.54$, $D_1 = D_2 = 5$ *mm and* $\eta = 1$ *in Eq. (5.1). Layback orientation along the weld run direction is 0°.*

5.3.3 Ray Incidence from Inhomogeneous Weld Material

Fig. 5.10 shows the longitudinal normal beam excitation on a free surface of an inhomogeneous austenitic weld material. The source is situated exactly on the weld centre line. A divergence of 100º is considered for the numerical calculation. The divergence of the rays increases (decreases) by 2° steps with respect to the central ray direction. It can be seen from Fig. 5.10 that the quasi longitudinal waves are not capable of propagating near to the weld centre line where the grain orientation varies rapidly. If the transmitted ray does not satisfy the Snells law, then the corresponding ray path is terminated. Otherwise sharp variations in the ray path will occur. As expected, Fig. 5.10 shows small weld coverage using normal beam excitation. The similar effects also occur for the quasi shear vertical wave incidence. The beam distortion and beam spreading in the weld region depends on the weld parameters such as slope of the columnar grain axis at the weld fusion faces and change of the grain orientation as a function of the distance x from the weld centre line. It can be concluded that, for the ultrasonic inspection of V-butt austenitic weld and base material interfaces, angle beam excitation is more suitable as compared to the normal beam excitation.

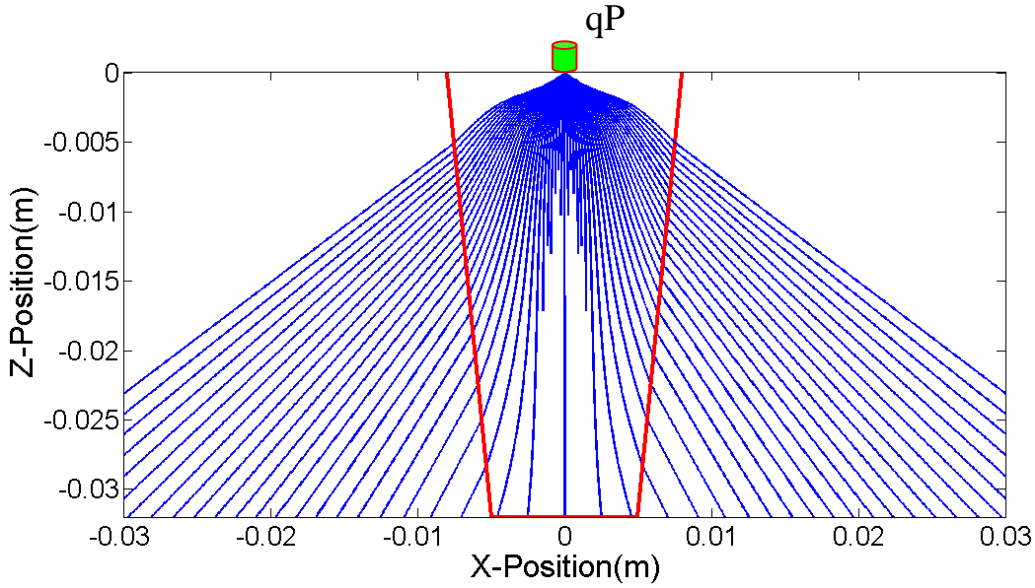

Figure 5.10: *A 0º quasi longitudinal (qP) ultrasonic beam propagation in the inhomogeneous austenitic weld material. Weld thickness = 32 mm.* $\alpha_1 = \alpha_2 = 5.36º$, $T_1 = -T_2 = -0.54$, $D_1 = D_2 = 5$ *mm and* $\eta = 1$ *in Eq. (5.1). Layback orientation along the weld run direction is 0°.*

5.3.4 Back wall Reflected Rays from Homogeneous Base Material and Inhomogeneous Weld Material

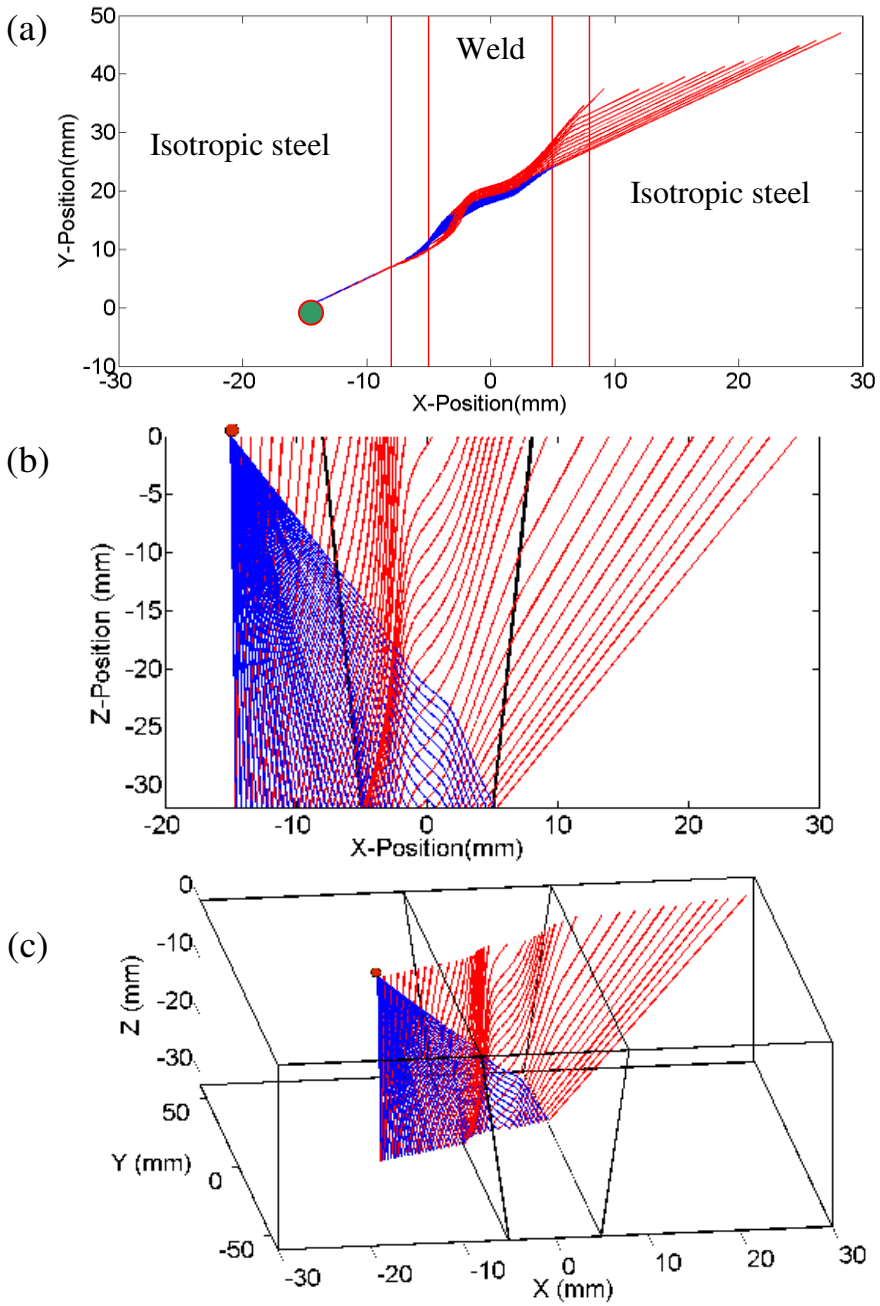

Figure 5.11: *A diverged longitudinal beam energy reflection behaviour in the inhomogeneous transversal isotropic austenitic weld material (a) top view (XY-plane) of the ray pattern, (b) ray pattern in the XZ-plane and (c) 3D ray energy pattern. Weld thickness = 32 mm.* $\alpha_1 = \alpha_2 = 5.36^{o}$, $T_1 = -T_2 = -0.54$, $D_1 = D_2 = 5$ *mm and* $\eta = 1$ *in Eq. (5.1). The layback orientation along the weld run direction is 10°. The range of incidence angles are in between 1° and 45º with 1° step size and assumed 45° azimuthal angle.*

The reflection behaviour of the ray in an isotropic steel material can be easily calculated based on the fundamental Snell's law whereas in case of inhomogeneous anisotropic material the reflection behaviour of the ray becomes more complicated, as explained in Chapter 3. The reflection behaviour of the ray at the free surface boundary of an anisotropic material is presented in chapter 4. As an illustration, Fig. 5.11 shows energy ray paths for the reflected longitudinal waves (isotropic medium) and quasi longitudinal waves (anisotropic medium) when a diverged longitudinal ray source is excited on isotropic austenite material. It is clear from Fig. 5.11 that the reflected longitudinal rays from back wall are significantly influenced by the anisotropy of the weld material and it results curved reflected energy paths.

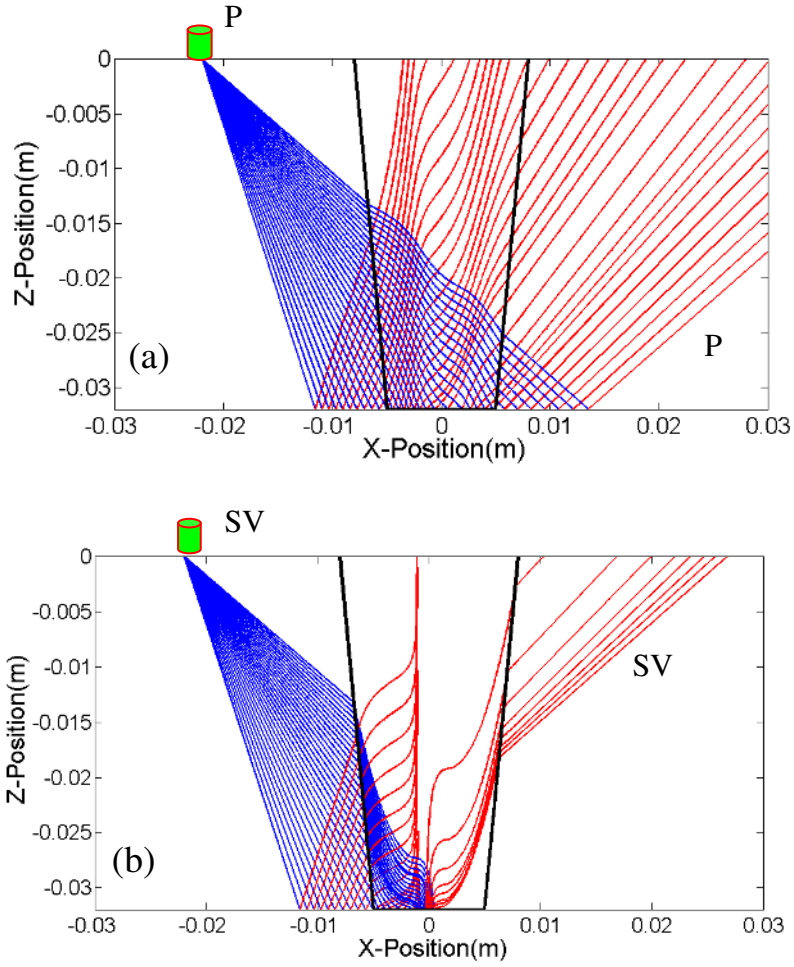

Figure 5.12: *Back wall reflected ray pattern for the 45° ultrasonic beam propagation in the inhomogeneous austenitic weld material. (a) Longitudinal, (b) shear vertical waves. Weld thickness = 32 mm.* $\alpha_1 = \alpha_2 = 5.36°$, $T_1 = -T_2 = -0.54$, $D_1 = D_2 = 5$ *mm and* $\eta = 1$ *in Eq. (5.1). The layback orientation in the weld material is 0°.*

The 2D reflected energy paths for the incident longitudinal and shear vertical waves are shown in Fig. 5.12. It can be seen from Figure 5.12, that the reflected SV waves exhibits a strong channelling effect and large beam skewing effects in the inhomogeneous weld region.

5.3.5 Back wall Mode Converted Reflected Rays from the Homogeneous Base Material and Inhomogeneous Weld Material

The procedure for calculating mode converted reflected ray paths in an austenitic weld material is similar to that described in section 5.3.4 and only the mode converted reflected ray is traced instead of tracing same reflected wave mode. The grain structure used for the ray tracing calculation is shown in Fig. 5.13(a). The layered representation of the inhomogeneous weld structure is depicted as dashed lines in Fig. 5.13(b). These layers represent the lines of constant crystal orientations and act as a virtual boundary between two austenitic weld metals with different crystal orientations. The resulted layered structure is derived from an empirical model, as explained in section 5.2. As an illustration only a few virtual boundaries are shown in Fig 5.13 (b) but in real ray tracing calculation we consider the virtual boundary if the adjacent cells exhibit different material properties.

The 2D energy ray paths for the mode converted reflected waves, when a 45º diverged longitudinal and shear vertical waves propagate into the inhomogeneous austenitic weld material, are shown in Fig. 5.13(c) and (d). A 30º beam divergence is considered for the ray tracing calculations. The ultrasonic transducer is situated 22 mm away from the weld centreline. It can be seen from Fig. 5.13(c) that the mode converted shear vertical waves are not capable of propagating at the weld flank as well as within the weld material and most of the reflected rays are evanescent. Whereas from Fig. 5.13(b), the mode converted longitudinal waves are capable of propagating at weld flank as well as in the weld region. From these observations, one can neglect the mode conversion effects, especially for the incident longitudinal wave, during the ultrasonic reflected beam field modelling as well as defect characterization in inhomogeneous weld materials.

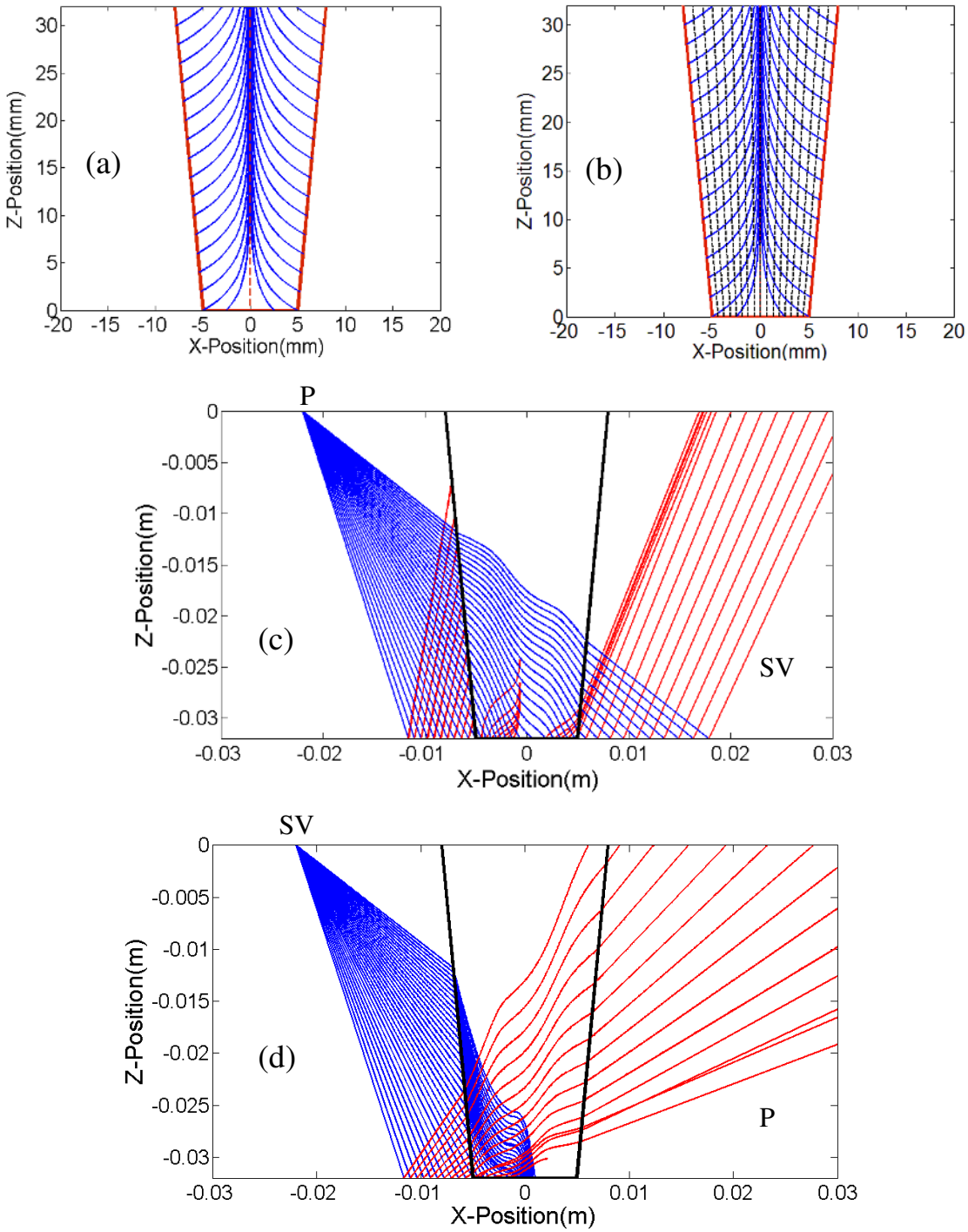

Figure 5.13: *(a) Inhomogeneous weld structure of the austenitic weld, (b) layered representation of the weld structure. Back wall mode converted reflected ray pattern for the 45° ultrasonic beam propagation in the inhomogeneous austenitic weld material. Incident (c) longitudinal, (d) shear vertical waves. Weld thickness = 32 mm.* $\alpha_1 = \alpha_2 =$ *5.36°,* $T_1 = -T_2 = -0.54$, $D_1 = D_2 = 5$ *mm and* $\eta = 1$ *in Eq. (5.1). Layback orientation in the weld material is 0°.*

When an acoustic wave propagates through an austenitic weld material, it is attenuated by scattering at the grain boundaries. The level of scattering at the grain boundaries depends on grain parameters such as size, shape, orientation and anisotropy of the grains [132-137]. In addition to the grain parameters, the scattering of ultrasound at the grain boundaries is also dependent on frequency of the ultrasonic transducer [138, 139]. Ernst et al. [140] measured the attenuation coefficients of the quasi longitudinal waves in columnar grained austenitic steel material and they found that attenuation coefficient increases with increasing frequency and propagation direction. The scattering coefficients at the grain boundaries are not included in the developed ray tracing method in this thesis work. Because the geometric features of the grains such as grain size and shape are not included in the ray tracing model. Instead, the weld geometry is assumed as inhomogeneous and anisotropic. The energy loss, mode conversion and phase changes due to the ray refraction at the grain boundaries are included in our ray tracing model. Additionally the directivity factor of the ray and finite dimension transducer effects such as interference phenomenon are successfully implemented.

The effect of inhomogeneous grain structure of the austenitic weld on mode converted reflected rays are shown in Fig. 5.14. In the presented analysis, the values of T_1 and T_2 in the mathematical empirical relation for modelling columnar grain orientation as described in section 5.2 are considered as 1. The resulted grain structure and its layered representation are shown in Fig. 5.14(a) and (b). It is clear from Fig. 5.14(a), increasing T_1 and T_2 values result fast changes in the crystal orientations within the weld material. It can be seen from Fig. 5.14(c), the mode converted reflected shear vertical waves are capable of propagating at the weld flank and show a significant channelling effect in the weld region. By increasing T_1 and T_2 values from 0.54 to 1, the reflection behaviour of the mode converted longitudinal waves are less influenced (see Fig. 5.14(d)) whereas the mode converted shear vertical waves show significant variation in the energy ray pattern. From the numerical calculations, it is observed that the small variation in the weld structure leads to the significant changes in the shear vertical wave energy ray pattern.

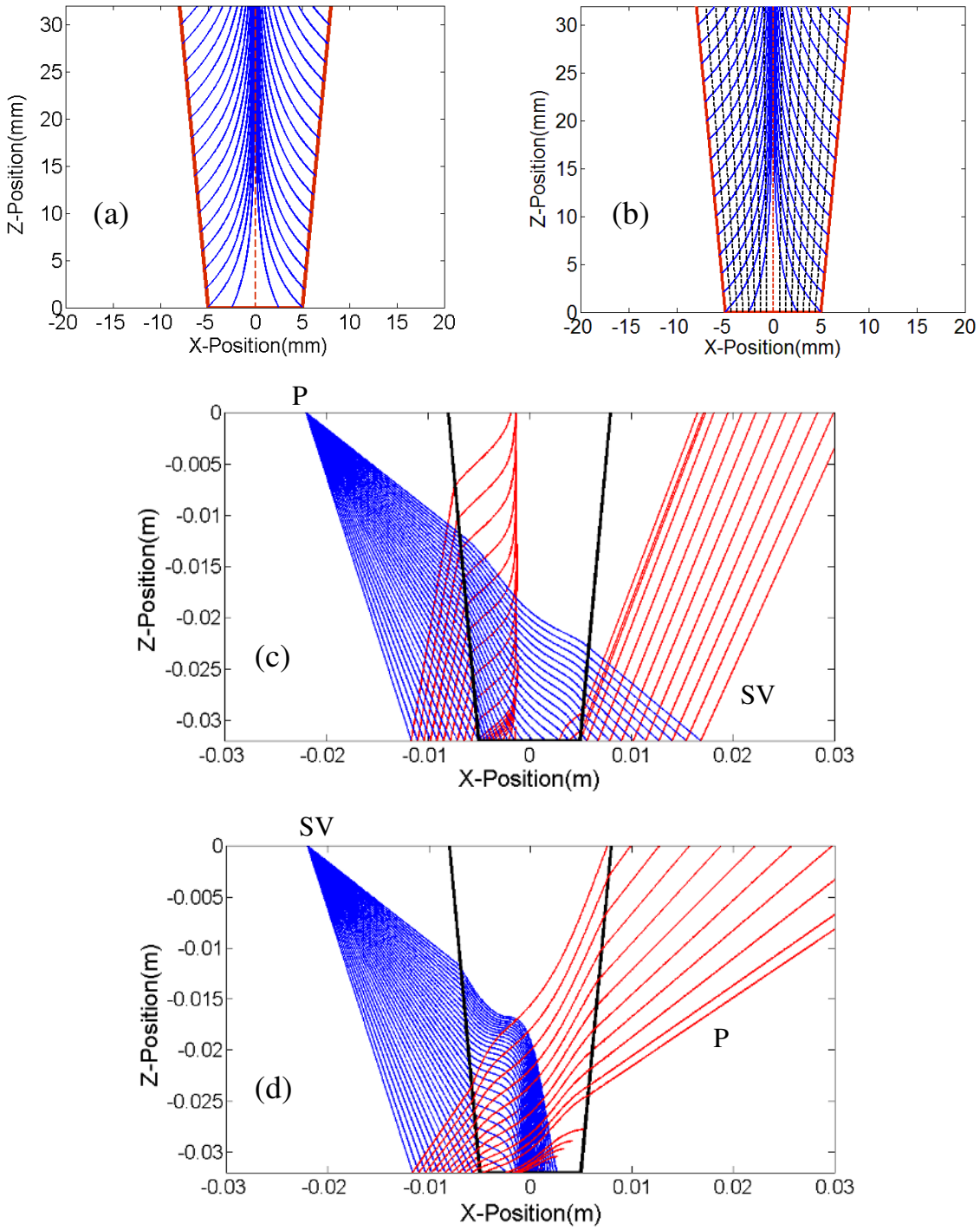

Figure 5.14: *(a) Inhomogeneous weld structure of the austenitic weld, (b) layered representation of the weld structure. Back wall mode converted reflected ray energy paths for the 45º ultrasonic beam propagation in the inhomogeneous austenitic weld material. Incident (c) longitudinal, (d) shear vertical waves. Weld thickness= 32 mm.* $\alpha_1 = \alpha_2 = 5.36º$, $T_1 = -T_2 = 1$, $D_1 = D_2 = 5$ *mm and* $\eta = 1$ *in Eq. (5.1). Layback orientation in the weld material is 0°.*

5.3.6 Ray Tracing of Mode Converted Rays at Weld Boundaries

The mode converted rays at the weld flank are solved and implemented in the ray tracing algorithm. The mode converted transmitted shear vertical wave at the weld flank shows a strong focussing effect in the weld centre region (see Fig. 5.15(a)). Whereas the mode converted transmitted longitudinal waves are incapable of propagating at the weld flank and most of the transmitted longitudinal waves are evanescent (see Fig. 5.15(b)). For the modelling of ray amplitudes generated by point sources and distributed sources in inhomogeneous anisotropic weld material, the mode conversion effects at the weld flank can be neglected.

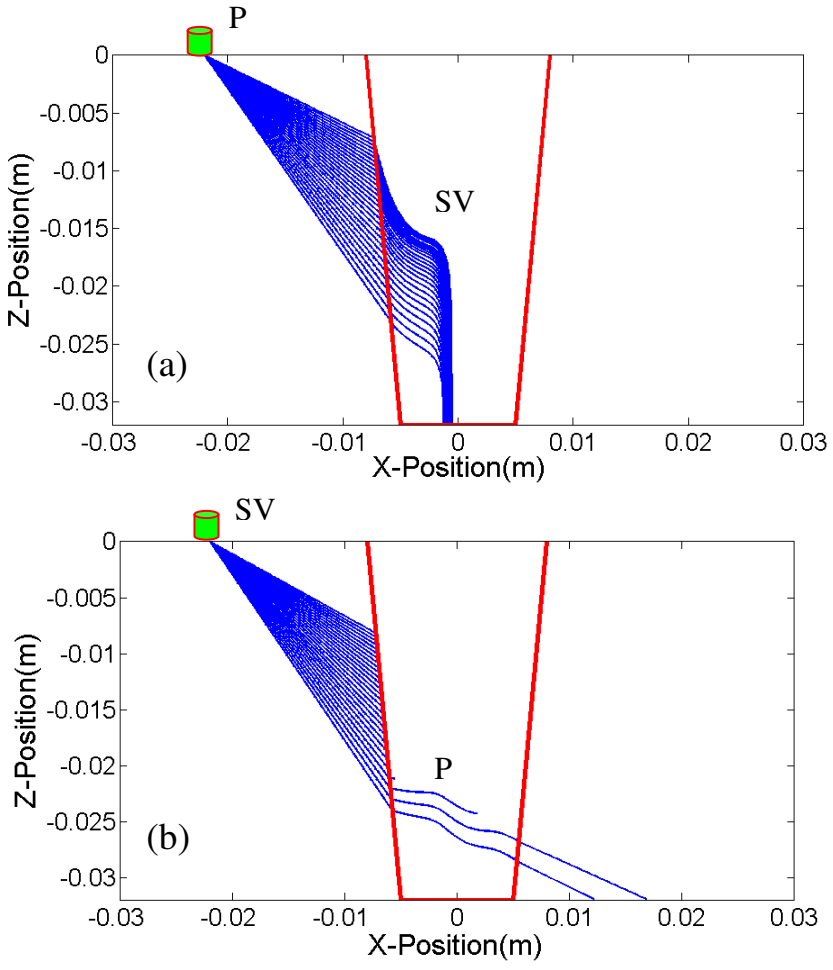

Figure 5.15: *Mode converted rays at the weld flank when a 45º ultrasonic beam propagates in the inhomogeneous austenitic weld material. Incident (a) longitudinal, (b) shear vertical waves. Weld thickness = 32 mm.* $\alpha_1 = \alpha_2 = 5.36º$, $T_1 = -T_2 = -0.54$, $D_1 = D_2 = 5$ *mm and* $\eta = 1$ *in Eq. (5.1).*

5.4 Ray Tracing Model for Distributed Sources

An illustration of the ray tracing model for distributed sources is shown in Fig. 5.16. A longitudinal wave (P) array transducer with 15 elements is used in the ray tracing calculation. Each element in the transducer is represented by a point source. The considered spacing between point sources is 1 mm. Therefore, the total length of the transducer is 15 mm. A beam divergence of 100º (i.e. between -50º and 50º with 10º step size) is used at each point source in the transducer. A step size of 0.1 mm is considered for discretizing the austenitic weld structure. The weld structure is depicted in Fig. 5.6. The weld geometry is discretized into 161 steps along the x-direction and 321 steps along the z-direction. The curved energy ray paths can be seen in Fig 5.16. As expected, the channeling effects at the right and left weld flanks can be observed in Fig. 5.16. Table 4 summarizes the ray tracing calculation time for different step sizes. The developed ray tracing algorithm for simulating distributed sources (so called array transducer) in this thesis is able to calculate the ray energy paths and amplitudes in less than 2 minutes for the discretization step size of 0.1 mm on a Dell Optiplex 780 Core 2 Duo 2.8 GHz/2.94-GB PC.

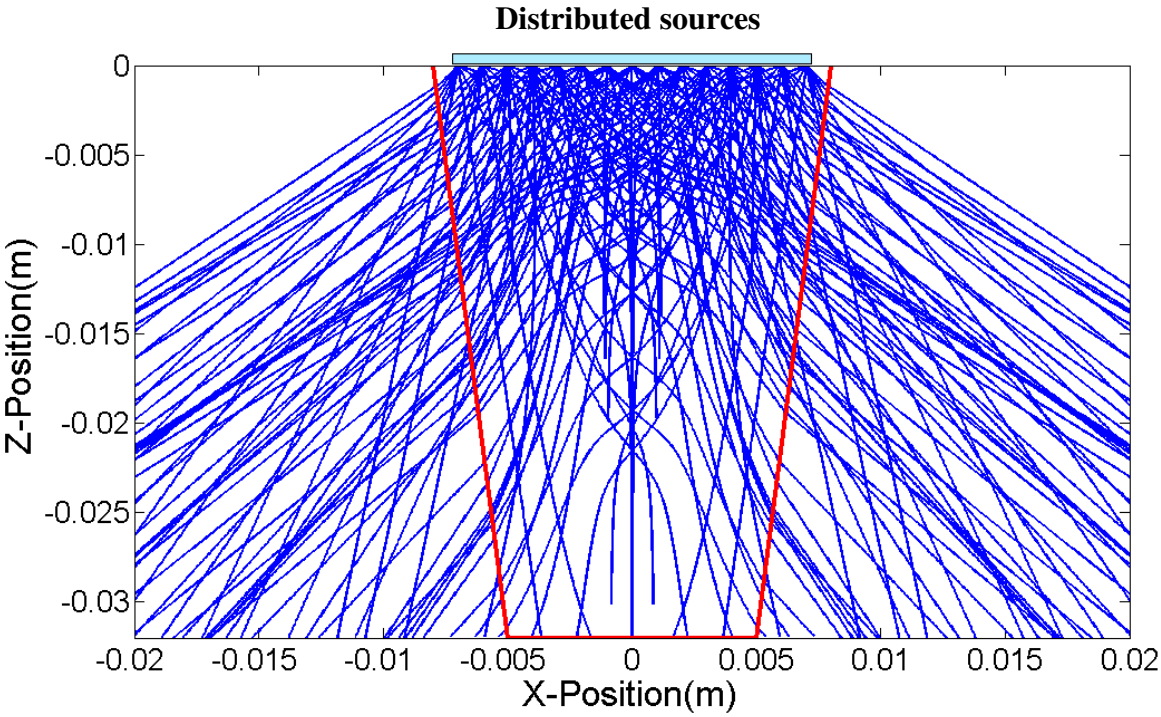

Figure 5.16: *Illustration of the ray tracing model for distributed sources.*

Table 4: *An array based ray tracing calculation time for different discretization step sizes.*

Number of point sources	Ray density at each point source	Incident ultrasonic wave type	Discretization step size (mm)	Computation time (minutes)
15	11	Longitudinal wave	0.05	3.76
			0.1	1.85
			0.2	0.96

The principal stages involved in evaluating ultrasonic ray amplitude profiles for distributed sources (finite dimension transducer) excitation on an inhomogeneous layered anisotropic material using ray tracing algorithm are described as follows:

- The finite aperture ultrasonic transducer is represented as several point sources. From each point source in the finite aperture transducer a diverged ultrasonic ray bundle is considered and allowed to propagate into the spatially varying inhomogeneous columnar grain structure of the austenitic weld material

- Stepping forward along the ray in the direction of Poynting vector (i.e. energy velocity direction), the ray's new position is calculated. And check that no region change has occurred. The steps 4 to 7 in section 5.3 are repeated.

- The final ultrasonic ray amplitudes along the observation region are obtained by employing proper inverse distance factors, phase relations and density of rays and their amplitudes.

- The constructive and destructive interferences are achieved by superposition of ray contributions from each source point over the observation line.

- The stored ray energy paths and amplitudes are plotted and the effect of inhomogenity, anisotropy on the ultrasonic field profile is analyzed.

If the transmitted ray does not satisfy the Snell's law, then the ray tracing algorithm terminates the ray. Such a ray is defined as evanescent ray and its amplitude decay in the direction perpendicular to the energy propagation, as stated in Chapter 3.

Fig. 5.17 illustrates the ray energy pattern for the 34º longitudinal wave angle beam transducer of 2.25 MHz central frequency in an inhomogeneous weld material. The transducer beam exit point is situated at 14 mm away from the weld centre line as shown in Fig. 5.16. The transducer active length is 12 mm and it is divided into several point sources. The distance between point sources is 1 mm. At each point source a diverged ray bundle is considered. The columnar grain structure used for the numerical simulation is shown in Fig. 5.6. The elastic constants for the weld material are the same ones to the elastic constants of X6 Cr Ni 18 11 material and assumed base material properties same as fine grained isotropic steel material which are presented in Table 1. It can be seen from Fig. 5.16 that the ray density is not uniform over the back wall of the weld component.

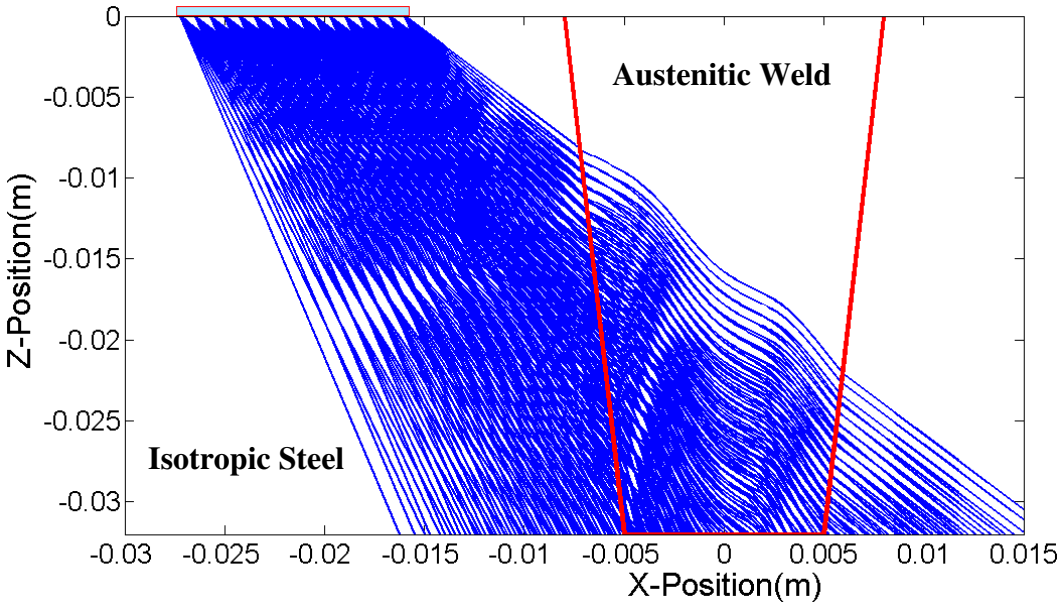

Figure 5.17: *Ultrasonic ray pattern for the 34º longitudinal beam propagation in the inhomogeneous austenitic weld material. Transducer center frequency 2.25 MHz and length 12 mm. The element to element distance is 0.75 mm.*

Influence of transducer discretization on near field length:

Near field of a piezoelectric transducer is defined as the region in which significant variations in the ultrasound intensity occur. This is due to the constructive and destructive interference of ultrasonic waves which originate from the ultrasonic transducer surface [27, 141, 142, 143]. Consequently, the flaw detection using ultrasonic technique in the near field region is limited. The length of the near field depends on the diameter of the transducer and wavelength of the ultrasonic wave. The length of the near field can be expressed as

$$N = \frac{D^2}{4\lambda} = \frac{D^2 f}{4v} \ , \tag{5.2}$$

where D is the diameter of the transducer, λ is the wavelength of the ultrasonic wave, v is the velocity of ultrasound in the medium and f is the transducer frequency.

For the considered transducer parameters in Fig 5.17, the near field effects are limited to a distance of about 13.7 mm. The novelty of the presented ray tracing model for distributed sources is that the ray amplitudes and phase information are incorporated and employed the superposition phenomenon which takes into account the interference effects. Consequently, the ray tracing model simulates the near field effects too. By representing the finite dimension transducer into several point sources and taking into account the interference effects in the near field region, the source can be placed close to the welded region. The presented ray tracing model is valid for both near field as well as far-field region of the source/receiver.

5.5 Ray Tracing Model for Transversal Cracks in Inhomogeneous Anisotropic Austenitic Welds

Figure 5.18 shows the specular reflection behaviour of longitudinal rays from the transversal crack in an inhomogeneous austenitic weld material. The crack face is assumed as free surface and the problem of reflection at the free surface boundary is solved in order to trace the specularly reflected rays from the crack. The presented illustration is very important for transversal crack detection in austenitic weld materials. The location of the specularly reflected rays from the flaw can be predicted from the ray

tracing model and hence it is possible to optimize the receiver position in order to obtain the significant amplitudes from the transversal crack.

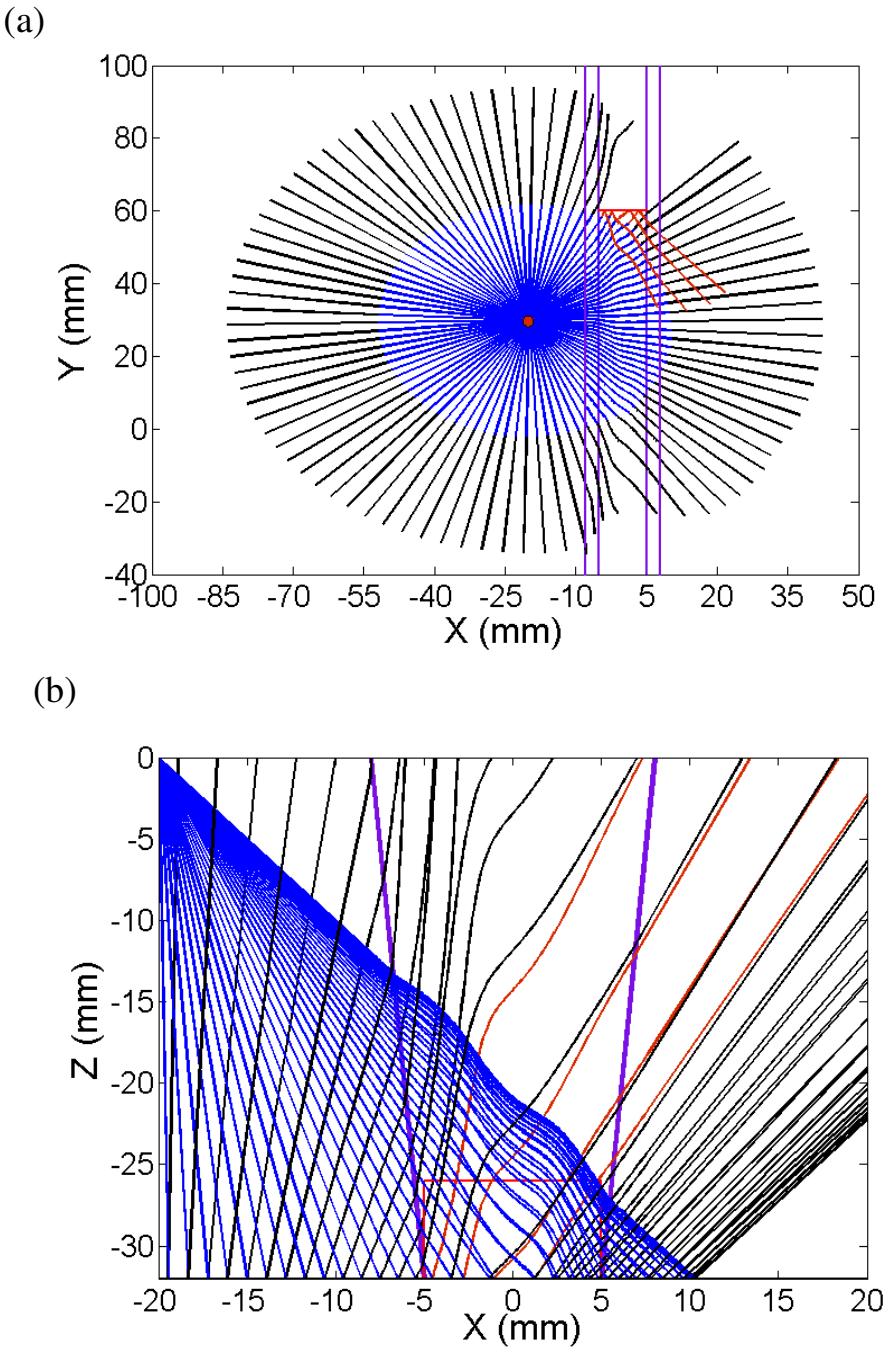

Figure 5.18: *Ultrasonic longitudinal ray pattern for incident 45° cone of rays in the inhomogeneous V-butt austenitic weld material with the presence of transversal crack. The transversal crack dimension is 10x1x6 mm^3. $\alpha_1 = \alpha_2 = 5.36°$, $T_1 = -T_2 = -0.54$, $D_1 = D_2 = 5$ mm and $\eta = 1$ in Eq. (5.1). Layback orientation in the weld material is 10°.*

5.6 Comparison of Ultrasonic Energy Ray Paths with Existed Results

In order to verify the validity of the presented ray tracing results in this thesis, we compared the ray paths qualitatively with the existed results [83, 86]. RAYTRAIM a commercially available 3D ray tracing software package developed by Ogilvy [77, 83] and it is used to understand the ultrasound propagation in an inhomogeneous austenitic weld material. This software package is primarily proposed for evaluation of ray paths, propagation times in inhomogeneous austenitic welds. Schmitz et al. [86] presented the 3D-ray-SAFT algorithm to calculate the direction of the ultrasound beam and deformation of the transmitted sound field in an austenitic weld material and discussed the qualitative comparison with experiments on unidirectional weld structure. The 3D-ray-SAFT algorithm does not evaluate the ray amplitude information. In comparison to existed ray tracing tools, the presented ray tracing method in this thesis is able to calculate not only ray paths and propagation times but also realistic ray amplitudes and it will be presented in the subsequent chapters. The elastic constants for the transversely isotropic austenitic steel 308 SS are taken from [23] and listed in Table 5.

Table 5: *Material properties for the transversely isotropic austenitic steel 308SS.* ρ*[kg/m*^{3}*],* C_{ij}*[GPa].*

Material parameter	Austenitic steel (308SS)
ρ	7900
C_{11}	263
C_{12}	98
C_{13}	145
C_{33}	216
C_{44}	129
C_{66}	82.5

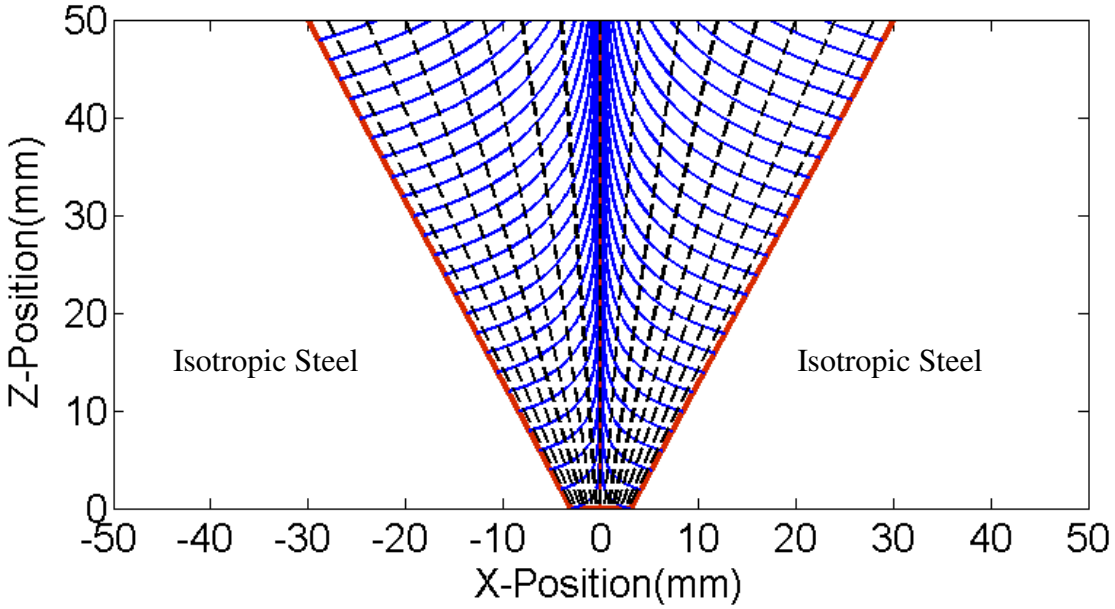

Figure 5.19: *Inhomogeneous weld structure of the V-butt austenitic weld material (dashed black lines: virtual layer boundaries). Weld thickness = 50 mm.* $D_1 = D_2 = 3$ *mm,* $\alpha_1 = \alpha_2 = 28.36^o$. $T_1 = -T_2 = -0.54$ *and* $\eta = 1$ *in Eq. (5.1).*

The elastic constants for the isotropic base material are assumed same ones to the elastic constants of ferritic steel which are given in Table 1. The weld structure used for the comparison is shown in Fig. 5.19. The boundary between two adjacent crystal orientations is represented by lines of constant crystal orientation which are shown as dashed lines in Figure 5.19. A detailed description on ray tracing procedure is presented in Section 5.3. A discretization step size of 0.1 mm is considered for the ray tracing calculation. Figure 5.20 shows comparison of energy ray paths calculated using presented ray tracing algorithm in this thesis with the existed ray tracing results [83, 86]. A 45º longitudinal rays are scanned across a MMA (Manual Metal Arc) V-butt inhomogeneous austenitic weld material as shown in Fig. 5.20. The obtained ray paths show a good qualitative agreement with Ogilvy [83] and Schmitz [86] results. The channelling effects of the transmitted longitudinal rays in an austenitic weld material show good agreement with the existed results (see Fig. 5.20).

The minor differences in ray paths are resulted due to the different assumptions of grain boundary between two adjacent columnar grains in the weld material. Schmitz et al. [86] assumed the grain boundary between two adjacent grains in the weld material

perpendicular to the direction of ray group velocity, whereas Ogilvy [83] assumed parallel to the local directions of constant ray group velocity magnitude. In the presented ray tracing model, the grain boundary is assumed parallel to the lines of constant crystal orientation.

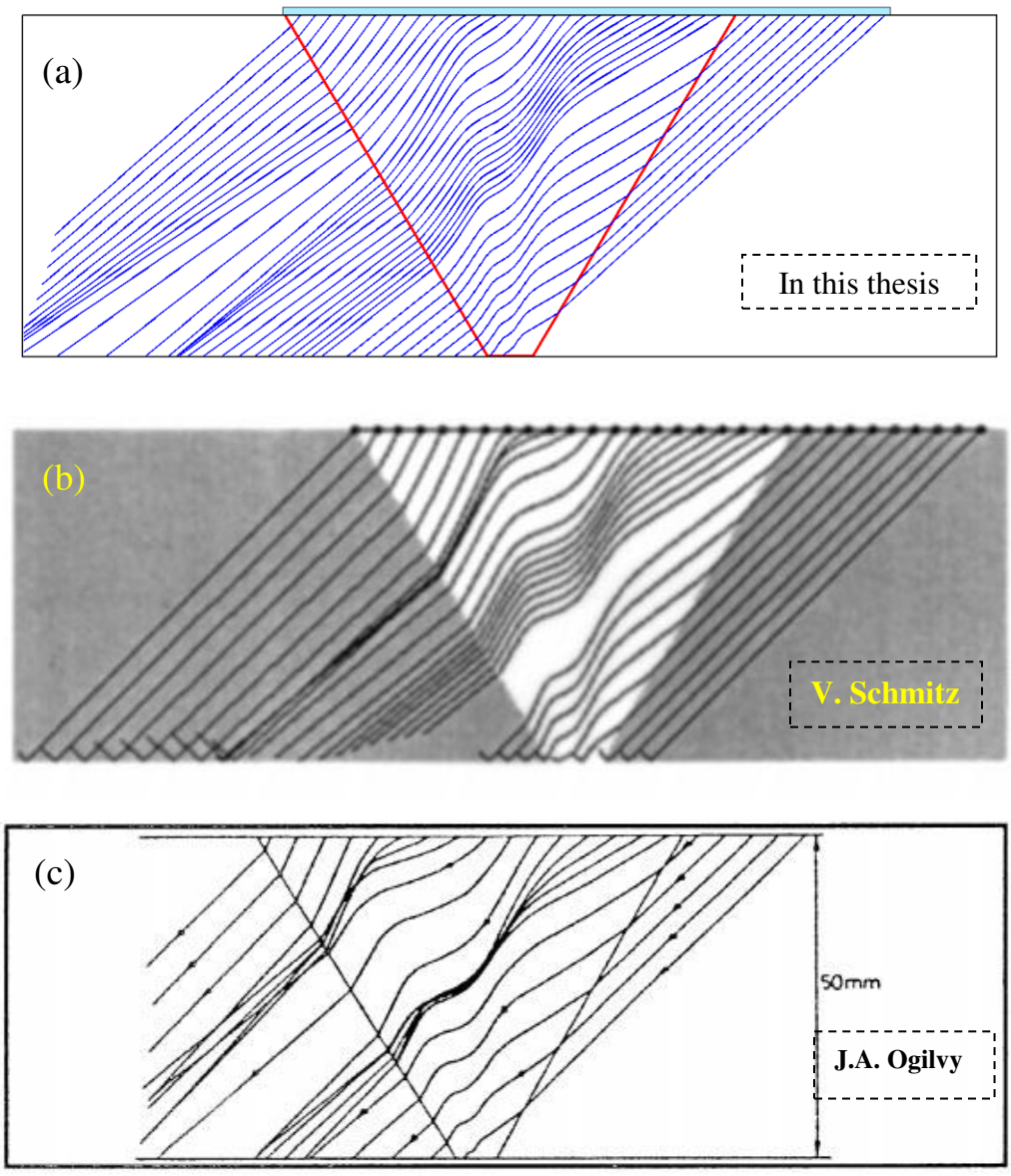

Figure 5.20: *Comparison of ultrasonic energy ray paths for 45º longitudinal line source in the inhomogeneous V-butt austenitic weld material. Ray tracing model (a) in this thesis, (b) by V. Schmitz et al. [86] and (c) by Ogilvy [83].*

Ray tracing procedure for evaluating ray energy paths and amplitudes for the point sources and distributed sources are presented in this chapter. The influence of inhomogeneous weld structure on energy ray paths for the three wave modes quasi longitudinal, quasi shear vertical and shear horizontal waves is discussed. The direct as well as mode converted reflected ray paths from the back wall of an austenitic weld material are traced. The specularly reflected rays from the transversal cracks in inhomogeneous austenitic welds are traced and important applications for the ultrasonic examination of transversal cracks are discussed. It is also observed that the mode converted rays are incapable of propagating at weld flanks as well as in the weld region and neglecting mode conversion effects in the ultrasonic beam field calculations is a good assumption. Qualitative comparison of calculated energy ray paths with the existed ray tracing results is presented and obtained good agreement. Quantitative comparison of ray tracing predictions with the Elastodynamic Finite Integration Technique (EFIT) results and experiments on real life austenitic welds are presented in the next chapters.

CHAPTER 6

Validation of Ray Tracing Model with 2D Elastodynamic Finite Integration Technique (EFIT)

6.1 Introduction

In this chapter, applications of the ray tracing model for the ultrasonic non- destructive evaluation and its validation using 2D Elastodynamic Finite Integration Technique (EFIT) model [45, 46, 47, 49] are discussed. The reason for selecting EFIT model to validate ray tracing model predictions is that EFIT has been successfully validated against experimental results [144]. Ultrasonic field profiles are calculated for point sources and finite dimension transducers using the ray tracing method. The results are compared first time quantitatively with 2D EFIT results. The reasons for minor differences between ray tracing model and EFIT results are discussed. The elastic parameters used for the quantitative evaluation of ultrasound field profiles in columnar grained austenitic weld materials are given in Table 1.

6.2 Elastodynamic Finite Integration Technique

The Elastodynamic Finite Integration Technique (EFIT) is a numerical time domain modelling tool to model the ultrasound wave propagation in isotropic and anisotropic inhomogeneous media. To model the elastodynamic wave propagation problems, EFIT discretizes the governing equations of linear elastodynamics i.e. Newton-Cauchy's equation of motion and the equation of deformation rate in integral form on a staggered voxel grid in space. The allocation of the vector and tensor components satisfies the transition conditions automatically, if the inhomogeneous material is discretized. For the time discretization an explicit leap-frog scheme is chosen. A complete formulation of linear elastodynamic equations using EFIT for anisotropic inhomogeneous media can be found in [45, 46, 48].

6.3 Quantitative Evaluation of Ultrasonic Transducer Response (A-scan/C-scan)

In this thesis work a 3D ray tracing method (RTM) is developed to evaluate transducer response quantitatively in a general layered anisotropic austenitic steel material. The developed ray tracing approach is schematically illustrated in Fig. 6.1. The effective displacement amplitude (u_{eff}) of an ultrasonic ray in a general layered anisotropic material is expressed as

$$u_{eff} = \frac{D_{eff}\left(\theta, R\right) * \left(T.F_{eff}\right) * \exp(-i\left(k \cdot R\right)_{eff})}{\sqrt{R_{eff}}}, \tag{6.1}$$

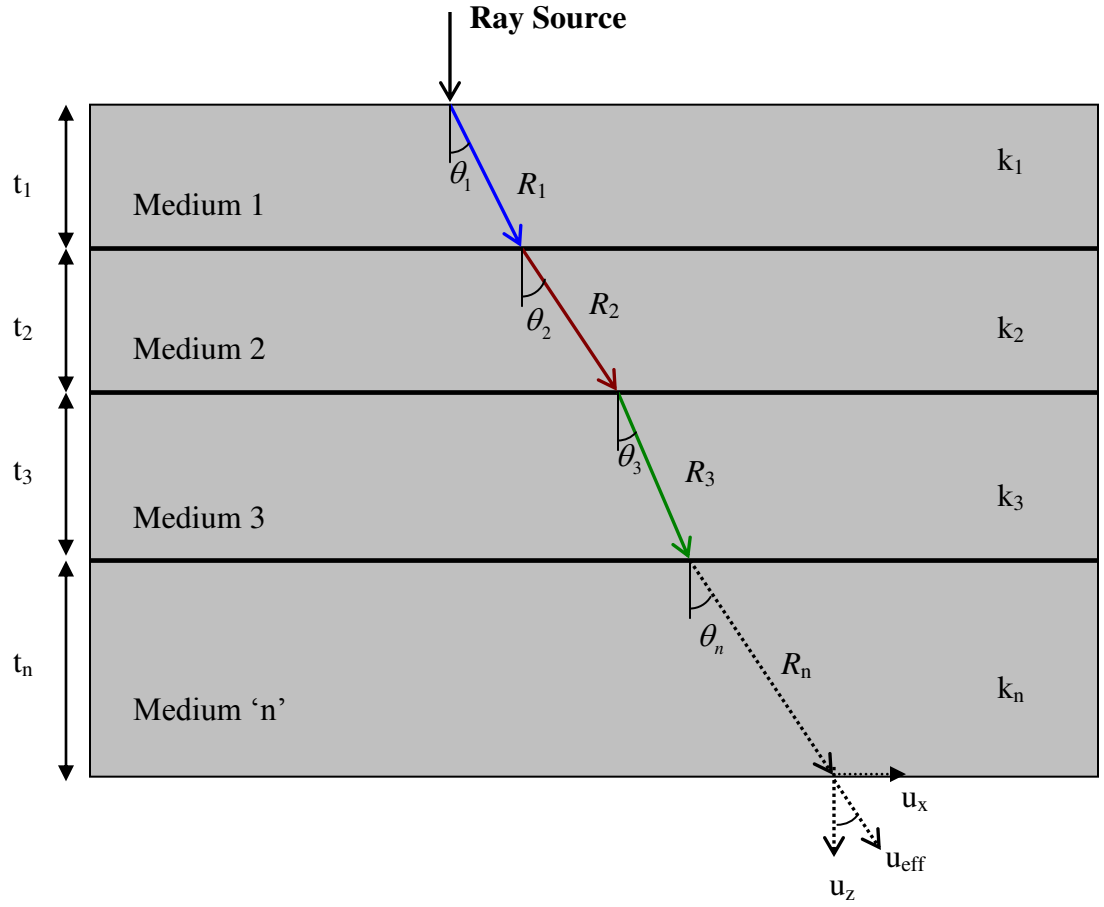

Figure 6.1: *Schematic of the transducer response evaluation in a general layered anisotropic material. Note: θ corresponds to the energy direction of the transmitted ray.*

where

$$D_{eff}\left(\theta,R\right)=D_1\left(\theta_1,R_1\right)*D_2\left(\theta_2,R_2\right)*D_3\left(\theta_3,R_3\right)*.....*D_n\left(\theta_n,R_n\right) \tag{6.2}$$

is the effective directivity factor of the ray,

$$T.F_{eff}=T.F\left(1,2\right)*T.F\left(2,3\right)*.....*T.F\left(n-1,n\right) \tag{6.3}$$

is the effective transmission factor and 1, 2, 3,……., n represent the medium 1, medium2, medium 3 and …….medium n, respectively. The effective distance can be evaluated as

$$\left(k\cdot R\right)_{eff}=k_1\cdot R_1+k_2\cdot R_2+k_3\cdot R_3+.....+k_n\cdot R_n, \tag{6.4}$$

$$R_{eff}=R_1+R_2+R_3+.....+R_n, \tag{6.5}$$

where k is the wavenumber and R_{eff} is the effective distance of the ray.

In case of finite dimension transducer response, the surface of a transducer is discretized into several point sources. From each point source in the finite aperture transducer a diverged ultrasonic ray bundle with a single fixed frequency is considered and allowed to propagate into the spatially varying layered austenitic steel material. The energy loss due to the ray transmission as well as mode conversion at each interface is calculated. Using an effective wave number and distance of the ray as described in Eqs. (6.4) and (6.5), the phase information of an individual ray is calculated. An inverse distance factor i.e. the denominator in Eq. (6.1) is introduced in the final ray amplitude calculation, which accounts the drop of displacement amplitudes due to the ultrasonic beam spread in the layered anisotropic material. The total ultrasonic field due to the finite dimension transducer is obtained by the cumulative effect of displacements produced by each element source. With this implementation, the constructive and destructive interferences are achieved in the A-scan signal. The same procedure for calculating an A-Scan signal is performed in 3-Dimnesional space which results a 2-Dimensional C-scan image for each depth of the material. A more detailed analysis on C-scan image in an anisotropic austenitic material will be presented in the next chapter.

6.4 Validation of Ray Tracing Model for Point Sources

6.4.1 Application to Homogeneous Isotropic Layered Materials

In order to validate the ray tracing model for homogeneous isotropic layered materials with EFIT, a 32 mm thick isotropic layered material is considered. The base material contains isotropic steel material in the upper medium and the aluminum material in the lower medium. The interface between isotropic steel and aluminum material is situated at a depth 16 mm from the excitation surface. A normal point force is excited on the free surface of the isotropic steel material and the normal component (U_z) of the longitudinal wave displacements along the back wall is evaluated. A point source with excitation frequency of 2.25 MHz is considered for the numerical calculations. In ray tracing calculations, a diverged ray bundle is considered at the excitation point and it is allowed to propagate from isotropic steel material into the aluminum material.

Figure 6.2(a) shows the ray energy path behavior and Figure 6.2(b) shows the 2D EFIT time domain snap shot relating to the absolute value of displacements in layered isotropic material. Figure 6.2(c) shows comparison of normal component of longitudinal wave displacements obtained from ray tracing model with EFIT model. We compared normalized amplitudes because of cell dependent amplitude values in both the approaches. It can be seen from Figure 6.2(c) that the ray tracing model results agree qualitatively with the EFIT model results. Quantitatively we observe a deviation of 3.75% at position -30 mm. For positions between -20 mm and 20 mm, an accuracy of 98.9% is obtained which is also a good quantitative result. Table 6 summarizes the comparison of amplitudes between ray tracing and EFIT at selected positions within the layered isotropic material. Beyond the position 20 mm, we observe a minimum amplitude difference of 0.0053 and a maximum amplitude difference of 0.0183 between ray tracing and EFIT results. Thus, the comparison of ray tracing results with the EFIT calculations demonstrates the applicability of theoretical considerations in the ray tracing approach. The reason for minor deviations (quantitatively <3.75%) will be presented in the following sections.

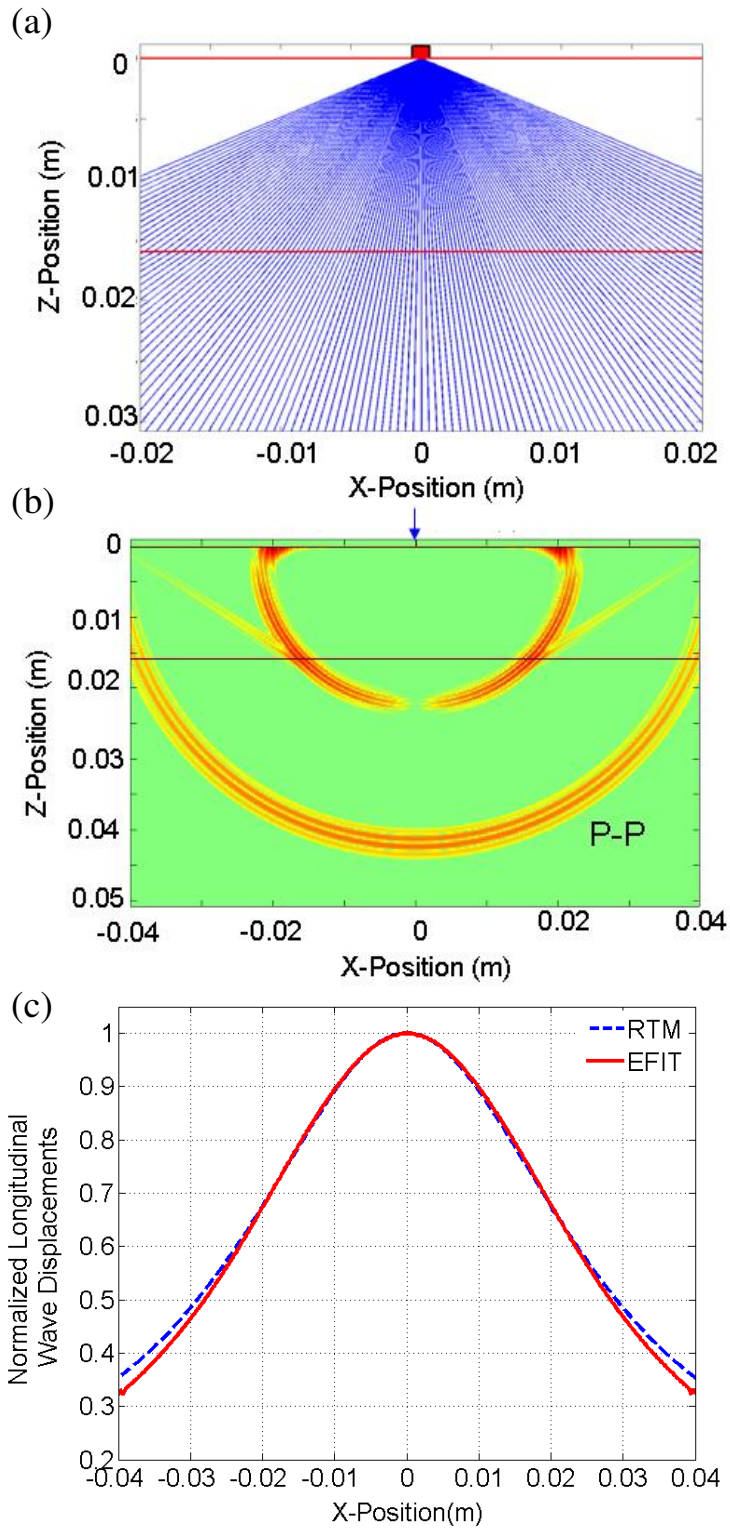

Figure 6.2: *Ultrasound field profiles for longitudinal waves generated by a normal point force in the homogeneous isotropic layered material. (a) 2D ray tracing model (RTM), (b) 2D-EFIT model and (c) ray tracing and EFIT model quantitative comparison at a depth of 32 mm.*

Table 6: *Comparison of ray tracing (RTM) amplitudes with EFIT model at selected X-positions within the homogeneous isotropic layered material.*

Position (mm)	Longitudinal wave amplitudes		Difference in amplitude	Error (%)
	RTM	EFIT		
-30	0.4812	0.4638	0.0174	3.75
-23	0.6108	0.6018	0.009	1.49
23.5	0.6016	0.5955	0.0061	1.02
30	0.4812	0.4675	0.0137	2.93

6.4.2 Application to Homogeneous Austenitic Stainless Steel Materials

In view of ultrasonic non-destructive evaluation of unidirectional columnar grained austenitic steel materials, ultrasound field profiles are computed for the normal point force excitation on a 32 mm thick austenitic steel material. In order to compare the ray tracing model results with EFIT results two different columnar grain orientations of the transversal isotropic austenitic steel material are considered. The selected columnar grain orientations in the transversal isotropic austenitic material are 0° and 50º respectively. The geometry of the homogeneous austenitic steel material is depicted in Fig. 6.3. The normal component of the quasi longitudinal wave displacements along the back wall evaluated from ray based model is compared with the EFIT model calculation. In the EFIT calculations, the austenitic steel geometry is discretized into square grid cells with a grid size of 0.1 mm. Whereas in the ray tracing model there is no need to discretize the geometry of the homogeneous austenitic material. Because the ray tracing approach calculates the displacement only at the material boundaries where the change in material properties occur. This is one of main advantages using ray tracing method as compared to the Finite Element (FE), Finite Difference (FD) and Finite Integration (FI) codes where the field calculations have to be performed for all points in the material geometry.

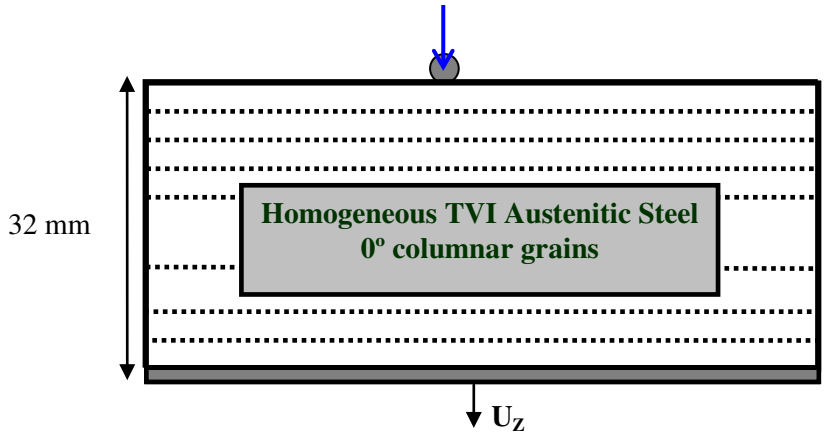

Figure 6.3: *Geometry of the homogeneous austenitic steel material with unidirectional columnar grain orientation used for the ray tracing model calculations.*

Fig. 6.4(a) shows the ultrasonic ray energy path behavior and Fig. 6.4(b) shows the 2D EFIT time domain snap shot related to the absolute value of displacements in an unidirectional columnar grained austenitic steel material with 0º columnar grain orientation. Fig. 6.4(c) shows comparison of quasi longitudinal ultrasound field profiles obtained from the ray tracing model and the EFIT model. An excellent qualitative agreement is achieved. The ultrasonic field profile obtained from EFIT shows maximum amplitudes at positions -23.6 mm and 23.5 mm whereas ray tracing model (RTM) shows at positions -24 mm and 24 mm (see Fig. 6.4(c)). Every single feature in the ultrasound field profile obtained from EFIT model including locations of the maximum and minimum amplitudes is also present in the ray tracing calculations and this confirms the validity of the ray tracing model results for columnar grained austenitic steel materials. Splitting of ultrasonic beam in the anisotropic austenitic steel material is also observed and consequently two distinct maxima occur in the ultrasonic beam profile (see Figure 6.4(c)).

Quantitatively we observe a deviation of 2.4% at position 15 mm. Table 7 summarizes the comparison of amplitudes between ray tracing and EFIT at selected positions within the columnar grained austenitic steel material. We obtain a minimum deviation of 0.02% with amplitude difference of 2e-4 at position 24 mm which is also a good quantitative result. Overall an accuracy of 97.4% is achieved using the ray tracing method.

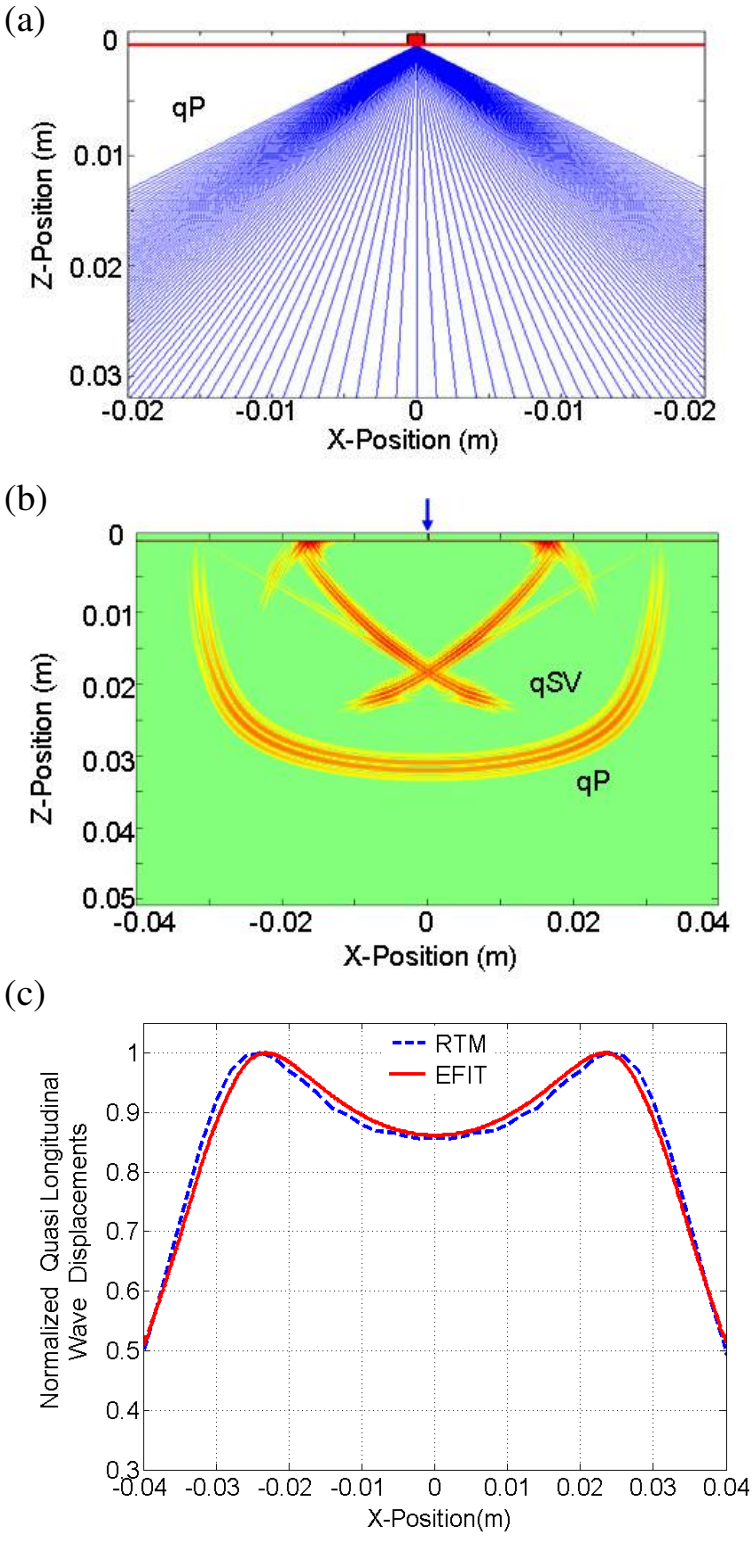

Figure 6.4: *Ultrasound field profiles for quasi longitudinal waves generated by a normal (qP) point force in the transverse isotropic austenitic material (X6CrNi18 11) with 0º columnar grain orientation. (a) 2D-ray tracing model (RTM), (b) 2D-EFIT model and (c) ray tracing and EFIT model quantitative comparison.*

Table 7: *Comparison of ray tracing model (RTM) amplitudes with EFIT model at selected X-positions within the homogeneous anisotropic austenitic steel material with 0°columnar grain orientation.*

Position (mm)	Quasi longitudinal wave amplitudes		Difference in amplitude	Error (%)
	RTM	EFIT		
-22	0.9914	0.9974	0.0060	0.6
-14	0.9058	0.9276	0.0218	2.35
0	0.8558	0.8606	0.0048	0.56
12	0.8957	0.909	0.0133	1.47
24	0.9978	0.9976	2e-4	0.02
-40	0.4968	0.5095	0.0127	2.49

During the validation process, it has been observed that the more reliable ultrasound fields using ray tracing model are evaluated by calculating the final ray amplitudes by taking into account density of rays over the observation line (i.e. along the back wall). Fig. 6.5(a) shows ultrasound energy ray path propagation behavior and Fig. 6.5(b) shows 2D EFIT time domain snap shot relating to the absolute value of displacements in unidirectional columnar grained austenitic steel material with 50º columnar grain orientation. Fig. 6.5(c) shows comparison of quasi longitudinal ultrasound field profiles obtained from ray tracing model and EFIT model and a good qualitative agreement is achieved. It can be seen from Figure 6.5(a) and 6.5(b), that the focusing effects are noticeable from both ray tracing and EFIT model. Quantitatively we observe a deviation of 5.5% at position -20 mm. As can be seen in Fig. 6.5(c), the results of both calculations (i.e. RTM and EFIT) show maximum amplitude at -2 mm. The field profile obtained from both models show non-symmetry with respect to the center position because of the anisotropy of the austenitic steel material.

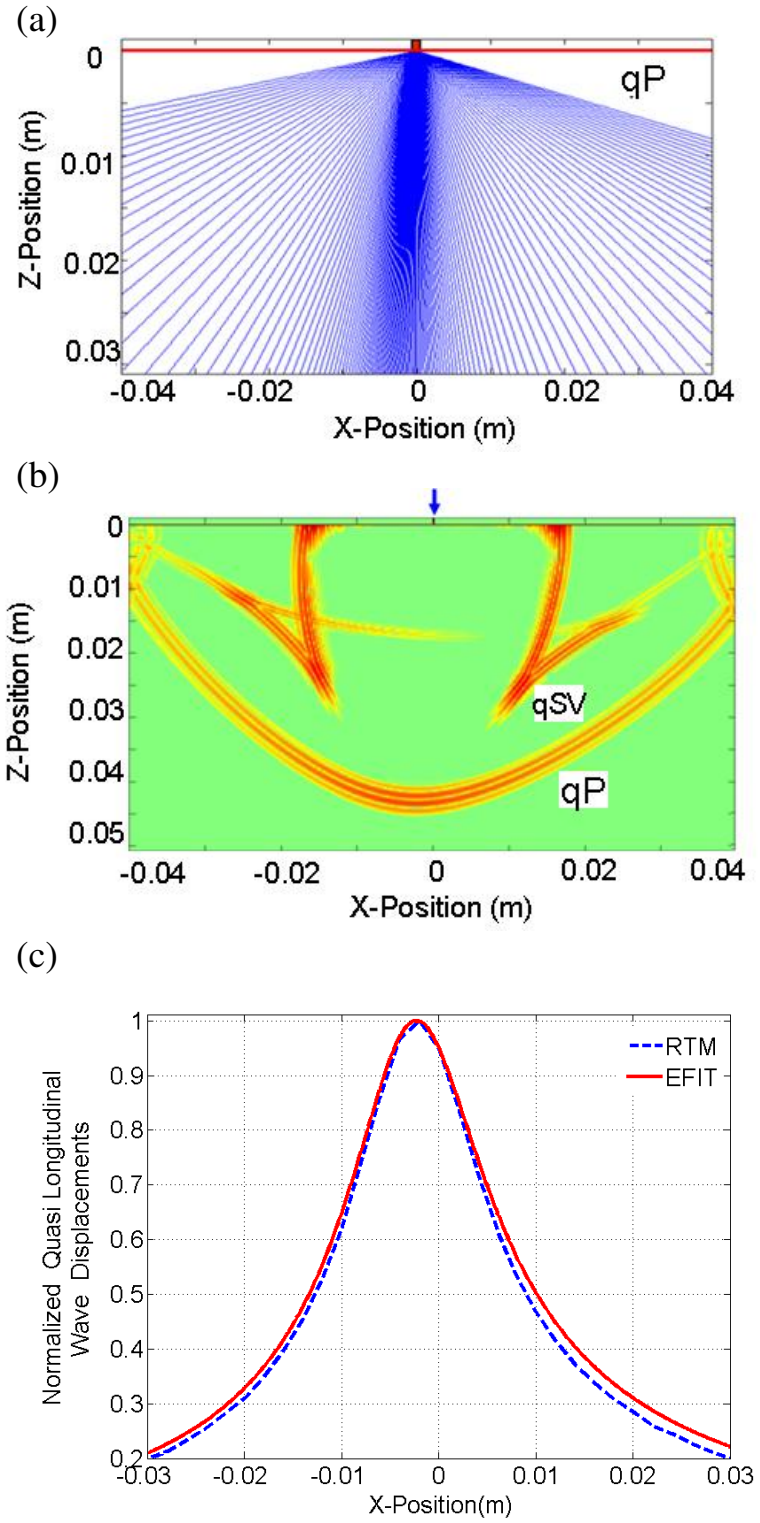

Figure 6.5: *Ultrasound field profiles for quasi longitudinal waves generated by a normal (qP) point force in the transverse isotropic austenitic material (X6CrNi1811) with 50º columnar grain orientation. (a) 2D-ray tracing model (RTM), (b) 2D-EFIT model and (c) ray tracing and EFIT quantitative comparison.*

Table 8: *Comparison of ray tracing model (RTM) amplitudes with EFIT model at selected X-positions within the homogeneous anisotropic austenitic steel material with 50°columnar grain orientation.*

Position (mm)	Quasi longitudinal wave amplitudes		Difference in amplitude	Error (%)
	RTM	EFIT		
-18	0.3481	0.3669	0.0188	5.12
4	0.7211	0.7481	0.0270	3.60
10	0.4679	0.5034	0.0355	7.05
20	0.2851	0.3105	0.0254	8.18

Table 8 summarizes the comparison results between RTM and EFIT at selected positions within the austenitic steel material with 50°columnar grain orientation. For the negative X-positions (i.e. between -30 mm and 0 mm) we observe a maximum deviation of 6.12% with amplitude difference of 0.0612 at a position -28 mm whereas for the positive X-positions a deviation of 8.22% with amplitude difference of 0.0266 at a position 22 mm is noticed (see Fig. 6.5(c)). Between positions -5 mm and 5mm, we observe an accuracy of 96.3 %. Quantitatively we achieved an accuracy of 91.5 % in the ray tracing model which is also a relative good quantitative result. Thus, the ray tracing model for homogeneous austenitic steel material with 2-Dimensional columnar grain orientation is verified by the EFIT results. It is obvious from Fig. 6.5(c) that the amplitude values obtained from the ray tracing model are below the EFIT values for all the positions. This may be due to the ray bundle discretization in the ray tracing algorithm. For the presented calculations we assumed a step size of 0.05° in the ray bundle discretization. Although ray tracing approach is fast computational scheme as compared to the numerical finite difference and integration techniques, it is only able to calculate the sound fields for a particular wave mode at a time.

6.4.3 Application to Layered Austenitic Clad Materials

In view of ultrasonic non-destructive evaluation of austenitic clad material where ultrasound energy propagates through the interface between isotropic steel material and transversal isotropic austenitic clad material, ultrasonic field profiles are evaluated. Ultrasound field profiles are simulated for normal point force excitation on isotropic base material of 32 mm thick austenitic clad material. The interface between isotropic steel and austenitic clad region is assumed parallel and it is situated at 16 mm depth. As a verification of ray tracing predictions, it is assumed that the austenitic clad region is homogeneous with columnar grains perpendicular to the interface i.e. 90° to the interface.

Fig. 6.6(a) shows ultrasonic ray energy propagation behavior and Fig. 6.6(b) shows 2D EFIT time domain snap shot relating to the absolute value of displacements in an anisotropic austenitic clad material. Qualitatively the diverging effects of the quasi longitudinal waves are apparent from both the models (see Fig. 6.6(a) and (b)). Fig. 6.6(c) shows the comparison of quasi longitudinal wave displacement profiles in 32 mm thick austenitic clad material obtained from ray tracing and EFIT models. It is obvious from Fig.6.6(c), that the ray tracing model results agree qualitatively well with EFIT results. As can be seen from Fig. 6.6(c), the predicted quasi longitudinal wave amplitude profiles from ray tracing model agree qualitatively well with 2D EFIT calculations. From Fig. 6.6(c), ultrasonic beam splitting is recognized and consequently two distinct maxima occur in the ultrasound field profile pattern. Quantitatively we observe a deviation of 7.94% at position -36 mm. Table 9 summarizes the comparison results between RTM and EFIT at selected positions within the layered austenitic steel material with 90° crystal orientation. At position 32 mm, the deviation is observed to be 2.96% which is also a relative good quantitative agreement. In Fig. 6.6(c), a dip can be observed in the normal direction (i.e. at position 0 mm) in both the models. This is due to the fact that the beam spreading effect is caused by the anisotropy of the austenitic clad material. Quantitatively we obtain an accuracy of 92% in the negative x-positions and 97% in the positive x-positions which confirms the validity of the ray tracing results for austenitic clad materials.

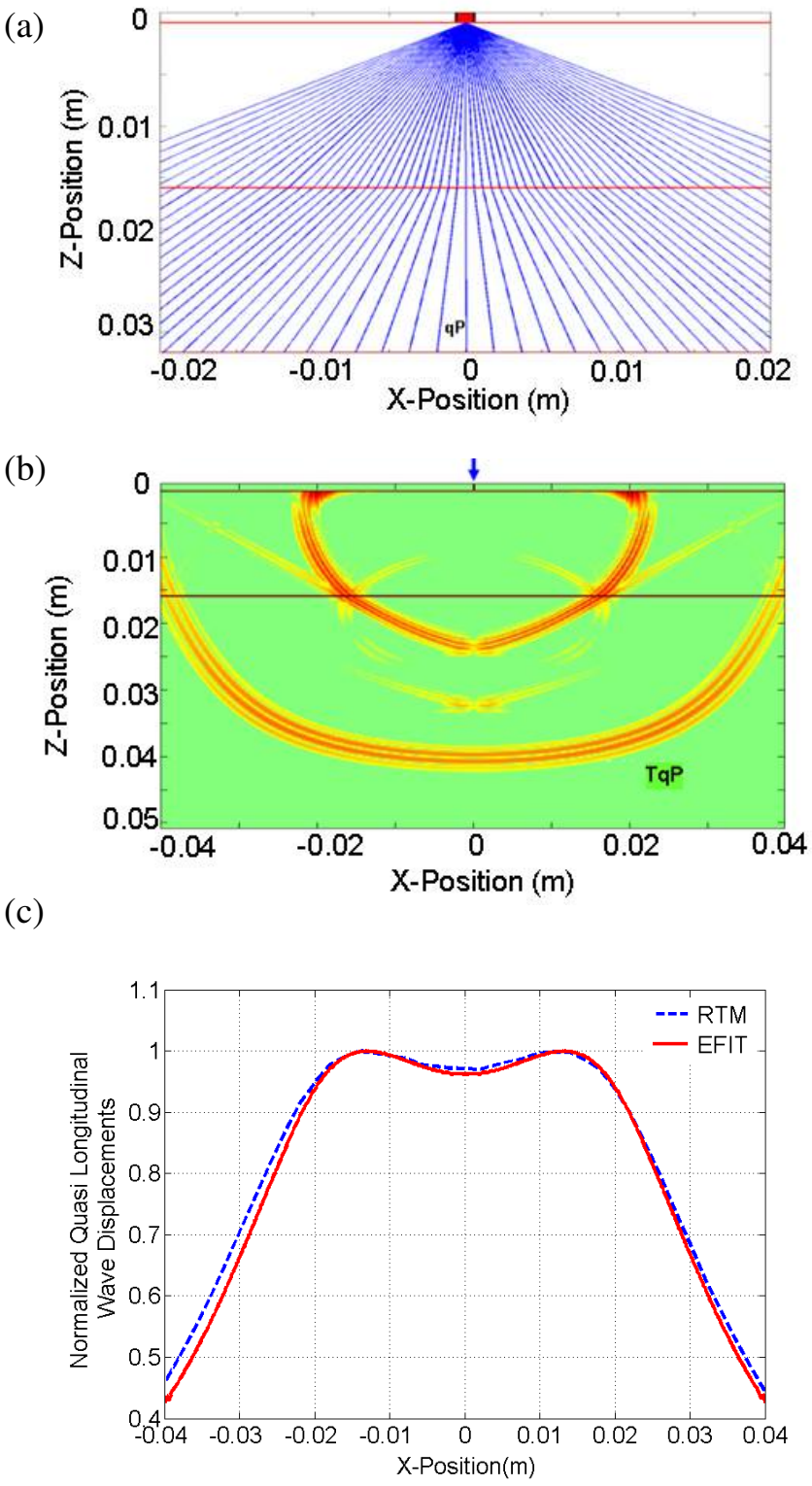

Figure 6.6: *Ultrasound field profiles for quasi longitudinal waves generated by a normal point force in the transverse isotropic austenitic clad material with 90º columnar grain orientation. (a) 2D ray tracing model (RTM), (b) 2D-EFIT model and (c) ray tracing and EFIT model quantitative comparison.*

Table 9: *Comparison of ray tracing model (RTM) amplitudes with EFIT model at selected X-positions within the layered anisotropic austenitic clad material with 90°columnar grain orientation.*

Position (mm)	Quasi longitudinal wave amplitudes		Difference in amplitude	Error (%)
	RTM	EFIT		
-36	0.5459	0.5057	0.0402	7.94
-15	0.9937	0.9957	0.0020	0.2
0	0.9711	0.9622	0.0089	0.92
14	0.9978	0.9981	3e-4	0.03
32	0.6293	0.6112	0.0181	2.96

Fig. 6.7(a) shows the ultrasonic ray energy propagation behavior and Fig. 6.7(b) shows the 2D EFIT time domain snap shot related to the absolute value of displacements in an anisotropic austenitic clad material. The assumed columnar grains in the austenitic clad region are oriented 50° to the interface. Qualitatively the focusing effects of the quasi longitudinal waves are apparent from both the models. Fig. 6.7(c) shows the comparison of quasi longitudinal wave displacement profiles in 32 mm thick austenitic clad material with normal point force excitation. As expected, the non-symmetrical ultrasonic field profile can be observed in Fig.6.7(c). It can be seen from Fig. 6.7(c), that the predicted quasi longitudinal wave amplitude profiles from ray tracing model agree qualitatively well with EFIT calculations. Quantitatively we observe a deviation of 8.56% and an amplitude difference of 0.0365 at position -24 mm. For the positions between 0 mm and 20 mm, we observe an accuracy of 98.8% with amplitude difference 0.003 which is also a relative good quantitative result.

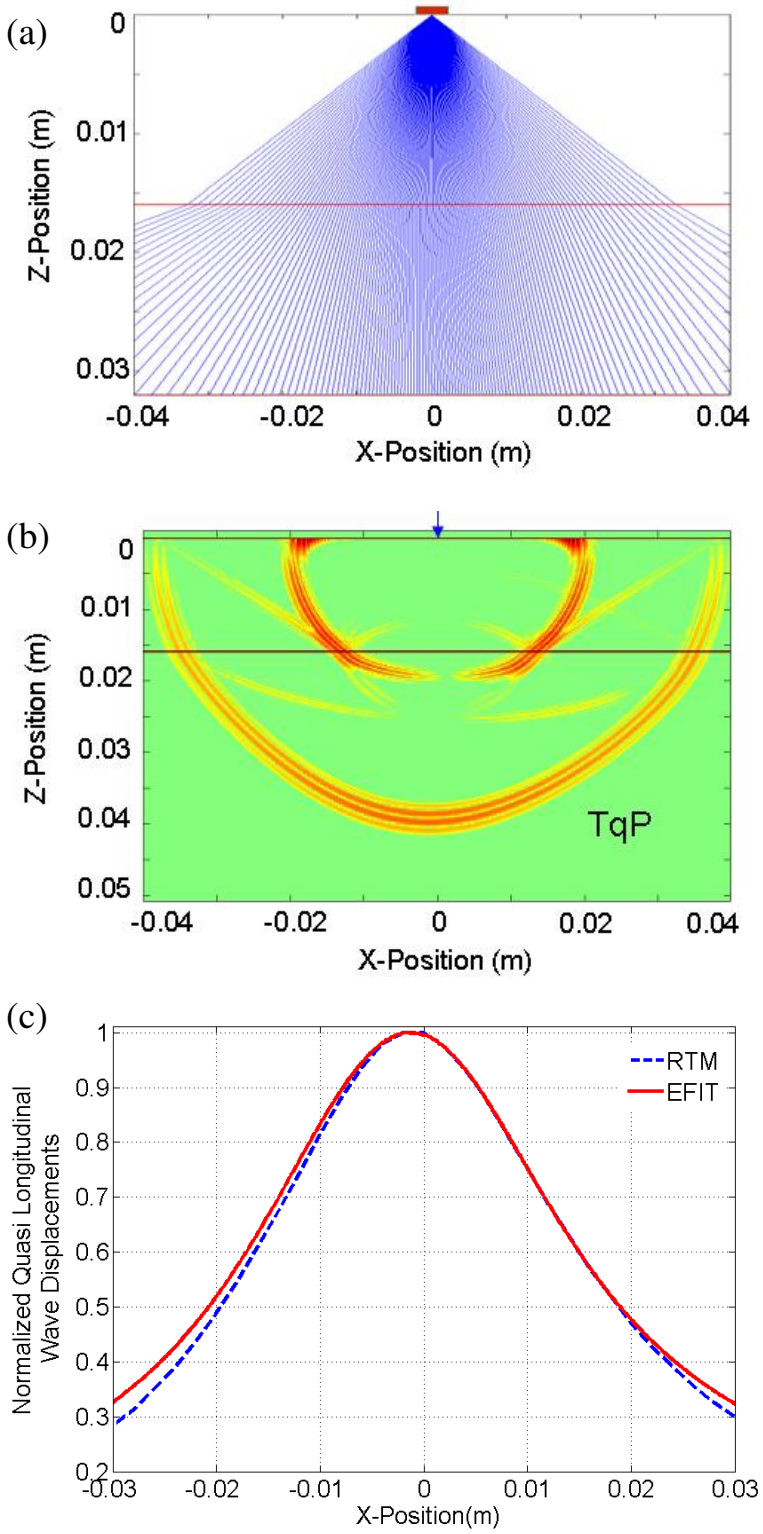

Figure 6.7: *Ultrasound field profiles for quasi longitudinal waves generated by a normal point force in the transverse isotropic austenitic clad material with 50º columnar grain orientations. (a) 2D ray tracing model (RTM), (b) 2D-EFIT model and (c) ray tracing and EFIT model quantitative comparison.*

Table 10: *Comparison of ray tracing model (RTM) amplitudes with EFIT model at selected X-positions within the layered anisotropic austenitic clad material with 50°columnar grain orientation.*

Position (mm)	Quasi longitudinal wave amplitudes		Difference in amplitude	Error (%)
	RTM	EFIT		
-24	0.3898	0.4263	0.0365	8.56
-16	0.6091	0.6353	0.0262	4.12
0	0.9993	0.9954	0.0039	0.39
28	0.3251	0.3468	0.0217	6.25

Table 10 summarizes the comparison results between RTM and EFIT at selected positions within the layered austenitic steel material with 50° crystal orientation. In the negative half region of the horizontal axis (i.e. x-axis), minor differences (quantitatively 8.6% deviation) between ray tracing model and EFIT model are observed. These differences are resulted because EFIT considers ultrasound generated from the source as pulse, whereas ray tracing model assumes monochromatic nature of the ultrasound field propagation. In the ray tracing calculation, at the point source a diverged ultrasonic ray bundle with a single fixed frequency is considered and allowed to propagate into the spatially varying layered austenitic steel material. A point source with excitation frequency of 2.25 MHz is considered for the numerical calculation. Although the ray tracing model assumes single frequency of the excited source, it takes into account the phase information of the ray during its propagation through the material boundaries. Therefore the obtained ultrasonic field profile using ray tracing method is frequency dependent. Additionally, the energy loss due to the ray transmission as well as mode conversion at the interface is implemented in the ray tracing method.

6.4.4 Application to Inhomogeneous Austenitic Weld Materials

The ultrasound field patterns are quantitatively evaluated in inhomogeneous austenitic weld material. Figure 6.8 shows the geometry of the austenitic weld material used for the model calculations.

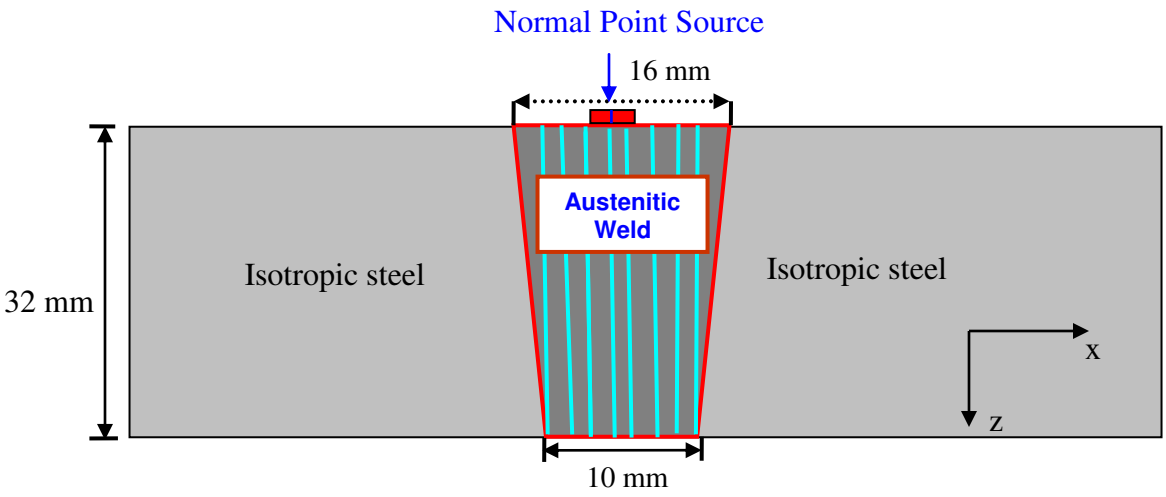

Figure 6.8: *Geometry of the austenitic weld material with vertical grain orientation used for the ray tracing model calculations.*

The comparison of the ray tracing model results with EFIT model calculations for normal point force excitation on 32 mm thick austenitic weld material is shown in Fig. 6.9. The austenitic weld material is considered as transversely isotropic and its elastic constants are presented in Table 1. The isotropic material properties of the base medium are considered to be those of ferritic steel and described in Table 1. A normal point source with excitation frequency of 2.25 MHz is considered for the numerical calculations. A diverged ray bundle is considered at the excitation source and rays are traced through weld boundaries by taking into account plane wave transmission coefficients and directivity factors. The reflection coefficients at the weld boundaries are disregarded in the ray tracing algorithm. Fig. 6.9(a) shows the ray energy propagation behavior in the austenitic weld material, which is surrounded by two isotropic steel materials. Fig. 6.9(b) shows 2D EFIT time domain snap shot relating to the absolute value of displacements in anisotropic austenitic weld material. For the validation of ray tracing model with EFIT results a simplified weld structure model with vertical grain orientation is considered.

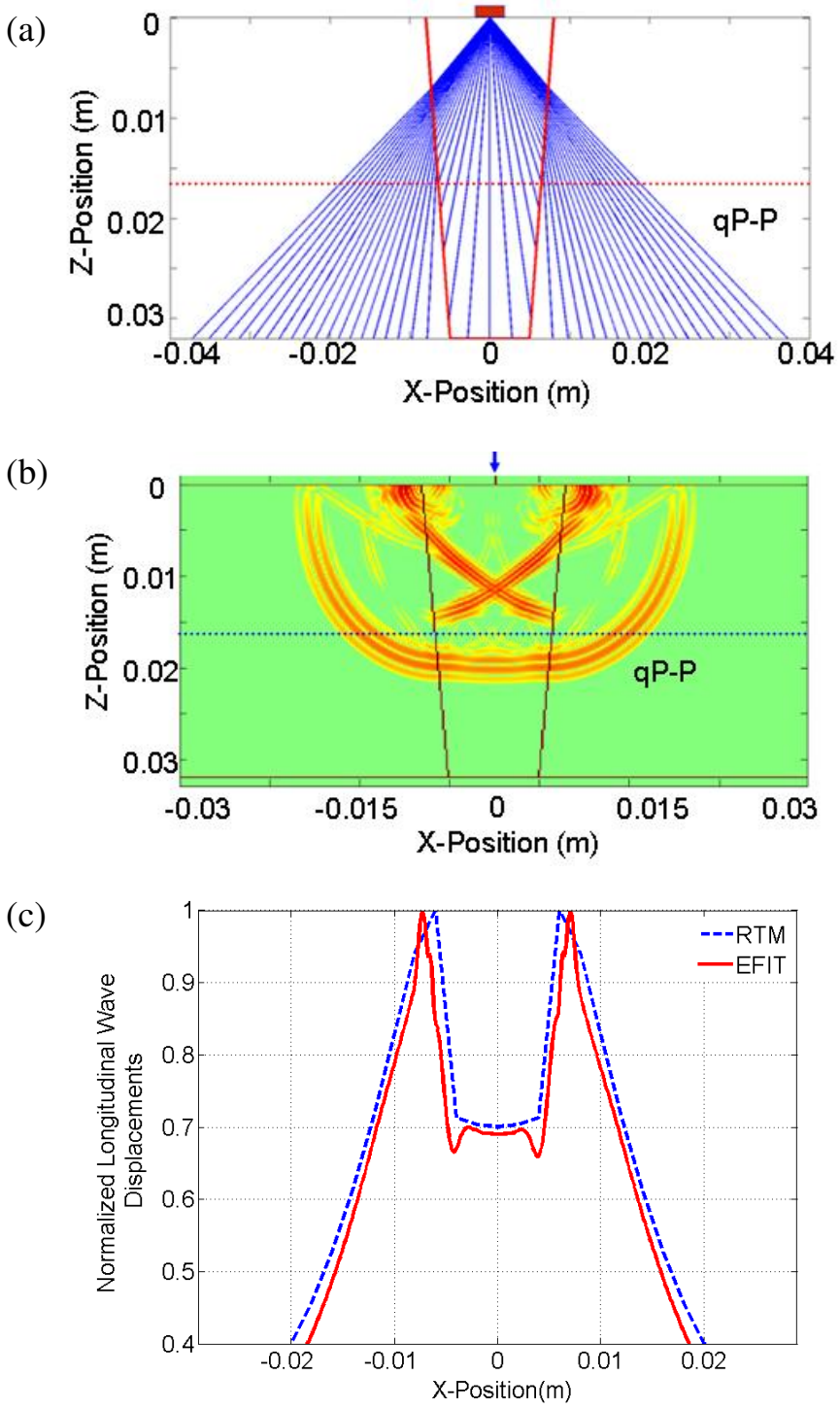

Figure 6.9: *Ultrasound field profiles for transmitted longitudinal waves generated by a normal (qP) point force in the austenitic weld material with 90º columnar grain orientation. (a) 2D ray tracing model (RTM), (b) 2D- EFIT model and (c) ray tracing and EFIT model comparison. Weld boundary inclination = 5.4º, gap between root faces = 10 mm and weld with vertical grain orientation.*

Table 11: *Comparison of ray tracing model (RTM) amplitudes with EFIT model at selected X-positions within the austenitic weld material with 90°columnar grain orientation.*

Position (mm)	Quasi longitudinal wave amplitudes		Difference in amplitude	Error (%)
	RTM	EFIT		
-15	0.5277	0.5302	0.0025	4.71
-10	0.8282	0.7973	0.0309	3.61
0	0.7004	0.6902	0.0102	1.48
12	0.714	0.6796	0.0344	5.06

It can be seen from Fig. 6.9(a), that the most of the incident rays are not capable of propagating (i.e. rays are evanescent) at the weld flanks. This is due to the anisotropic grain structure of the austenitic weld. The transmitted longitudinal wave (TqP) displacements are evaluated at a depth 16 mm from the excitation surface. The evaluated displacement profile along the horizontal axis (i.e. x-axis) from the ray tracing model shows a good qualitative agreement with EFIT calculations (see Fig. 6.9(c)). Splitting of ultrasound filed pattern is apparent from both the models. Table 11 shows the quantitative comparison between ray tracing and EFIT results at selected positions within the austenitic weld material. Quantitatively we observe a deviation of 4.71% and an amplitude difference of 0.0025 at position -15 mm. Along the normal direction (i.e. at position 0 mm) a minimum deviation of 1.48% is observed which is a relative good quantitative agreement.

In the ray tracing calculation, the maximum amplitudes in the ultrasonic field profile are observed at the positions -6.2 mm and 6.2 mm whereas in the EFIT model the maximum amplitudes are noticed at the positions -7.1 mm and 6.9 mm (see Fig. 6.9(c)). We observe two dips at positions -4.2 mm and 3.9 mm in the EFIT results. The reason for

occurring these dips are due to the interaction of mode converted waves with the transmitted quasi longitudinal waves in the austenitic weld material. In case of ray tracing calculation, no dips are observed in the field profile and it is due to the fact that currently displacement contributions from mode converted waves are not considered in the ray tracing model. Overall a mean accuracy of 94.5% is achieved in the ray tracing calculation which confirms the validity of the ray tracing model results for the acoustically anisotropic austenitic weld material.

6.5 Validation of Ray Tracing Model for Distributed Sources

6.5.1 Application to Homogeneous Isotropic Materials

Fig. 6.10 shows the comparison of ultrasound beam profiles for the transmitted longitudinal waves for a finite aperture normal beam transducer (2.25 MHz frequency, 12 mm length of active transducer area) excited on 32 mm thick isotropic steel material. For the numerical calculations the transducer aperture is discretized into 16 elements and the distance between the elements is 0.75 mm. A ray bundle is considered at each element of finite dimension transducer and the displacements at any region of interest in the material are computed by the cumulative effect of displacements produced by the each element source as described in Chapter 5. The constructive and destructive interferences are achieved by superposition of ray contributions from each source point over the observation line. Figure 6.10(a) shows the ray path behavior in isotropic steel material for the finite aperture normal beam transducer. The ultrasonic beam profile obtained from the ray tracing model shows qualitatively good agreement with the 2D EFIT calculations (see Fig. 6.10(b)). Table 12 shows comparison between ray tracing and EFIT results at selected positions in Fig. 6.10(b).

Quantitatively we observe a deviation of 5.53 % at position 4.5 mm and between positions -6.5 mm and 6.5 mm, an accuracy of 98.8% is obtained which is a relative good quantitative agreement. It can be seen from Fig. 6.10(b) that the side lobes are visible in both the calculations.

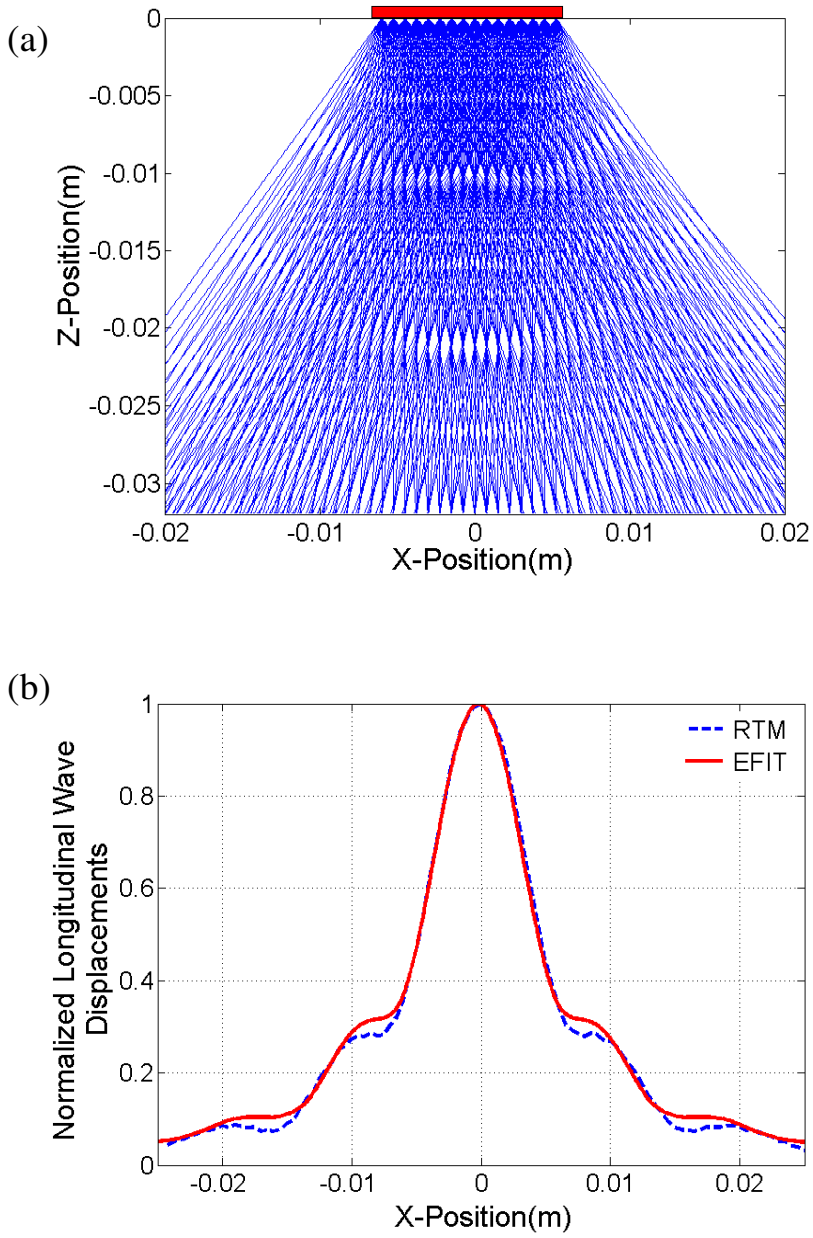

Figure 6.10: *Comparison of longitudinal wave displacement profiles calculated using 2D ray tracing model (RTM) and 2D EFIT model for the longitudinal normal beam finite dimension transducer (2.25 MHz frequency, 12 mm width) in the isotropic steel material. (a) 2D ray tracing model for distributed sources, (b) ray tracing model and EFIT quantitative comparison.*

Table 12: *Comparison of ray tracing model (RTM) amplitudes with EFIT model at selected X-positions within the isotropic steel material for the array source excitation.*

Position (mm)	Longitudinal wave amplitudes		Difference in amplitude	Error (%)
	RTM	EFIT		
4.5	0.5093	0.4826	0.0267	5.53
7.5	0.2847	0.3169	0.0322	10.1
10	0.2699	0.2734	0.0035	1.2

A maximum deviation of 10.1% is observed at positions -7.4 mm and 7.5 mm where an amplitude difference of 0.0322 is noticed between ray tracing and EFIT results. This is due to the single frequency assumption in the ray tracing calculation. During the validation process it is observed that the ray tracing model results agree well with EFIT results when EFIT assumes longer pulse excitation because then the excited signal has monochromatic behavior.

6.5.2 Application to Homogeneous Austenitic Steel Materials

Fig. 6.11 shows comparison of ultrasound beam profiles for the transmitted longitudinal waves for a finite aperture normal beam transducer (2.25 MHz frequency, 12 mm length) excited on 32 mm thick transversal isotropic austenitic steel material. The assumed columnar grain orientation in the austenitic steel material is 0º. Figure 6.11(a) shows ray energy path behavior for the finite aperture normal beam transducer in homogeneous austenitic steel material. As expected the ray pattern is influenced by the anisotropy of the austenitic material resulting in ultrasonic beam spreading and uneven distribution of rays over the observation line (i.e. back wall). Figure 6.11(b) shows 2D EFIT time domain snap shot relating to the absolute value of displacements in homogeneous anisotropic austenitic steel material. A raised cosine pulse with 2 cycles is used in EFIT calculation.

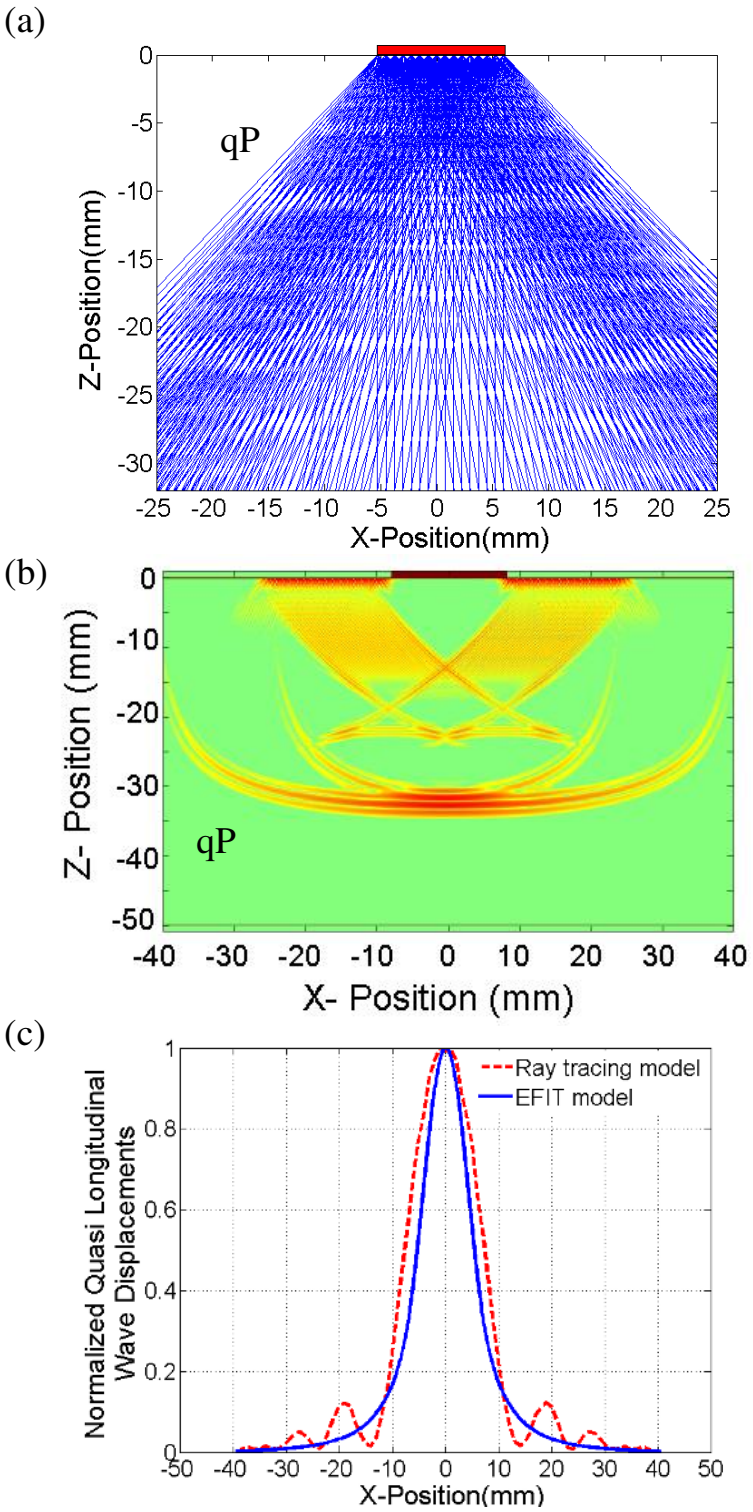

Figure 6.11: *Comparison of longitudinal wave displacement profiles calculated using 2D ray tracing model and 2D EFIT model for the longitudinal normal beam finite dimension transducer (2.25 MHz frequency, 12 mm width) in the transverse isotropic austenitic material (X6CrNi1811). (a) 2D ray tracing model for distributed sources, (b) 2D-EFIT model and (c) ray tracing model and EFIT quantitative comparison. The columnar grain orientation in the austenitic steel material is 0°.*

Table 13: *Comparison of ray tracing model (RTM) amplitudes with EFIT model at selected X-positions within the transverse isotropic austenitic steel material with 0° columnar grain orientation for the array source excitation.*

Position (mm)	Quasi longitudinal wave amplitudes		Difference in amplitude	Error (%)
	RTM	EFIT		
3	0.8336	0.8145	0.0191	2.34
11	0.1382	0.1436	0.0054	3.76

Figure 6.11(c) shows comparison of normal component of ultrasonic field pattern obtained from ray tracing model with EFIT results. It can be seen from Fig. 6.11(c) that the ray tracing model results agree qualitatively well with the EFIT results. The side lobes are observed in the ray tracing calculations and these are resulted due to the constructive and destructive interferences of the rays from each element source in the finite aperture transducer. The amplitudes of the side lobes depend on pitch size, number of elements and frequency of the finite aperture transducer. The predicted main lobe in the ultrasonic field profile using ray tracing model agrees qualitatively well with the EFIT results.

Table 13 shows the comparison of ray tracing and EFIT results at selected positions within the anisotropic austenitic material. Quantitatively we observe a deviation of 3.76% and an amplitude difference of 0.0054 at position 11 mm which is a relative good quantitative agreement. Additionally, the ray tracing amplitude profile shows a full width at half maximum (FWHM) of 11.9 mm whereas FWHM of 10.5 mm is observed in the EFIT amplitude profile. As can be seen from Fig. 6.11(c) that the EFIT amplitude profile shows no side lobes which are previously observed in case of isotropic steel material (see Fig. 6.10(c)). This is due the broadband frequency spectrum used in the EFIT simulation. In Fig. 6.10(c) a raised cosine pulse with 4 cycles is used leading to narrowband frequency spectrum (i.e. close to monochromatic case). Consequently side lobes are observed in Fig. 6.10(c). Hence, a short pulse always suppresses the side lobe formation in the ultrasonic amplitude profile as shown in Fig. 6.11(c).

6.5.3 Application to Layered Austenitic Steel Materials

Figure 6.12 shows the comparison of ultrasonic beam profiles for the transmitted quasi longitudinal waves for a finite aperture normal beam transducer (2.25 MHz, 12 mm length) excited on 32 mm thick homogeneous austenitic clad material. The assumed columnar grain orientation in the austenitic clad region is 50º. The interface between isotropic base and austenitic clad material is situated at 16 mm. The material properties for the isotropic steel and anisotropic austenitic material are described in Table 1. For the numerical calculations the transducer aperture is discretized into 16 elements and the distance between the elements is 0.75 mm. A ray bundle is considered at each element of finite dimension transducer and the displacements at any region of interest in the material are computed by the cumulative effect of displacements produced by the each element source. The focusing effect of the quasi longitudinal beam is apparent from both models (see Fig. 6.12(a) and (b)). This is due to the anisotropic effect of the austenitic clad material. The ultrasonic beam profile obtained from the ray tracing model shows qualitatively good agreement with the EFIT calculations (see Fig. 6.12(c)). Table 14 shows the quantitative comparison of ray tracing and EFIT results at selected positions within the austenitic clad material.

Quantitatively we observe a deviation of 2.98% at position 2.5 mm which is also a relative good quantitative result. Between positions -15mm and 15mm an accuracy of 94.5% is achieved in the ray tracing calculation. It can be noticed from Fig. 6.12(c) that the maximum amplitude occurs at 1.5 mm in both the calculations. Additionally, an amplitude difference of 0.042 is observed at position 20.5 mm. It is observed that beyond the position 20.5 mm the ray tracing results show a fast drop in amplitudes. The minor deviations (i.e. quantitatively an amplitude difference of 0.0432) result in the region far away from the centre can be eliminated with the monochromatic assumption in EFIT model.

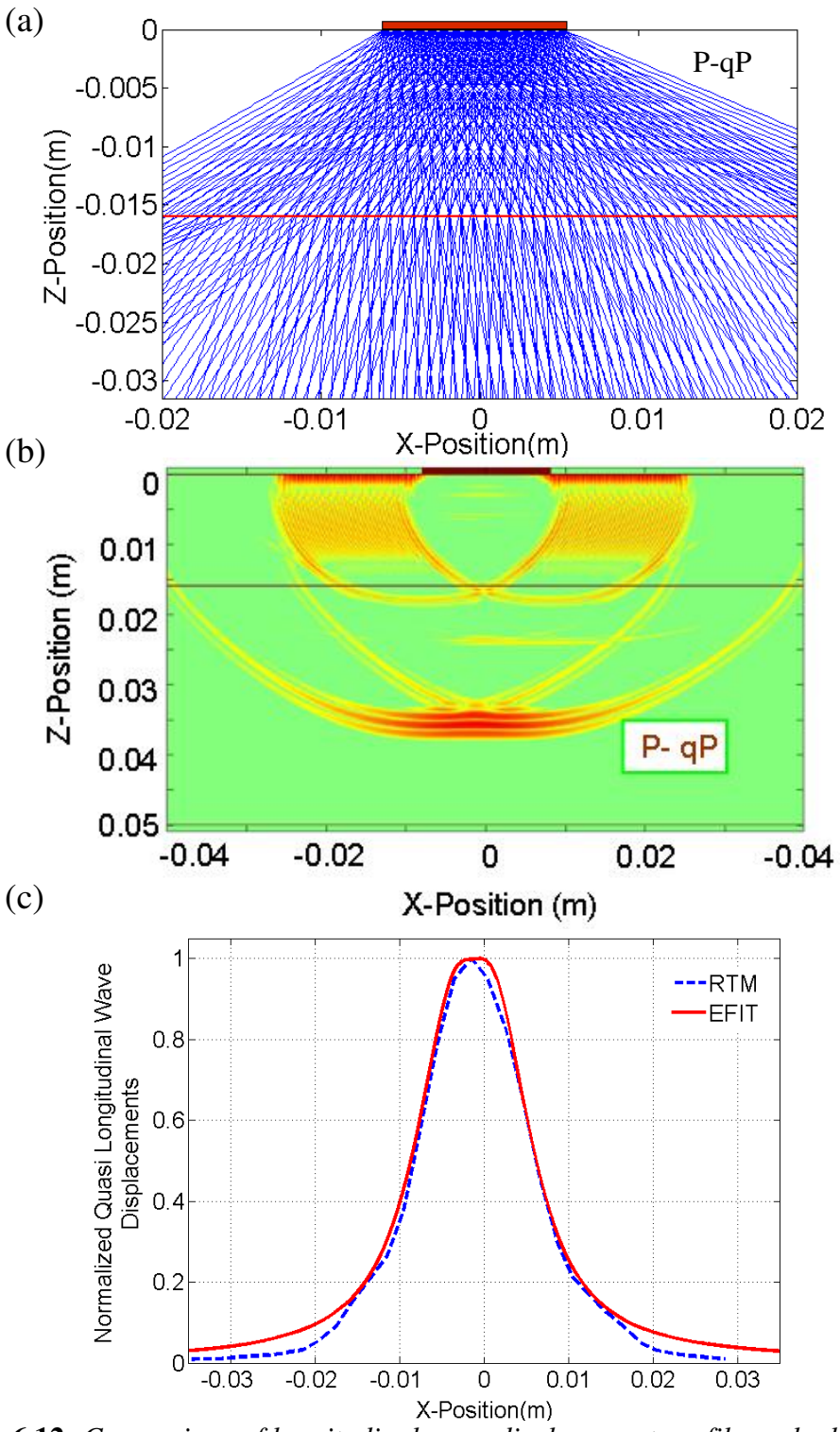

Figure 6.12: *Comparison of longitudinal wave displacement profiles calculated using 2D ray tracing model and 2D EFIT model for the longitudinal normal beam finite dimension transducer (2.25 MHz frequency, 12 mm width) in the austenitic clad material. (a) 2D ray tracing model distributed sources, (b) 2D-EFIT model and (c) ray tracing model (RTM) and EFIT quantitative comparison. The columnar grain orientation in the austenitic clad region is 50°.*

Table 14: *Comparison of ray tracing model (RTM) amplitudes with EFIT model at selected X-positions within the layered austenitic cladded material with 50°columnar grain orientation.*

Position (mm)	Quasi longitudinal wave amplitudes		Difference in amplitude	Error (%)
	RTM	EFIT		
-13.5	0.2077	0.2186	0.0109	5.24
0	0.9679	0.9977	0.0298	2.98
2.5	0.8326	0.8749	0.0423	4.83
10.5	0.2127	0.2194	0.0067	3.05

The applications of ray tracing model for the ultrasonic non-destructive evaluation of anisotropic materials such as austenitic welds and austenitic clad materials are discussed. Quantitative comparison of ultrasound fields obtained from ray tracing model and 2D EFIT model for point source as well as finite dimension transducer excitation on homogenous isotropic layered materials, anisotropic layered materials and austenitic weld materials are presented in this chapter. Comparison results show excellent quantitative agreement between both the models. This confirms the validity of the ray tracing model results. The reasons for minor differences between ray tracing and EFIT models are discussed. Quantitative evaluation of an ultrasonic C-scan image in homogeneous and layered anisotropic austenitic steel materials using 3D ray tracing method is presented in chapter 7.

CHAPTER 7

Quantitative Evaluation of Ultrasonic C-scan Image in Homogeneous and Layered Anisotropic Austenitic Steel Materials using 3D Ray Tracing Method

7.1 Introduction

In this chapter, ultrasonic C-scan image in homogeneous and layered anisotropic austenitic steel materials are evaluated first time quantitatively using 3D ray tracing method. The influence of columnar grain orientation and layback orientation on ultrasonic C-scan image in an anisotropic austenitic steel material is investigated. The applications of ultrasonic C-scan image for the ultrasonic non-destructive testing of anisotropic austenitic steel materials are presented. The predicted ultrasonic fields for the angle beam array transducer in an inhomogeneous austenitic weld material are compared quantitatively with a commercially available NDT simulation tool (CIVA).

7.2 Quantitative Determination of Ultrasonic C-scan Image in an Anisotropic Austenitic Steel Material

An ultrasonic C-scan image is defined as an image representing the ultrasonic amplitude distribution over the sectional area of the component. Generally ultrasonic C-scan images are used for the non-destructive characterization of volumetric defects in materials [145, 146, 147, 148, 149, 150]. In case of isotropic materials, the calculation of an ultrasonic C-scan image is a straightforward approach because the wave phase velocity and group velocity directions are equal. Whereas in homogeneous and layered anisotropic materials, due to the directional dependency of ultrasonic wave propagation, it is very important to consider all the anisotropic effects of the material while calculating an ultrasonic C-scan image. In this research work, the ultrasonic C-scan image in homogenous and layered anisotropic austenitic steel materials is quantitatively evaluated and its importance to the practical ultrasonic non-destructive testing of anisotropic austenitic steel and clad materials is explored. The influence of columnar grain angle and layback orientation on an ultrasonic C-scan image in anisotropic austenitic steel material is presented in the next sections.

7.2.1 Effect of Columnar Grain Orientation on Ultrasonic C-scan Image

Figure 7.1(a) shows the set-up used for the calculating ultrasonic C-scan image for a normal beam contact transducer (2.25 MHz frequency, 0.1 mm length) in columnar grained anisotropic austenitic steel material using 3D ray tracing method. The considered thickness of the austenitic steel material is 32 mm. The coordinate representation of the material geometry is depicted in Fig. 7.1(b). According to the 3D ray tracing method, a diverged ray bundle is considered at the transducer excitation point and it is allowed to propagate along its energy direction into the anisotropic material. The 3D ray directivity in an isotropic material (or) anisotropic material is calculated using Lamb's reciprocity theorem as explained in chapter 4. The ultrasonic ray amplitudes along the back wall of the anisotropic austenitic material are calculated by incorporating inverse distance and phase factors as described in chapter 3. The ultrasonic C-scan image is obtained by plotting the amplitudes over the calculated xy-plane.

Figure 7.2 shows the simulated quasi longitudinal normal beam C-scan images in the xy-plane for selected columnar grain orientations of the austenitic material which are 0º, 15º, 45º, 75º and 90º. For the numerical calculations, a cone of ray bundles with polar angular range from 0º to 50º with 0.5º step size and azimuthal angular range between 0º and 360º with 2º step size is considered. The presented ray amplitudes in the Fig. 7.2 are normalized to their respective maxima. It can be seen from Fig. 7.2 that the ultrasonic C-scan images are strongly influenced by the columnar grain orientation of the austenitic material. The reasons for deformation of the circular shape of an ultrasonic C-scan image can be explained due to the effect of anisotropy on the ray bundle propagation. From Fig. 7.2, it is observed that the pattern of the ultrasonic C-scan image for the 0º columnar grain orientation of the austenitic steel material is similar to that generally found in isotropic steel material. Whereas for the other columnar grain orientations, the ultrasonic C-scan images are deformed from the isotropic case and some unusual beam focusing and beam spreading phenomena are observed.

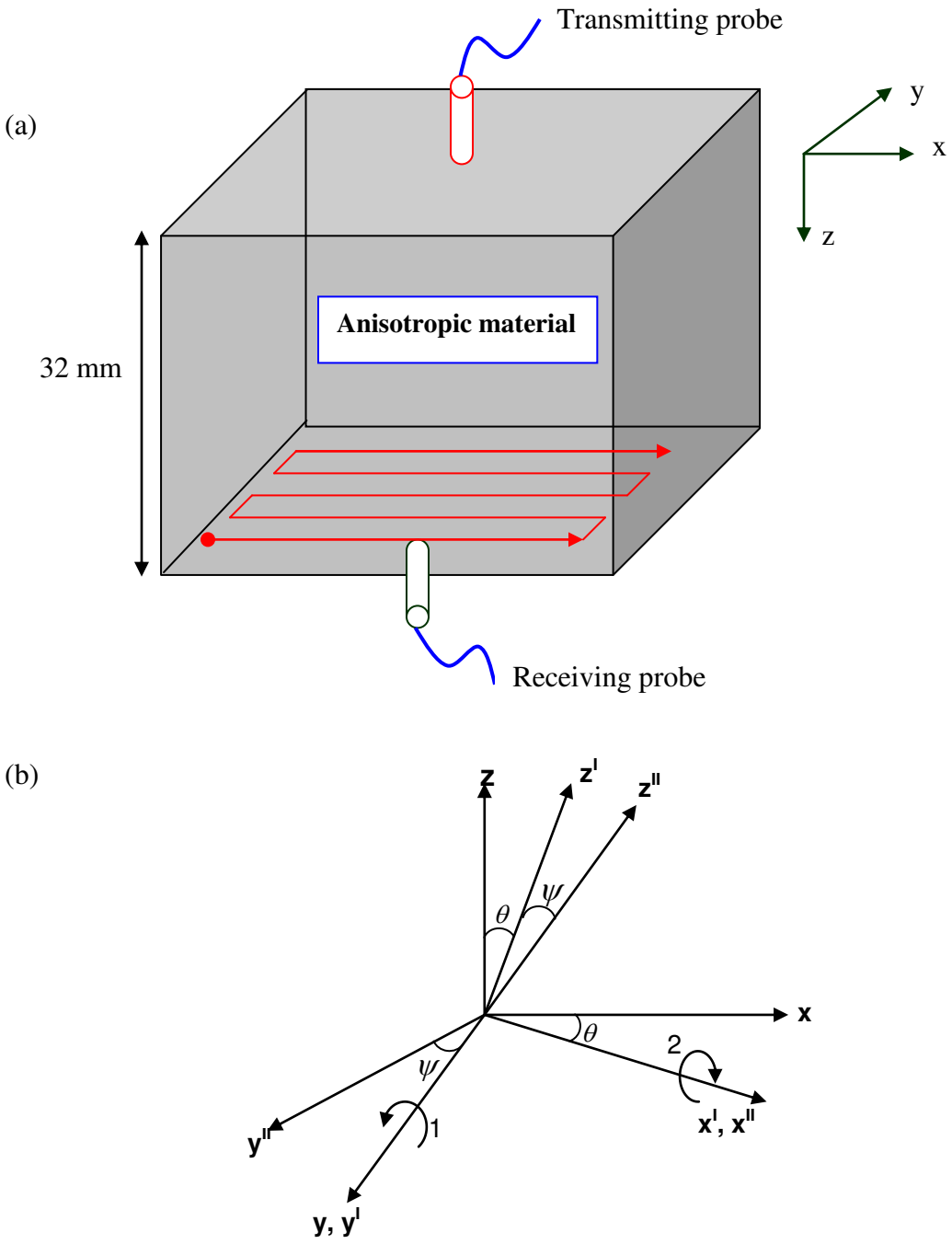

Figure 7.1: *(a) Geometry used for evaluating ultrasonic C-scan image in 32 mm thick anisotropic columnar grained austenitic steel material using 3D ray tracing method, (b) definition of columnar grain orientation and layback orientation in the austenitic steel material.* θ *represents the columnar grain orientation and* ψ *represents the lay back orientation.*

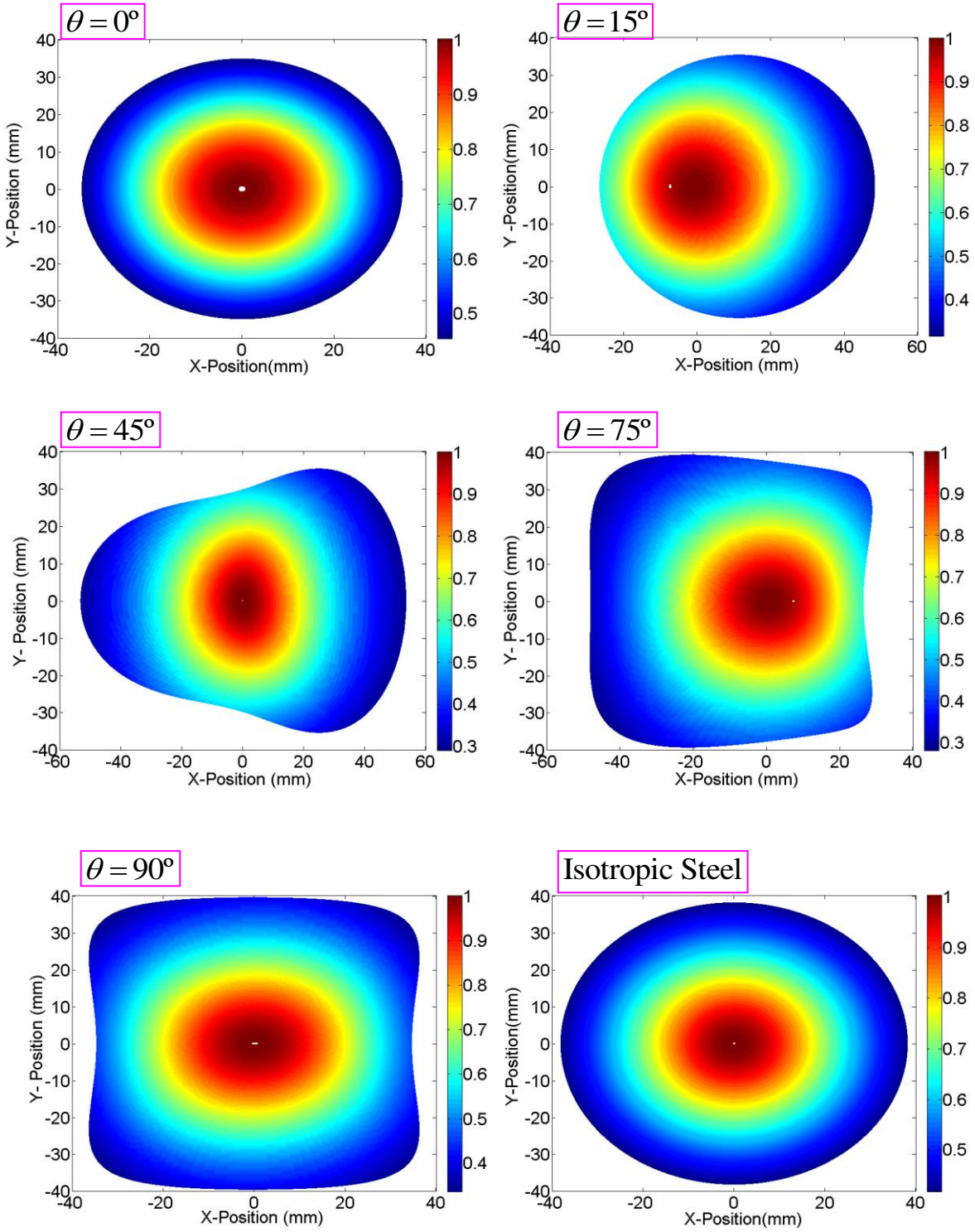

Figure 7.2: *Ultrasonic quasi longitudinal wave C-scan images along the back wall surface of the 32 mm thick anisotropic columnar grained austenitic steel material (X6CrNi1811) using normal beam longitudinal contact transducer (2.25 MHz centre frequency, 0.1 mm width). 'θ' represents the columnar grain orientation of the austenitic steel material. Layback orientation is assumed as 0º.*

The ultrasonic C-scan image for the 45º columnar grain shows strong focusing effects of the ultrasonic beam in the negative half of x-positions and highly divergent in the positive half of x-positions (see Fig. 7.2). The ultrasonic C-scan images for the 15º and 75º columnar grain orientations are largely deviated from the isotropic behaviour because for these columnar grain orientations large beam skewing angles are observed.

7.2.2 Effect of Layback Orientation on Ultrasonic C-scan Image

Figure 7.3 shows the calculated quasi longitudinal ultrasonic C-scan images in the xy-plane for different layback orientations (i.e. grain tilt along the xy-plane) of the austenitic steel material using 3D ray tracing method. The columnar grain is oriented in 3D space of the laboratory coordinate system of the anisotropic austenitic steel material (see Fig. 7.1(b)). The assumed columnar grain orientation of the austenitic steel material is 45º and it is kept constant. The selected layback orientations for the present investigation are 0º, 15º, 30º, 45º, 75º and 90º. The beam deflection and beam distortion phenomena in the ultrasonic C-scan images can be observed in Fig. 7.3. From the quantitative analysis on ultrasonic fields, it has been observed that the presence of layback orientation reduces the ultrasonic beam coverage and sound field intensity in an austenitic steel material. The presented ray tracing method is also capable of calculating ultrasonic C-scan image for the other two wave modes namely quasi shear vertical and pure shear horizontal waves in an anisotropic austenitic steel material.

7.2.3 Quantitative Determination of Ultrasonic C-scan Image in Layered Anisotropic Austenitic Steel Material

A 3D ray tracing method is developed for evaluating ultrasonic C-scan image in a layered anisotropic austenitic steel material. In the presented investigation, ultrasonic C-scan image is quantitatively determined in 32 mm thick layered austenitic clad material where 16 mm as isotropic steel material, 8 mm as austenitic steel material with 20º columnar grain orientation and 8 mm as austenitic steel material with 45º columnar grain orientation.

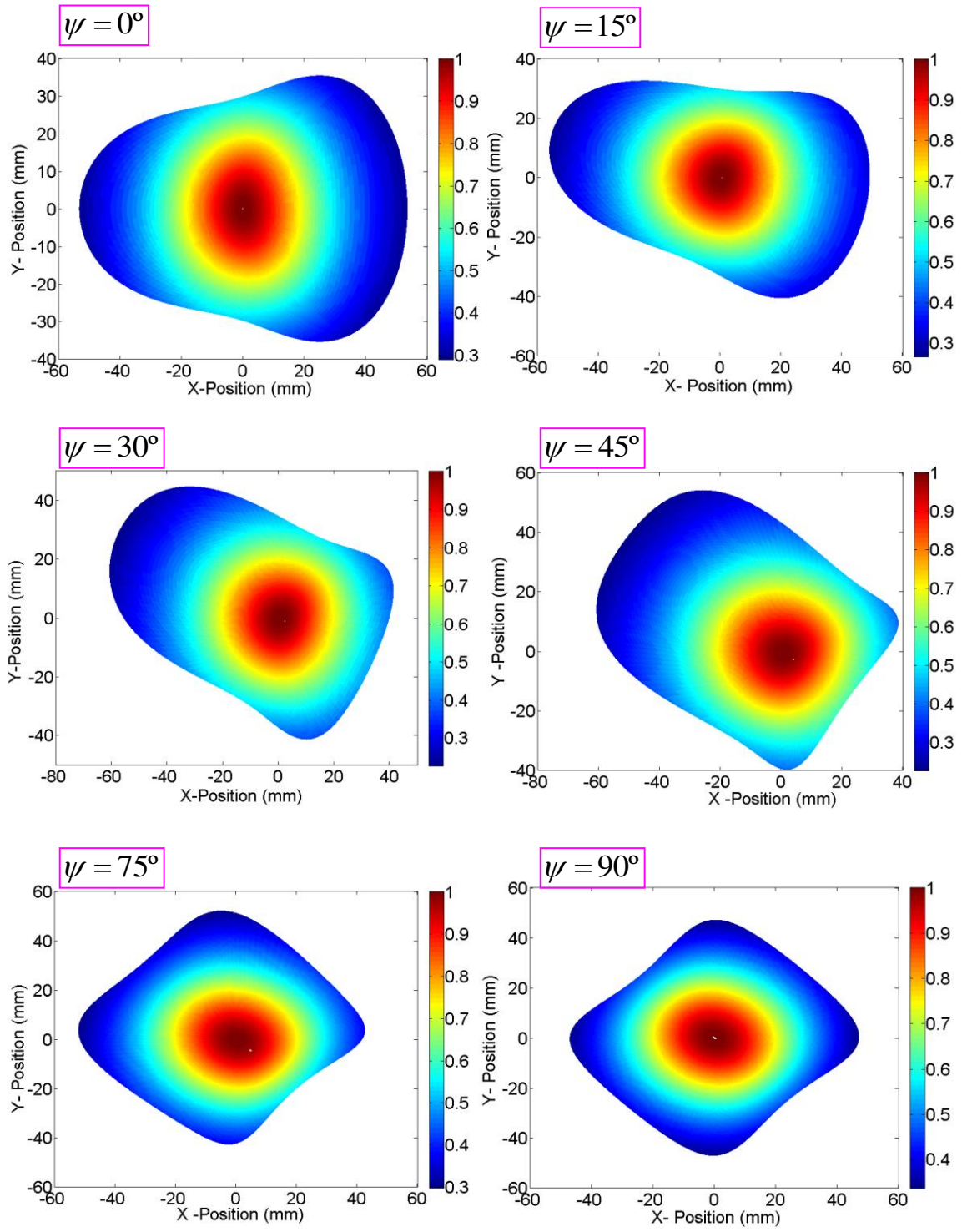

Figure 7.3: *Ultrasonic quasi longitudinal wave C-scan images along the back wall surface of the 32 mm thick anisotropic columnar grained austenitic steel material (X6CrNi1811) using normal beam longitudinal contact transducer (2.25 MHz centre frequency, 0.1 mm width). 'ψ' represents the layback orientation of the austenitic steel material. Columnar grain orientation is assumed as 45º which is kept constant.*

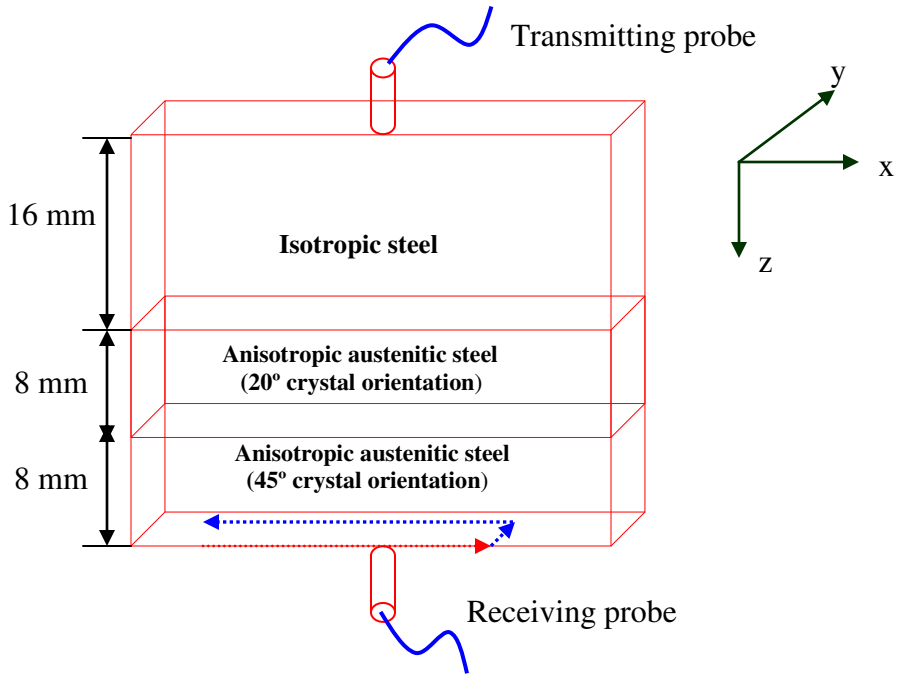

Figure 7.4: *Geometry used for evaluating ultrasonic C-scan image in 32 mm thick layered anisotropic austenitic steel material using 3D ray tracing method.*

A normal beam ultrasonic transducer (2.25 MHz frequency, 0.1 mm width) is excited on the surface of the isotropic steel material and ultrasonic field distribution is evaluated over the XY plane at a depth of 32 mm from the top surface. Figure 7.4 shows the geometry used for calculating ultrasonic C-scan image in layered austenitic clad material. Figure 7.5 shows 3D ultrasonic ray propagation in an anisotropic layered austenitic steel material for the 20º longitudinal wave incidence. The 3D ray tracing model is capable to simulate the ray paths in both side view (C-scan) and top view (B-scan) representation (see Fig. 7.5 (a), (b) and (c)). As expected from the Figure 7.5, the ultrasonic ray paths are bended due to the anisotropy of the austenitic clad material. The calculated ultrasonic C-scan image for the normal beam contact transducer (with centre frequency 2.25 MHz) in an anisotropic layered austenitic clad material is shown in Figure 7.6. The ray energy transmission coefficients at the interface between isotropic and austenitic material as well as the interface between two austenitic steel materials are taken into account in the ray tracing model while calculating the ultrasonic C-scan image. It is observed that the shape of the ultrasonic C-scan image is deformed from circular shape (i.e. isotropic behaviour) into an elliptical shape (see Fig. 7.6).

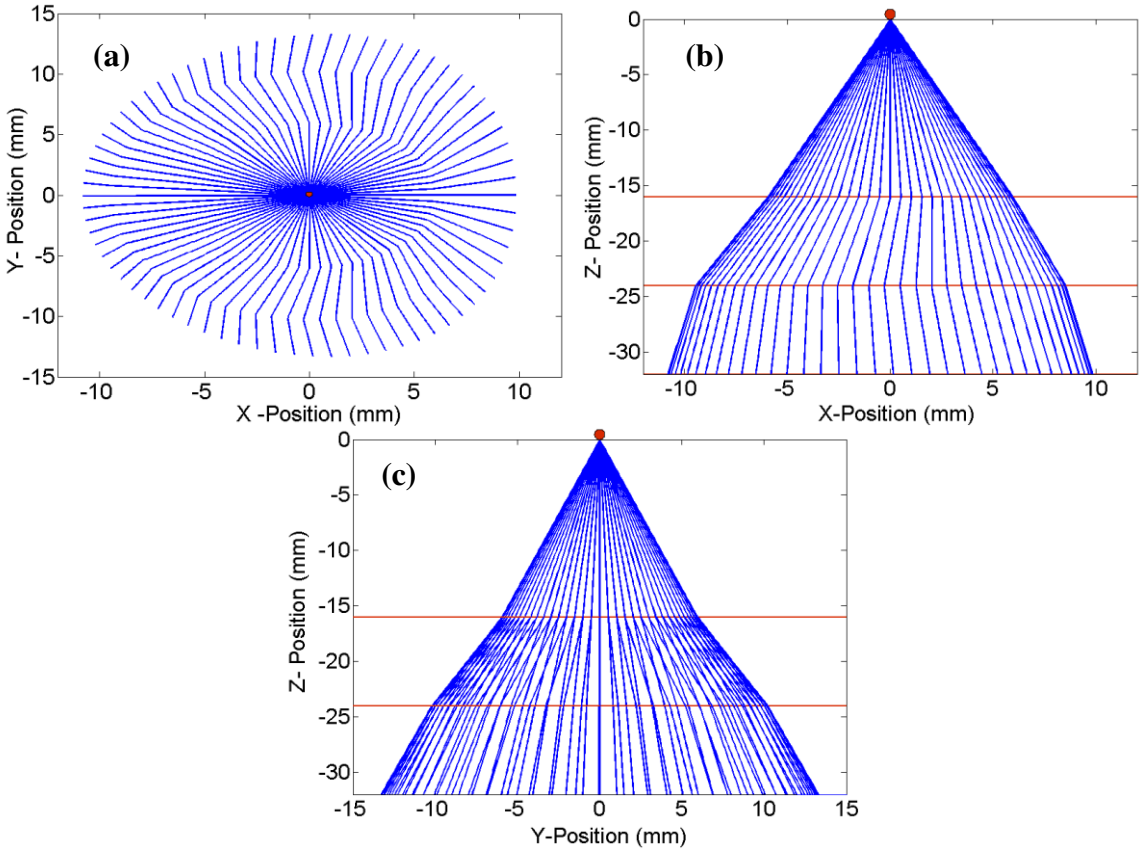

Figure 7.5: *3D ultrasonic ray propagation in 32 mm thick multi layered austenitic steel material. Calculated ray pattern along (a) XY plane, (b) XZ plane and (c) YZ plane. The polar angle for the ray tracing calculation is 20º and the azimuthal angular range is between 0º and 360º.*

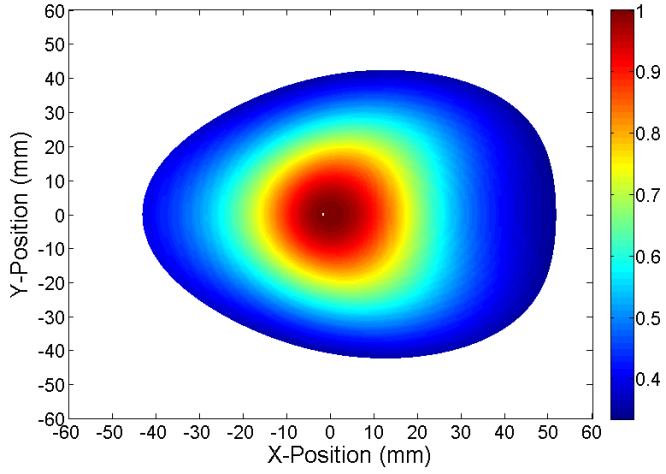

Figure 7.6: *The ultrasonic quasi longitudinal C-Scan image calculated for a normal beam contact transducer (2.25 MHz centre frequency and 0.1mm width) along the back wall surface of the multi layered anisotropic austenitic steel material using 3D ray tracing method.*

7.3 Comparison of Ray Tracing Model Results with CIVA Simulation Tool

In this section, the ray tracing model predictions on inhomogeneous anisotropic austenitic weld material are compared against those from CIVA, a commercial non-destructive modeling and simulation tool [151]. The reason for selecting CIVA tool for verifying the ray tracing model results is that CIVA model is successfully validated against experiments [152]. Although CIVA simulation tool is able to calculate the ultrasound fields in inhomogeneous materials, its calculation procedure is different from the presented ray tracing method in this thesis and it will be discussed in the next sections.

7.3.1 Description on CIVA Simulation Tool

The ultrasonic NDT simulation software CIVA uses the so-called "Pencil Method" for ultrasonic field computation [153]. Pencil method for computation of elastodynamic fields is an extension of Deschamps's formulations [154], originally derived for electromagnetic waves in isotropic media. A pencil is a bundle of rays emanating from a point source along the geometrical path (axial ray) and diverging slightly [92, 155], as demonstrated in Fig. 7.7. The paraxial rays on the pencil envelope can be described by a four-component 'pencil vector' ψ, where ds_x and ds_y are the x- and y-components of the slowness vector dS (see Fig. 7.7). Given the pencil vector at point 1, the pencil vector at point 2 may be calculated through the so called pencil propagation matrix L, as follows:

$$\Psi_2 = L \cdot \Psi_1 = \begin{bmatrix} A_{2\times2} & B_{2\times2} \\ C_{2\times2} & D_{2\times2} \end{bmatrix} \cdot \Psi_1 \tag{7.1}$$

where *A*, *B*, *C* and *D* are 2x2 matrices. The pencil propagation matrix *L* can be calculated [92] for propagation of a pencil into a homogeneous isotropic medium ($L_{\text{iso/homo}}$) and homogeneous anisotropic medium ($L_{\text{aniso/homo}}$). At an interface, points 1 and 2 are two points located immediately before and immediately after the interface.

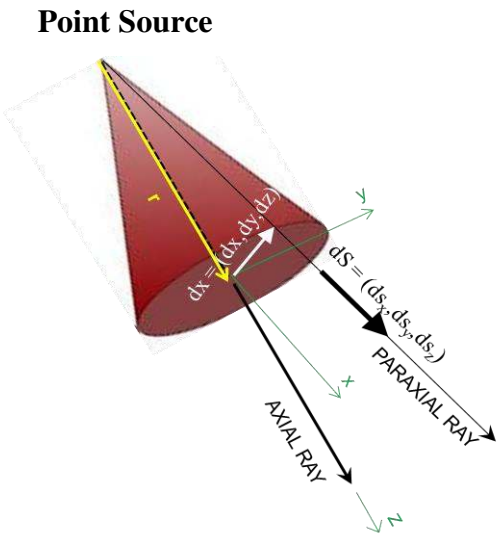

Figure 7.7: *Pencil Method for ultrasonic field computation [153].*

Transmission or reflection at a curved interface will be accounted for through $L_{interface}$. The energy loss due to transmission or reflection coefficients is not considered in the pencil propagation matrix [92]. Depending on the propagation path, the pencil propagation matrix corresponding to the ultrasonic wave propagation into anisotropic and heterogeneous media is established by combing the related pencil propagation matrices, as follows:

$$\Psi_{@\,\text{comp.pt.}} = L\Psi_{@\,\text{source}} = M \cdot L_{\text{iso v aniso/homo}}(1)\Psi_{@\,\text{source}} \tag{7.2}$$

$$M = \left(\prod_{i=1}^{n-1} L_{\text{iso v aniso/homo}}(i+1) \bullet L_{\text{interface}}(i) \right). \tag{7.3}$$

The divergence factor (*DF*), giving the evolution of amplitude, is derived from the pencil propagation according to:

$$DF^2 = s^2 \det\left(B_{2\times 2}\right) , \tag{7.4}$$

where *s* is the slowness in the medium of the source.

The loss of amplitude at encountered interfaces (due to transmission or reflection coefficients) is taken into account later by applying a factor to the final divergence factor. Combined with the classical Rayleigh integral to account for transducer diffraction, the pencil method can be used to predict the ultrasonic fields radiated into complex structures by arbitrary transducers [152]. Thus the ultrasonic modeling tools in CIVA are based on semi-analytical solutions. The CIVA model is specifically designed for the industrial context. The radiation of the transducer is described by a diffraction integral (i.e. Raleigh integral) and this integral is evaluated numerically. Generally the CIVA simulation is performed on CAD environment.

7.3.2 Comparison Results on Inhomogeneous Austenitic Weld Material

Figure 7.8 shows the geometry of the austenitic weld material and its inhomogeneous weld structure which is used for the present comparative study between ray tracing and CIVA model. The inhomogenity in the austenitic weld region is discretized into several homogeneous layers with different crystal orientations. The grain orientation in an each layer is determined using the mathematical function given by Ogilvy [77]. The detailed description on mathematical function was presented in chapter 5. The assumed base region of the austenitic weld material consists of fine grained austenitic steel material. The elastic parameters of the base material are considered same as that of isotropic steel material. The elastic constants and density of the transversal isotropic austenitic weld (X6 Cr Ni 18 11) are presented in Table 1.

The transducer used was a linear phased array longitudinal wave transducer of 2.25 MHz frequency from SONAXIS. The transducer consists of 16 elements, each 0.65 mm wide with 0.1 mm gap in between each pair of elements (incident dimension of 12 mm). A commercial angle beam array transducer (SONAXIS) is modelled which generates 42º longitudinal waves into the isotropic steel material. The transducer beam exit point is situated 22 mm away from the weld flank. The simulated weld grain model using mathematical function as described in Eq. (5.1) was designed in the CAD environment and it was implemented in the CIVA simulation tool.

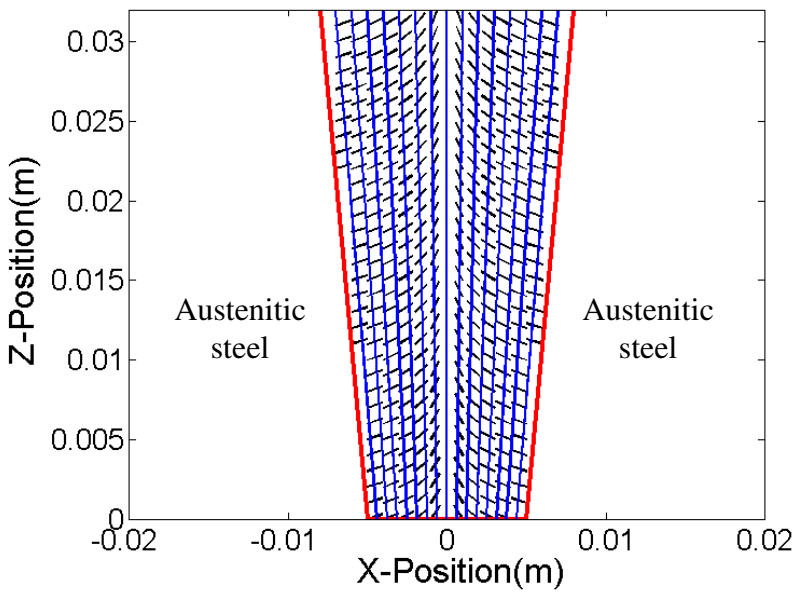

Figure 7.8: *Inhomogeneous weld structure of the austenitic weld material (X6CrNi1811) used for the ray tracing and CIVA comparisons. Weld boundary inclination angle = 5.4º. $T_1 = -T_2 = -0.54$, $D_1 = D_2 = 5$ mm, and $\eta = 1$ in Eq. (5.1).*

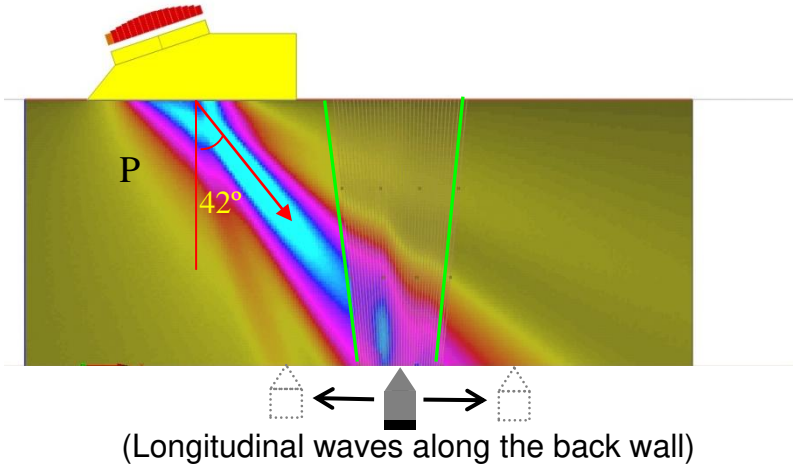

Figure 7.9: *Ultrasonic beam field calculation using CIVA simulation tool for the 42º P-wave angle beam transducer (2.25 MHz central frequency, 12 mm width) in the inhomogeneous austenitic weld material (X6CrNi1811).*

Figure 7.9 shows the beam field computation for the 42º longitudinal wave transducer in an inhomogeneous austenitic weld material using CIVA simulation tool. The ultrasonic beam field distortion can be visible at weld boundaries as well as inside the weld region. Figure 7.10 shows the comparison of normalized longitudinal wave displacements for the 42º P-wave transducer calculated along the back wall of the

austenitic weld material using ray tracing model (RTM) and CIVA simulation tool. A very good qualitative agreement between ray tracing model and CIVA simulation tool is achieved. The splitting of ultrasonic beam profile in the inhomogeneous weld region can be observed from both the models (see Fig. 7.10). The sudden fall of amplitudes outside the weld region (to the right) are observed in case of CIVA model because the beam field calculation using CIVA were performed with low beam divergence of the transducer. Quantitatively we observe a deviation of 8.86% at position 1 mm which is also a relative good quantitative result. It can be seen from Fig.7.10 that the maximum amplitude locations are differ by 0.5 mm. A minimum deviation of 1.88 % is observed at the weld flanks (see Table 15). Between the positions -5 mm and 0 mm, an accuracy of 89.5% is achieved in the ray tracing calculation. The differences (quantitatively a maximum deviation of 15. 95%) between ray tracing model and CIVA were observed and these are present because CIVA executes the beam field computation with a finite broadband pulse input whereas ray tracing model performs the calculations in its continuous wave mode (i.e. single frequency content in the input pulse).

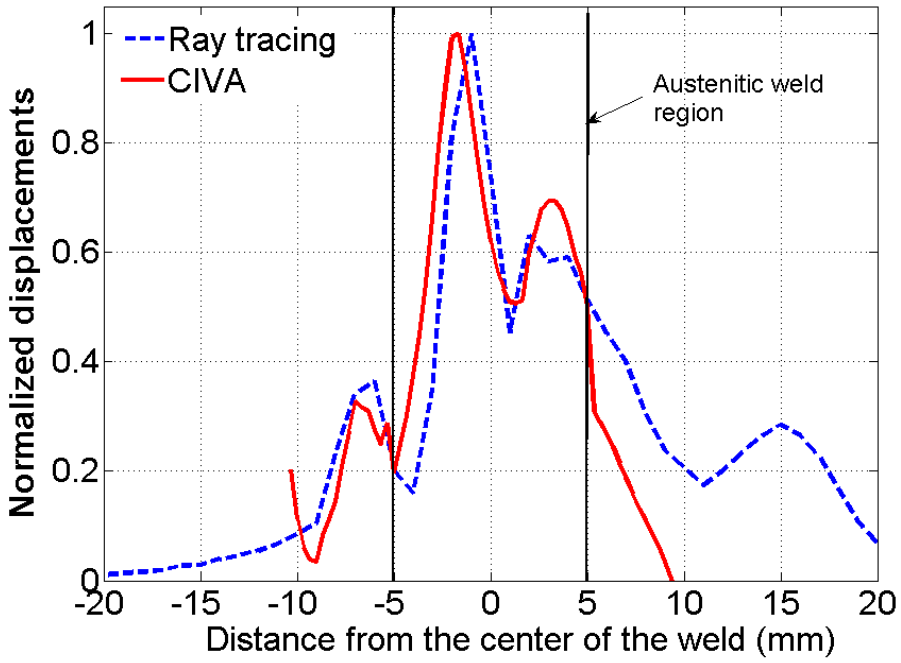

Figure 7.10: *Comparison of ultrasonic field profiles calculated using ray tracing model and CIVA simulation for the 42° P-wave angle beam transducer (2.25 MHz central frequency, 12 mm length) in the inhomogeneous austenitic weld material (X6CrNi1811).*

Table 15: *Comparison of ray tracing model (RTM) amplitudes with CIVA simulation at selected X-positions within the inhomogeneous austenitic weld material.*

Position (mm)	Quasi longitudinal wave amplitudes		Difference in amplitude	Error (%)
	RTM	CIVA		
-5	0.2005	0.1968	0.0037	1.88
1	0.4537	0.5086	0.0549	8.86
3	0.5835	0.6943	0.1108	15.95
5	0.5126	0.5022	0.0104	2.07

In this chapter, ultrasonic C-scan images in a homogeneous and multi layered anisotropic austenitic steel materials are quantitatively evaluated using 3D ray tracing method. The influence of columnar grain orientation and layback orientation on ultrasonic C-scan image in an anisotropic columnar grained austenitic steel material is investigated and its practical consequences to the ultrasonic non-destructive testing of anisotropic austenitic materials are presented. The anisotropic phenomenon such as beam focusing, beam splitting and beam spreading can be explained on the basis of predicted ultrasonic C-scan image. The calculated ultrasonic field profiles for the angle beam array transducer in an inhomogeneous austenitic weld material with spatially varying crystal orientation using ray tracing model are quantitatively compared with CIVA simulation results and achieved good agreement. This confirms the validity of the ray tracing model predictions in an inhomogeneous austenitic weld material. Comparison of ray tracing model results with experiments on real life austenitic weld materials will be presented in the chapter 8.

CHAPTER 8

Comparison of Ray Tracing Model Results with Experiments on Inhomogeneous Austenitic Welds

8.1 Introduction

In this chapter simulated ultrasonic fields using ray tracing model are compared quantitatively with the experiments in inhomogeneous austenitic welds and austenitic clad materials. Experimental technique used for the ultrasound field measurements in austenitic welds and clad materials is discussed. Approximate evaluation of crystal orientations in the austenitic weld material based on Ogilvy's [77] mathematical empirical relation is presented. Finally, the reasons for differences between ray tracing model and experiments are discussed.

8.2 Experimental Set up and Data Acquisition

8.2.1 Investigated Samples

In order to compare the ray tracing model results with experiments, two different specimens are considered. A 32 mm thick austenitic weld material and a 62 mm thick austenitic clad material were used for quantitatively evaluating ultrasound field profiles along the back wall. In case of austenitic clad component the interface between isotropic steel and anisotropic austenitic steel is situated at 50 mm depth. The more detailed description of weld parameters, transducer specifications and elastic constants are discussed in the Section 8.3.

8.2.2 Experimental Technique

Experimental technique involved in measuring the ultrasound field profiles consists of a piezo-electric transducer (acting as transmitter) and it is attached on the fixed position on the inspected test specimen and an electro dynamical probe (acting as receiver) scanning along the back wall surface of the test specimen.

Measuring principle of an electrodynamic probe:

The electrodynamic probe transforms the particle displacement at a conductive testing surface into a voltage which scales proportional to the particle velocity [156, 157]. Fig. 8.1(a) shows the generation of eddy currents using the electrodynamic probe. The mechanism is based on a permanent magnetic field, which is applied to the conductive surface area. When the ultrasonic wave is moving through this magnetic field, eddy currents are generated by the particle displacement as shown in Fig. 8.1(a). The physical principle behind this effect is based on the Lorentz force and can be observed for moved electrical conductors in a magnetic field like an eddy current brake or an electric generator. The generated eddy currents in turn cause an alternating magnetic field above the sample's surface. This alternating magnetic field strength then can be detected by a detection coil as shown in Fig. 8.1(b). The induced voltage in the coil scales proportional to the particle velocity. The voltage can be determined as a function of time with any ultrasonic device using a simple preamplifier for impedance adaption. Therefore the application of electrodynamic probe is very cost-efficient.

Significant advantages of an electrodynamic probe as compared to existing techniques:

There exist a number of different methods for visualizing the ultrasound fields such as Schlieren-technique [158, 159] and laser vibrometer [160, 161]. The reason for selecting the electrodynamic probe for the experiments is that the electrodynamic technique requires no particular material properties, such as transparent media in the case of Schlieren-technique and well-reflecting surfaces in case of laser vibrometer. The previous studies [162] proved that the electrodynamic probes in some special experimental arrangements can also be able to visualize sound waves in non-conductive materials. In contrast to other visualization techniques the electrodynamic probes can detect particle displacements in all three spatial directions. Furthermore they provide a high bandwidth yielding a high SNR even when using high frequencies. Thus the electrodynamical probes can be used as a cheap and easy-to-handle alternative to laser techniques and other optical approaches.

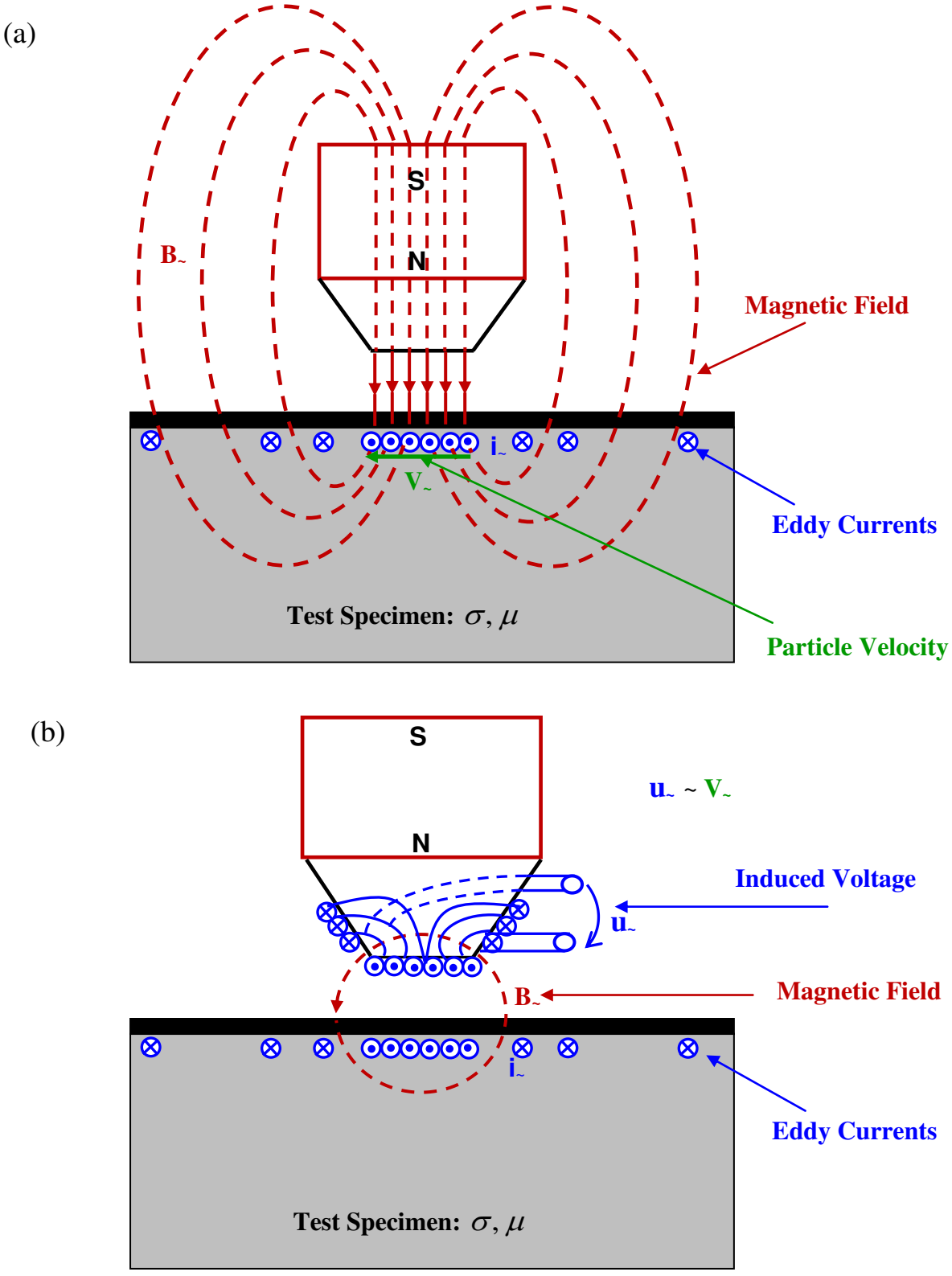

Figure 8.1: *Principle of the electrodynamic probe (a) generation of eddy currents and (b) measurement of eddy currents.*

Data acquisition system contains in house developed Compas XL which can send and receive the data through maximum of 128 channels and process the captured experimental data [163]. The sketch of the laboratory based experimental setup is shown in Fig. 8.2. The photograph of the automated ultrasonic phased array device and transducers used for the sound field measurements are shown in Fig. 8.3 and Fig. 8.4.

8.2.3 Experiments

For the ultrasonic field measurements, a linear array transducer with 16 elements, a centre frequency of 2.25 MHz and length of 12 mm was used to emit the ultrasound pulse into the 32 mm thick anisotropic austenitic weld material as well as a 62 mm thick austenitic clad component and the ultrasound field profiles along the back wall surface is scanned using an electrodynamic probe.

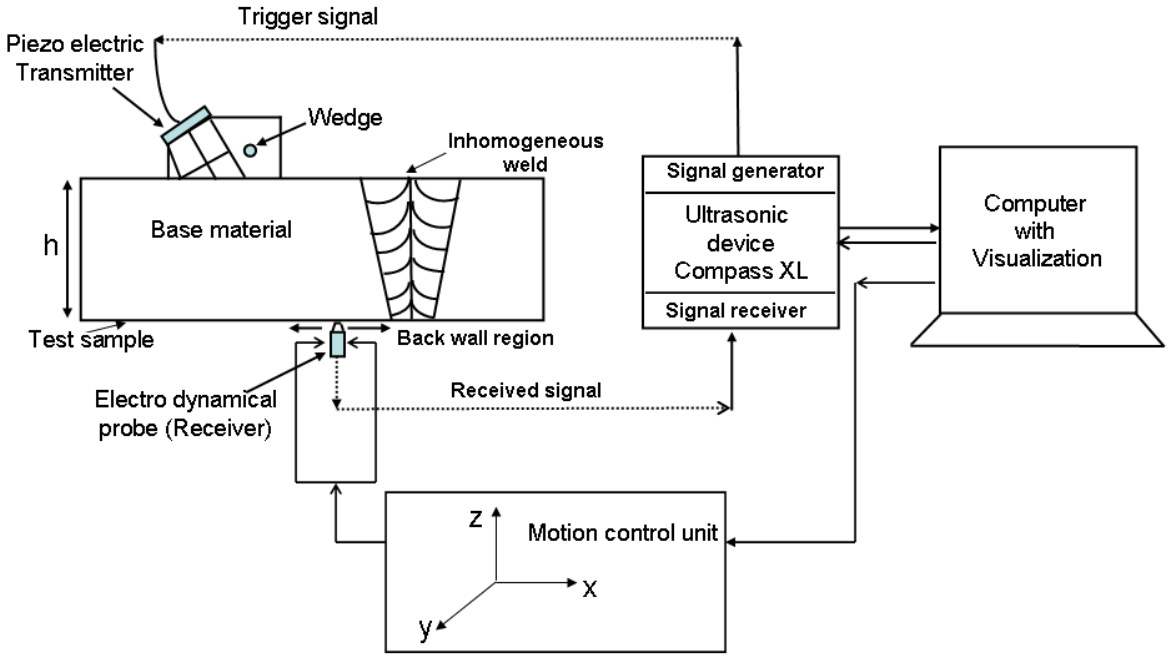

Figure 8.2: *Schematic of the experimental set up used for ultrasound field measurements*.

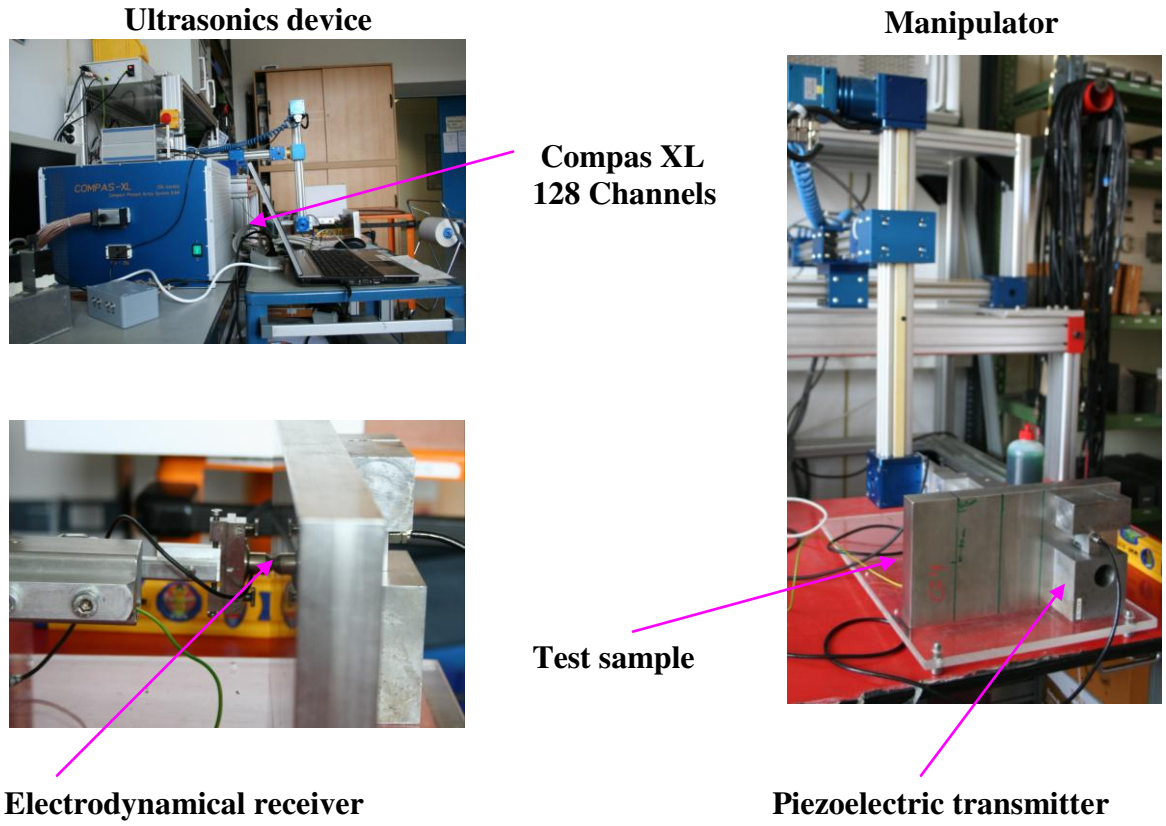

Figure 8.3: *Photograph of the automated phased array ultrasonic device used for the ultrasonic field measurements*

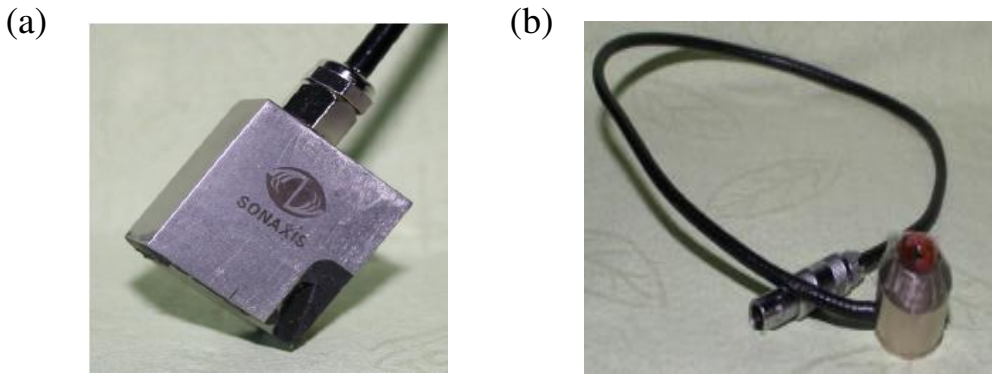

Figure 8.4: *Photograph of the (a) 16 element phased array transducer (transmitter), (b) electro dynamical probe (receiver) used for the ultrasonic field measurements.*

The following four experiments are performed in order to compare the ray tracing model results

- A phased array transducer was used to generate a longitudinal normal beam and it is mounted on the base material of the austenitic weld component and the ultrasound field profile was measured along the back wall surface (homogeneous region of the test specimen)
- A phased array transducer was used to generate a 34° longitudinal beam and it is mounted on the base material (14 mm away from the weld centre line) and the ultrasound field profiles are measured along the back wall surface (including both homogenous base material and inhomogeneous weld region)
- A phased array transducer was used to generate a 42° longitudinal beam and it is mounted on the base material (22 mm away from the weld centre line) and ultrasound field profiles are measured along the back wall surface (including both homogenous base material and inhomogeneous weld region)
- A phased array transducer was used to generate a longitudinal normal beam and it is mounted on the base material of the austenitic clad component. The ultrasound field profiles are measured along the back wall surface.

8.3 Comparison Results

In this section the ray tracing model results are compared with experiments on several configurations generally occurring during the ultrasonic non-destructive evaluation of inhomogeneous anisotropic materials such as austenitic weld materials and austenitic clad materials.

8.3.1 Austenite Base Material

The first experimental comparison with ray tracing model was carried out on the base material of the austenitic weld component. First we investigated the base material of the austenitic weld component which is essential to obtain the material thickness and the ultrasonic field distribution in the base material.

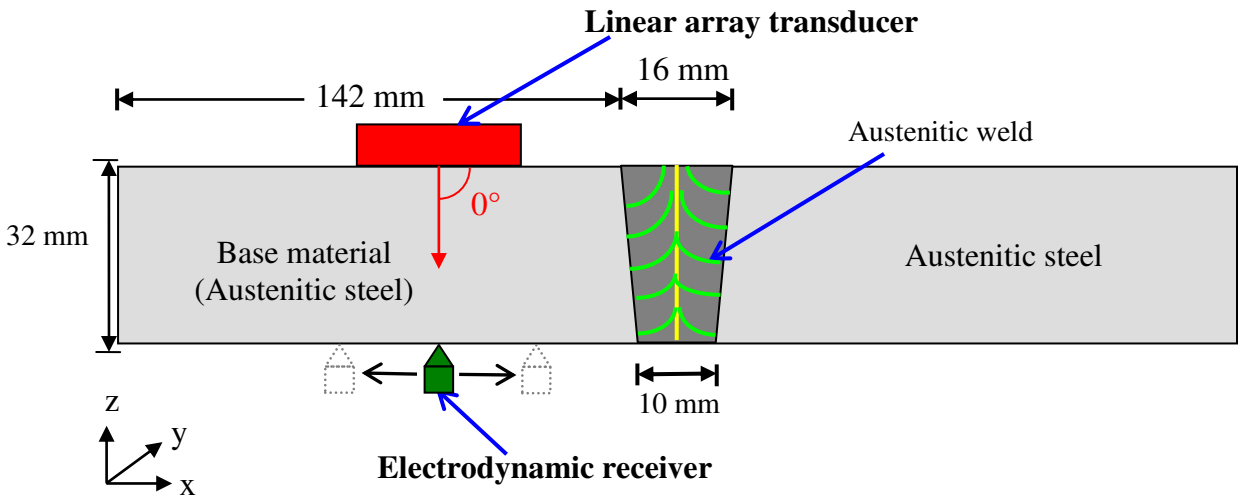

Figure 8.5: *Geometry used for the ultrasound field measurements in the austenite base material*

In the ray tracing model, it is assumed that the parameters of the base material (i.e. fine grained austenitic steel material) are same as that of the isotropic steel material. The material properties of the isotropic steel material are presented in Table 1. Fig. 8.5 shows the geometry used for the ultrasound field measurements in the austenitic base material.

Fig. 8.6(a) shows the measured C-scan image along the back surface of the isotropic austenitic base material. It is obvious from Fig. 8.6(a) that the base material of the austenitic weld shows nearly uniform distribution of the sound fields and it confirms that the base material exhibits isotropic material behavior. Fig. 8.6(b) shows a comparison of simulated longitudinal field profile distribution along the back wall of the austenite base material with the experimental amplitudes. An excellent qualitative agreement between simulated and experimentally evaluated beam profiles is achieved. Table 16 shows the comparison of ray tracing and experimental amplitudes at selected positions in Fig. 8.6(c). Quantitatively we observe a deviation of 4.78% at position 3.5 mm which is also a relative good quantitative result. Between positions -6.5 mm and 6.5 mm an accuracy of 93.5% is achieved in the ray tracing results. At position 10 mm we observe a maximum amplitude difference of 0.0798 which is due to the single frequency assumption in the ray tracing simulation. It can be seen from Fig. 8.6(b) that the amplitude deviations occur only in the

side lobes. This is due to the large frequency bandwidth of the transducer signal which reduces the side lobe amplitudes.

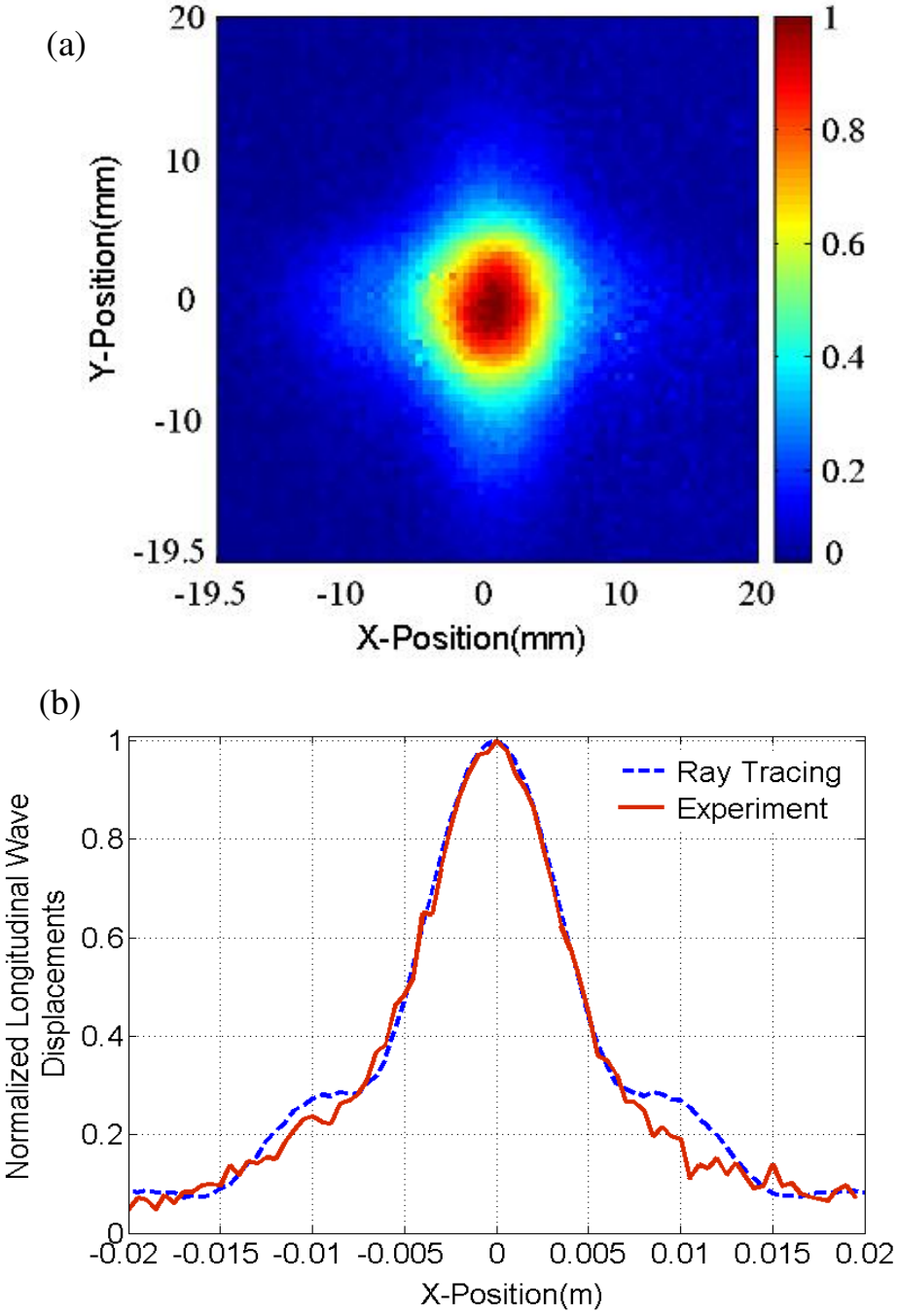

Figure 8.6: *(a) Experimental C-scan image at the back wall surface of the base metal of the austenitic weld component using longitudinal normal beam contact transducer (2.25 MHz frequency, 12 mm width) and (b) comparison of 2D ray tracing model and experimental results for ultrasound field profile distribution at the back wall. Amplitudes are extracted from the experimental C-Scan at y = 0.*

Table 16: *Comparison of ray tracing model (RTM) amplitudes with experiments at selected X-positions within the isotropic austenitic steel material.*

Position (mm)	Longitudinal wave amplitudes		Difference in amplitude	Error (%)
	RTM	Experiment		
-10	0.2730	0.2363	0.0367	15.53
-5	0.4713	0.4822	0.0109	2.26
3.5	0.6545	0.6246	0.0299	4.78
18.5	0.08245	0.08692	0.0045	5.14

8.3.2 Austenitic Weld Material

The second experimental comparison of ray tracing model was carried out on 32 mm thick austenitic weld component. The material properties of the transversely isotropic austenitic weld component are assumed same as that of austenitic steel X6 Cr Ni 18 11 which are described in Table 1. A 34º longitudinal wave angle beam transducer of 2.25 MHz central frequency and 12 mm length of active transducer area was used to excite the ultrasonic pulse on the base material of the inhomogeneous and anisotropic austenitic weld specimen and ultrasound field profiles along the back wall surface (includes weld region) were measured with the help of electrodynamical probes. The transducer beam exit position is situated 14 mm away from the weld centre line. The main intention of this experimental investigation was to visualize the ultrasonic beam distortion due to complex microstructure of the austenitic weld. Figure 8.7 shows the geometry of the austenitic weld component and location of the transmitter beam exit point used for the measurements.

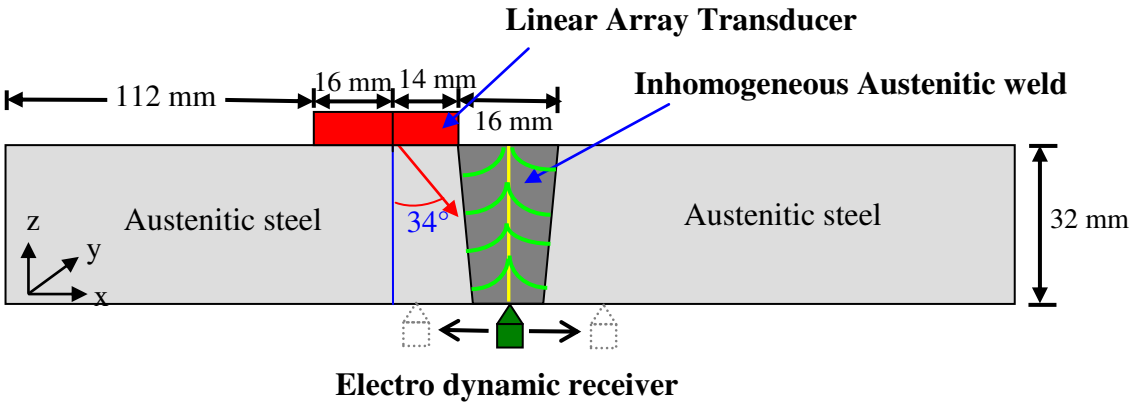

Figure 8.7: *Geometry of the austenitic weld component and location of the transmitter used for the sound field measurements*

Optimization of weld structure model for obtaining crystal orientations in the austenitic weld:

The following procedure was used for obtaining approximate crystal orientations in the austenitic weld specimen:

(1) the weld parameters D_1, D_2, α_1 and α_2 in the mathematical function G(x,z) as described in Eq. 5.1 were obtained directly by careful observation in the real austenitic weld specimen and these parameters are $\alpha_1 = \alpha_2 = 5.36°$, $D_1 = D_2 = 5$ mm, which are input for the weld structure simulation,

(2) the parameter η is set to be 1 in the simulation. The reason for setting $\eta = 1$ is described in section 5.3,

(3) the parameters T_1 and T_2 in Eq. (5.1) are varied until an optimum match was reached between the modelled grain structure and macrograph of the austenitic weld specimen.

Figure 8.8 shows the comparison between simulated weld structure and macrograph of the austenitic weld specimen for different T_1 and T_2 values. It can be seen from Fig. 8.8 that the simulated microstructure of the weld for the low T_1 and T_2 values shows low variations in the crystal orientations from weld flank to the weld center. By increasing the T_1 and T_2 values, the variation in the simulated crystal orientations increases and at an optimum T_1, T_2 values the simulated weld structure matches approximately with the grain orientations in the macrograph of the weld as shown Fig. 8.8 (g).

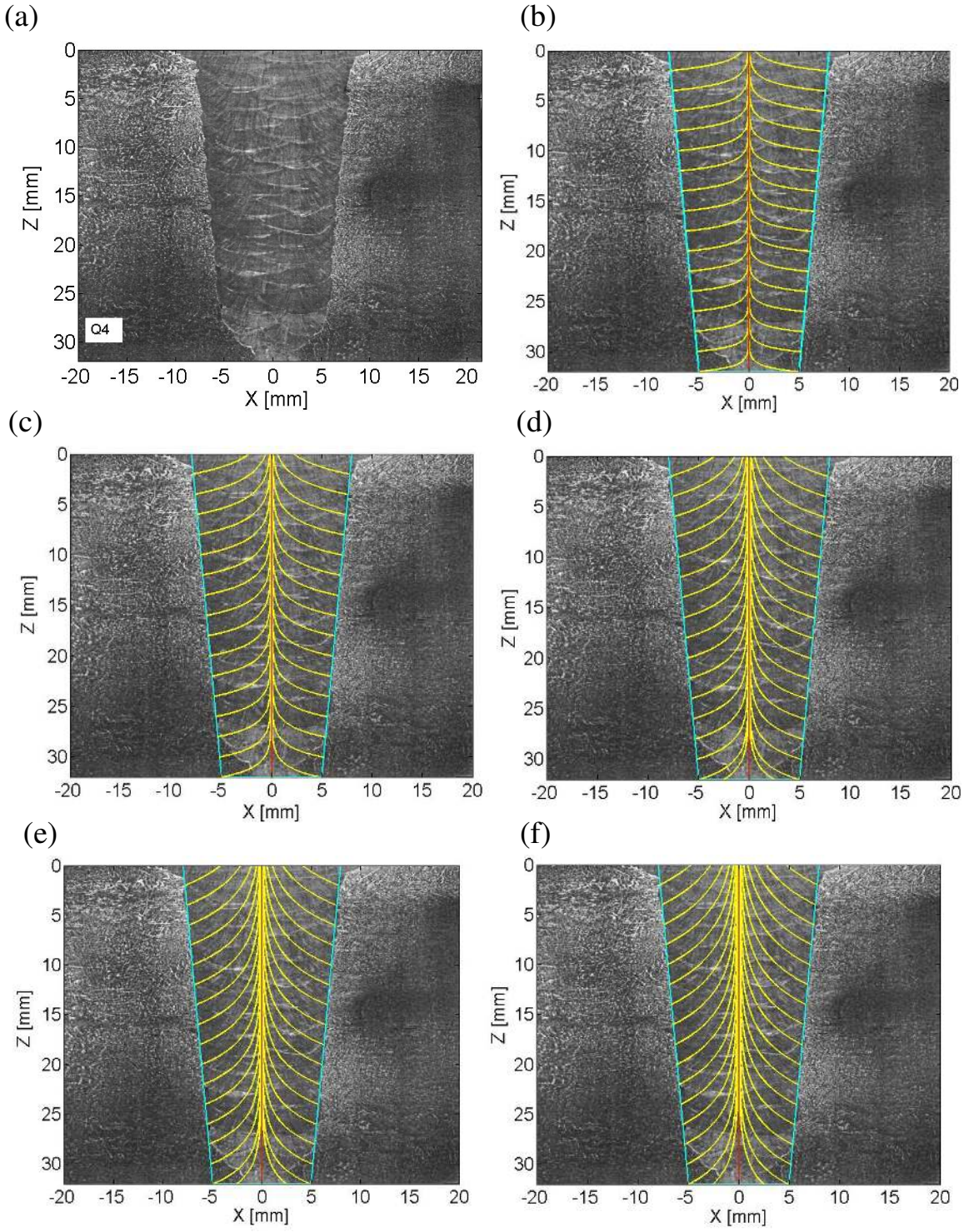

Figure 8.8: *Optimization of the weld model parameters for obtaining real crystal orientations in the austenitic weld material (a) macrograph of the austenitic weld. The comparison between weld structure model and micrograph by varying T_1, T_2 values in Eq. 5.1. (b) $T_1 = -T_2 = -0.1$, (c) $T_1 = -T_2 = -0.2$, (d) $T_1 = -T_2 = -0.3$, (e) $T_1 = -T_2 = -0.4$ and (f) $T_1 = -T_2 = -0.5$.*

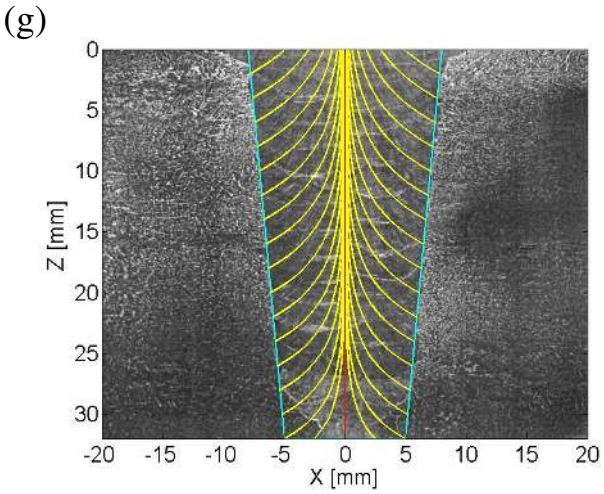

Figure 8.8: *Continued the optimization process (g) $T_1 = -T_2 = -0.54$ in Eq. 5.1.*

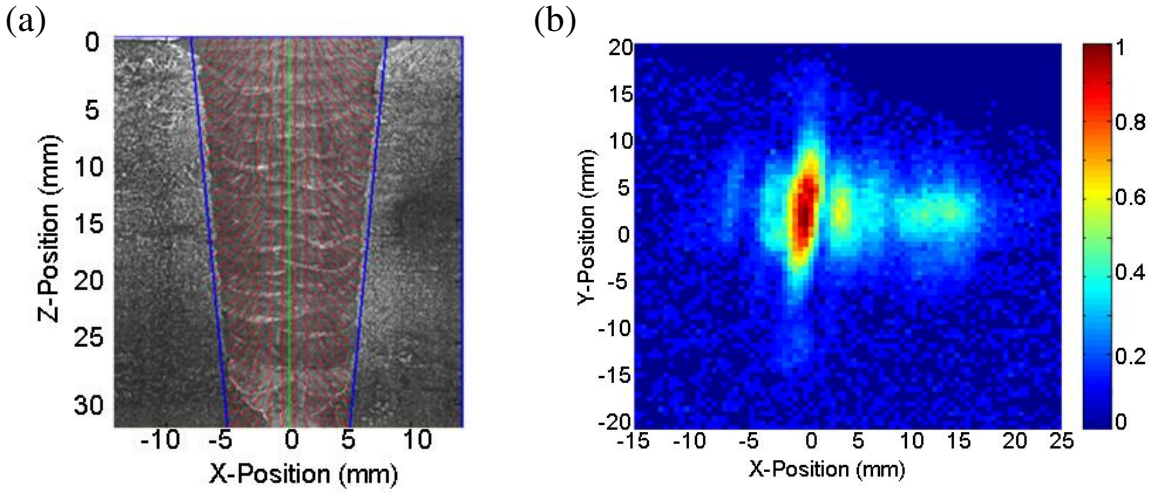

Figure 8.9: *(a) Inhomogeneous austenitic weld structure model for the test specimen and (b) experimental C-scan image at the back wall surface of the austenitic weld component using 34º longitudinal angle beam contact transducer (2.25 MHz frequency, 12 mm width).*

Fig. 8.9(a) shows the grain structure model used for the austenitic weld specimen. Weld parameters are optimized in the empirical relation given in Eq. (5.1) such a way that to match with the macrograph of the austenitic weld specimen. Fig. 8.9(b) shows the C-scan image measured along the back wall surface of the austenitic weld material in order to visualize the ultrasound beam distortion. As expected, the shape of the ultrasound field pattern was distorted due to the inhomogenity of the austenitic weld material (see Fig. 8.9(b)). The severity of ultrasound field distortion depends on the anisotropy of the inhomogeneous austenitic weld material.

Fig. 8.10(a) shows the ray path behavior for the 34º longitudinal wave finite aperture transducer in an inhomogeneous austenitic weld material. The finite aperture transducer of length 12 mm is divided into 16 point sources.

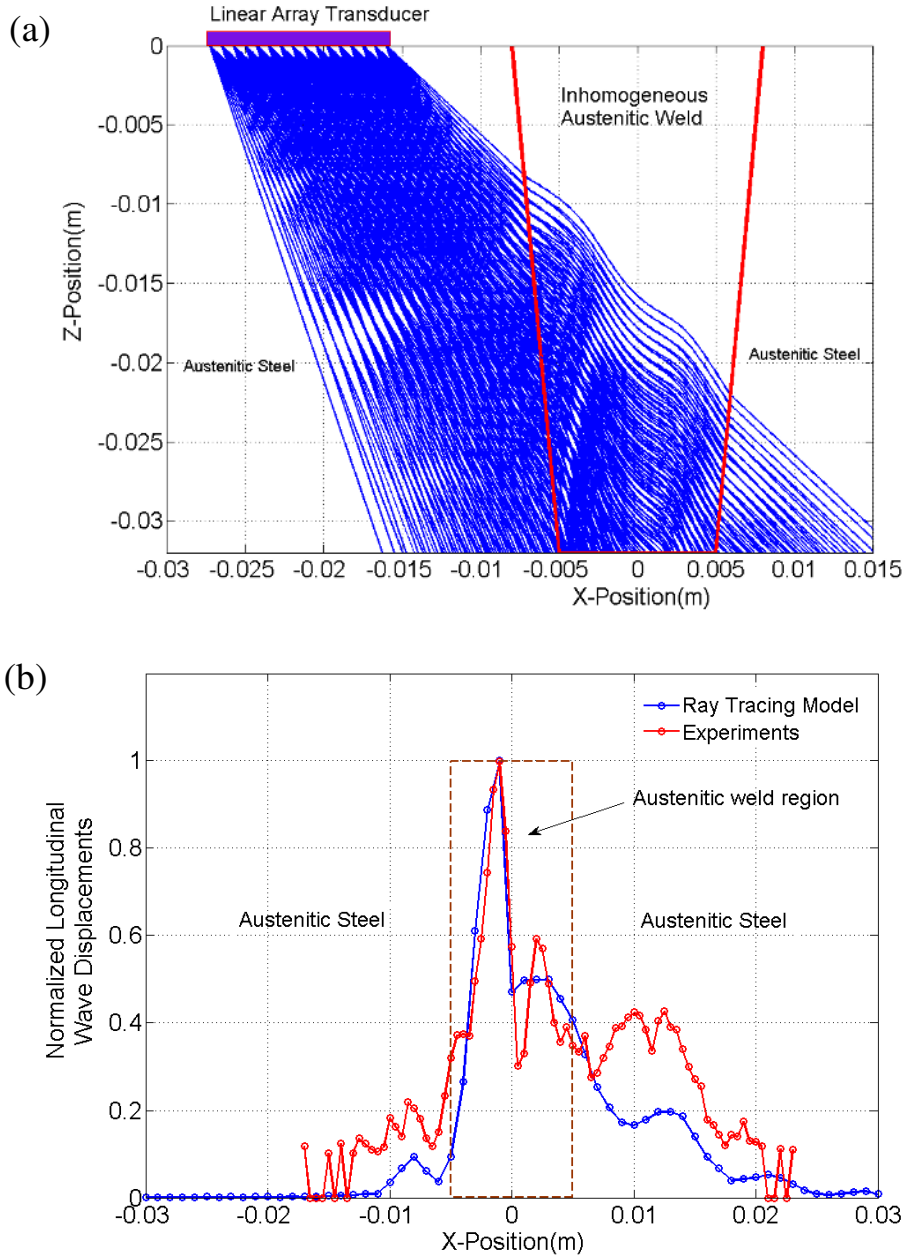

Figure 8.10: *(a) Ray tracing pattern for the 34º longitudinal angle beam array transducer (16 elements), (b) comparison of ray tracing model and experimental results for ultrasound field profile distribution at the back wall surface of the inhomogeneous austenitic weld material. Amplitudes are extracted from the experimental C-Scan (see Fig. 8.9(b)) at y = 0.*

Importance of density of rays in the ray amplitude calculation:

The procedure for evaluating ray amplitudes in an anisotropic layered austenitic material is presented in Chapter 6, which takes into account directivity, transmission coefficients, and phase information of the ray. It can be observed from Fig. 8.10(a) that the ray density at each cell along the back wall is not equally distributed. Therefore, density of rays should be calculated at each discretized cell for calculating realistic ray amplitudes in inhomogeneous weld materials. Figure 8.11 illustrates the importance of ray density along the back wall of the specimen. As an example in Fig. 8.11 the final ray amplitude in the cells 7 and 8 can be expressed as

$$A = \frac{A_1 + A_2 + A_3 + A_4 + A_5}{5}, \tag{8.1}$$

$$C = \frac{C_1 + C_2 + C_3}{3}. \tag{8.2}$$

The superposition of ray amplitudes in a cell leads to constructive or destructive interference depending on the phase of an each ray. If the two rays carry equal amplitudes with opposite phases, then the resulted amplitude becomes zero as shown in Fig. 8.11.

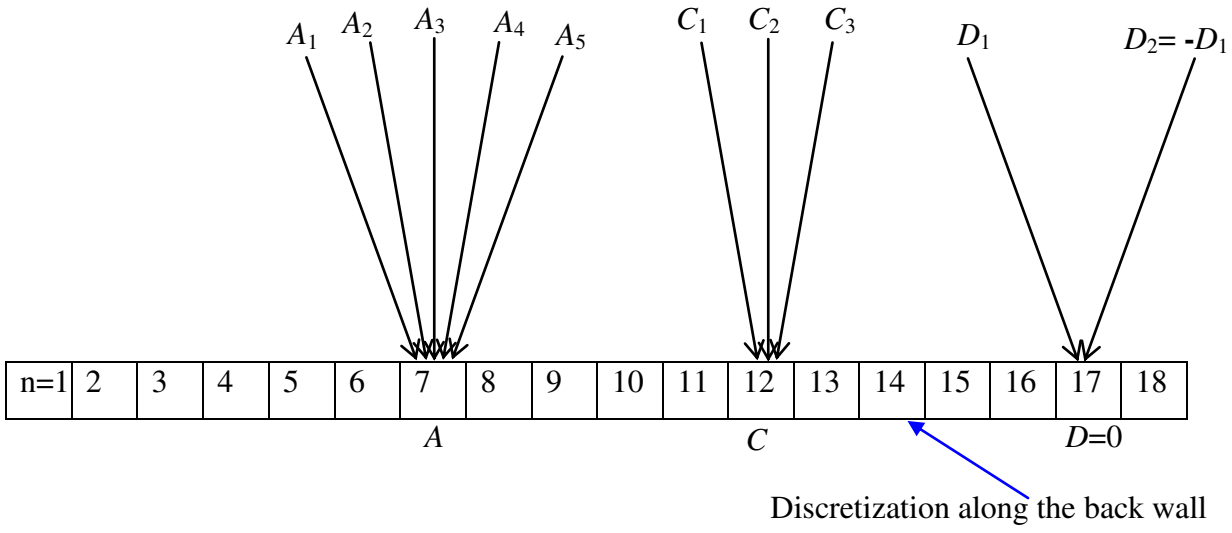

Figure 8.11: *Illustration of importance of density of rays along the back wall in evaluating ultrasonic ray amplitudes. n is the cell number. A, C and D represent the final ray amplitudes.*

Thus, the density of rays plays a key role in evaluating final ray amplitudes along the back wall of the austenitic weld material.

Figure 8.10(b) shows the comparison of normalized normal component of longitudinal wave displacements along the back wall of austenitic weld material simulated from ray tracing model with that of experimental results. A good qualitative agreement was achieved. Locations of the maximum amplitudes and main lobe predicted from the ray tracing model have shown good agreement with the experimental results. Table 17 summarizes the comparison of ray tracing amplitudes with experiments at selected positions within the inhomogeneous austenitic weld material.

Quantitatively we observe a deviation of 15.86% at position 2 mm which is also a relative good quantitative result. At position 16 mm which is far away from the weld region (i.e. beyond 5 mm), a maximum amplitude difference of 0.0847 is noticed. It can be seen from Fig. 8.10(c) that the experimental result shows a drop in amplitude near the weld centre. Additionally, at position 2.3 mm the experimental result shows second peak in the amplitude profile and it is not observed in the ray tracing results. The reason for discrepancies between experiments and simulation will be discussed in next sections.

Table 17: *Comparison of ray tracing model (RTM) amplitudes with experiments at selected X-positions within the inhomogeneous austenitic weld material for the case of 34°longitudinal wave incidence*.

Position (mm)	Longitudinal wave amplitudes		Difference in amplitude	Error (%)
	RTM	Experiment		
-4	0.2659	0.3721	0.1062	28.54
2	0.4995	0.5937	0.0942	15.86
5	0.4061	0.3488	0.0573	16.42
7	0.2539	0.2868	0.0329	11.47

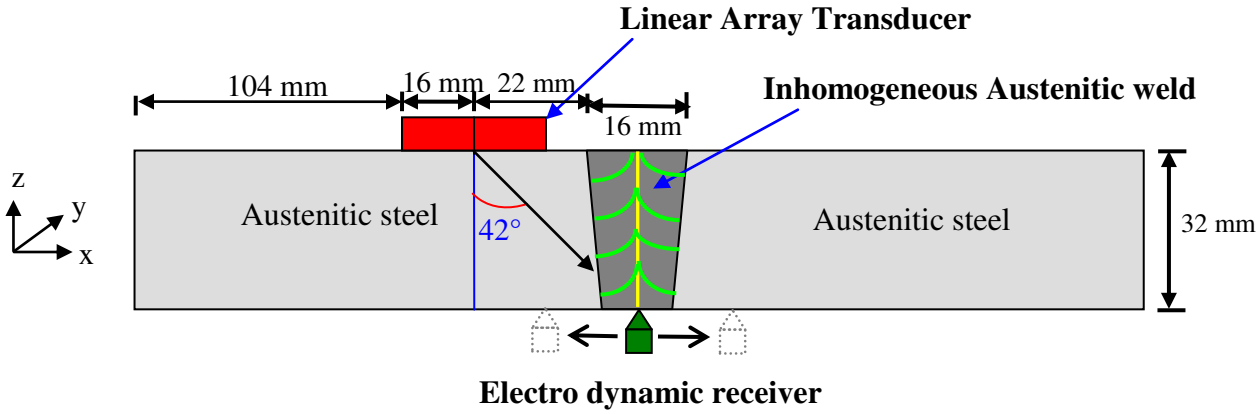

Figure 8.12: *Geometry of the austenitic weld component and location of the transmitter used for the sound field measurements.*

In order to verify the reliability of the ray tracing model results, simulated ultrasonic fields are compared with the measurement results for the different transducer parameters. The selection of transducer incident angle and location of the beam exit position are optimized based on the ray tracing model calculations. From the ray tracing model, it is predicted that for the 42º incident angle (instead of 34°) and 22 mm separation between transducer beam exit point and weld boundary are the optimal parameters for injecting ultrasonic beam into the weld root of the austenitic weld material. Fig. 8.12 shows the geometry of the austenitic weld component and transducer parameters used for the ultrasonic field measurement along the back wall. Grain structure used for the ray tracing model calculations is shown Fig. 8.9(a).

Fig. 8.13 shows the experimental ultrasonic C-scan image at the back wall surface of the austenitic weld material using 42º longitudinal angle beam transducer. It can be seen from Fig. 8.13, that the significant ultrasonic displacements are noticed near the weld root region which is qualitatively visualized from the ray tracing predictions. Splitting of ultrasonic beam in the austenitic weld region is apparent from the Fig. 8.13. One can observe a non-uniform distribution of the particle displacements in the measurement area which is due to anisotropic inhomogeneous material properties of the austenitic weld.

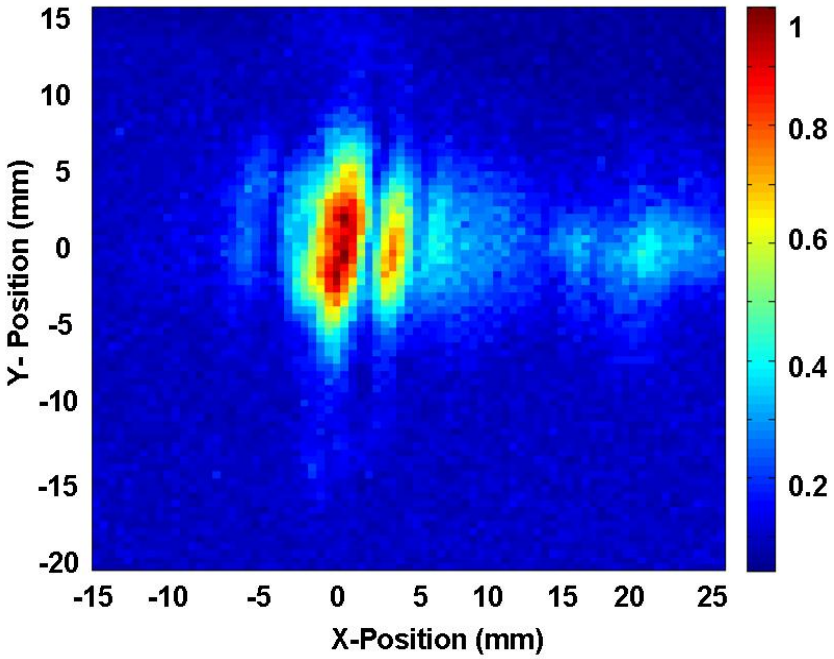

Figure 8.13: *Experimental C-scan image at the back wall surface of the austenitic weld component using 42º longitudinal angle beam contact transducer (2.25 MHz frequency, 12 mm length of active transducer area).*

Fig. 8.14(a) shows, predicted ray pattern for the 42º longitudinal angle beam transducer in inhomogeneous austenitic weld material. The transducer is situated 22 mm away from the weld centre line. It is obvious from Fig. 8.14(a) that the ray density is more in the austenitic weld region. Figure 8.14(b) shows the comparison of normal component of longitudinal wave displacements along the back wall of austenitic weld material simulated from ray tracing model with that of experimental results. A good qualitative agreement was achieved. Location of the maximum amplitudes and main lobe as well as side lobes predicted from the ray tracing model has shown good agreement with the experimental result. The reasons for minor differences will be discussed in section 8.4. Table 18 summarizes the comparison of ray tracing amplitudes with experiments at selected positions within the austenitic weld material.

Quantitatively we observe a deviation of 23.69% at position 5 mm. A shift of 0.5 mm in the maximum amplitude location is noticed in the ray tracing calculation (see 8.14(b).

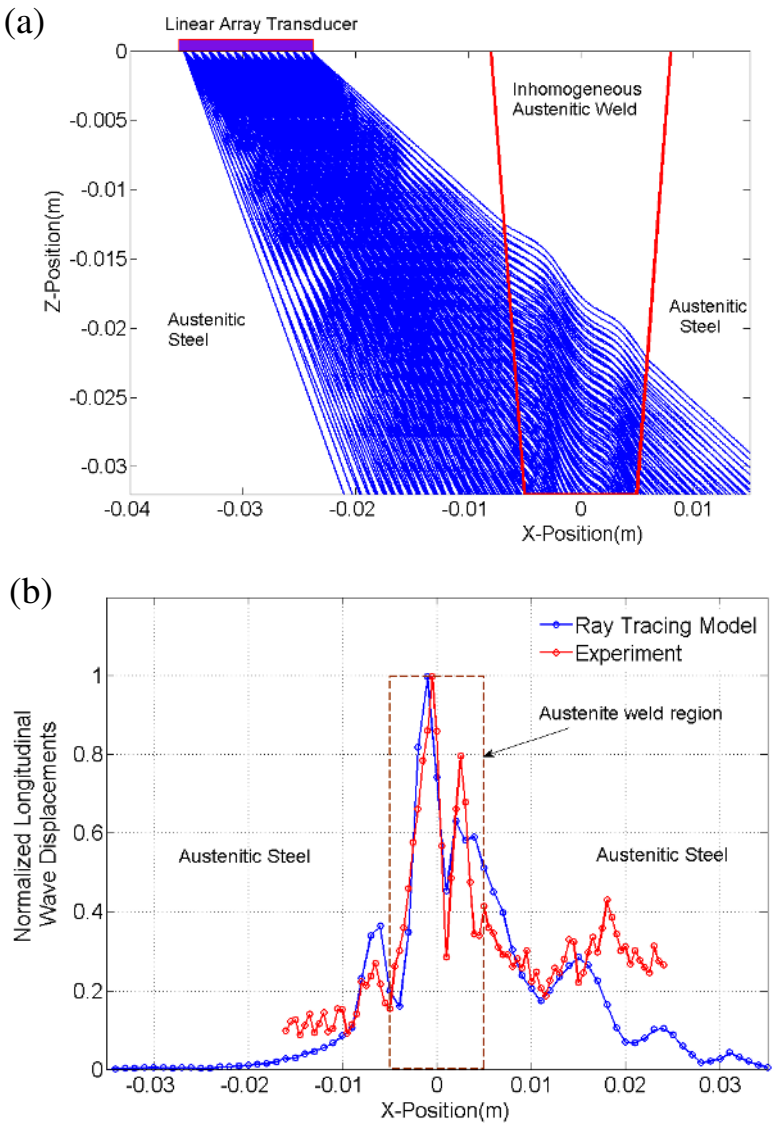

Figure 8.14: *(a) Ray tracing pattern for the 42º angle (P-wave) beam array transducer (16 elements), (b) comparison of ray tracing model and experimental results for ultrasound field profile distribution at the back wall surface of the inhomogeneous austenitic weld material.*

Furthermore, the side lobes are noticeable from both ray tracing and experiments. A minimum deviation of 6.92% is observed at position -10 mm which is also a relative good quantitative result. It is obvious from Fig. 8.14(b) that the ray tracing amplitudes agree well for positions left to the weld centre whereas for positions right to the weld centre we observe more differences (quantitatively an amplitude difference of 0.1688). The main reasons for discrepancies between simulation and experiments will be discussed in Section 8.4.

Table 18: *Comparison of ray tracing model (RTM) amplitudes with experiments at selected X-positions within the inhomogeneous anisotropic austenitic weld material for the case of 42° longitudinal wave incidence.*

Position (mm)	Longitudinal wave amplitudes		Difference in amplitude	Error (%)
	RTM	Experiment		
-8	0.2323	0.2225	0.0098	4.4
- 5	0.2005	0.1541	0.0464	30.11
3	0.5835	0.6793	0.0958	14.1
5	0.5126	0.4144	0.0982	23.69
10	0.2061	0.2229	0.0168	7.53

8.3.3 Austenitic Clad Material

The fourth experimental comparison of an ray tracing model was carried out on 62 mm thick austenitic clad component where we used 50 mm as isotropic steel material and 12 mm as anisotropic austenitic clad region. The assumed columnar grain orientation in the austenitic clad region is 45°. The geometry of the austenitic clad material is depicted in Fig. 8.15(a). Fig. 8.15(b) shows the measured B-scan image along the back wall surface of the austenitic clad component due to normal beam contact transducer excited on isotropic steel material of the austenitic clad component.

From the Fig. 8.15(b), we observed that the most of the ultrasound field was concentrated in the probe centre region. The columnar grain orientation of 45° in the ray tracing model was considered based on the experimental observation. The assumed material parameters of the isotropic base and anisotropic clad material in the ray tracing simulations are taken same as those of fine grained steel material and transverse isotropic austenitic steel material respectively which are listed in Table 1.

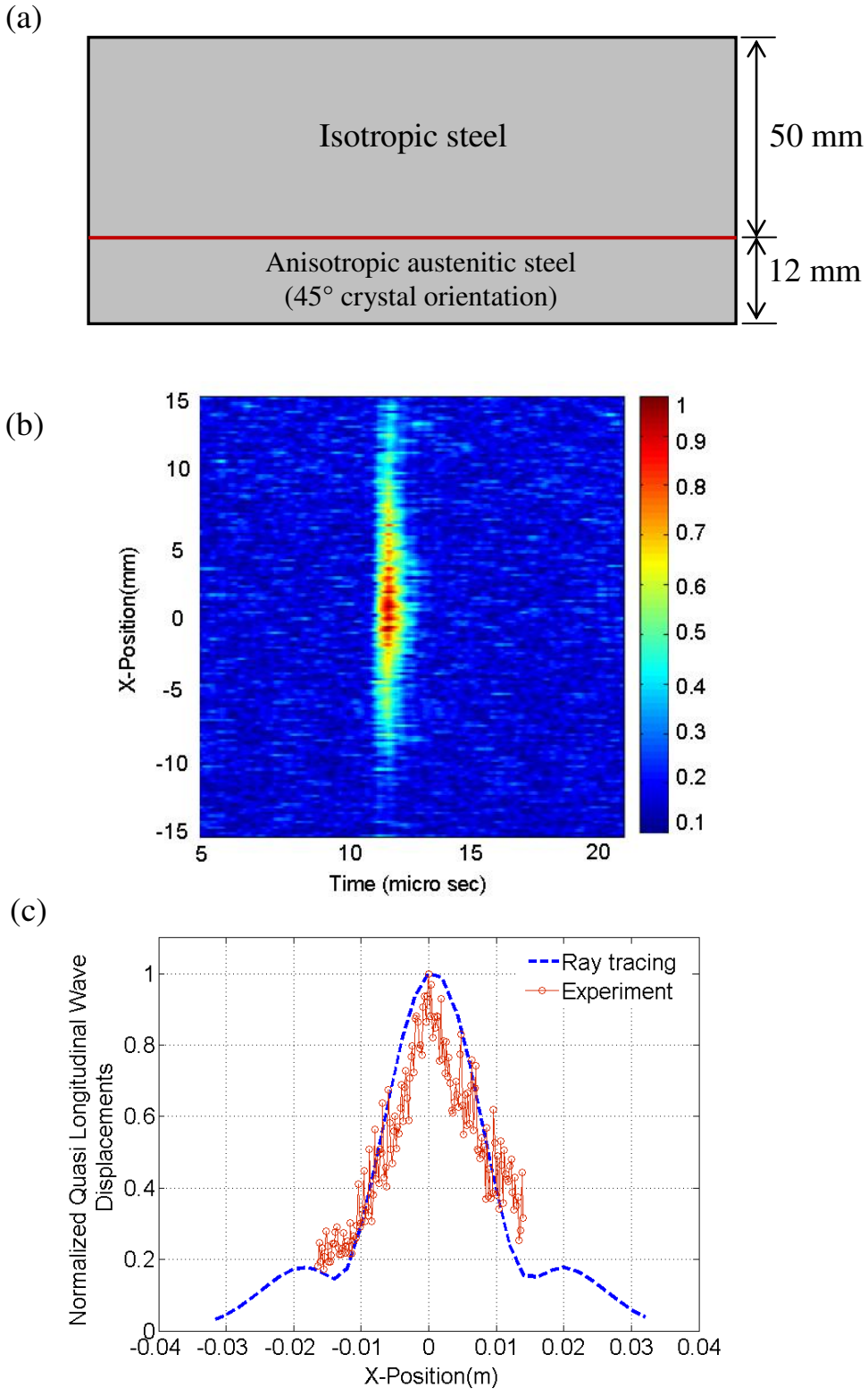

Figure 8.15: *a) Geometry of the test specimen, b) experimental B-scan image at the back wall of the 62 mm thick anisotropic austenitic clad component using longitudinal normal beam contact transducer (2.25 MHz frequency, 12 mm length of active transducer area) and c) comparison of 2D ray tracing model and experimental results for ultrasonic field profile distribution at the back wall.*

Table 19: *Comparison of ray tracing model (RTM) amplitudes with experiments at selected X-positions within the layered austenitic cladded material for the longitudinal normal beam incidence.*

Position (mm)	Longitudinal wave amplitudes		Difference in amplitude	Error (%)
	RTM	Experiment		
-10	0.2888	0.3024	0.0136	4.49
6	0.7512	0.6868	0.0644	9.38
10	0.3913	0.3815	0.0098	2.56

Fig. 8.15(c) shows comparison of predicted transmitted quasi longitudinal ultrasound field profiles for longitudinal normal beam transducer with the experiments. A good qualitative agreement is obtained. Table 19 shows the quantitative comparison of ray tracing amplitudes with experiments at selected positions in Fig. 8.15(c).

Quantitatively we observe deviation of 9.38% at position 6 mm. At position 10 mm we observe a deviation of 2.56% which is also a relative good quantitative result. The reason for noise that is occurring in the experimental A-scan is due to the uneven back wall surface of the austenitic cladded material.

8.4 Discussion on Discrepancies between Ray Tracing and Experiments

The discrepancies between an ray tracing model and the experiments are due to the following main reasons

(a) Attenuation of ultrasound beam at the columnar grain boundaries is currently not included in the ray tracing model,

(b) in practice ultrasound is generated from the transducer as a pulse, whereas ray tracing model assumes a monochromatic nature of the ultrasonic field propagation,

(c) due to the local thermal gradients in austenitic weld materials, the grains could be tilted both in the direction of welding and in the plane perpendicular to it. The columnar grain tilt along the weld run direction is defined as layback orientation. Welds typically have a layback angle in between 5° and 10°. In the present ray tracing model we made an approximation that columnar grain orientation exist within the incidence plane and assumed no lay back orientation,

(d) the grain boundaries are considered to be planar and smooth. The individual grain geometry is not considered in the ray tracing model, instead the whole weld metal is assumed to be polycrystalline material with transverse isotropic symmetry,

(e) limitation in spatial resolution using electrodynamic probes which means that the electromagnetic probe acts as spatial integrator (like an averaging filter) and it is approximately about 2 mm,

(f) quantitative evaluation of single wave mode field profile using electro dynamical probes is quite difficult. An electrodynamic probe optimized for longitudinal wave detection also fractionally detects the shear wave and vice versa. Furthermore the voltage amplitude may depend on several factors such as the gap between probe and test coupling surface, the alignment between the detection coil and the direction of the detected particle displacement, and the conductivity of the tested component,

(g) elastic constants for the austenitic weld material used in the ray tracing model are taken from the literature and they are not exactly in accordance with those of the test specimen.

The above mentioned aspects lead to further improving ray tracing predictions in inhomogeneous anisotropic austenitic welds and austenitic clad materials. Although we here just give the qualitative nature of the error sources, it can be assumed that they have in

total high impact on the accuracy of the results. It is then a remarkable result to deal with more or less small quantitative discrepancies between theory and experiments.

In this chapter, experiments have been performed on 32 mm thick inhomogeneous austenitic weld material, 62 mm thick austenitic clad material and quantitatively measured the ultrasound beam distortion and field profiles using electrodynamic probes. The inhomogenity in the weld material is modeled based on the Ogilvy's [77] mathematical empirical relation and the ultrasound beam propagation and ultrasound field profiles are accurately computed using ray tracing model. The simulated ultrasound field profiles using ray tracing model along the back wall of an austenitic weld component and austenitic clad material compared with the experimental results and good quantitative agreement is achieved. The reasons for differences between simulation and experimental results are discussed.

CHAPTER 9

Conclusions

9.1 Review of Thesis

The present Ph.D. thesis shows how to combine the most important ultrasound wave propagation parameters such as directivity, transmission coefficients, phase information and mode conversions in a new analytical 3D ray tracing method in order to determine the ultrasound wave propagation quantitatively for the first time in an acoustically inhomogeneous austenitic weld material. The developed ray tracing method was successfully employed for evaluating both point source as well as array transducer ultrasound fields quantitatively in inhomogeneous anisotropic austenitic weld materials. The developed ray tracing method has provided greater insight in understanding the influence of 3-Dimensional inhomogeneous columnar grain structure on an ultrasonic wave propagation as well as its interaction with defects in inhomogeneous anisotropic austenitic weld materials and eventually the ultrasonic non-destructive testing and evaluation (NDT&E) of transversal cracks in an inhomogeneous anisotropic austenitic weld material has been improved by optimizing the experimental parameters.

Ultrasonic wave propagation in anisotropic materials with arbitrary stiffness matrices of 21 elastic constants was solved three dimensionally and explicit analytical expressions for Poynting vector and energy velocities were presented in chapter 2. The influence of 3D columnar grain orientation (i.e. including layback orientation) on phase velocity, slowness vector, energy velocity, polarization vector, beam divergence, beam spreading factor and beam skewing for the three wave modes quasi longitudinal (qP), quasi shear vertical (qSV) and pure shear horizontal (SH) waves were analyzed in the context of practical ultrasonic non-destructive testing of transversely isotropic austenitic weld materials. In order to provide a deep understanding of anisotropic phenomenon to the reader, the ultrasonic wave propagation in an anisotropic austenitic steel material were compared with that generally found in isotropic steel material. The important

features of each ultrasonic wave mode (i.e. qP, qSV, SH waves) in columnar grained austenitic steel material were emphasized.

The derived fundamental concepts such as slowness, polarization and energy velocity vectors in chapter 2 were applied in chapter 3 in order to solve the problem of ultrasonic wave propagation at an interface between two general anisotropic materials for a 3D geometry. Explicit analytical expressions were presented for energy reflection and transmission coefficients at an interface between two arbitrarily oriented transversely isotropic materials. The influence of columnar grain orientation (i.e. including lay back orientation) on ultrasonic plane wave energy reflection and transmission coefficients for the below given interfaces which generally occurring during the ultrasonic non-destructive testing of austenitic weld materials were quantitatively analyzed.

- Interface between isotropic steel and anisotropic austenitic steel materials.
- Interface between Perspex wedge (PMMA) and anisotropic austenitic steel materials.
- Interface between anisotropic austenitic steel and isotropic steel materials.
- Interface between anisotropic austenitic steel material and isotropic Perspex wedge material (PMMA).
- Interface between two anisotropic austenitic steel materials.
- Interface between water (coupling medium) and anisotropic austenitic steel material.
- Interface between anisotropic austenitic steel material and water.
- Interface between anisotropic austenitic steel material and free surface (i.e. crack face, back wall surface).

The quantitative analysis on energy transported by direct as well as mode converted waves in columnar grained austenitic weld materials were analyzed for different columnar grain orientations and layback orientations of the austenitic weld material. The existence of reflected or transmitted second branch of quasi shear vertical waves (qSV(2)) and its consequence to the ultrasonic non-destructive testing of austenitic weld materials were examined. Valid domains of incident wave vector angles, angular

dependency of energy reflection and transmission coefficients and critical angles for the reflected and transmitted waves were discussed. Energy reflection behavior of three wave modes at a free surface boundary of columnar grained austenitic steel material was investigated and their importance during the ultrasonic non-destructive testing of cracks in anisotropic austenitic welds was discussed. The evaluated reflection and transmission coefficients in austenitic weld materials were validated using fundamental reciprocity relations for the reflected and transmitted plane elastic waves. The results of this chapter were employed in chapter 5 to determine the 3D ultrasonic ray propagation in inhomogeneous anisotropic austenitic weld materials.

In chapter 4, the ray directivity in general anisotropic material was analytically evaluated three dimensionally based on Lamb's reciprocity theorem [109, 111]. The point source directivity for the three wave modes quasi longitudinal, quasi shear vertical and shear horizontal waves for the excitation of normal as well as tangential forces on semi-infinite columnar grained transversal isotropic austenitic steel material were presented. The influence of columnar grain orientation and layback orientation on ray directivity in columnar grained anisotropic austenitic steel material was analyzed. The results of this chapter were employed in chapter 6, chapter 7 and chapter 8 to determine the accurate ultrasonic ray amplitudes and ultrasonic C-Scan images in inhomogeneous anisotropic austenitic weld materials.

In chapter 5, a 3D ray tracing method for evaluation of ultrasonic ray propagation and amplitudes for point sources and distributed sources in an inhomogeneous austenitic weld material were presented. The inhomogenity of the austenitic weld material was modeled based on the previously developed mathematical empirical relation [77] for the grain orientation. The inhomogenity in the austenitic weld material was discretized into several homogeneous layers with different crystal orientations. The 3D ray paths for the three wave modes qP, qSV and SH waves in inhomogeneous austenitic weld materials were presented. The influence of columnar grain orientation and layback angle on ray paths in austenitic welds were analyzed. The mode converted rays at the weld boundaries and back wall surface were traced and influence of weld microstructure (i.e. grain growth

parameters) on mode converted rays were discussed. The critical defects such as transversal cracks in austenitic weld materials were introduced in the 3D ray tracing algorithm and specularly reflected rays from the transversal cracks were determined. Application of 3D ray tracing model for the ultrasonic inspection of transversal cracks in austenitic weld material was illustrated. The calculated ray paths in austenitic weld materials were validated qualitatively with the existing ray tracing results.

In chapter 6, the ray tracing model results were quantitatively validated using 2D Elastodynamic Finite Integration Technique (EFIT) [45, 46, 48].The point source as well as array source ultrasonic fields obtained from the ray tracing model in layered inhomogeneous isotropic material, homogeneous anisotropic material, layered anisotropic material and inhomogeneous austenitic weld material were compared quantitatively with the 2D EFIT results. Quantitatively we observed a mean deviation of 8.6% and amplitude difference of 0.0402 in the point source generated ultrasound fields whereas a deviation of 10.2% and amplitude difference of 0.0423 was observed in case of finite dimension transducer generated displacement fields. The above discrepancies, which mainly occur in the region far away from the source normal direction, were due to the monochromatic assumption in the ray tracing calculations. The results show that an ray tracing approach can be used for evaluating ultrasound propagation quantitatively in anisotropic layered austenitic materials.

In chapter 7, the ultrasonic C-scan image in homogeneous and layered anisotropic austenitic steel materials was quantitatively evaluated. The influence of columnar grain orientation and lay back orientation on ultrasonic C-scan image in anisotropic austenitic steel material was analyzed. The calculated ultrasonic C-scan image in an anisotropic austenitic steel material was compared with that found in isotropic steel material. The applications of ultrasonic C-scan image for ultrasonic non-destructive testing of anisotropic austenitic steel materials were presented. The calculated ultrasonic field profiles in inhomogeneous austenitic welds with spatially varying weld structure using ray tracing model were quantitatively compared with commercially available NDT simulation tool (CIVA). Quantitatively we observed a minimum deviation of 1.88 % at

the weld flanks. Between the positions -5 mm and 0 mm, an accuracy of 89.5% is achieved in the ray tracing calculation. The differences (quantitatively a maximum deviation of 15. 95%) between ray tracing model and CIVA were observed and these are present because CIVA executes the beam field computation with a finite broadband pulse input whereas ray tracing model performs the calculations in its continuous wave mode.

In chapter 8, the ultrasonic beam fields in inhomogeneous austenitic weld materials and clad components were measured using ultrasonic through transmission technique where piezo-electric transducer acts as transmitter and electrodynamical probe acts as receiver. The weld parameters were optimized in the empirical function [77] such a way that to match with the real micrograph of the austenitic weld specimen. The measured normal beam as well as angle beam ultrasonic field profiles along the backwall of inhomogeneous austenitic weld material and austenitic clad material was compared with the ray tracing predictions. The reliability analysis of the ray tracing predictions was carried out by comparing the ray tracing results with experiments for different transducer parameters (i.e. transducer position and transducer excitation angle). It turned out that the deviation was about 5.2% in the isotropic austenitic steel material, 16.5% in the austenitic weld material and 5.46% in the austenitic cladded material. The results show that an ray tracing approach can be used for evaluating ultrasound propagation quantitatively in acoustically inhomogeneous anisotropic austenitic materials.

9.2 Summary of Findings

9.2.1 Ultrasonic Ray Propagation in General Anisotropic Materials

- Ultrasonic wave propagation in general anisotropic materials is solved three dimensionally yielding phase velocity, slowness, energy velocity, polarization vector for the three wave modes namely quasi longitudinal, quasi shear vertical and quasi shear horizontal waves [P1].
- The variations of phase velocity, slowness vector and energy velocity with incidents angle are calculated for the three wave modes qP, qSV and SH waves in

columnar grained transversely isotropic austenitic steel material. It has been found that the existence of layback orientation (i.e. columnar grain tilt along the weld run direction) results complicated non-symmetrical phase velocity and energy velocity surfaces. It has been shown that the qSV waves are strongly influenced by the anisotropy of the austenitic material as compared to the qP and SH waves.

- The numerical algorithm for evaluating phase velocity, slowness and energy velocity surfaces in anisotropic materials three dimensionally are written in MATLAB (version R2010a) software.
- The general anisotropic phenomenon such as beam divergence, beam skewing and beam spreading factors for qP, qSV and SH waves are analyzed in the context of practical ultrasonic testing of austenitic weld materials and the range of optimum incident angles which are preferable for the ultrasonic inspection of austenitic welds are presented.

9.2.2 Effect of Columnar Grain Orientation on Energy Reflection and Transmission Behaviour in Anisotropic Austenitic Weld Materials

- The effect of columnar grain orientation on energy reflection and transmission behaviour in anisotropic austenitic weld materials is quantitatively analyzed. The quantitative results are presented for both real (propagating region) and complex (inhomogeneous region) domain of the reflected and transmitted normal components of slowness vectors. The results of this investigation have been published in [P3] and [P8].
- Explicit analytical expressions for energy reflection and transmission coefficients at a boundary separating two transversely isotropic austenitic steel materials are presented.
- It has been found that some incident angles, the reflected (or) transmitted energy coefficients for the second branch of quasi shear vertical waves (qSV(2)) may carry all the incident energy.

- The numerical algorithm for evaluating amplitude, energy reflection and transmission coefficients in anisotropic austenitic weld materials three dimensionally are written in MATLAB (version R2010a) software.

9.2.3 3D Ray Tracing Method for Quantitative Evaluation of Ultrasound in Inhomogeneous Anisotropic Austenitic Welds

- 3D ray tracing method is developed for determining the ultrasonic energy ray paths for the three wave modes qP, qSV and SH waves in inhomogeneous austenitic weld materials. The results of this investigation have been published in [P9].
- The influence of weld microstructure on ultrasonic energy ray paths in inhomogeneous austenitic welds is presented.
- Ultrasonic energy ray paths are calculated for point sources and linear array transducers.
- The directivity factor of the ultrasonic wave in general anisotropic materials are solved three dimensionally using Lamb's reciprocity theorem. The method is applied to calculate the 3D ray directivities in an anisotropic austenitic steel material with 3D columnar grain orientation (i.e. including layback orientation). It has been found that the displacements for the qP waves produced by the y-direction tangential force (i.e. SH wave) are much less as compared to the x-directional force (i.e. qSV waves). Strong focusing effects are obtained for the qSV wave directivity patterns.
- It has been proved that ray tracing procedure is not only provide qualitative information on ultrasonic ray paths but also able to provide quantitative information on ultrasonic ray amplitudes.
- The ultrasound fields for point sources and distributed sources (i.e. array transducers) in inhomogeneous anisotropic materials using ray tracing method are successfully determined.
- The ray tracing model results are compared quantitatively with the 2D Elastodynamic Finite Integration Technique (EFIT) and obtained excellent

quantitative agreement. The results of this investigation have been published in [P1] and [P4].

- Experiments are conducted on real life austenitic welds and austenitic clad materials using piezoelectric array based transducer (acting as transmitter) and ultrasonic beam fields are calculated using electrodynamical probes. Based on the ray tracing predictions, the experimental parameters such as transducer position and excitation angle are optimized in order to transmit maximum energy into the weld root region of the austenitic weld material. The results of this investigation have been published in [P10].
- Experimentally measured ultrasonic field profiles on back wall surface of the inhomogeneous anisotropic austenitic weld material and austenitic clad material are compared with the ray tracing predictions and obtained good quantitative agreement. The results of this investigation have been published in [P1] and [P9].
- Ultrasonic C-scan images in homogeneous and layered anisotropic austenitic steel materials are calculated quantitatively using 3D ray tracing method and found that the ultrasonic C-scan images are strongly depend on both the columnar grain orientation and layback orientation of the austenitic material. The application of ultrasonic C-scan images for ultrasonic characterization of anisotropic austenitic materials is discussed. The calculated ultrasonic ray amplitudes in inhomogeneous austenitic welds using ray tracing model are compared with the commercially available NDT simulation tool (CIVA) and achieved good quantitative agreement. The results of this investigation have been published in [P6].
- The numerical algorithm for evaluating ultrasonic energy ray propagation as well as its interaction with defects in inhomogeneous austenitic weld materials three dimensionally are written in MATLAB (version R2010a) software. The algorithm is capable of calculating ultrasonic wave mode conversions at the back wall and weld boundaries.

9.2.4 Applications of 3D Ray Tracing Method for Ultrasonic Non-Destructive Inspection of Transversal Defects in Austenitic Welds

- 3D ray tracing model for determining the optimal experimental parameters for ultrasonic non-destructive testing of transversal defects in austenitic weld materials are discussed. The ray tracing model is able to compute the specularly reflected rays from the transversal cracks in an inhomogeneous austenitic weld material.

9.3 Areas of Continued Research and Future Perspectives

- The weld model considered in the present work does not contain the welding input parameters such as number of weld passes, inclination angle of the each pass, direction of the temperature gradient but it has included the spatial variation of the columnar grain orientation in an austenitic weld material. The individual grain geometry is not included in the weld model. In the future, it is suggested that the ray tracing predictions in an inhomogeneous austenitic weld will be further improved by taking into consideration of the above weld pool information in the weld model.

- The minor differences between ray tracing and Elastodynamic Finite Integration Technique (EFIT) model can be removed by considering an ultrasound is generated from the transducer as a pulse in the ray tracing model.

- The minor differences between experimental ultrasonic field profiles and ray tracing model can be eliminated by incorporating below important features in the ray tracing model

    a) Attenuation of an ultrasound beam at the columnar grain boundaries will be considered.

b) Precise elastic constant data of the real life austenitic weld material will be considered for the beam field calculations. Inverse problems may help in determining precise elastic constant data of the austenitic weld material. The elastic constant data in the ray tracing simulation will be varied iteratively and the process is continued till the model results will match with the experimental results. By using the above iterative procedure, there is a possibility to obtain the approximated elastic constant data of the austenitic weld material. However, this iterative process requires large computational time. But having in mind that a ray tracing as an total analytical approach is much faster than any numerical method, the ray tracing tool is highly suitable for inverse calculations dealing with large number of iterations.

- The developed ray tracing procedure in this thesis has wide general applicability such as ultrasound field evaluation in spatially varying layered composite materials and inhomogeneous concrete structure.

References

1. International Institute of Welding: Handbook of Ultrasonic examination of austenitic and dissimilar welds. DGZfP/DVS-Verlag, Berlin, 2008.

2. D. S. Kupperman, K. J. Reimann, Ultrasonic wave propagation and anisotropy in austenitic stainless steel Weld metal. *IEEE Transactions on Sonics and Ultrasonics*, Vol. **27**, pp.7-15, 1980.

3. H. Yoneyama, S. Shibata, M. Kishigami, Ultrasonic testing of austenitic stainless steel welds, *Proceedings of 9th World Conference on Non Destructive Testing (WCNDT)*, 3B-11, pp. 1-9, 1979.

4. X. Edelmann, Ultrasonic examination of austenitic welds at reactor pressure vessels, *Nuclear Engineering and Design,* Vol. **129**, pp. 341-355, 1991.

5. A. Erhard, G. Schenk, W. Möhrle, H. J. Montag, Ultrasonic phased array technique for austenitic weld inspection, *Proceedings of 15th World Conference on Non-Destructive Testing(WCNDT)*, *Nuclear Industry*, 2000.

6. P. Kemnitz, U. Richter, H. Klüber, Measurement of the acoustic field on austenitic welds: a way to higher reliability in ultrasonic tests, *Nuclear Engineering and Design*, Vol. **174**, pp. 259-272, 1997.

7. S. Hirsekorn, P. W. Van Andel, U. Netzelmann, Ultrasonic methods to detect and evaluate damage in steel, *Nondestructive Testing and Evaluation*, Vol. **15,** pp. 373-393, 2000.

8. R. J. Hudgell, G. M. Worrall, J. Ford, B. S. Gray, Ultrasonic characterisation and inspection of austenitic welds, *International Journal of Pressure Vessels and Piping*, Vol. **39**, pp. 247-263, 1989.

9. L. Bernus, W. Rathgeb, R. Schmid, F. Mohr, M. Krönig, Current in-service inspections of austenitic stainless steel and dissimilar metal welds in light water nuclear power plants, *Nuclear Engineering and Design*, Vol. **151,** pp. 539-550, 1994.

10. I. J. Stares, C. Duffil, J. A. Ogilvy, C. B. Scruby, On-line weld pool monitoring and defect detection ultrasonic, *NDT International*, Vol. **23**, pp. 195-200, 1990.

11. S. Baby, T. Balasubramanian, R. J. Pardikar, Ultrasonic study for detection of inner diameter cracking in pipeline girth welds using creeping waves, *International Journal of Pressure Vessels and Piping*, Vol. **80,** pp. 247-263, 2003.

12. R. J. Hudjell, B. S. Gray, Ultrasonic inspection of austenitic materials- state of the art report, *UKAEA Northern Division Report*, ND-R-1201(R), 1985.

13. Ph. Dombret, Methodology for the Ultrasonic testing of austenitic stainless steel, *Nuclear Engineering and Design*, Vol. **131,** pp. 279-284, 1991.

14. S. A. David, S. S. Babu, J. M. Vitek, Welding: Solidification and Microstructure, *Journal of the Minerals, Metals and Materials Society*, Vol. **55**, pp. 14-20, 2003.

15. O. Grong, Metallurgical Modeling of Welding, *The Institute of Materials*, University Press, Cambridge, 1997.

16. S. A. David, T. Debroy, Current issues and problems in welding science, *SCIENCE*, Vol. **257,** pp. 497-502, 1992.

17. T. Debroy, S. A. David, Physical processes in fusion welding, *Review of Modern Physics*, Vol. **67,** pp. 85-112, 1995.

18. V. K. Munikoti, On the propagation of elastic waves in acoustically anisotropic materials and at their boundaries during non destructive inspection with ultrasound, *Dissertation*, Technische Universität Berlin, D 83, 2001.

19. S. Bauer, Metallography in the project SMT4 - CT95-2012, Effect of Ultrasonic Scattering on Inspection of Austenitic Weld, funded by the Commission of the European Communities under the Standards and Measurements & Testing Programme, Project Report, BAM Lab 8.42, 1996-1999.

20. J. Ye, J. Moysan, S. J. Song, H. J. Kim, B. Chassignole, C. Gueudre, O. Dupond, Influence of welding passes on grain orientation: The example of a multi-pass V-weld, *International Journal of Pressure Vessels and Piping*, Vol. **94**, pp. 17-21, 2012.

21. B. Chassignole, R. E. Guerjouma, M. A. Ploix, T. Fouquet, Ultrasonic and structural characterization of anisotropic austenitic stainless steel welds: Towards a higher reliability in ultrasonic non destructive testing, *NDT&E International*, Vol.**43**, pp. 273-282, 2010.

22. A. Erhard, V. Munikoti, G. Brekow, U. Tessaro, D. Tscharntke, Model for the improvement of dissimilar weld inspection, *Proceedings of 16th World Conference on NDT (WCNDT)*, Signal Processing, 2004.

23. J. A. Ogilvy, Ultrasonic beam profiles and beam propagation in an austenitic weld using a theoretical ray tracing model, *Ultrasonics*, Vol. **24**, pp. 337-347, 1986.

24. G. J. Curtis, N. Ibrahim, Texture studies of austenitic weld metal using elastic surface waves, *Metal Science*, Vol. **15**, pp. 566-573, 1981.

25. B. R. Dewey, L. Adler, R. T. King, K. V. Kook, Measurement of anisotropic elastic constants of type 308 stainless steel electro slag welds, *Experimental Mechanics*, Vol. **17**, pp. 420-426, 1977.

26. E. Neumann, S. Hirsekorn, G. Hübschen, T. Just, R. Schmid, Ultraschallprüfung von austenitichen Plattierungen, Mischnähten und austenitischen Schweißnähten, Theorie-Praxis-Regelwerke, Expert-Verlag, Renningen Malmscheim, 1995.

27. K. Matthies u.a., Ultraschallprüfung von austenitichen Werkstoffen, DVS-Verlag, Berlin, 2009.

28. H. Yoneyama, Ultrasonic flaw detection in austenitic welds, *Welding International*, Vol. **9,** pp. 494-499, 1995.

29. X. Edelmann, Application of ultrasonic testing techniques on austenitic welds for fabrication and in-service inspection, *NDT International*, Vol. **14**, pp. 125-133, 1981.

30. E. Neumann, M. Roemer, T. Just, K. Matthies, E. Nabel, E. Mundry, Development and improvement of ultrasonic testing techniques for austenitic nuclear components, *Proceedings of International Conference on NDE in the Nuclear Industry*, Salt Lake City, Utah, USA, pp. 84-105, 1978.

31. I. N. Ermolov, B. P. Pilin, Ultrasonic inspection of materials with coarse grain anisotropic structures, *NDT International* , Vol. **9**, pp. 275-280, 1976.

32. A. W. E. Neumann, On the state of the art of the inspection of austenitic welds with ultrasound, *International Journal of Pressure Vessels and Piping*, Vol. **39**, pp. 227-246, 1989.

33. E. Neumann, Physikalische Grundlagen der Ultraschallprüfung von austenitischen Schweißverbindungen, Teil 1: Die Richtunsgabhängigkeit der Schallgeschwindigkeit, *Materialprüfung*, Vol. **32**, pp. 227-231, 1990.

34. V. Munikoti, G. Brekow, U. Tessaro and A. Erhard, Ultrasonic testing for transverse discontinuities in dissimilar welds: Theoritical and Experimental results, *Materials Evaluation*, Vol. **62**, pp. 1148-1153, 2004.

35. S. Hirsekorn, Directional dependence of ultrasonic propagation in textured crystals, *Journal of Acoustical Society of America*, Vol. **79**, pp. 1269-1279, 1986.

36. M. Vijayendra, E. Neumann, Ultraschall-Polarisation in Werkstoffen mit Textur- Physikallische Grundlagen der Ultraschallprüfung von austenitischen Schweißverbindungen, *Materialprüfung*, Vol. **35**, pp. 260-264, 1993.

37. M. Kurtulmus, I. Yükler, Effects of probe properties on ultrasonic inspection of austenitic stainless steel weldments, *Scientific Research and Essays*, Vol. **6,** pp. 305-312, 2011.

38. P. A. Kapranos, V. N. Whittaker, Difficulties in the ultrasonic inspection of 316 austenitic steel welds arising from acoustic impedance mismatch, *Nondestructive testing communications*, Vol. **1**, pp. 81-92, 1983.

39. M. Vijayendra, K. Matthies, E. Neumann and R. Schmid, Über die Veränderung der Ultraschallwellen in akustisch anisotropen Werkstoffen und über Konsequenzen für die Prüfung, dargestellt am Beispiel der austenitisch-ferritischen Mischverbindungen, Qualitätssicherung und Werkstoffprüfung, DGZfP, Vol. **39**, pp. 137-150, 1994.

40. T. N. Claytor, D. S. Kupperman, K. J. Reimann, Visualization of ultrasonic beam distortion in anisotropic stainless steel, *Journal de Physique*, Vol. **46**, pp. 795-799, 1985.

41. T. Seldis, C. Pecorari, Scattering induced attenuation of an ultrasonic beam in austenitic steel, *Journal of the Acoustical Society of America*, Vol. **108**, pp. 580-587, 2000.

42. R. A. Roberts, D. S. Kuppermann, Ultrasonic beam distortion in transversely isotropic media, *Review of progress in quantitative NDE*, eds. D. O. Thompson, and D. E. Chimenti, Vol. **7A**, pp. 49-56, Plenum Press, New York, 1988.

43. K. Balasubramaniam, Y. Ji, Skewing of the acoustic wave energy vector in stacked 1-3 anisotropic material systems, *Journal of Sound and Vibration*, Vol. **236**, pp. 166-175, 2000.

44. J. A. Ogilvy, Identification of pulse-echo rays in austenitic steels, *NDT International*, Vol. **17**, pp. 259-264, 1984.

45. R. Marklein, Numerische verfahren zur Modelierung von akustischen, elektromagnetischen, elastischen und piezoelektrischen Wellen ausbreitungsproblemen in Zeitbereich basierend auf der Finiten Integrsationtechnik, Shaker Verlag, Aachen, 1997.

46. P. Fellinger, R. Marklein, K. J. Langenberg, S. Klaholz, Numerical modeling of elastic wave propagation and scattering with EFIT – elastodynamic finite integration technique, *Wave motion*, Vol. **21,** pp. 47-66, 1995.

47. R. Marklein, R. Barmann, K. J. Langenberg, The ultrasonic modeling code EFIT as applied to inhomogeneous dissipative isotropic and anisotropic media, *Review of progress in quantitative NDE*, eds. D. O. Thompson, and D. E. Chimenti, Vol. **14**, pp. 251-258, Plenum Press, New York, 1995.

48. K. J. Langenberg, R. Hannemann, T. Kaczorowski, R. Marklein, B. Koehler, C. Schurig, F. Walte, Application of modeling techniques for ultrasonic austenitic weld inspection, *NDT&E International*, Vol. **33,** pp. 465-480, 2000.

49. P. K. Chinta, R. Marklein, W. Odorico, R. Koch, A. Maurer, Numerical modeling of ultrasonic phased array transducers and their application, *Proceedings of 9th European Conference for Non Destructive Testing (ECNDT)*, Berlin, 2006.

50. K. J. Langenberg, R. Marklein, Transient elastic waves applied to nondestructive testing of transversely isotropic lossless materials: a coordinate free approach, *Wave Motion*, Vol. **41,** pp. 247-261, 2005.

51. P. K. Chinta, K. Mayer, K. J. Langenberg, Numerical modeling of elastic waves in Anisotropic media using 3D-elastodynamic finite integration technique, *International Congress on Ultrasonics*, AIP Conference Proceedings, Vol. **1433**, pp. 487-490, 2012.

52. K. Harumi, M. Uchida, Computer simulation of Ultrasonics and Its applications, *Journal of Nondestructive Evaluation*, Vol. **9,** pp. 81-99, 1990.

53. J. A. G. Temple, Modeling the propagation and scattering of elastic waves in inhomogeneous anisotropic media, *Journal of Physics D: Applied Physics*, Vol. **21,** pp. 859-874, 1988.

54. E. Baek, H. Yim, Numerical modeling and simulation for ultrasonic inspection of anisotropic austenitic welds using the mass spring lattice model, *NDT&E International*, Vol. **44,** pp. 571-582, 2011.

55. J. Westlund, On the propagation of ultrasonic testing using boundary integral equation methods, *Ph.D. Thesis*, Charles University of Technology, Gothenburg, Sweden, 2011.

56. Ch. Zhang, D. Gross, A 2D hyper singular time-domain traction BEM for transient elastodynamic crack analysis, *Wave Motion*, Vol. **35**, pp. 17-40, 2002.

57. A. Saez, J. Dominguez, BEM analysis of wave scattering in transversely isotropic solids. International Journal for Numerical Methods in engineering, Vol. **44**, pp: 1283-1300, 1999.

58. M. Spies, P. Fellinger and K. J. Langenberg, Elastic waves in homogeneous and layered transversely isotropic media: Gaussian Wave Packets and Greens functions, Review of progress in quantitative NDE, eds. D. O. Thompson, and D. E. Chimenti, Vol. **11**, pp. 961-968, Plenum Press, New York, 1992.

59. M. Spies, Elastic waves in homogeneous and layered transversely isotropic media: Plane waves and Gaussian wave packets. A general approach, *Journal of acoustical society of America*, Vol. **95**, pp. 1748-1760, 1994.

60. M. Spies, Analytical methods for modeling of ultrasonic non-destructive testing of anisotropic media, *Ultrasonics*, Vol. **42,** pp**.** 213-219, 2004.

61. M. Spies, Transducer modeling in general transversely isotropic media via point source synthesis: Theory, *Journal of Nondestructive Evaluation*, Vol. **13**, pp. 85-99, 1994.

62. M. Spies, R. A. Roberts, Modeling of transducer fields in weld material: A comparison of three generically different approaches, *Review of progress in quantitative NDE,* eds. D. O. Thompson, and D. E. Chimenti, Vol. **19**, pp. 961-968, AIP Conference Proceedings, 2000.

63. M. Spies, Transducer field modeling in anisotropic media by superposition of Gaussian base functions, *Journal of Acoustical Society of America*, Vol. **105**, pp. 633-638, 1999.

64. M. Spies, Modeling of transducer fields in inhomogeneous anisotropic materials using Gaussian beam superposition, *NDT&E International*, Vol. **33**, pp. 155-162, 2000.

65. M. Spies, Gaussian beam modeling for commercial transducers applied to aero engine disk inspection, *Proceedings of 9th European Conference on Non Destructive Testing*, Modeling and Signal Processing, pp. 1-8, 2006.

66. M. Spies, Ultrasonic field modeling for immersed components using Gaussian beam superposition, Ultrasonics **46** (2007), pp. 138-147.

67. J. Ye, H. J. Kim, S. J. Song, S. S. Kang, K. Kim, M. H. Song, Model based simulation of focused beam fields produced by a phased array ultrasonic transducer in dissimilar metal welds, *NDT&E International*, Vol. **44**, pp. 290-296, 2011.

68. H. Jeong, L. W. Schmerr, Ultrasonic beam propagation in highly anisotropic materials simulated by multi Gaussian beams, *Journal of Mechanical Science and Technology*, Vol. **21**, pp: 1184-1190, 2007.

69. B. A. Auld, Acoustic fields and waves in solids, Vols. **1** and **2**, Krieger, Melbourne, 1990.

70. M. J. P. Musgrave, Crystal Acoustics, Holden Day, San Francisco, Cambridge, London, Amsterdam, 1970.

71. F. I. Fedorov, Theory of elastic waves in crystals, Plenum Press, New York, 1968.

72. L. M. Brekhovskikh, Waves in layered media, Academic Press, San Diego, 1980.

73. K. J. Langenberg, R. Marklein, K. Mayer, Ultrasonic non destructive Testing of Materials- Theoretical foundations, CRC-Press, Taylors & Francis Group, 2012.

74. R. G. Payton, Elastic wave propagation in transversely isotropic media, Martinus Nijhoff Publishers, The Hauge, Boston, Lancaster, 1983.

75. J. A. Johnson, N. M. Carlson, D. M. Tow, Ray trace calculations for ultrasonic fields, *Research in Nondestructive Testing and Evaluation*, Vol. **3,** pp. 27-39, 1991.

76. T. Furukawa, K. Date, Ray model for computer simulation of ultrasonic testing, *Review Progress in Quantitative NDE*, eds. D.O. Thomson and D.E. Chimenti, Plenum Press, New York, Vol. **14**, pp. 1111-1118, 1995.

77. J. A. Ogilvy, Computerized ultrasonic ray tracing in austenitic steel, *NDT International*, Vol. **18,** pp. 67-77, 1985.

78. J. A. Ogilvy, The influence of austenitic weld geometry and manufacture on ultrasonic inspection of welded joints, *British Journal of Nondestructive Testing*, Vol. **29,** pp. 147-156, 1987.

79. J. A. Ogilvy, Modeling of ultrasonic wave behavior in austenitic steel, *Proceedings of 7th International Conference on NDE in the Nuclear Industry*, pp. 431-434, 1985.

80. J. A. Ogilvy, A model for elastic wave propagation in anisotropic media with applications to ultrasonic inspection through austenitic steel, *British Journal of Nondestructive Testing*, Vol. **27**, pp. 13-21, 1985.

81. J. A. Ogilvy, On the focused beams in austenitic welds, *British Journal of Nondestructive Testing*, Vol. **29**, pp. 238-246, 1987.

82. J. A. Ogilvy, Ultrasonic reflection properties of planar defects with in austenitic welds, *Ultrasonics*, Vol. **26,** pp. 318-327, 1988.

83. J. A. Ogilvy, *A layered media model for ray propagation in anisotropic inhomogeneous materials, Applied Mathematical Modeling*, Vol. **14,** pp. 237-247, 1990.

84. B. M. Hawker, S. F. Burch, A. Rogerson, Application of the RAYTRAIM ray tracing program and RAYKIRCH post processing program to the ultrasonic inspection of austenitic stainless steel welds in nuclear plant, *Proceedings of 1st International Conference on NDE in relation to Structural Integrity for Nuclear and pressure components,* Vol. **2**, pp. 899-911, 1998.

85. M. G. Silk, A computer model for ultrasonic propagation in complex orthotropic structures, *Ultrasonics*, Vol. **19**, pp. 208-212, 1981.

86. V. Schmitz, F. Walte, S.V. Chakhlov, 3D ray tracing in austenite materials, *NDT&E International*, Vol. **32**, pp. 201-213, 1999.

87. V. Schmitz, M. Krönig, S. Chakhlov, Modeling of sound fields through austenitic welds, *Review Progress in Quantitative NDE*, eds. D.O. Thomson and D.E. Chimenti, AIP Conference Proceedings, Vol. **19**, pp. 969-975, 2000.

88. M. Spies, W. Jager, Synthetic aperture focusing for defect reconstruction in anisotropic media, *Ultrasonics*, Vol. **41**, pp. 125-131, 2003.

89. A. Shlivinski, K. J. Langenberg, Defect imaging with elastic waves in inhomogeneous anisotropic materials with composite geometries, *Ultrasonics*, Vol. **46**, pp. 89-104, 2007.

90. C. Höhne, S. Kolkoori, M. U. Rahman, R. Boehm, J. Prager, SAFT imaging of transverse cracks in austenitic and dissimilar welds, *Journal of Nondestructive Evaluation*, Vol. **32**, pp. 51-66.

91. G. D. Connolly, M. J. S. Lowe, S. I. Rokhlin, J. A. G. Temple, Synthetically focused imaging techniques in simulated austenitic steel welds using an ultrasonic phased array, *Review Progress in Quantitative NDE*, eds. D.O. Thomson and D.E. Chimenti, AIP Conference Proceedings, Vol. **29**, pp. 871-878, 2010.

92. N. Gegembre, A. Lhemery, Pencil method for elastodynamics: application to ultrasonic field computation, *Ultrasonics*, Vol. **38,** pp. 495-499, 2000.

93. P. Calmon, A. Lhemery, I. L. Taibi, R. Raillon, L. Paradis, Modeling for the computation of ultrasonic fields and interaction with defects in realistic NDT configurations, *Nuclear Engineering Design*, Vol. **180,** pp. 271-283, 1998.

94. S. Chatilon, N. Leymarie, G. Rougeron, Simulation of ultrasonic inspection involving multiple skips and realistic defects, eds. D.O. Thomson and D.E. Chimenti, *Review Progress in Quantitative NDE*, AIP Proceedings, Vol. **30**, pp. 83-90, 2010.

95. S. Mahaut, S. Chatillon, N. Leymarie, F. Jenson, P. Calmon, Simulation tools for predicting non destructive testing of heterogeneous and anisotropic structures, *Proceedings of 1st International Congress on Ultrasonics*, pp. 1-4, 2007.

96. A. Apfel, J. Moysan, G. Corneloup, T. Fouauet, B. Chassignole, Coupling an ultrasonic propagation code with a model of the heterogeneity of multi pass welds to simulate ultrasonic testing, *Ultrasonics*, Vol. **43**, pp. 447- 456, 2005.

97. A. Apfel, J. Moysan, G. Corneloup, B. Chassignole, Simulation of the influence of the grains orientation on ultrasounds, *Proceedings of 16th World Conference on NDT (WCNDT)*, 2004.

98. J. Moysan, C. Gueudre, M. A. Ploix, G. Corneloup, Ph. Guy, R. Elguerjouma, B. Chassignole, Advances in ultrasonic testing of austenitic steel welds: Towards a 3D description of the material including attenuation and optimization by inversion, Ultrasonic wave propagation in non homogeneous media, *Proceedings in Physics*, Vol. **128**, pp. 15-24, 2009.

99. J. Moysan, G. Corneloup, B. Chassignole, C. Gueudre, M. A. Ploix, Modeling of welded material for ultrasonic testing using MINA: Theory and Applications, eds. D.O. Thomson and D.E. Chimenti, *Review of Progress in Quantitative NDE*, AIP Conference Proceedings, Vol. **32**, pp. 1219-1226, 2012.

100. S. Deydier, P. Calmon, O. Petillon, Modeling of ultrasonic propagation into carbon fibre reinforced epoxy composites using a ray theory based homogenization method, Proceedings of 9th European Conference on Nondestructive Testing (ECNDT), pp. 1-8, Berlin, 2006.

101. S. Deydier, N. Gengembre, O. Petillon, V. Mengeling, Ultrasonic field computation into multilayered composites using a homogenization method based on ray theory, eds. D.O. Thomson and D.E. Chimenti, *Review Progress in Quantitative NDE*, AIP Conference Proceedings, Vol. **24**, pp. 1057-1064, 2005.

102. G. D. Connolly, M. J. S. Lowe, S. I. Rokhlin, J. A. G. Temple, Use of Fermat's principle to aid the interpretation of the ultrasonic inspection of anisotropic welds, eds. D.O. Thomson and D.E. Chimenti, *Review Progress in Quantitative NDE*, AIP Conference Proceedings, Vol. **27,** pp. 1018-1025, 2008.

103. G. D. Connolly, M. J. S. Lowe, J. A. G. Temple, S. I. Rokhlin, The application of Fermat's principle for imaging anisotropic and inhomogeneous media with application to austenitic weld inspection, Pro. R. Soc. A, Vol. **465**, pp. 3401-3423, 2009.

104. G. D. Connolly, M. J. S. Lowe, S. I. Rokhlin, J.A.G. Temple, Modeling the propagation of elastic waves in generally anisotropic materials and austenitic steel welds, eds. D.O. Thomson and D.E. Chimenti, *Review Progress in Quantitative NDE*, AIP Conference Proceedings, Vol. **27,** pp. 1026-1033, 2008.

105. G. D. Connolly, Modelling of the propagation of ultrasound through austenitic steel welds, *PhD Thesis*, Imperial College, London, UK, 2009.

106. G. D. Connolly, M. J. S. Lowe, S. I. Rokhlin, J. A. G. Temple, Correction of ultrasonic array images to improve reflector sizing and location in inhomogeneous materials using a ray tracing model, *Journal of acoustical society of America*, Vol. **127**, pp. 2802-2812, 2010.

107. Q. Liu, H. Wirderlius, A 2D model of ultrasonic wave propagation in an austenitic weld, *NDT&E International*, Vol. **40**, pp. 229-238, 2007.

108. S. Halkjaer, M. P. Soresen, W. D. Kristensen, The propagation of Ultrasound in an austenitic weld, Ultrasonics, Vol. **38**, pp. 256-261, 2000.

109. L.Ya. Gutin, Sound radiation from an infinite plate excited by a normal point force, *Soviet Physics: Acoustics*, American Institute of Physics, Vol. **9**, pp. 256, 1964.

110. A. E. Lord, Geometric Diffraction Loss in Longitudinal and shear wave attenuation measurements in an isotropic half apace, *Journal of Acoustical Society of America*, Vol. **39**, pp. 650-662, 1966.

111. K. Wu, P. B. Nagy, L. Adler, Far field radiation of a vibrating point source in anisotropic media, *Journal of Nondestructive Evaluation*, Vol. **10**, pp. 71-78, 1991.

112. V. T. Buchwald, Elastic waves in anisotropic media, Proceedings of the Royal Society of London. Series A, Mathematical and Physical Sciences, Vol. **253**, pp. 563-580, 1959.

113. M. J. P. Musgrave, On the propagation of elastic waves in aelotropic media 1: General principles. *Proceedings of Royal Society of London: Series A*, Mathematical and Physical Sciences, Vol. **229**, pp. 339-355, 1959.

114. I. N. Bronstein, K. A. Semendyayev, Handbook of mathematics, Springer, Berlin, Heidelberg, 1985.

115. M. Conry, Notes on wave propagation in anisotropic elastic solids, http://80.68.92.234/anisotropic_with_lamb_waves.pdf, 2005.

116. V. K. Munikoti, E. Neumann, Reflection and Transmission coefficients at the interface between austenitic base and weld metal, *Journal of Physics D: Applied Physics*, Vol. **25**, pp. 1504-1512, 1992.

117. N. L. Carroll, V. F. Humphery, J. D. Smith, Energy and phase velocity considerations required for attenuation and velocity measurements of anisotropic composites, *Ultrasonics*, Vol. **40**, pp. 525-530, 2002.

118. R. A. Roberts, Ultrasonic beam transmission at the interface between an isotropic and transversely isotropic half space, *Ultrasonics*, Vol. **26**, pp. 139-147, 1988.

119. E. G. Henneke, Reflection and refraction of a stress wave at a plane boundary between anisotropic media, *Journal of Acoustical Society of America*, Vol. **51,** pp. 210-216, 1972.

120. S. I. Rokhlin, T. K. Bolland, L. Adler, Reflection and refraction of elastic waves on a plane interface for general anisotropic media, *Journal of Acoustical Society of America*, Vol. **79**, pp. 906-918, 1986.

121. S. Kolkoori, M. U. Rahman, J. Prager, Effect of columnar grain orientation on energy reflection and transmission behaviour in anisotropic austenitic weld materials, *Journal of Nondestructive Evaluation* , Vol. **31**, pp. 253-269, 2012.

122. R. W. D. Nickalls, The quartic equation: Invariants and Euler's solution revealed, *The Mathematical Gazette*, Vol. **93**, pp. 66-75, 2009.

123. S. I. Rokhlin, T. K. Bolland, L. Adler, Splitting of domain of angles for incident wave vectors in elastic anisotropic media, *Journal of Applied Physics*, Vol. **59**, 3672-3677, 1986.

124. I. Y. Mooshabad, F. J. Margetan, T. A. Gray, R. B. Thompson, Reflection of ultrasonic waves from imperfect interfaces: a combined boundary element method and independent scattering model approach, *Journal of Nondestructive Evaluation*, Vol. **11**, pp. 141-149, 1992.

125. J. M. Baik, R. B. Thompson, Ultrasonic scattering from imperfect interfaces: a quasi static model, *Journal of Nondestructive Evaluation***,** Vol. **4**, pp. 177-196, 1984.

126. P. B. Nagy, Ultrasonic classification of imperfect interfaces, *Journal of Nondestructive Evaluation*, Vol. **11**, pp.127-139, 1992.

127. K. Wu, P. B. Nagy, L. Adler, A general technique for wave propagation problems in anisotropic media, eds. D. O. Thomson, D. E. Chimenti, *Review of Progress in Quantitative NDE*, AIP Conference Proceedings, Vol. **10**, Plenum press, New York, 1991.

128. T. H. Tan, Reciprocity relations for scattering of plane elastic waves, *Journal of Acoustical Society of America*, Vol. **61**, pp. 928-931, 1977.

129. H. Lamb, on the propagation of Tremors over the surface of an elastic solid. *Philosophical Transactions Royal Society of London*, Vol. **203**, pp. 359-371, 1904.

130. H. Ernst, Experimentelle Verifizierung von Modellvorstellungen zur Schallausbreitung in anisotropen Materialien, *Dissertation*, Technische Universitat Bergakademie Freiberg, 2004.

131. S. R. Kolkoori, M. U. Rahman, P. K. Chinta, M. Kreutzbruck, M. Rethmeier, J. Prager, Ultrasonic field profile evaluation in acoustically inhomogeneous anisotropic materials using 2D ray tracing model: Numerical and experimental comparison, *Ultrasonics*, Vol. **53**, pp. 396-41, 2012.

132. S. Hirsekorn, The scattering of ultrasonic waves in polycrystalline materials with texture, *Journal of Acoustical Society of America*, Vol. **77**, pp. 832-843, 1985.

133. M. Ploix, P. Guy, R. Elguerjouma, J. Moysan, G. Corneloup, B. Chassignole, Attenuation assessment for NDT of austenitic stainless steel welds, *Proceedings of 6th European Conference on Non-Destructive Testing (ECNDT)*, Berlin, 2006.

134. T. Seldis, C. Pecorari, Scattering induced attenuation of an ultrasonic beam in austenitic steel, *Journal of Acoustical Society of America*, Vol. **108,** pp. 580-587, 2000.

135. V. Dorval, F. Jenson, G. Coneloup, J. Moyesan, Accounting for structural noise and attenuation in the modeling of the ultrasonic testing of polycrystalline materials, *Review of Progress in Quantitative NDE*, eds. D. O. Thompson, D. E. Chimenti, AIP Conference Proceedings, Vol. **29**, pp. 1309-1316, 2010.

136. S. P. Gornaja, N. P. Aljoshin, Attenuation of ultrasonic waves in austenitic steel welds, *Nondestructive Testing and Evaluation*, Vol. **13**, pp. 149-168, 1997.

137. F. Jenson, T. Fortuna, L. Doudet, Modeling of ultrasonic propagation in a coarse grain structure, eds. D.O. Thomson and D.E. Chimenti, *Review of Progress in Quantitative NDE*, AIP Conference Proceedings, Vol. **28**, pp. 1201-1208, 2010.

138. V. K. Munikoti, E. Neumann, Extension of Ahmed & Thomson theory to general elastic plane quasi wave propagation in textured polycrystalline material, eds. D.O. Thomson and D.E. Chimenti, *Review of Progress in Quantitative NDE*, Vol. **17**, pp. 1657-1664, 1998.

139. S. Ahmed, R. B. Thompson, P. D. Panetta, Ultrasonic attenuation as influenced by elongated grains, eds. D.O. Thomson and D.E. Chimenti, *Review of Progress in Quantitative NDE*, AIP Conference Proceedings, Vol. **22**, pp. 109-116, 2003.

140. H. Ernst, V. Munikoti, E. Neumann, Messung der Schwächung von longitudinalen Ultraschallwellen in austenitischem stengelkristallinem Gefüge, Deutschen Gesellschaft für Zerstörungsfreie Prüfung (DGZfP), 1999, pp. 615-626.

141. N. Dube, Introduction to phased array ultrasonic technology applications, R/D Tech Guidline, First edition, Canada, 2004.

142. L. Azhar, Y. Shi, S. C. Wooh, Beam focussing of linear phased arrays, *NDT&E International*, Vol. **33**, pp. 189-198, 2000.

143. Ultrasonic Transducers: Technical Notes, Olympus. http://www.olympus-ims.com/en/ultrasonic-transducers.

144. F. Walte, C. Shuring, M. Spies, K. J. Langenberg, S. Klaholz, Experimental evaluation of ultrasonic simulation techniques in anisotropic materials, eds. D. O. Thomson, D. E. Chimenti, *Review of Progress in Quantitative NDE*, Vol. **16**, Plenum Press, New York, 1997.

145. T. Hasiotis, E. Badogiannis, N. G. Tsouvalis, Applications of Ultrasonic C-scan techniques for tracing defects in laminated composite materials, *Proceedings of 4th International Conference on NDT*, Hellenic society for NDT, 11-14 October 2007.

146. A. B. Doyum, M. Dürer, Defect characterization of composite honeycomb panels by Non-destructive inspection methods, *Proceedings of DGZfP Jahrestagung*, ZfP in Anwendung, Entwicklung und Forschung Weimar, 2002.

147. T. Wangt, J. Saniie, Evaluation of ultrasonic C-Scan attenuation image, *IEEE Ultrasonics Symposium*, Vol. **2**, pp. 791-794, 1991.

148. D. A. Hutchins, A. C. Pardoe, D. R. Billson, E. L. Hines, Neural network correction of ultrasonic C-scan images, *Ultrasonics*, Vol. **37**, pp. 263-272, 1999.

149. M. Thorton, L. Han, M. Shergold, Progress in NDT of resistance spot welding of aluminum using ultrasonic C-scan, *NDT&E International*, Vol. **48**, pp.30-38, 2012.

150. G. A. Gordon, S. Canumalla, B. R. Tittmann, Ultrasonic C-Scan imaging for material characterization, *Ultrasonics*, Vol. **31**, pp. 373-380, 1993.

151. P. Calmon, S. Mahaut, S. Chatillon, R. Raillon, CIVA: An expertise platform for simulation and processing NDT data, *Ultrasonics*, Vol. **44**, pp. 975-979, 2006.

152. S. Mahaut, S. Lonne, S. Chatillon, G. Cattiaux, Validation of CIVA simulation tools for UT examination, *Proceedings of 4th International Conference on NDE in relation to Structural Integrity for Nuclear and Pressurized Components*, 2004.

153. CIVA Version 10 user manual.

154. G. A. Deschamps, Ray techniques in electromagnetics, *Proceedings of the IEEE*, Vol. **60**, pp. 1022-1035, 1972.

155. N. Gengembre, Pencil method for ultrasonic beam computation, *Proceedings of World Conference on Ultrasonics*, pp. 1533-1536, 2003.

156. U. Völz, H. Mrasek, K. Matthies, M. Kreutzbruck, Visualization of sound propagation in solids using electrodynamic probes, *Proceedings of 10th European Conference on Non-Destructive Testing*, Moscow, 2010.

157. U. Völz, H. Mrasek, K. Matthies, H. Wüstenberg, M. Kreutzbruck, Electrodynamic Approach for Visualization of Sound Propagation in Solids, *Review of Progress in Quantitative NDE*, eds. D. O. Thompson and D. E. Chimenti, AIP Conference Proceedings, Vol. **28A**, pp. 758-765, 2008

158. N. F. Declercq, J. Degrieck, O. Leroy, Schlieren photography to study sound interaction with highly absorbing materials, *Ultrasonics*, Vol. **43**, pp. 505–507, 2005.

159. T. Neumann, H. Ermert, Schlieren visualization of ultrasonic wave fields with high spatial resolution, Ultrasonics, Vol. **44**, pp. 1561–1566, 2006.

160. B. Köhler, Dispersion Relations in Plate Structures Studied with a Scanning Laser Vibrometer, *Proceeding of 6th European Conference on NonDestructive Testing (ECNDT)*, Berlin, 2006.

161. S. Yashiro, J. Takatsubo, H. Miyauchi, N. Toyama, A novel technique for visualizing ultrasonic waves in general solid media by pulsed laser scan, *NDT&E International*, Vol. **41**, pp. 137–144, 2008.

162. H. Ernst, V. K. Munikoti, H. Wüstenberg, Experimentelle Verifizierung von Modellvorstellungenzur Schallausbreitung in anisotropen Materialien, *ZfP-Zeitung*, Vol. **92**, pp.36-40, 2004.

163. G. Schenk, U. Völz,, E. Dohse, L. Bauer, COMPASXL: outstanding number of channels with a new phased array system, *Proceedings of 6th European Conference on NonDestructive Testing (ECNDT)*, Vol. **11**, pp. 25–29, Berlin, 2006.

Appendix A Transformation Matrices [M], [N] and Elastic Constant Matrix [c^T]

The coordinate transformation matrix, which resulted after performing a clock wise rotation with rotation angle 'θ'about the y-axis as shown in Fig. 2.1, can be given as

$$[a] = \begin{bmatrix} \cos\theta & 0 & -\sin\theta \\ 0 & 1 & 0 \\ \sin\theta & 0 & \cos\theta \end{bmatrix} \tag{A.1}$$

The transformation matrices [M] and [N] in Eq. (2.11) are expressed as [69]

$$[M] = \begin{bmatrix} \cos^2\theta & 0 & \sin^2\theta & 0 & -\sin 2\theta & 0 \\ 0 & 1 & 0 & 0 & 0 & 0 \\ \sin^2\theta & 0 & \cos^2\theta & 0 & \sin 2\theta & 0 \\ 0 & 0 & 0 & \cos\theta & 0 & \sin\theta \\ \frac{\sin 2\theta}{2} & 0 & \frac{-\sin 2\theta}{2} & 0 & \cos 2\theta & 0 \\ 0 & 0 & 0 & -\sin\theta & 0 & \cos\theta \end{bmatrix}, \tag{A.2}$$

$$[N] = \begin{bmatrix} \cos^2\theta & 0 & \sin^2\theta & 0 & \frac{\sin 2\theta}{2} & 0 \\ 0 & 1 & 0 & 0 & 0 & 0 \\ \sin^2\theta & 0 & \cos^2\theta & 0 & \frac{-\sin 2\theta}{2} & 0 \\ 0 & 0 & 0 & \cos\theta & 0 & -\sin\theta \\ -\sin 2\theta & 0 & \sin 2\theta & 0 & \cos 2\theta & 0 \\ 0 & 0 & 0 & \sin\theta & 0 & \cos\theta \end{bmatrix}. \tag{A.3}$$

The transformed elastic constants in the new coordinate system i.e. matrix [c^T] in Eq. (2.11) can be expressed as

$$\left[\mathbf{c}^T\right]=\begin{bmatrix} c_{11}^T & c_{12}^T & c_{13}^T & c_{14}^T & c_{15}^T & c_{16}^T \\ c_{12}^T & c_{22}^T & c_{23}^T & c_{24}^T & c_{25}^T & c_{26}^T \\ c_{13}^T & c_{23}^T & c_{33}^T & c_{34}^T & c_{35}^T & c_{36}^T \\ c_{14}^T & c_{24}^T & c_{34}^T & c_{44}^T & c_{45}^T & c_{46}^T \\ c_{15}^T & c_{25}^T & c_{35}^T & c_{45}^T & c_{55}^T & c_{56}^T \\ c_{16}^T & c_{26}^T & c_{36}^T & c_{46}^T & c_{56}^T & c_{66}^T \end{bmatrix}, \tag{A.4}$$

where

$$c_{11}^T = c_{11}\cos^4\theta + 2c_{13}\cos^2\theta\sin^2\theta + c_{33}\sin^4\theta + c_{44}(\sin 2\theta)^2,$$
$$c_{12}^T = c_{12}\cos^2\theta + c_{13}\sin^2\theta,$$
$$c_{13}^T = c_{11}\cos^2\theta\sin^2\theta + c_{13}\left(\cos^4\theta + \sin^4\theta\right) + c_{33}\cos^2\theta\sin^2\theta - c_{44}(\sin 2\theta)^2,$$
$$c_{14}^T = 0,$$
$$c_{15}^T = \left(c_{11}\cos^2\theta - c_{33}\sin^2\theta - c_{13}\cos 2\theta\right)0.5\sin 2\theta - c_{44}\cos 2\theta\sin 2\theta,$$
$$c_{16}^T = 0,$$
$$c_{22}^T = c_{11}^T,$$
$$c_{23}^T = c_{12}\sin^2\theta + c_{13}\cos^2\theta,$$
$$c_{24}^T = 0,$$
$$c_{25}^T = \left(c_{12} - c_{13}\right)0.5\sin 2\theta,$$
$$c_{26}^T = 0,$$
$$c_{33}^T = c_{11}\sin^4\theta + 2c_{13}\cos^2\theta\sin^2\theta + c_{33}\sin^4\theta + c_{44}(\sin 2\theta)^2,$$
$$c_{34}^T = 0,$$
$$c_{35}^T = \left(c_{11}\sin^2\theta + c_{33}\cos^2\theta + c_{13}\cos 2\theta\right)0.5\sin 2\theta + c_{44}\cos 2\theta\sin 2\theta,$$
$$c_{44}^T = c_{44}\cos^2\theta + c_{66}\sin^2\theta,\ c_{45}^T = 0,$$
$$c_{46}^T = \left(c_{66} - c_{44}\right)0.5\sin 2\theta,$$
$$c_{55}^T = \left(c_{11} - 2c_{13} + c_{33}\right)\left(0.5\sin 2\theta\right)^2 - c_{44}\left(\cos 2\theta\right)^2,\ c_{56}^T = 0,$$
$$c_{66}^T = c_{44}\sin^2\theta + c_{66}\cos^2\theta.$$

Appendix B Elements of a_m, b_m and c_m with $m = 1,2,3,4,5,6$

The explicit expression for a_m, b_m and c_m with $m = 1,2,3,4,5,6$ in Eqs. (2.35), (2.36) and (2.37) are expressed as follows

$$\left.\begin{aligned}
a_1 &= 2c_{16}l_x + (c_{12} + c_{66})l_y + (c_{14} + c_{56})l_z \\
a_2 &= 2c_{15}l_x + (c_{14} + c_{56})l_y + (c_{13} + c_{55})l_z \\
a_3 &= 2c_{56}l_x + (c_{46} + c_{25})l_y + (c_{36} + c_{45})l_z \\
a_4 &= c_{66}l_x + c_{26}l_y + c_{46}l_z \\
a_5 &= c_{55}l_x + c_{45}l_y + c_{35}l_z \\
a_6 &= c_{11}l_x + c_{16}l_y + c_{15}l_z
\end{aligned}\right\} \tag{B.1}$$

$$\left.\begin{aligned}
b_1 &= (c_{66} + c_{12})l_x + 2c_{26}l_y + (c_{46} + c_{25})l_z \\
b_2 &= (c_{56} + c_{14})l_x + 2c_{46}l_y + (c_{36} + c_{45})l_z \\
b_3 &= (c_{46} + c_{25})l_x + 2c_{24}l_y + (c_{44} + c_{23})l_z \\
b_4 &= c_{26}l_x + c_{22}l_y + c_{24}l_z \\
b_5 &= c_{45}l_x + c_{44}l_y + c_{34}l_z \\
b_6 &= c_{16}l_x + c_{66}l_y + c_{56}l_z
\end{aligned}\right\} \tag{B.2}$$

$$\left.\begin{aligned}
c_1 &= (c_{56} + c_{14})l_x + (c_{46} + c_{25})l_y + 2c_{45}l_z \\
c_2 &= (c_{55} + c_{13})l_x + (c_{45} + c_{36})l_y + 2c_{35}l_z \\
c_3 &= (c_{45} + c_{36})l_x + (c_{23} + c_{44})l_y + 2c_{34}l_z \\
c_4 &= c_{46}l_x + c_{24}l_y + c_{44}l_z \\
c_5 &= c_{35}l_x + c_{34}l_y + c_{33}l_z \\
c_6 &= c_{15}l_x + c_{55}l_y + c_{56}l_z
\end{aligned}\right\} \tag{B.3}$$

The Eqs. (B.1), (B.2) and (B.3) are employed in Eqs. (2.35), (2.36) and 2.37) to determine the ultrasonic ray Poynting vector (energy vector) directions and energy velocity magnitudes in general anisotropic media.

Appendix C Coefficients of Six Degree Polynomial Equation

The normal components of reflected and transmitted ray slowness components are obtained from the six degree polynomial equation. The simplified expressions for the coefficients in six degree polynomial equation are determined from the Christoffel's matrix [18, 26, 120]. The Christoffel's matrix is split into three (3x3) matrices where the first matrix L consists of terms containing S_x^2, S_y^2 and $S_x \cdot S_y$, the second matrix M consists of terms containing $S_x \cdot S_z$, $S_y \cdot S_z$ and the third matrix N consists of terms connected with S_z^2 .

$$L=\begin{bmatrix} \alpha_L & \beta_L & \delta_L \\ \beta_L & \varepsilon_L & \chi_L \\ \delta_L & \chi_L & \xi_L \end{bmatrix}, M=\begin{bmatrix} \alpha_M & \beta_M & \delta_M \\ \beta_M & \varepsilon_M & \chi_M \\ \delta_M & \chi_M & \xi_M \end{bmatrix}, N=\begin{bmatrix} C_{55} & C_{45} & C_{35} \\ C_{45} & C_{44} & C_{34} \\ C_{35} & C_{34} & C_{33} \end{bmatrix}. \tag{C.1}$$

where

$$\left.\begin{aligned} \alpha_L &= C_{11}S_x^2 + C_{66}S_y^2 + 2C_{16}S_x \cdot S_y \\ \varepsilon_L &= C_{66}S_x^2 + C_{22}S_y^2 + 2C_{26}S_x \cdot S_y \\ \xi_L &= C_{55}S_x^2 + C_{44}S_y^2 + 2C_{45}S_x \cdot S_y \\ \beta_L &= C_{16}S_x^2 + C_{26}S_y^2 + (C_{12}+C_{66})S_x \cdot S_y \\ \delta_L &= C_{15}S_x^2 + C_{46}S_y^2 + (C_{14}+C_{56})S_x \cdot S_y \\ \chi_L &= C_{56}S_x^2 + C_{24}S_y^2 + (C_{25}+C_{46})S_x \cdot S_y \end{aligned}\right\} \tag{C.2}$$

$$\left.\begin{aligned} \alpha_M &= 2(C_{15}S_x + C_{56}S_y) \\ \varepsilon_M &= 2(C_{46}S_x + C_{24}S_y) \\ \xi_M &= 2(C_{35}S_x + C_{34}S_y) \\ \beta_M &= (C_{56}+C_{14})S_x + (C_{46}+C_{25})S_y \\ \delta_M &= (C_{13}+C_{55})S_x + (C_{45}+C_{36})S_y \\ \chi_M &= (C_{36}+C_{45})S_x + (C_{44}+C_{23})S_y \end{aligned}\right\} \tag{C.3}$$

The coefficients of the six degree polynomial Eqs. (3.8) and (3.9) in S_z are expressed as follows

$$
\begin{aligned}
A &= \begin{vmatrix} C_{55} & C_{45} & C_{35} \\ C_{45} & C_{44} & C_{34} \\ C_{35} & C_{34} & C_{33} \end{vmatrix}, \\
B &= \begin{vmatrix} \alpha_M & \beta_M & \delta_M \\ C_{45} & C_{44} & C_{34} \\ C_{35} & C_{34} & C_{33} \end{vmatrix} + \begin{vmatrix} C_{55} & C_{45} & C_{35} \\ \beta_M & \varepsilon_M & \chi_M \\ C_{35} & C_{34} & C_{33} \end{vmatrix} + \begin{vmatrix} C_{55} & C_{45} & C_{35} \\ C_{45} & C_{44} & C_{34} \\ \delta_M & \chi_M & \xi_M \end{vmatrix}, \\
C &= \begin{vmatrix} \alpha_L & \beta_L & \delta_L \\ C_{45} & C_{44} & C_{34} \\ C_{35} & C_{34} & C_{33} \end{vmatrix} + \begin{vmatrix} \alpha_M & \beta_M & \delta_M \\ \beta_M & \varepsilon_M & \chi_M \\ C_{35} & C_{34} & C_{33} \end{vmatrix} + \begin{vmatrix} \alpha_M & \beta_M & \delta_M \\ C_{45} & C_{44} & C_{34} \\ \delta_M & \chi_M & \xi_M \end{vmatrix} \\
&\quad + \begin{vmatrix} C_{55} & C_{45} & C_{35} \\ \beta_L & \varepsilon_L & \chi_L \\ C_{35} & C_{34} & C_{33} \end{vmatrix} + \begin{vmatrix} C_{55} & C_{45} & C_{35} \\ \beta_M & \varepsilon_M & \chi_M \\ \delta_M & \chi_M & \xi_M \end{vmatrix} + \begin{vmatrix} C_{55} & C_{45} & C_{35} \\ C_{45} & C_{44} & C_{34} \\ \delta_L & \chi_L & \xi_L \end{vmatrix}, \\
D &= \begin{vmatrix} \alpha_L & \beta_L & \delta_L \\ \beta_M & \varepsilon_M & \chi_M \\ C_{35} & C_{34} & C_{33} \end{vmatrix} + \begin{vmatrix} \alpha_M & \beta_M & \delta_M \\ C_{45} & C_{44} & C_{34} \\ \delta_M & \chi_M & \xi_M \end{vmatrix} + \begin{vmatrix} \alpha_M & \beta_M & \delta_M \\ \beta_L & \varepsilon_L & \chi_L \\ C_{35} & C_{34} & C_{33} \end{vmatrix} \\
&\quad + \begin{vmatrix} \alpha_M & \beta_M & \delta_M \\ \beta_M & \varepsilon_M & \chi_M \\ \delta_M & \chi_M & \xi_M \end{vmatrix} + \begin{vmatrix} \alpha_M & \beta_M & \delta_M \\ C_{45} & C_{44} & C_{34} \\ \delta_L & \chi_L & \xi_L \end{vmatrix} + \begin{vmatrix} C_{55} & C_{45} & C_{35} \\ \beta_L & \varepsilon_L & \chi_L \\ \delta_M & \chi_M & \xi_M \end{vmatrix} \\
&\quad + \begin{vmatrix} C_{55} & C_{45} & C_{35} \\ \beta_M & \varepsilon_M & \chi_M \\ \delta_L & \chi_L & \xi_L \end{vmatrix}, \\
E &= \begin{vmatrix} \alpha_L & \beta_L & \delta_L \\ \beta_L & \varepsilon_L & \chi_L \\ C_{35} & C_{34} & C_{33} \end{vmatrix} + \begin{vmatrix} \alpha_L & \beta_L & \delta_L \\ \beta_M & \varepsilon_M & \chi_M \\ \delta_M & \chi_M & \xi_M \end{vmatrix} + \begin{vmatrix} \alpha_L & \beta_L & \delta_L \\ C_{45} & C_{44} & C_{34} \\ \delta_L & \chi_L & \xi_L \end{vmatrix} \\
&\quad + \begin{vmatrix} \alpha_M & \beta_M & \delta_M \\ \beta_L & \varepsilon_L & \chi_L \\ \delta_M & \chi_M & \xi_M \end{vmatrix} + \begin{vmatrix} \alpha_M & \beta_M & \delta_M \\ \beta_M & \varepsilon_M & \chi_M \\ \delta_L & \chi_L & \xi_L \end{vmatrix} + \begin{vmatrix} C_{55} & C_{45} & C_{35} \\ \beta_L & \varepsilon_L & \chi_L \\ \delta_L & \chi_L & \xi_L \end{vmatrix}, \\
F &= \begin{vmatrix} \alpha_L & \beta_L & \delta_L \\ \beta_L & \varepsilon_L & \chi_L \\ \delta_M & \chi_M & \xi_M \end{vmatrix} + \begin{vmatrix} \alpha_L & \beta_L & \delta_L \\ \beta_M & \varepsilon_M & \chi_M \\ \delta_L & \chi_L & \xi_L \end{vmatrix} + \begin{vmatrix} \alpha_M & \beta_M & \delta_M \\ \beta_L & \varepsilon_L & \chi_L \\ \delta_L & \chi_L & \xi_L \end{vmatrix}, \\
G &= \begin{vmatrix} \alpha_L & \beta_L & \delta_L \\ \beta_L & \varepsilon_L & \chi_L \\ \delta_L & \chi_L & \xi_L \end{vmatrix}.
\end{aligned}
\tag{C.4}
$$

Appendix D Analytical Evaluation of Quartic Equation

The quartic equation resulting from the characteristic Eq. (3.10)

$$Ax^4 + Bx^3 + Cx^2 + Dx \ + E = 0 \tag{D.1}$$

where $x = S_z$ is the vertical component of the slowness vector.

Eq. (3.21) can be solved analytically [114] as follows:

Reduced quartic equation is obtained by employing $y = x + \left(B / 4A\right)$ in Eq. (D.1) and the resulting quartic equation is given as

$$y^4 + py^2 + qy + r = 0 \tag{D.2}$$

where

$$\left.\begin{aligned} p &= \left(\frac{C}{A}\right) - \left(\frac{3B^2}{8A^2}\right) \\ q &= \left(\frac{B^3}{8A^3}\right) - \left(\frac{BC}{2A^2}\right) + \left(\frac{D}{A}\right) \\ r &= \left(\frac{-3B^4}{256A^4}\right) + \left(\frac{B^2C}{16A^3}\right) - \left(\frac{BD}{4A^2}\right) + \left(\frac{E}{A}\right) \end{aligned}\right\} \tag{D.3}$$

Euler's method can be employed to solve the reduced quartic equation.

Assuming $y = u + v + w$ and substitution of y in Eq. (D.2), yields

$$\left.\begin{aligned} &4\alpha_1 + \left(\alpha_2\right)^2 + p\alpha_2 + r + \alpha_3\left(4\alpha_2 + 2p\right) + \alpha_4\left(8\alpha_5 + q\right) = 0 \\ &\alpha_1 = v^2w^2 + w^2u^2 + u^2v^2 \\ &\alpha_2 = v^2 + u^2 + w^2 \\ &\alpha_3 = uv + vw + wu \\ &\alpha_4 = u + v + w \\ &\alpha_5 = uvw \end{aligned}\right\} \tag{D.4}$$

The resulting cubic resolvent equation

$$z^3 + 2pz^2 + \left(p^2 - 4r\right)z - q^2 = 0 \tag{D.5}$$

where $u = \pm\frac{\sqrt{z_1}}{2}, v = \pm\frac{\sqrt{z_2}}{2}, w = \pm\frac{\sqrt{z_3}}{2}$ are the roots of the cubic resolvent equation.

Now by substituting $Z = z + 2\frac{p}{3}$ in the cubic resolvent equation, Eq. (D.5) yields a reduced cubic equation as

$$Z^3 + P_1 Z + Q = 0 \tag{D.6}$$

where

$$P_1 = \left(p^2 - 4r\right) - \left(4p^2 / 3\right),\ Q = \left(16p^3 / 27\right) - \left(2p\frac{\left(p^2 - 4r\right)}{3}\right) - q^2 \tag{D.7}$$

The roots of the cubic Eq. (D.6) can be obtained from the Cardano's Method [114] and by assuming Z= h + k and substituting into the Eq. (D.6), the resulting cubic roots are given as

$$Z_1 = h + k,\ Z_2 = \beta_1 h + \beta_2 k,\ Z_3 = \beta_2 h + \beta_1 k \tag{D.8}$$

where

$$\left.\begin{aligned} h &= \sqrt[3]{-\frac{Q}{2} + \sqrt{\left(\frac{P_1}{3}\right)^3 + \left(\frac{Q}{2}\right)^2}},\ k = \frac{-P}{3h} \\ \beta_1 &= \frac{-1}{2} + \frac{i\sqrt{3}}{2},\ \beta_2 = \frac{-1}{2} - \frac{i\sqrt{3}}{2} \end{aligned}\right\} \tag{D.9}$$

Back substitution and solving the equation yields

$$z_i = Z_i - 2\left(\frac{p}{3}\right),\ i=1,2,3 \tag{D.10}$$

The four roots of the quartic equation can be deduced as

$$\left.\begin{aligned} \mathrm{y}_1 &= 0.5\left(\sqrt{z_1} + \sqrt{z_2} - \sqrt{z_3}\right),\ y_2 = 0.5\left(\sqrt{z_1} - \sqrt{z_2} + \sqrt{z_3}\right) \\ y_3 &= 0.5\left(-\sqrt{z_1} + \sqrt{z_2} + \sqrt{z_3}\right),\ y_4 = 0.5\left(-\sqrt{z_1} - \sqrt{z_2} - \sqrt{z_3}\right) \end{aligned}\right\} \tag{D.11}$$

The roots of the quartic Eq. (D.1) resulting from the characteristic equation are obtained by

$$S_z^{NqP,qSV} = x_k = y_k - \left(\frac{B}{4A}\right), k = 1,2,3,4 \tag{D.12}$$

N represents the reflected (or) transmitted wave.

Appendix E Analytical Expressions for Reflection and Transmission Coefficients at an Interface between two Transversely Isotropic Materials

$$a_{11} = -\cos\left(\theta_s^{IqP}\right), a_{12} = -\cos\left(\theta_s^{RqP}\right)\left(\frac{p^{RqP}}{p^{IqP}}\right), a_{13} = \sin\left(\theta_s^{RqSV}\right)\left(\frac{p^{RqSV}}{p^{IqP}}\right),$$

$$a_{14} = -\cos\left(\theta_s^{TqP}\right)\left(\frac{p^{TqP}}{p^{IqP}}\right), a_{15} = \sin\left(\theta_s^{TqSV}\right)\left(\frac{p^{TqSV}}{p^{IqP}}\right), a_{21} = \sin\left(\theta_s^{IqP}\right)$$

$$a_{22} = -\sin\left(\theta_s^{RqP}\right)\left(\frac{p^{RqP}}{p^{IqP}}\right), a_{23} = -\cos\left(\theta_s^{RqSV}\right)\left(\frac{p^{RqSV}}{p^{IqP}}\right), a_{24} = \sin\left(\theta_s^{TqP}\right)\left(\frac{p^{TqP}}{p^{IqP}}\right),$$

$$a_{25} = \cos\left(\theta_s^{TqSV}\right)\left(\frac{p^{TqSV}}{p^{IqP}}\right)$$

$$a_{31} = \left(C_{13}\sin\left(\theta_s^{IqP}\right) + C_{35}\cos\left(\theta_s^{IqP}\right)\right) + \left(\left(C_{33}\cos\left(\theta_s^{IqP}\right) + C_{55}\sin\left(\theta_s^{IqP}\right)\right)\cot\left(\theta^{IqP}\right)\right)$$

$$a_{32} = \left(\left(C_{13}\sin\left(\theta_s^{RqP}\right) + C_{35}\cos\left(\theta_s^{RqP}\right)\right) + \left(\left(-C_{33}\cos\left(\theta_s^{RqP}\right) + C_{35}\sin\left(\theta_s^{RqP}\right)\right)\cot\left(\theta^{RqP}\right)\right)\left(\frac{p^{RqP}}{p^{IqP}}\right)\right)$$

$$a_{33} = \left(\left(-C_{13}\cos\left(\theta_s^{RqSV}\right) + C_{35}\sin\left(\theta_s^{RqSV}\right)\right) + \left(\left(C_{33}\sin\left(\theta_s^{RqSV}\right) - C_{35}\cos\left(\theta_s^{RqSV}\right)\right)\cot\left(\theta^{RqSV}\right)\right)\left(\frac{p^{RqSV}}{p^{IqP}}\right)\right)$$

θ_s^{IqP}, θ_s^{RqP}, θ_s^{TqP}, θ^{IqP}, θ^{RqP}, θ^{TqP} are the polarization directions and phase directions for incident, reflected and transmitted qP waves

θ_s^{RqSV}, θ_s^{TqSV}, θ^{RqSV}, θ^{TqSV} are the polarization directions and phase directions for reflected and transmitted qSV waves

p^{IqP}, p^{RqP}, p^{TqP} are the polarization magnitudes for the incident, reflected and transmitted qP waves

p^{RqSV}, p^{TqSV} are the polarization magnitudes for the reflected and transmitted qSV waves

$$a_{34} = \left(\left(C_{13}^{1} \sin\left(\theta_s^{TqP} \right) - C_{35}^{1} \cos\left(\theta_s^{TqP} \right) \right) + \left(\left(C_{33}^{1} \cos\left(\theta_s^{TqP} \right) - C_{35}^{1} \sin\left(\theta_s^{TqP} \right) \right) \cot\left(\theta^{TqP} \right) \right) \left(\frac{p^{TqP}}{p^{IqP}} \right) \right)$$

$$a_{35} = \left(\left(-C_{13}^{1} \cos\left(\theta_s^{TqSV} \right) + C_{35}^{1} \sin\left(\theta_s^{TqSV} \right) \right) + \left(\left(-C_{33}^{1} \sin\left(\theta_s^{TqSV} \right) + C_{35}^{1} \cos\left(\theta_s^{TqSV} \right) \right) \cot\left(\theta^{TqSV} \right) \right) \left(\frac{p^{TqSV}}{p^{IqP}} \right) \right)$$

$$a_{41} = \left(-C_{15} \sin\left(\theta_s^{IqP} \right) - C_{55} \cos\left(\theta_s^{IqP} \right) \right) + \left(\left(-C_{35} \cos\left(\theta_s^{IqP} \right) - C_{55} \sin\left(\theta_s^{IqP} \right) \right) \cot\left(\theta^{IqP} \right) \right)$$

$$a_{42} = \left(\left(-C_{15} \sin\left(\theta_s^{RqP} \right) + C_{55} \cos\left(\theta_s^{RqP} \right) \right) + \left(\left(-C_{35} \cos\left(\theta_s^{RqP} \right) + C_{55} \sin\left(\theta_s^{RqP} \right) \right) \cot\left(\theta^{RqP} \right) \right) \left(\frac{-p^{RqP}}{p^{IqP}} \right) \right)$$

$$a_{43} = \left(\left(-C_{15} \cos\left(\theta_s^{RqSV} \right) - C_{55} \sin\left(\theta_s^{RqSV} \right) \right) + \left(\left(C_{35} \sin\left(\theta_s^{RqSV} \right) + C_{55} \cos\left(\theta_s^{RqSV} \right) \right) \cot\left(\theta^{RqSV} \right) \right) \left(\frac{-p^{RqSV}}{p^{IqP}} \right) \right)$$

$$a_{44} = \left(\left(C_{15}^{1} \sin\left(\theta_s^{TqP} \right) - C_{55}^{1} \cos\left(\theta_s^{TqP} \right) \right) + \left(\left(C_{35}^{1} \cos\left(\theta_s^{TqP} \right) - C_{55}^{1} \sin\left(\theta_s^{TqP} \right) \right) \cot\left(\theta^{TqP} \right) \right) \left(\frac{p^{TqP}}{p^{IqP}} \right) \right)$$

$$a_{45} = \left(\left(C_{15}^{1} \cos\left(\theta_s^{TqSV} \right) + C_{55}^{1} \sin\left(\theta_s^{TqSV} \right) \right) + \left(\left(-C_{35}^{1} \sin\left(\theta_s^{TqSV} \right) - C_{55}^{1} \cos\left(\theta_s^{TqSV} \right) \right) \cot\left(\theta^{TqSV} \right) \right) \left(\frac{p^{TqSV}}{p^{IqP}} \right) \right)$$

$$\mathbf{M_1} = \begin{bmatrix} a_{12} & a_{13} & a_{14} & a_{15} \\ a_{22} & a_{23} & a_{24} & a_{25} \\ a_{32} & a_{33} & a_{34} & a_{35} \\ a_{42} & a_{43} & a_{44} & a_{45} \end{bmatrix}, \mathbf{M_2} = \begin{bmatrix} a_{11} & a_{13} & a_{14} & a_{15} \\ a_{21} & a_{23} & a_{24} & a_{25} \\ a_{31} & a_{33} & a_{34} & a_{35} \\ a_{41} & a_{43} & a_{44} & a_{45} \end{bmatrix}, \mathbf{M_3} = \begin{bmatrix} a_{12} & a_{11} & a_{14} & a_{15} \\ a_{22} & a_{21} & a_{24} & a_{25} \\ a_{32} & a_{31} & a_{34} & a_{35} \\ a_{42} & a_{41} & a_{44} & a_{45} \end{bmatrix}$$

$$\mathbf{M_4} = \begin{bmatrix} a_{12} & a_{13} & a_{11} & a_{15} \\ a_{22} & a_{23} & a_{21} & a_{25} \\ a_{32} & a_{33} & a_{31} & a_{35} \\ a_{42} & a_{43} & a_{41} & a_{45} \end{bmatrix}, \mathbf{M_5} = \begin{bmatrix} a_{12} & a_{13} & a_{14} & a_{11} \\ a_{22} & a_{23} & a_{24} & a_{21} \\ a_{32} & a_{33} & a_{34} & a_{31} \\ a_{42} & a_{43} & a_{44} & a_{41} \end{bmatrix}.$$

Amplitude coefficients for the reflected and transmitted plane elastic waves

$$A^{RqP} = \frac{\det(\mathbf{M_2})}{\det(\mathbf{M_1})}, A^{RqSV} = \frac{\det(\mathbf{M_3})}{\det(\mathbf{M_1})}, A^{TqP} = \frac{\det(\mathbf{M_4})}{\det(\mathbf{M_1})}, A^{TqSV} = \frac{\det(\mathbf{M_5})}{\det(\mathbf{M_1})} \tag{E.1}$$

Nomenclature

Symbols

Symbol	Dimension	Meaning
k	mm^{-1}	Wave number
A		Amplitude coefficient
$\mathbf{p}$		Polarization vector
r	mm	Distance
x,y,z	mm	Cartesian coordinates
$\mathbf{S}$		Strain field
$\mathbf{T}$	N/m^2	Stress field
ω	rad/s	Angular frequency
c_{ij}	GPa	Material elastic constant
u		Particle displacement
ρ	Kg/m^3	Material density
$[\mathbf{M}]$		Bond transformation matrix
l_x, l_y, l_z		Directional cosines
$\mathbf{\Gamma}_{ij}$		Christoffels matrix
θ	(°)	Columnar grain angle
ψ	(°)	Layback angle
V_{qP}	m/s	Quasi longitudinal wave velocity
V_{qSV}	m/s	Quasi shear vertical wave velocity
V_{SH}	m/s	Pure shear horizontal wave velocity
S_{qP}	s/m	Quasi longitudinal wave slowness

S_{qSV}	s/m	Quasi shear vertical wave slowness
S_{SH}	s/m	Pure shear horizontal wave slowness
$\mathbf{P}_{av}$	$N/m.s$	Average Poynting vector
$\mathbf{U}_{av}$	$Kg/m.s^2$	Average energy density
β	(°)	Beam skewing angle
$E^{R\alpha}$		Energy reflection coefficient
$E^{T\alpha}$		Energy transmission coefficient
i		Imaginary unit $i=\sqrt{-1}$
I		Incident wave
K_1, K_2, K_3	GPa	Shear and longitudinal stiffness constants
$D_{\alpha,I}(\theta)$		Directivity of the source
η		Change of grain orientation as a function of distance x
V_g	m/s	Energy velocity
σ	S/m	Material conductivity
μ	F/m	Material permittivity
$B_{\|}$	T	Magnetic field
$u_{\|}$	V	Induced voltage
$G(x,z)$		Empirical function for grain orientation
$T_1,\ T_2$		Slope at the left and right weld flanks
$[a]$		Coordinate transformation matrix
λ	mm	Wavelength
f	MHz	Transducer frequency

Abbreviations

Abbreviation	Meaning
RAYTRAIM	Ray Tracing Model for Anisotropic and Inhomogeneous Materials
RTM	Ray Tracing Model
EFIT	Elastodynamic Finite Integration Technique
BEM	Boundary Element Method
FEM	Finite Element Method
GBS	Gaussian Beam Superposition
RMSLM	Rectangular Mass Spring Lattice Model
FDM	Finite Difference Method
MINA	Modeling of Anisotropy from Notebook of Arc Welding
SAFT	Synthetic Aperture Focusing Technique
NDT	Non-Destructive Testing
BS	Beam Spread
BD	Beam Divergence
FBSM	Finite Boundary Stiffness Model
TIGW	Tungsten Inert Gas Welding
SNR	Signal to Noise Ratio
SAWT	Surface Acoustic Wave Technique
HAZ	Heat Affected Zone
TF	Transmission Factor

List of Figures

List of Tables

List of Publications from this Ph.D. work

[P1] S. R. Kolkoori, M. U. Rahman, P. K. Chinta, M. Kreutzbruck, M. Rethmeier, J. Prager, Ultrasonic field profile evaluation in acoustically inhomogeneous anisotropic materials using 2D ray tracing model: Numerical and experimental comparison, *Ultrasonics*, Vol. **53**, pp. 396-411, 2013.

[P2] S. R. Kolkoori, C. Hoehne, J. Prager, M. Rethmeier, M. Kreutzbruck, Quantitative evaluation of ultrasonic C-scan image in acoustically homogeneous and anisotropic layered materials using 3D ray tracing method, *Ultrasonics* (Under review).

[P3] Sanjeevareddy Kolkoori, M. U. Rahman, Jens Prager, Effect of columnar grain orientation on energy reflection and transmission behaviour in anisotropic austenitic weld materials, *Journal of Nondestructive Evaluation*,Vol. **31**, pp. 253 269, 2012.

[P4] S. R. Kolkoori, M. U. Rahaman, P. K. Chinta, M. Kreutzbruck, J. Prager, Quantitative evaluation of ultrasonic sound fields in anisotropic austenitic welds using a 2D ray tracing model, *Review of Progress in Quantitative Non-destructive Evaluation*, American Institute of Physics**,** Vol. **31**, pp.1227-1234, 2012.

[P5] Christian Hoehne, Sanjeevareddy Kolkoori, Mehbub Ur Rahman, Rainer Boehm, Jens Prager, SAFT Imaging of Transverse Cracks in Austenitic and Dissimilar Welds, *Journal of Nondestructive Evaluation*, Vol.**32**, pp. 51-66, 2013.

[P6] S. R. Kolkoori, P. Shokouhi, C. Hoehne, M. U. Rahman, M. Kreutzbruck, J. Prager, A comparative study of ray tracing and CIVA simulation for ultrasonic examination of anisotropic inhomogeneous austenitic welds, *Review of Progress in Quantitative Nondestructive Evaluation*, American Institute of Physics**,** Vol. **32**, pp. 1043-1050, 2013.

[P7] S. R. Kolkoori, M. U. Rahaman, P. K. Chinta, R. Boehm, J. Prager, Simulation of ultrasonic sound fields in anisotropic materials using 2-D ray tracing method, *International Congress on Ultrasonics*, American Institute of Physics**,** Vol. **1433**, pp.743-746, 2012.

[P8] S. R. Kolkoori, M. U. Rahaman, J. Prager, M. Kreutzbruck, Acoustic wave energy skewing and coefficients for the reflection and transmitted plane waves in general homogeneous transversal isotropic austenitic material, *Proceedings of 8th International Conference on NDE in relation to Structural Integrity for Nuclear and Pressurized Components*, Deutsche Gesellschaft für Zerstörungsfreie Prüfung (DGZfP), pp. 845-854, 2011.

[P9] Sanjeevareddy Kolkoori, Mehbub Ur Rahman, J. Prager, 3D Ray tracing model for ultrasound field evaluation in inhomogeneous anisotropic materials: Model and Experimental Validation, 38. Deutsche Jahrestagung für Akustik, *Proceedings of Deutsche Gesellschaft für Akustik*, pp. 959-960, 2012.

[P10] M. U. Rahman, S. R. Kolkoori, J. Prager, Elastische Wellenausbreitung in austenitischen Schweißnähten: Numerische Simulationen und deren messtechnische Validierung, *Proceedings of Deutsche Gesellschaft für Akustik*, Vol. **37**, pp. 341-342, 2011.

[P11] S. R. Kolkoori, M. U. Rahman, P. K. Chinta, J. Prager, Computationally efficient ray tracing algorithm for simulation of transducer generated ultrasonic fields in anisotropic materials, *Proceedings of Nondestructive Testing and Evaluation*, pp. 483-486, 2012.